Characterising Spinal Cord Injury-Induced Osteoporosis in a Rat Model using micro-Computed Tomography and Histology

Flynn James Lachendro

A thesis presented for the degree of Doctor of Engineering (EngD)

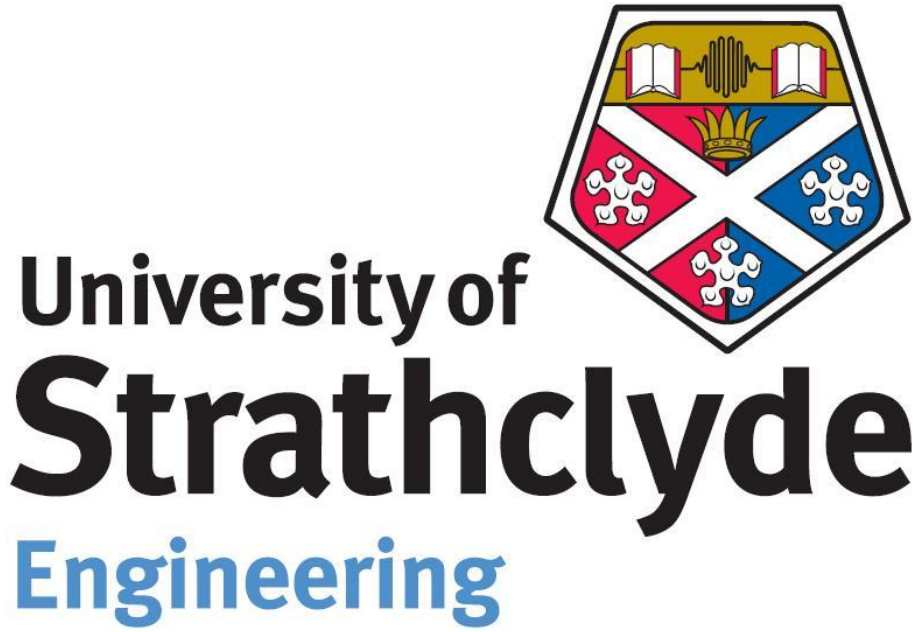

Department of Biomedical Engineering

14th November, 2022

Declaration

All research in this thesis is original, and the author's own. This thesis has been written entirely by the author, and has not been used previously for any examination leading to the awarding of a degree.

Signed:

Flynn James Lachendro

14/11/2022

Abstract

Severe spinal cord injury (SCI) can result in the complete or partial paralysis of sublesional (below the level of injury) limbs. Associated with this are a large number of secondary complications which include a higher risk of bone 'fragility fractures' due in part to the removal of muscle-driven bone stimulation. The fractures occur most commonly in the trabecular bone-rich distal femur and proximal tibia during movements such as falls and transferring from bed to wheelchair. The occurrence of these fractures increases with time post-injury. Complications arising from these fractures decrease quality of life and increase morbidity and mortality in the affected population.

This thesis aims to characterise the acute and chronic effects of complete SCI in the distal femur and proximal tibia using a rat model, through analysing the bone quantity and microarchitecture, resorption activity and blood supply using several newly developed methods to give deeper understanding of the condition. The high-resolution obtained with micro computed-tomography (microCT) is utilised to present new insights into the bone's morphological and topological changes following SCI. Additionally, quantitative histology is employed to analyse the average number of osteoclasts (bone removing cells) and blood vessels in the affected regions. Insights from microCT and histology are combined where possible to provide a more complete picture of the progression of SCI-induced osteoporosis from the acute to chronic stages.

Following SCI, rapid bone loss was found in the trabecular bone, which worsened slightly by the chronic stages. At 2 weeks post-injury (the acute stage), bone volume fraction was seen to reduce by 61% in the proximal tibia compared to age-matched, sham-operated controls. A 71% decrease was seen by 11 weeks post-injury (the chronic stage). This trend was also displayed in the average trabecular thickness (↓12/23%) and number (↓55/64%) in the two sets of rats, respectively. Only analysed at the chronic timepoint, the distal femur mirrored the proximal tibia results in trabecular bone loss.

SCI also exhibited a significant effect on the rod-like/plate-like distribution of trabeculae in the distal femur, with median ellipsoid factor increasing by 163%, whereas no such change was detected at either timepoint in the proximal tibia. These results suggest that the plate-to-rod transition thought to affect osteoporotic bone occurs in a region-specific manner.

The node type abundance (relative numbers of trabecular junctions of 3, 4 or 5 trabeculae) was significantly altered in both the distal femur (4N nodes) and proximal tibia (3N nodes) in chronic SCI rats, however it remained unaltered in the proximal tibia in acute SCI rats. The average angle between trabeculae was not altered in chronic SCI rats in both the distal femur and the proximal tibia, however, the in acute SCI rats, the proximal tibia exhibited a significantly reduced mean inter-trabecular angle in each of the three node types. These results suggest that the bone microarchitecture suffers in acute SCI due to an impairment in the trabecular topology; the trabeculae are less-optimally aligned for mechanical load transmission due to bone remodelling effects and trabecular breakages. This impairment appears to be recovered in chronic SCI rats, with the slightly altered node type abundance ratios remaining as evidence of long-term disruption in the bone remodelling balance.

The cortical bone exhibited a slower response to SCI, with no change in proximal tibia cortical area in acute SCI rats, but a decrease of 18% in chronic SCI rats. Cortical bone tissue mineral density was not seen to be altered in either acute or chronic rats compared to sham controls. These results indicate that bone quality impairment due to SCI is due to morphological and topological changes in the affected bone, as opposed to a decrease in the average density of the bone mineral.

Also only analysed in chronic SCI rats, the histology results helped provide a deeper understanding of the bone cell response to complete SCI. The trabecular resorption activity was not seen to be altered at the chronic stage, but the trabecular microvessel density was seen to significantly decrease by 52% compared to control in the chronic SCI distal femur. No significant change in cortical microvessel density was observed. This suggests region-specific changes in blood supply to trabecular bone, whilst cortical bone vasculature appeared to remain unaffected. The results also illustrate that

the initial bone loss effects are likely due to increased resorption activity of each osteoclast, as opposed to greater numbers of the bone removing cells.

Combined, the findings from the microCT and histology assessments lend weight to the idea that bone loss following SCI occurs site-specifically and at different rates throughout the sublesional long bones. They also highlight that the rapid onset of trabecular bone microarchitecture reduction is worsened by an impairment in the network's topology and local morphometry. Additionally, the results suggest that activity of the pre-existing osteoclasts increases to produce the resorption effects following SCI, as opposed to a greater recruitment of new osteoclasts to the affected sites. Although the trabecular topology (mean inter-trabecular angle) is shown to recover the initial impairment over time, the mean local morphometry (ellipsoid factor) can display significant lasting effects due to chronic SCI. Finally, it is indicated that the blood network in trabecular bone is significantly diminished at the chronic timepoint post-injury.

Contents

List of Tables

List of Figures

Appendices

List of Equations

List of Abbreviations

General

BLC: Bone Lining Cell | **BRC**: Bone Remodelling Compartment | **DF**: Distal Femur

dOP: disuse Osteoporosis | **GP**: Growth Plate | **HSB**: Hue, Saturation, Brightness

MSS: Metaphyseal Secondary Spongiosa | **MSC**: Mesenchymal Stem Cell

OP: Osteoporosis | **PS**: Primary Spongiosa | **PT**: Proximal Tibia

ROI: Region Of Interest | **SCI**: Spinal Cord Injury | **SD**: Sprague-Dawley (rat)

VOI: Volume Of Interest

Microscale Computed Tomography

AC: Attenuation Coefficient | **ADU**: Analogue to Digital Unit

BMD: Bone Mineral Density | **BS/BV**: Bone Surface / Bone Volume

BV: Bone Volume | **BV/TV**: Bone Volume / Total Volume

CaHA: Calcium Hydroxyapatite | **CCD**: Charged Couple Device

Conn.D: Connectivity Density | **CT**: Computed Tomography | **Ct.Ar**: Cortical Area

DXA: Dual energy X-ray Absorptiometry | **Ecc**: Eccentricity | **EF**: Ellipsoid Factor

FD: Fractal Dimension | **FDK**: Feldkamp-David-Kress (algorithm)

ITA: Inter-Trabecular Angle | **J**: Polar Second Moment of Area

Ma.Ar: Medullary Area | **microCT**: microscale Computed-Tomography | **px**: Pixel(s)

Tt.Ar: Total Area | **Tb.N**: Trabecular Number | **Tb.Sp**: Trabecular Separation

Tb.Th: Trabecular Thickness | **TMD**: Tissue Mineral Density

Histology

ABC: Avidin-Biotin Complex | **BIM**: Basic Incubation Medium

CATK: Cathepsin K | **DAB**: Diaminobenzidine

EDTA: Ethylenediaminetetraacetic Acid | **EtOH**: Ethanol

FFPE: Formalin-Fixed, Paraffin-Embedded | **GFP**: Green Fluorescent Protein

H&E: Haematoxylin & Eosin **| HSC**: Haematopoietic Stem Cell

HRP: Horseradish Peroxidase | **IHC**: Immunohistochemistry

Mv.D: Microvessel Density | **NBF**: Neutral-Buffered Formalin

Oc.S/BS: Osteoclast Surface per Bone Surface | **PBS**: Phosphate-Buffered Saline

TRAP: Tartrate-Resistant Acid Phosphatase | **vWF**: von Willebrand Factor

Acknowledgements

I would like to thank Dr. Jonathan Williams for providing invaluable technical expertise in microCT and digital image processing, as well as performing the vast majority of animal care and surgeries. Also to Dr. Sylvie Coupaud for her constant support, oversight and organisational help. Dr. Susan Chalmers is thanked for her expertise in histology and aid in procuring essential lab resources. Many thanks to Dr. John Riddell, who enabled this study through provision of the animal cohorts and laboratory facilities necessary for completing the work. I am very grateful to Margaret Nilsen for her technical guidance in the histology lab, and to Dr. Mairi Sandison for providing quality feedback on the histology section of this thesis. Many thanks to Prof. Stuart Reid for enabling completion of this project via continued academic support in the face of COVID-19 delays.

The constant encouragement from Ingrid Martin as well as my parents, friends and EngD companions is the main reason that I managed to complete this thesis. I will always be so thankful for all of your kind words.

Chapter 1: Introduction

Bone continually renews its structure by replacing its mineral, collagenous and cellular components throughout a normal lifespan. The process of removing old bone and replacing it with new material is known as the bone remodelling cycle. An imbalance in this cycle (higher resorption than formation levels) leads to a reduction in bone mineral density. Once bone density reduces to a level below 2.5 standard deviations from the age-matched average, the condition is defined as osteoporosis (London *et al.* 1999).

Osteoporosis causes an increased fracture risk in those affected, with numerous quality of life issues for affected patients (Johnell & Kanis 2006). The form regarding the immobilised population is known as disuse osteoporosis (dOP) (Li *et al.* 2005). In patients affected by disuse, the number and efficacy of different rehabilitation techniques is diminished. Additionally, the risk of fracture significantly increases in the sublesional bones. This presents a major problem to clinical staff (Eser *et al*. 2004).

The most common cause of disuse is stroke (Kuriakose & Xiao 2020). The second most common is spinal cord injury (SCI) (Armour *et al*. 2016). SCI results primarily from falls as well as automotive and sporting accidents, with around 180,000 new cases annually (Lee *et al*. 2013). The injury can be either a contusion to the spinal cord (most common in humans), or a complete transection.

The distinction between dOP (which has a variety of causes and can occur in the absence of SCI) and SCI-induced osteoporosis is important. SCI brings about different effects than conditions such as auto-immune disease, poisoning, low gravity, bed rest and stroke due to the damage or severing of the spinal cord. This causes impairment to bone homeostasis by inducing altered hormone levels, loss of nerve fibres and loss of vasculature in the affected regions (Guertin 2011, Tan *et al.* 2013).

The drop in bone formation in the long bones following SCI appears to be primarily due to the disuse i.e. the decrease in instigating osteogenic signals from the mechanical load-sensitive osteocytes in bone (Bonewald 2011). Such mechanical loads come in three varieties: muscular contractions surrounding and attached to bone, static gravity effects when standing, and ground reaction forces from locomotion (Lau & Guo 2011).

The bone remodelling cycle occurs on osseous surfaces as a combination of actions by numerous neighbouring cell types and supply routes (Hauge *et al.* 2001). As surface to volume ratio and blood vessel density is greater in trabecular bone than in cortical (Lafage-Proust *et al.* 2015), trabecular bone is much more significantly affected by changes to the bone remodelling balance and hence by SCI, at least in the acute time periods following injury (Osterhoff *et al*. 2016). Nonetheless, it is still useful to characterise the condition in as many bone types and via as many analyses as possible.

This project aims to characterise SCI-induced osteoporosis via examination of the osseous (bone quantity and microarchitecture) and intraosseous (osteoclasts and blood vessels) material in a rat model of complete SCI, to provide deeper understanding of the condition. Micro computed-tomography (microCT) and histology are the two main techniques used, within which multiple analysis protocols are developed for insight. The protocols and results produced herein serve as a basis for a wide variety of potential future studies into the condition. This is vital if any effective treatments are to be developed, as the pathophysiology of SCI-induced osteoporosis differs greatly from other modes such as age-related and post-menopausal osteoporosis (Lau & Guo 2011).

The chosen model of SCI is a rat model of SCI via complete transection of the spinal cord at the thoracic 9 (T9) vertebra. This is selected to mimic the SCI experienced by humans in the clinical setting. Fragility fractures present a significant long-term risk to SCI patients in the clinical setting, causing a severe detriment to the quality of life alongside the other side-effects of paralysis (which include chronic pain, heart and lung complications and spasticity) (Sezer 2015). The rate of fracture in the SCI human population compared to the able-bodied population is around twice as high and these patients present much longer recovery times, if they heal at all (Vestergaard *et al*. 1998, Frotzler et al., 2015).

In this project, microCT scans are produced at the trabecular-rich distal femur and proximal tibia in the rat, as these are the two regions most affected by SCI (Eser *et al*. 2004). Utilising this time-intensive, high-resolution X-ray imaging technique (compared to the more clinically apt methods like dual energy X-ray absorptiometry

(DXA)) allows for more detailed insights into bone microarchitectural changes following SCI.

Standard microCT analysis (Bouxsein *et al.* 2010) is performed (for both trabecular and cortical bone) alongside two novel analyses which have been recently developed: ellipsoid factor (EF) (Doube 2015) and inter-trabecular angle (ITA) (Reznikov *et al*. 2016). Comparisons are made between acute (2 weeks post-injury) and chronic (11 weeks post-injury) SCI rats and age-matched sham-operated controls. Additionally, microCT results are compared between the distal femur and proximal tibia, to compare the effects of SCI in different affected bones.

Ellipsoid factor (EF) is an alternative to structure model index (SMI) as a measure of the general rod-like or plate-like local geometries in trabecular bone (Salmon *et al*. 2015). EF analysis is utilised to give an indication of both the average local shapes in trabecular bone and the spatial distribution of these different geometries. The inter-trabecular angles (ITAs) are analysed as a bone topological measurement alongside the spatial distribution of the trabecular junctions (nodes) of different connectedness within each volume.

With the bone itself examined using microCT, the intraosseous material is analysed using histology and immunohistochemistry (IHC). Staining protocols are developed and optimised from pre-existing standard methods. They are utilised to highlight the osteoclasts and endothelial cells via staining for tartrate-resistant acid phosphatase (TRAP) and CD34, respectively. Comparisons are made between chronic SCI and control rats, whereas the acute dataset could only be analysed using microCT. Quantification of the histological images is performed in a standard manner for TRAP, with a custom analysis method used for CD34 measurement of microvessel density.

In this thesis a literature review is given first, highlighting the anatomy and physiology of the types of bone and bone regions analysed in this project, as well as an overview of the bone cells involved in the bone remodelling cycle and their associated signal pathways. Two individual chapters follow for microCT and histology, with both chapters containing their own literature review and methodology. Combining trabecular and cortical bone analysis alongside resorption activity and vascular density assessments allows for a more detailed insight into SCI-induced osteoporosis.

To finish, a discussion is presented within which the results of the study are compared to each other and to those currently understood in the literature. Future work is also suggested for the advancement of the understanding of SCI effects in bone, in an effort to mitigate the quality of life detriment primarily due to increased fracture risk.

1.1 Thesis Chronology

This study was limited due to the impact of the COVID-19 pandemic on lab access. The initial project plan included many aspects of the studies outlined in the 'Future Work' section; 30 rats were planned for analysis at n=5 with 5 sham controls at the 2 week, 6 week and 16 weeks post-injury timepoints. Such a multi-timepoint cross sectional study would enable a pseudo-longitudinal analysis into the progression of SCI-induced osteoporosis as the condition worsens. As the pandemic reduced the practically viable analysis to a chronic timepoint (11 weeks) at n=3 and an acute (2 weeks) dataset at n=5/6, some of these comparisons remain to be examined. The lab closure also necessitated a change to the project plan, as the histology could no longer be completed as initially devised. To produce quality content over the lockdown, additional microCT analyses (EF and ITA) were added to the planned set of microCT parameters for analysis. The initial research aim was to add to the knowledgebase on bone quality reduction following SCI through utilising microCT and histology, and so the addition of the new microCT analyses did not significantly alter the overall objectives of the project.

Figure 1.1 details the project changes made in the face of the COVID-19 delays:

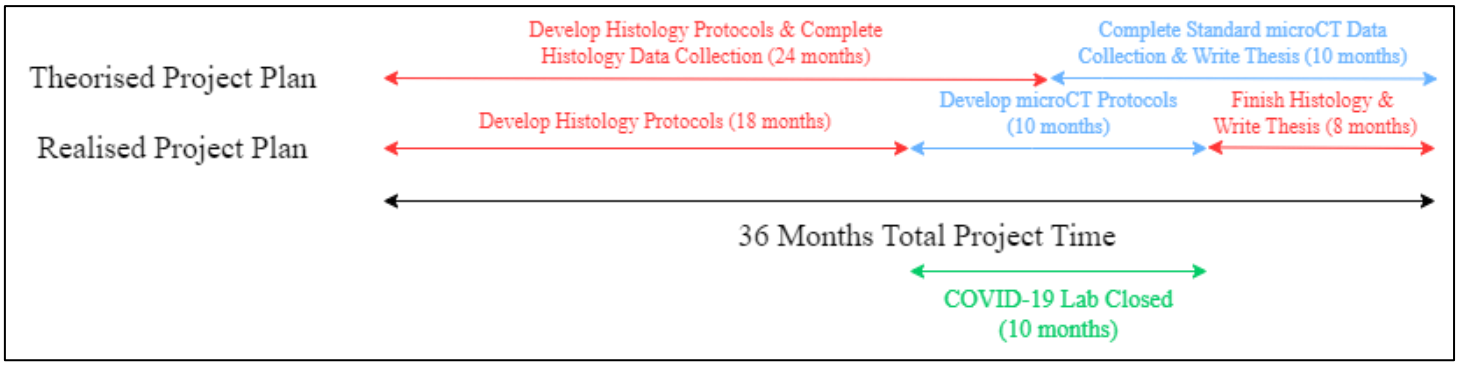

Figure 1. 1: COVID-19 Altered Project Plan

Chapter 2: General Literature Review

This literature review serves as a separate entity to the literature reviews in Chapters 3 and 4, which are more chapter-specific. This general review contains anatomy of the two types of long bone studied; the femur and the tibia. It also details the physiology; how the various cell types in bone contribute in the bone remodelling process. An outline of osteoporosis is presented which includes causes, definitions and analysis metrics. The final section focuses more specifically on SCI-induced osteoporosis.

2.1 Long Bone Anatomy & Physiology

2.1.1 Bone's Organisation

Bone is the material which comprises the majority of the skeleton; the structure in the body which provides all around support and movement capabilities, as well as maintaining mineral and blood homeostasis and shielding the internal organs from external forces (Lopes *et al*. 2018).

Bone's constituents can be described in a different manner according to the scale at which it is analysed. This is referred to as the hierarchical structure of bone (Rho, Kuhn-Spearing & Zioupos 1998). Figure 2.1 details a recent categorisation of the different structures and scales in bone:

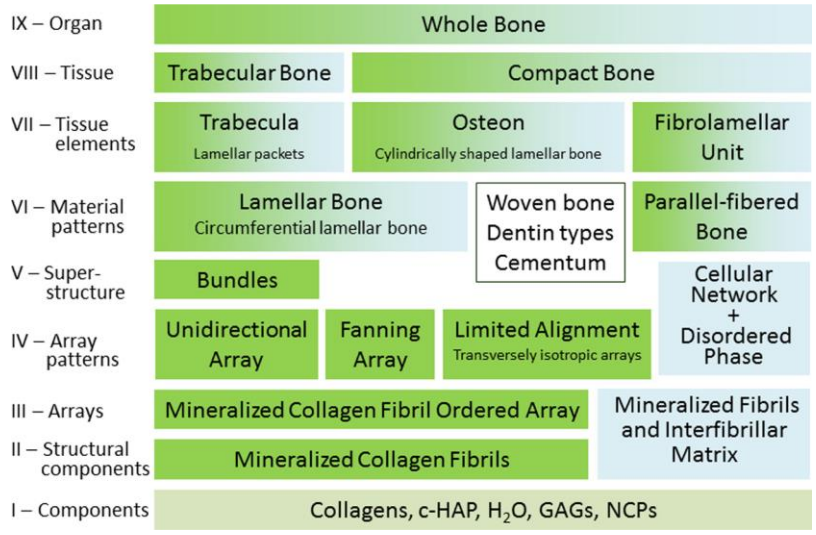

Figure 2. 1: Hierarchical organization of bone. Reproduced from Reznikov et al. 2014.

At the macroscale, there are generally five different classifications of bones in the mammalian skeleton: long, short, sesamoid, flat and irregular. This study focuses on SCI-induced osteoporosis and so the two bones studied are those which are most commonly affected by the condition. These are the femur and tibia, both of which are long bones (Jensen-Jarolim 2017). The following description therefore uses long bones as subjects for the examples.

At the nanoscale, all bone is comprised of three main constituents, water, type I collagen and carbonated hydroxyapatite. The hydroxyapatite forms in crystals around fibrils of collagen. This provides structure and order to the material as the scale increases in scope. Figure 2.2 details the layered orientation of hydroxyapatite crystals in lamellar (layered) bone:

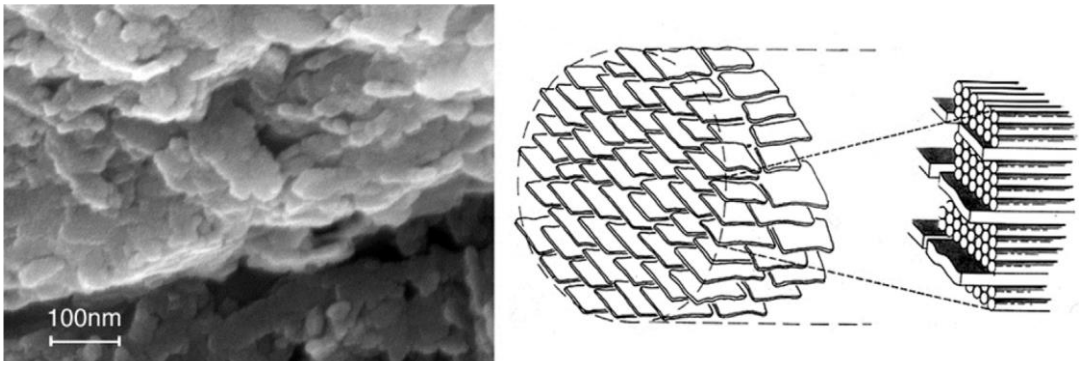

Figure 2. 2: Scanning electron microscopy image at nanoscale in baboon lamellar bone. Hydroxyapatite crystals are arranged in layers. Reproduced from Reznikov et al. 2014.

The hydroxyapatite crystals share a very similar orientation to the major axis of the collagen fibrils they form around. Within an aligned three-dimensional arrangement of these mineralised fibrils, disordered hydroxyapatite crystals sit in between the layers, as do non-aligned collagen fibrils. Figure 2.3 displays this arrangement:

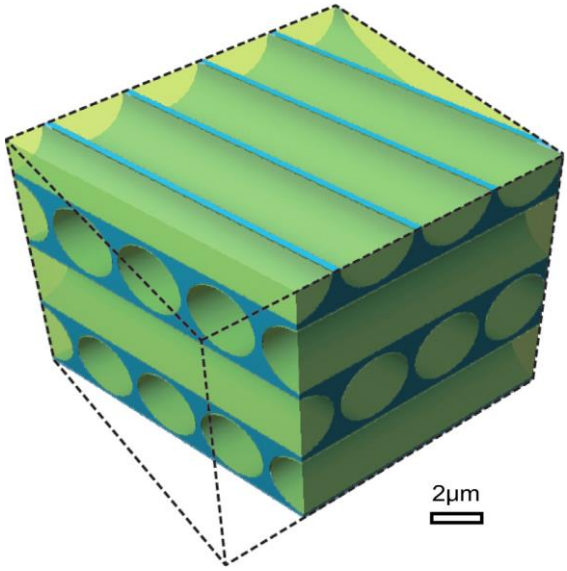

Figure 2. 3: Lamellar bone arrangement. Green – ordered material. Blue – disordered material. Reproduced from Reznikov et al. 2014.

Moving upwards to the microscale, numerous aligned mineralised collagen fibrils form arrays, and multiple aligned arrays form bundles. Bundles form with each array in a decidedly similar orientation to the other arrays in the bundle. Neighbouring bundles, however, can be offset from one another by as much as 80^{o}. This is common in bone regions where multi-directional loads occur e.g. trabecular bone in the long bone epiphyses and metaphyses. In cortical bone, bundles are offset by a much smaller average angle, leading to columnar structures which are best suited for the compressive loads expressed there.

2.1.3 Anatomy and Vasculature: Cortical Bone

In the regions of the long bones where the mechanical loading is closely aligned with the bone's major axis i.e. axially along the shaft, a certain type of bone is predominant. This bone is termed cortical bone; it is comprised of a very dense collection of columnar bundles which themselves are formed of concentric layers (lamellae) of mineralised tissue. These bundles are known as osteons, and they have a hollow centre. The space running through the middle of each osteon is known as a Haversian canal. It provides room for the blood vessels which run throughout cortical bone, supplying it with all essential nutrient transfer and signalling factors. Transverse canals in cortical bone are smaller, but perform the same function. They are known as Volkmann's canals (Rhinelander 1974).

Cortical bone is porous to an extent, in order to allow a blood network to flow through it in the form of Volkmann's and Haversian canals. Through histological reconstruction (H&E staining of successive 5μm sections followed by digital stacking and computer-based 3D reconstruction), Kim *et al*. (2015) showed that the Haversian / Volkmann network is much more complex and densely connected at the endosteal side of the cortex, as opposed to the periosteal side. Figure 2.4 illustrates this finding:

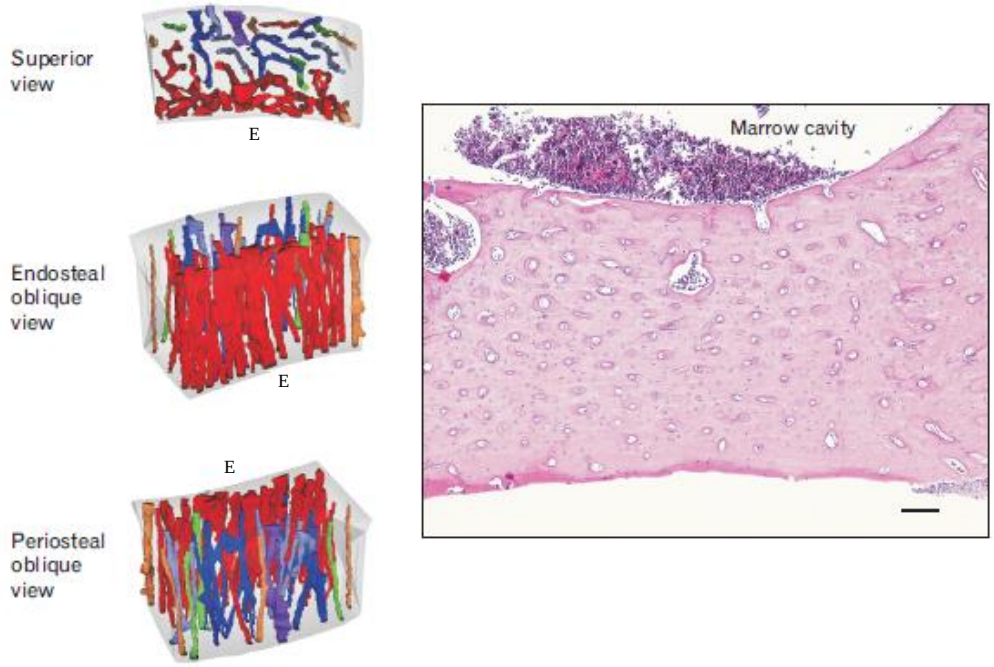

Figure 2. 4: Haversian and Volkmann's canals forming a dense endosteal network, and a comparatively more sparse periosteal network in Wistar rat femoral cortical bone. E: indicates endosteal side. Right side image stained with H&E, scale bar 100μm. Reproduced from Kim et al. 2015.

2.1.4 Anatomy and Vasculature: Trabecular Bone

The other main bone type in the long bones is known as trabecular bone. Figure 2.5 displays a typical long bone; a femur:

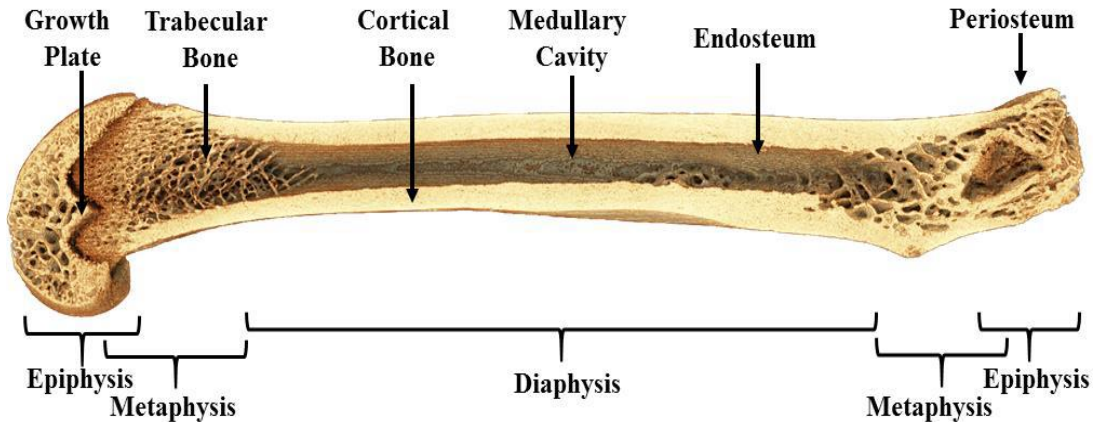

Figure 2. 5: Trabecular and cortical bone location in a typical long bone. MicroCT scan of a 10 week old SD rat. Reproduced from Williams 2019.

Trabecular bone is made up of a sprawling 3D network of interconnected struts (called trabeculae) which create a structure well-suited for different directions of load. For this reason, trabecular bone is found at the ends (epiphyses and metaphyses) of the long bones, close to the joints. It is not found in any great volume in the diaphysis. All trabeculae generally tend towards two different morphologies; rod-like and plate-like. Although in reality the morphologies can be different to this generalisation, the similarity is sufficient such that rod-like / plate-like models are the most commonly utilised methods of analysing trabecular bone's morphological adaptation to mechanical loads (Parfitt *et al*. 1987). The morphology of the local trabecular bone varies with the region in the skeleton. For example, Figure 2.6 displays rod-like and plate-like trabeculae in the lumbar spine and femoral head, respectively:

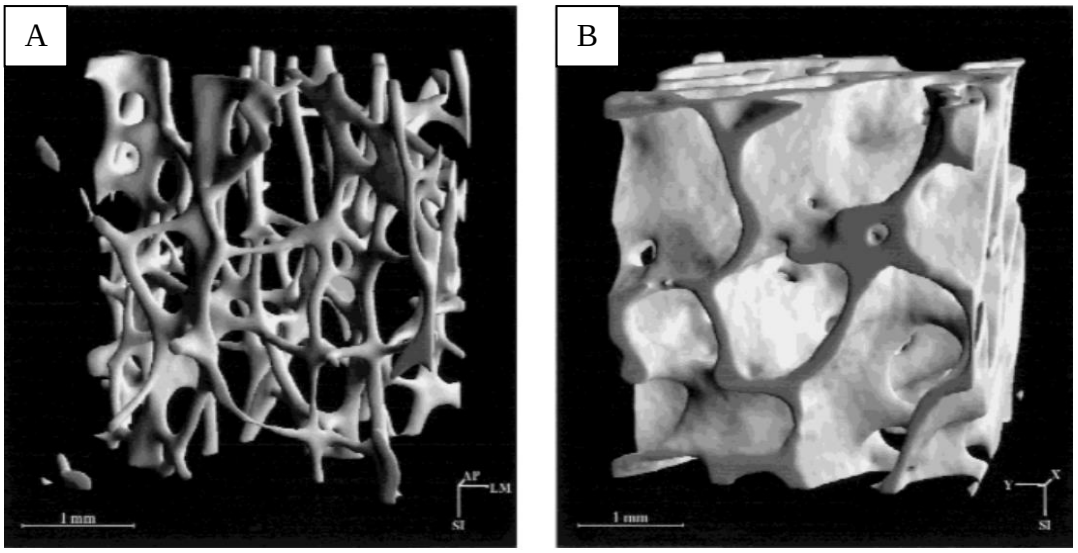

Figure 2. 6: Typical trabecular morphologies in human bone: A: rod-like trabeculae in the lumbar spine region B: plate-like trabeculae in the femoral head region. Reproduced from Hildebrand et al. 1987.

The blood vessels supplying metaphyseal trabecular regions of long bone are themselves smaller capillaries stemming from large arteries which enter the medullary cavity through a transverse canal in the diaphysis known as a nutrient foramen. The nutrient arteries split into smaller and smaller capillaries, usually terminating in the metaphysis or endosteal regions. Exiting through the same nutrient foramen, a large central vein drains the blood and nutrient waste from these medullary and endosteal capillaries. The epiphyses of the long bones are not supplied by the diaphyseal nutrient artery. Instead, they have their own blood supply, stemming from a vascular plexus around the articular cartilage at joints like the knee and hip (Ramasamy 2017). Figure 2.7 shows a typical long bone blood network:

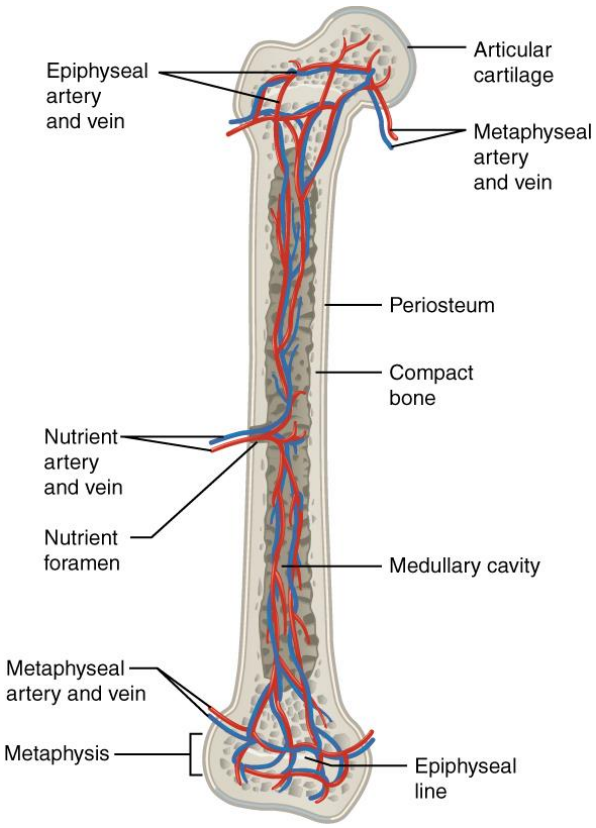

Figure 2. 7: Femur blood network and nutrient foramen. Reproduced from Betts et al. 2017.

The smaller blood vessels supplying trabecular bone are not as ordered as those found in cortical bone. As they occupy the spaces between the anisotropic trabecular network, many trabecular blood vessels are sinusoidal in shape, traversing back and forth between numerous struts (Ramasamy *et al*. 2016). This highly-branched, sprawling network of sinusoids is also the common pattern for blood vessel organisation in the diaphyseal region.

In the epiphyses and metaphyses around the growth plate, a different blood vessel shape is observed alongside the sinusoids. Longer endothelial columns originate immediately adjacent to the growth plate, and extend from the ends of the bone towards the middle, parallel to the long axis. These columns have been shown in mice to exhibit less branching capillaries and a larger average diameter than their sinusoidal neighbours. Additionally, immunostaining showed a significant increase in the expression of endothelial markers CD31 and Endomucin in these blood vessels when compared to the marrow sinusoids. It is because of this ‘high’ and ‘low’ expression of these markers that the larger columnar vessels are termed ‘Type H’ vessels, and the

sinusoids they connect to are termed ‘Type L’. Figure 2.8 displays this distinct bone blood vessel subtype:

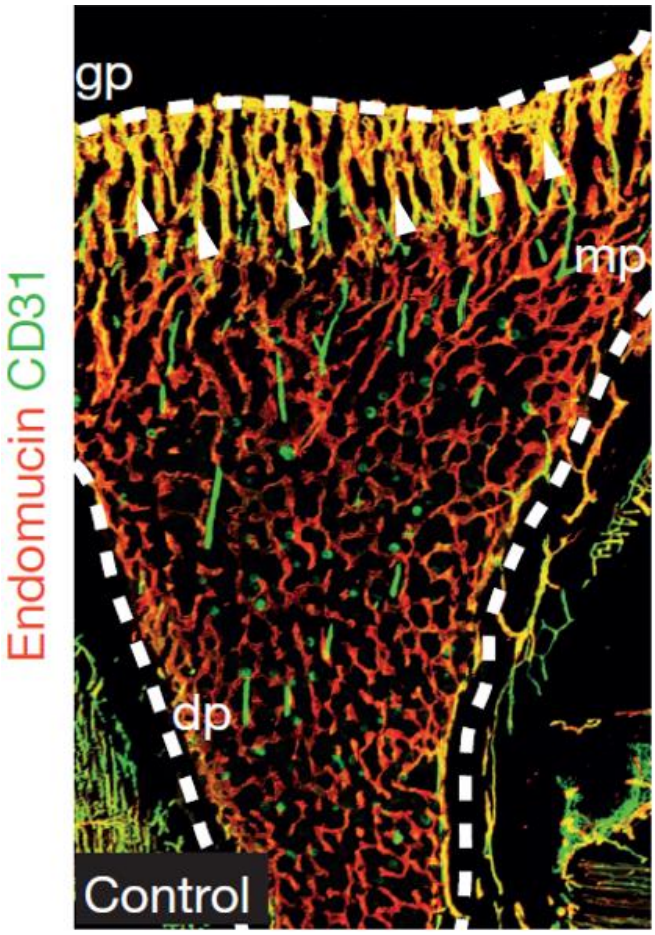

Figure 2. 8: Type H (CD31^{hi}Emcn^{hi} - arrowheads) and Type L vessels in the mouse tibia. gp: growth plate. mp: metaphysis. dp: diaphysis. Reproduced from Kusumbe, Ramasamy & Adams 2014.

The presence and number of Type H vessels in long bone has been proven to decrease with aging (and hence the onset of osteoporosis), bringing about a decrease in bone remodelling activity and trabecular bone density. For this reason, type H vessels are thought to play a key role in maintaining trabecular bone mass via provision of essential nutrients, bone cell precursors and signal factors to the necessary remodelling sites (Kusumbe, Ramasamy & Adams 2014).

2.2 Bone Cells

Bone is comprised of four main cell types (Florencio-Silva *et al*. 2015):

- Osteoblasts - Bone building cells.
- Bone Lining cells - Quiescent (inactive) osteoblasts which demarcate the areas for activity and inactivity by osteoblast and osteoclasts, as well as other roles.
- Osteocytes - Mature osteoblasts which fulfil the primary structural requirement of bone, as well as acting as signalling cells.
- Osteoclasts - Bone removing (resorbing) cells.

Figure 2.9 displays these four cell types during normal bone remodelling (bone remodelling is explained later in this chapter):

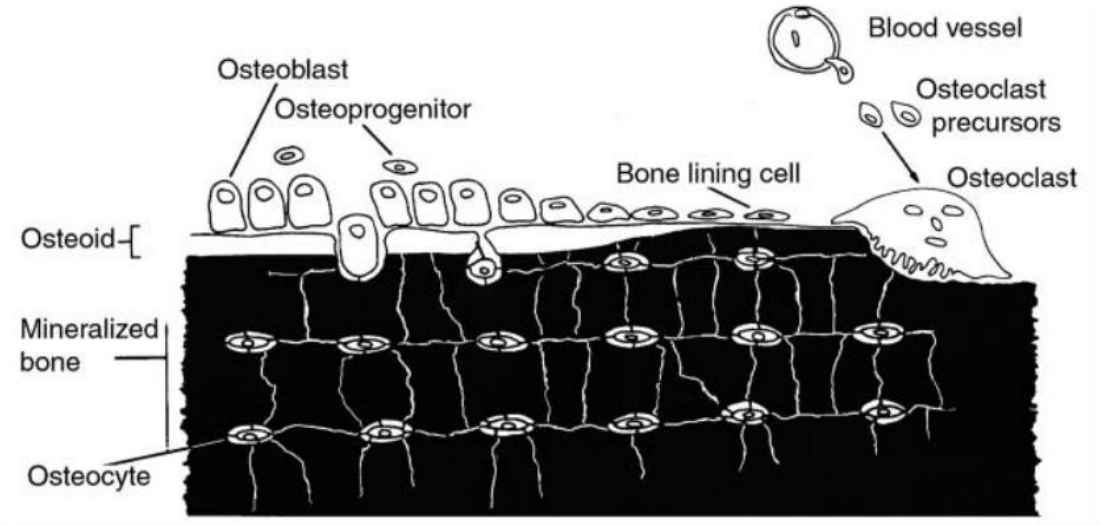

Figure 2. 9: The four cell types in bone. Reproduced from Downey & Siegel 2006.

2.2.1 Osteoblasts

Osteoblasts (OBs) are known as the bone-building cells in the skeleton. When active, OBs are cuboidal in shape and their main role is to secrete new bone (known as osteoid) where needed (Donahue *et al*. 1995). Active OBs perform this secretion in specialised compartments. The canopies of these compartments are formed of the mesenchymal cells of the nearby bone marrow (Kristensen *et al*. 2014). The creation of these 'bone remodelling compartments' (BRCs) is instigated by signals sent from neighbouring osteocytes (Hauge *et al*. 2001).

Active osteoblasts are the cells responsible for depositing osteoid onto a cartilage scaffold (as part of a process called endochondral ossification) during bone growth (Mackie *et al*. 2008). They also deposit osteoid onto freshly resorbed regions of bone, directly following the activity of osteoclasts during bone remodelling. These regions which have been resorbed by osteoclasts are known as Howship's Lacunae (Everts *et al*. 2001).

Figure 2.10 contains an osteoblast depositing osteoid onto a chondrocyte scaffold:

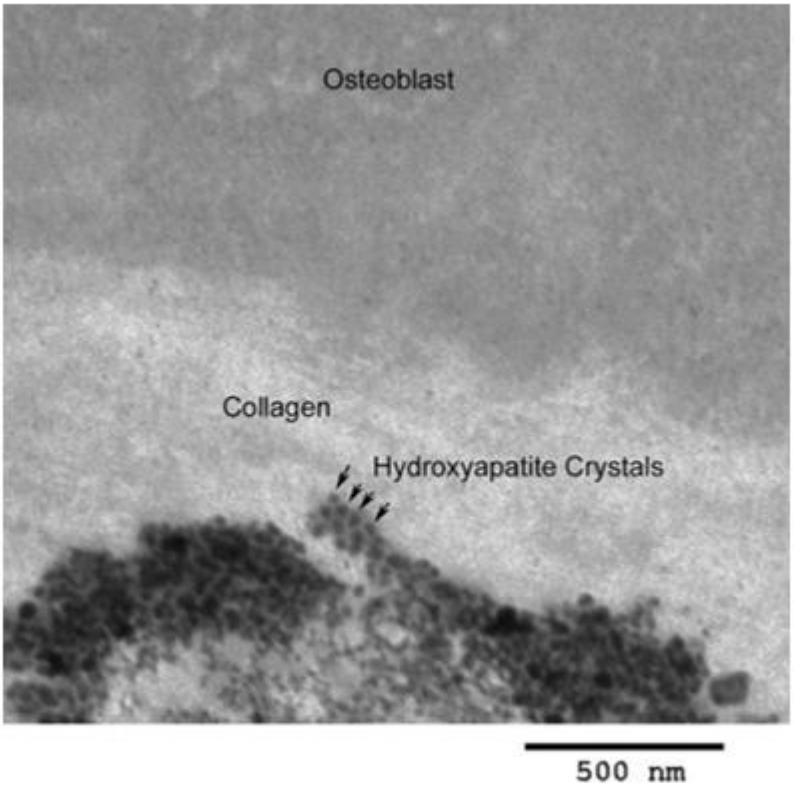

Figure 2. 10: Osteoid deposition on type I collagen, taken by transmission electron micrograph (TEM). Reproduced from Blair et al. 2018.

Osteoblasts are derived from fibroblastic mesenchymal stromal cells. Due to their pluripotent nature, these cells are also termed mesenchymal stem cells (MSCs). The most important signal protein for commitment of MSCs to osteoblasts is the transcription factor runt-related transcription factor 2 (Runx2) (Rutkovskiy, Stenslokken & Vaage 2016).

2.2.2 Bone Lining Cells

Inactive OBs lining the bone sites where resorption and osteoid deposition are not taking place are termed ‘bone lining cells’ (BLCs) (Hauge *et al*. 2001). BLCs form a barrier between osteoclasts and the surfaces of bone which should not be resorbed. Additionally, they have been proven to secrete osteoclastic differentiation factors (mainly a signalling ligand known as RANK-L) and their dummy-binding inhibitors (Osteoprotegerin), thereby controlling the formation and resorption rates during bone remodelling (Streicher *et al*. 2017).

2.2.3 Reversal Cells

Located behind resorbing osteoclasts and before bone forming osteoblasts in the Howship’s Lacuna, reversal cells are a recently identified cell of somewhat unknown definition (Raggatt & Partridge 2010). During bone remodelling, reversal cells provide the bridge between bone removal and bone restitution via secretion of osteoclast and osteoblast signal factors.

Reversal cells have also been suggested to ‘prepare’ the bone remodelling site for inbound osteoclasts and osteoblasts. This involves two key stages:

1. Resorption of unwanted collagen fibrils from the Howship’s Lacunae prior to and following osteoclastic activity.
2. Deposition of a new collagen layer at the site of required osteoid secretion for inbound osteoblasts.

Figure 2.11 displays bone lining cells (identified at the time as BLCs - these are potentially reversal cells by today’s definition) performing their role in preparing the bone remodelling site:

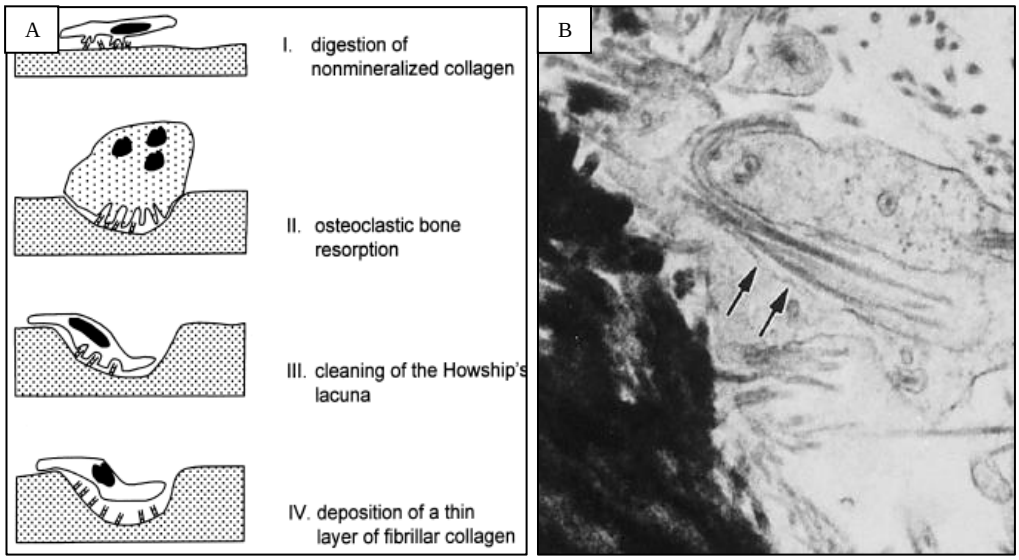

Figure 2. 11: The bone lining cell (BLC) performing its function in aiding the transition from osteoclastic resorption to osteoblastic deposition. AI: The BLC removing unwanted collagen fibrils from the demarcation line between mineralised bone and surrounding tissue. AII: An osteoclast secretes bone resorbing enzymes onto the cleaned area. AIII: The BLC removes the residue from the osteoclast activity. AIV: The BLC deposits a new collagen layer onto the site, facilitating an improved arrangement for the subsequent osteoid secretions by inbound osteoblasts. B: 'Enwrapment' of collagen fibrils which protrude from the mineralised bone surface (black arrows). Reproduced from Everts et al. 2002.

Reversal cells have been suggested to be mononuclear preosteoclasts (Eriksen *et al*. 1984) and even phagocytic cells (Tran Van, Vignery & Baron 1982) due to their ability to resorb collagen fibrils. In recent times, however, reversal cells have been identified as osteoblastic progenitor cells, and confirmed as such through staining for osteoblastic differentiation markers osterix and smooth muscle actin (Andersen *et al*. 2013). As BLCs are also defined as osteoblastic cells, this means that reversal cells are potentially just activated BLCs, which have migrated to the bone remodelling region in order to activate and deposit new bone. In an effort to acknowledge this, a review has mentioned both reversal and BLC types under the designation of 'bone surface cells' (Delaisse 2014).

2.2.4 Osteocytes

Once an osteoblast has deposited osteoid for some time, it begins to transform into an osteocyte. This development in combination with osteoid deposition forms the process of osteogenesis (Franz-Odendaal, Hall & Witten 2006). The osteoblast lifespan before it begins the osteocyte transition is ~3 months in humans (Parfitt 1994).

Immature osteocytes are osteoblasts which have relocated into the osteoid layer following cessation of their role in depositing the new bone material. They are sometimes termed osteoid osteocytes. Mature osteocytes have completed mineralisation of their local area, becoming fixed in place in the process. Mature osteocytes joined together by the dendritic structures they project during mineralisation form the main cellular component of mature bone (Bonewald 2008). Figures 2.12 and 2.13 display osteocytes in the bone matrix and an osteoblast's transition from a precursor to a mature osteocyte, respectively:

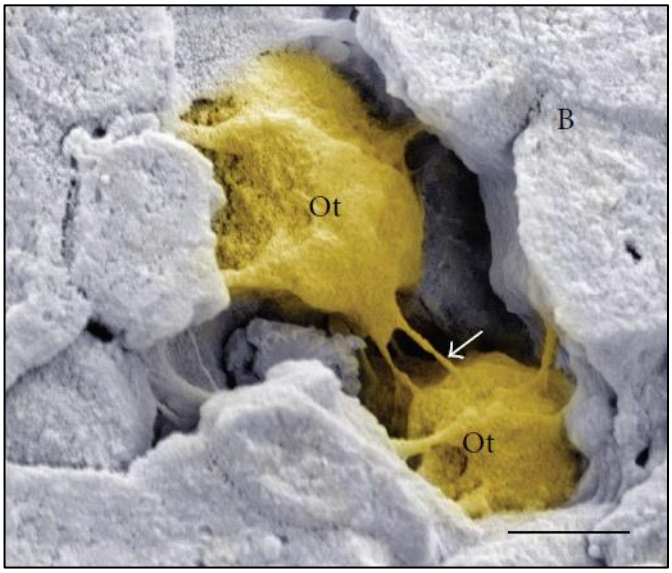

Figure 2. 12: Scanning electron microscopy image of osteocytes (Ot) in between hydroxyapatite bone matrix (B). White arrow: Cytoplasmic intercellular structures (dendrites). Scale bar: 2μm. Reproduced from Florencio-Silva et al. 2015.

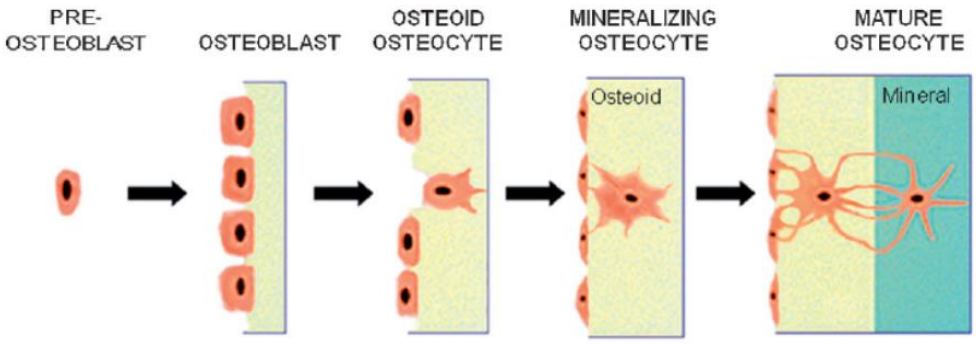

Figure 2. 13: Osteocyte formation and maturation. Reproduced from Bonewald 2008.

Trabecular osteocytes are rounded in shape. In comparison, where they are part of the cortical bone matrix, osteocytes are more elongated. This elongation enhances the polarity of those osteocytes which is essential for the mechano-sensing role they perform. When a mechanical stress is applied to a bone surface it results in an electric polarization; the piezoelectric effect (Fukada & Yasuda 1957). This is the mechanism through which osteocytes are deemed mechano-sensing cells. Mechano-sensing osteocytes stimulate the recruitment of osteoblast progenitors to the bone remodelling surface (Birmingham *et al*. 2012). Although less active in terms of movement than an osteoblast, an osteocyte nevertheless remains active and performs other key functions in addition to osteoblast recruitment (Florencio-Silva *et al*. 2015). Apoptotic osteocytes have been shown to direct osteoclasts to their location via RANK-L signalling on their dendrites. This is to instigate bone removal at the 'dead' site and help improve the mechanical properties of the bone (Plotkin 2014). Osteocytes also secrete an osteogenic inhibitor called sclerostin in response to mechanical loading, in order to maintain bone homeostasis. This process is detailed in section 2.4: Bone Remodelling.

2.2.5 Osteoclasts

Osteoclasts are the bone removing cells in the skeleton. They are comparatively larger than osteoblasts, and their main function is to secrete lytic (membrane-splitting) enzymes which break down old mineralised bone in preparation for new osteoid deposition by incoming osteoblasts. Osteoclasts are polykaryons, that is to say they can be distinguished by their multiple nuclei. Unlike osteoblasts which can trace their cell lineage to mesenchymal stem cells (MSCs), osteoclasts differentiate from haematopoetic stem cells (HSCs) under the influence of a combination of signal factors, mainly CSF-1 and RANK-L (Boyle, Simonet & Lacey 2003).

Figure 2.14 depicts an osteoclast becoming activated and beginning to resorb bone material:

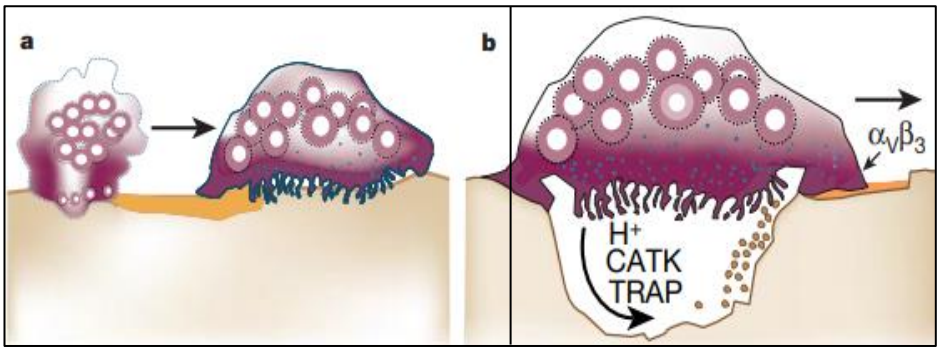

Figure 2. 14: Osteoclast activation and resorption. A: A preosteoclast is recruited by the signal factors CSF-1 and RANKL, attaching to the bone surface and undergoing differentiation into a mature osteoclast. B: The osteoclast is triggered by RANKL to release hydrogen protons (H+) and lytic enzymes like Tartrate-resistant Acid Phosphatase (TRAP) and Cathepsin K (CATK). The protons act to acidify the Howship's Lacuna environment, which activates TRAP and CATK. $A_V\beta3$ is an integrin; a transmembrane binding protein, essential for forming a seal prior to enzymatic removal of bone. Reproduced from Boyle, Simonet & Lacey 2003.

Osteoclasts have been shown to secrete a growth factor known as Platelet-Derived Growth Factor, specifically the isoform PDGF-BB. PDGF-BB produced by non-resorbing osteoclasts instigates migration and differentiation of the neighbouring osteoblastic progenitor cells in the bone lining cells, mesenchymal canopy, and marrow capillaries, thereby modulating the bone remodelling cycle (Kristensen *et al*. 2014, Kreja *et al*. 2010, Sanchez-Fernandez *et al*. 2008).

2.3 Coupling of Angiogenesis and Osteogenesis

PDGF-BB is also secreted by osteoclast progenitor cells, and plays a part to induce angiogenesis at the bone remodelling sites. Crucially, PDGF-BB was shown to produce a majority of type H blood vessels, as opposed to type L. As explained previously, the absence of type H blood vessels correlates with a significant reduction in bone formation, due to their vital role in recruitment of osteoblast progenitors at the bone remodelling compartment (Peng *et al*. 2020). Figure 2.15 displays osteoclastic cells producing angiogenic factors, promoting type H vessel formation and recruiting preosteoblasts to the remodelling site:

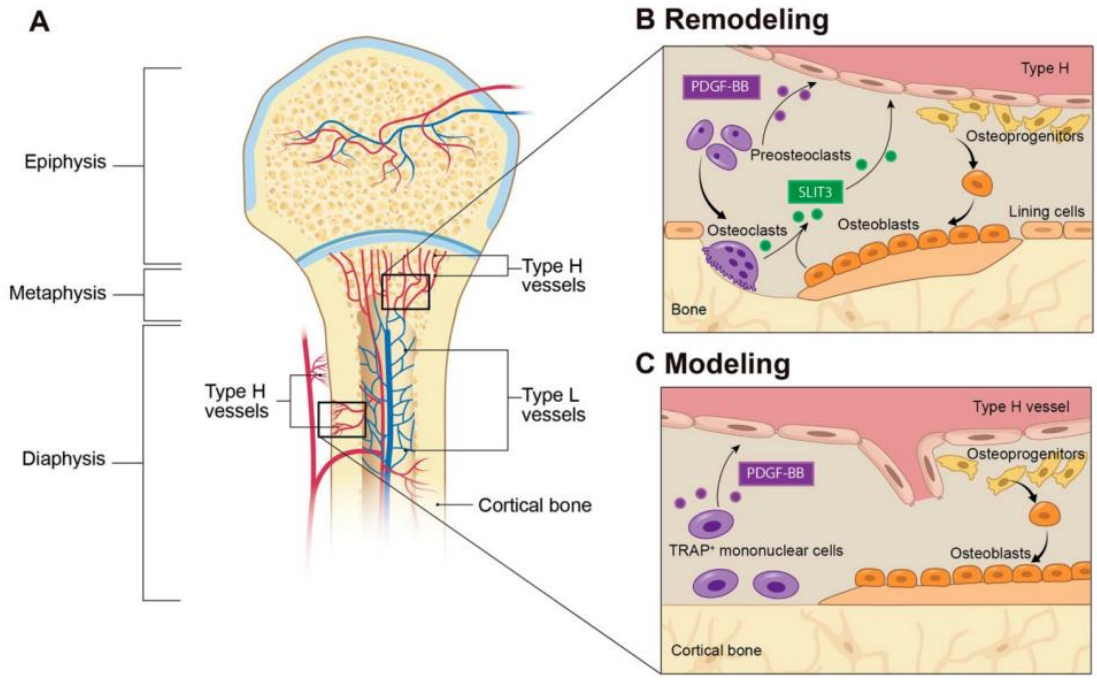

Figure 2. 15: Type H vessels, preosteoclasts and their associated signal factors in trabecular bone. Reproduced from Peng et al. 2020.

Through this mechanism of type H vessel angiogenesis via PDGF-BB, osteoclastic cells are said to aid in providing the link between angiogenesis and osteogenesis (Xie *et al*. 2014). Another main angiogenic factor secreted by bone cells is vascular endothelial growth factor (VEGF). VEGF is secreted by differentiating osteoblasts and osteoclasts in the BRC (Chim *et al*. 2013), which induces angiogenesis as well as

acting as a chemoattractant to osteoclastic and osteoblastic cells in the vicinity. VEGF has been shown to be expressed by osteocytes responding to microdamage in bone (Tatsumi *et al*. 2007), and by apoptotic osteocytes signalling for resorption at their site of cell death (Cheung *et al*. 2011).

In combination with angiogenic effects on the blood network by bone cells, the blood network is crucial to the differentiation, proliferation, recruitment and activity of the bone cells. This is due to the blood network transporting oxygen, hormones, cytokines and bone precursor cells to the bone remodelling units around the skeleton (Chim *et al*. 2013). In addition to the supply role, vasculature supplies a scaffold for bone forming cells and aids them in depositing bone in the right areas. This is most noticeable during endochondral ossification (a mechanism of bone modelling), with blood vessels invading the cartilage plate in the epiphysis of a long bone. Scaffolds comprised of cartilage cells and blood vessels arise as a result (Collin-Osdoby 1994).

An overview of the coupled angiogenic and osteogenic processes in response to microdamage is given in Figure 2.16:

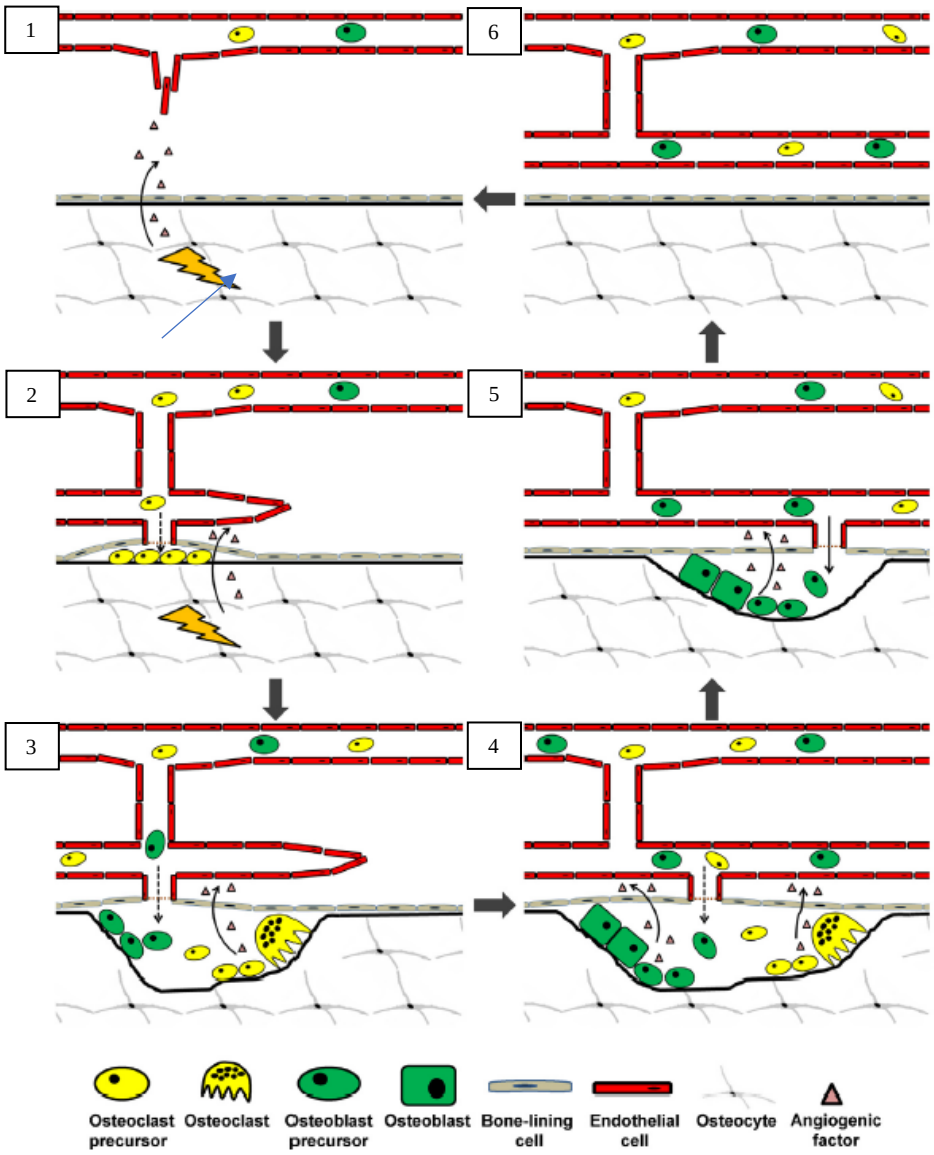

Figure 2. 16: Bone cells controlling angiogenesis in the BRC via signalling factors in response to an external stimulus (blue arrow). 1: Stimulus triggers a release of angiogenic factors by osteocytes. 2: Osteoclast precursors are recruited to the BRC. 3: Osteoclast precursors differentiate and osteoblast precursors are recruited behind them. 4: Osteoblast precursors differentiate, depositing osteoid on the resorbed bone surface. 5: Angiogenic signals released by osteoblasts in the BRC signal blood vessels to form. 6: The new blood network is in place, carrying preosteoclasts and osteoblasts for recruitment to new BRCs. Reproduced from Chim et al. 2013.

2.4 Bone Remodelling

Various studies have shown that homeostasis in bone and effective action of the involved cells leads to healthy angiogenesis in bone, and vice versa. If either the blood network or bone cells in the skeleton are disrupted in their proliferation and function, the bone remodelling balance will be affected. Figure 2.17 contains the cells and signalling factors which are discussed in this section for reference. Only the main contributing signalling processes from each cell type are discussed:

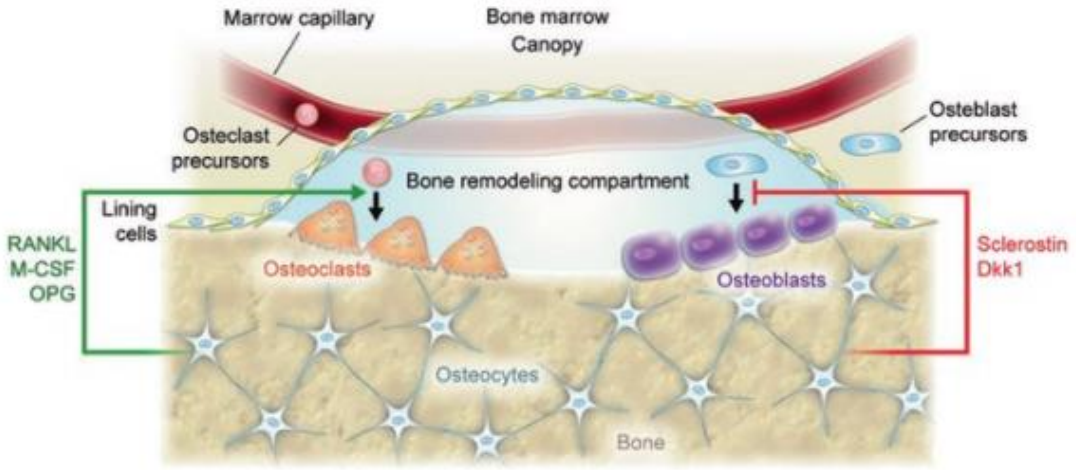

Figure 2. 17: Bone remodelling compartment components. Green arrow: Osteoclast modulating factors. Red arrow: Osteoblast modulating factors. Reproduced from Gasser & Kneissel 2017.

The transmembrane signalling protein RANK is named as such as it is the Receptor Activator of Nuclear factor Kappa β, which is a transcription factor known as the 'master regulator of innate immunity' (Salminen *et al*. 2008). RANK has been proven to be the main signal factor which induces osteoclastogenesis through binding with its soluble ligand, RANK-L, during RANK forward signalling (Li *et al*. 2000). Osteoclasts rely on soluble RANK-L forward signalling in order to differentiate and to produce their crucial lytic enzymes. In addition to osteoclastic promotion by soluble RANK-L (forward signalling), reverse signalling is performed by osteoclasts producing vesicular RANK which promotes osteoblast differentiation via triggering the signal factor Runx2. Additionally, during osteoblastogenesis from reverse signalling, membranous RANK expression on osteoblasts is reduced, which lessens osteoblast inhibition from forward signalling. Osteoblasts and osteoclasts therefore

influence the opposite cell type via reverse and forward RANK signalling (Cao 2018). Figure 2.18 illustrates forward and reverse RANK signalling:

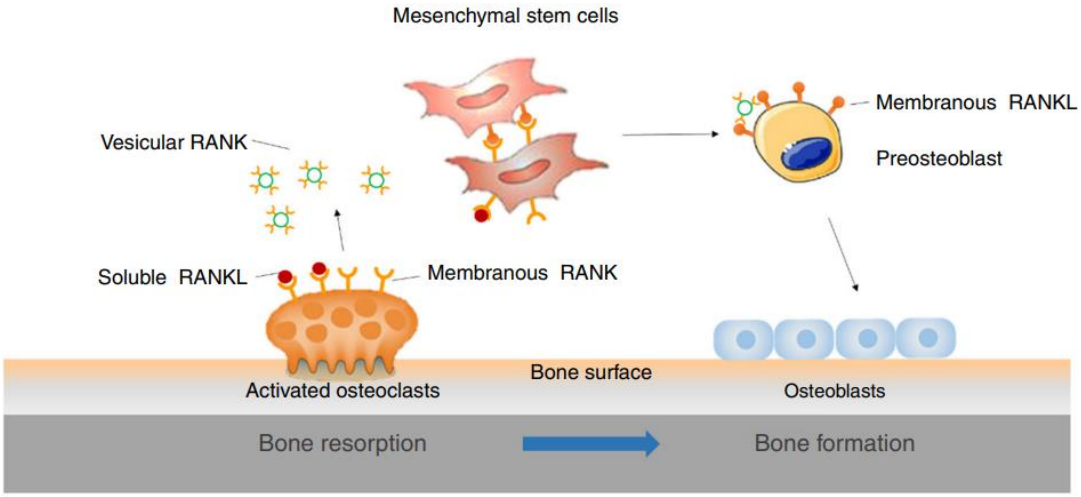

Figure 2. 18: The bi-directional bone remodelling control by osteoblasts and osteoclasts on their opposite cell type. Osteoclasts secrete vesicular RANK which binds to membranous RANK-L on osteoblast precursors, promoting osteoblast differentiation. Osteoblasts, on the other hand, secrete soluble RANK-L which binds to membranous RANK on osteoclasts to promote resorption. Reproduced from Cao 2018.

Neighbouring osteoblasts and osteocytes in the bone remodelling compartment region also control the rate of bone resorption through expression of a protein known as Osteoprotegerin (OPG). OPG is in the family of tumour necrosis factors, and its abundance has been proven (in transgenic mice) to significantly increase bone mass (Simonet *et al*. 1997). OPG achieves this through acting as a dummy receptor for soluble RANK-L, meaning that the available RANK binding sites on osteoclasts are not activated. The osteoclast promoting RANK forward signalling is arrested, and bone mass rises as a result (Kobayashi *et al*. 2016).

As well as secreting OPG, active osteocytes express and release sclerostin in response to mechanical loading. Sclerostin is a growth factor which inhibits the Wnt / Lrp5 mechano-transduction pathway. As Wnt signalling is essential to the osteogenesis process (Runx2 activation), an increase in sclerostin therefore limits the bone mass and acts to regulate osteogenesis. Through this mechanism, osteocytes modulate and control bone homeostasis (Poole *et al*. 2005, Robling *et al*. 2007).

To summarise, during bone remodelling:

- Osteocytes release various signalling proteins to instigate signal pathways which result in either promotion or inhibition of osteoblastic or osteoclastic differentiation.
- Osteoblasts and osteoclasts themselves also contribute their own modulating signals to each other, acting to balance out the required rate of resorption and deposition in each compartment as bone remodelling occurs.
- Some BLCs are recruited after the osteoclasts and before the osteoblasts, acting as reversal cells to couple the processes of resorption and formation. These reversal cells also secrete RANK-L and its dummy receptor OPG to regulate the bone remodelling balance in their local region.

Figure 2.19 simplifies this complex interdependent process, showing the different bone remodelling (im)balances:

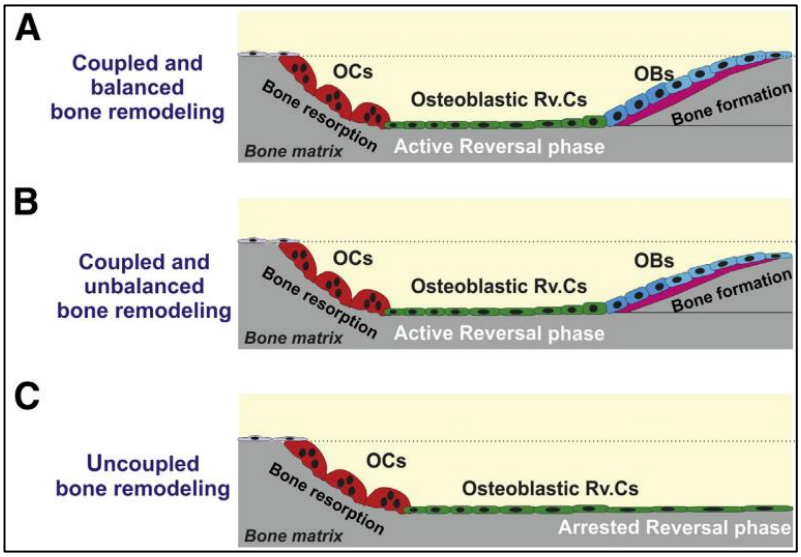

Figure 2. 19: The 3 different types of bone remodelling. A: Bone resorbed by osteoclasts (OCs) in the Howship's Lacuna is fully replaced by osteoblasts (OBs). B: The net change in bone mass is negative; more bone is resorbed than deposited as OB recruitment and activity is diminished. C: None of the resorbed bone is recovered by inbound OBs. Although severe, this bone loss mechanism is less prevalent than coupled, unbalanced remodelling. Reproduced from Andersen et al. 2013.

The diagram previous highlights that bone mass is reduced from either a comparative lack of osteoblast activity or increase in osteoclast activity. In reality, it is almost always due to a combination of the two. SCI-induced osteoporosis occurs as a result of this imbalance in the bone remodelling cycle.

2.5 Osteoporosis

The clinical standard for assessment of bone mineral density (BMD) to diagnose osteoporosis is a technique known as dual-energy X-ray absorptiometry (DXA – see section 3.1.3). As DXA is a 2D scanning technique, the resulting BMD values are in units of bone mineral content (mass of hydroxyapatite) per area, usually g/cm^2. Osteoporosis is currently defined within WHO guidelines as (Kanis 1994):

- Normal: BMD within 1 standard deviation (SD) from the reference mean for young adults of the patient's gender.
- Low bone mass (osteopenia): BMD more than 1 SD lower but less than 2.5 SDs lower than the age-matched reference mean.
- Osteoporosis: BMD more than 2.5 SDs lower than the age-matched reference mean.

Osteoporosis is a global disease (it is not endemic to a specific region), affecting men and women at different rates according to age and fracture site. For example, a 2006 study found that osteoporosis is linked to almost nine million bone fractures per year. Of these, the majority of fractures occur in women. This bias ranges from 80% (forearm) to 58% (spine) across the four most common fracture sites (Johnell & Kanis 2006).

The yearly occurrence of hip fractures in developing countries has been found to be increasing in recent years (Thambiah & Yeap 2020). In the EU, a 2013 study found that fragility fractures in the year 2010 cost the combined health services 37 billion euros annually (Hernlund *et al*. 2013).

Osteoporosis has a massive impact on global healthcare systems and affected patients. For example, fragility fractures of the hip were found to be fatal in 15-20% of those aged 60+ in Australia (Bliuc *et al*. 2013). If the fracture occurs in vertebrae, knock-on effects of long term pain, issues with balance, problems with digestion and respiration are common (Rinonapoli *et al*. 2021).

2.6 SCI-Induced Osteoporosis

2.6.1 Overview

The German anatomist Julius Wolff was the first to propose the theory that bone responds to its mechanical environment over time by changing its architecture. This system was named the 'mechanostat' and was further explored by Harold Frost by applying modern knowledge of bone's inter and intra-cellular mechanisms for regulating bone mineral density and structural geometry (Frost 2003). This theory has been strengthened in its validity by many studies of varying mechanical environment in bone (Rolvien & Amling 2021).

Disuse osteoporosis (dOP) is a condition which is strongly related to bone's mechanostat. It affects a much smaller subset of the osteoporotic population; immobilised patients. Immobilisation is usually the result of paralysis caused by spinal cord injury (SCI) and disease. It occurs in rarer cases like prolonged low-gravity (astronauts) and bed-rest studies (Rolvien & Amling 2021).

Figure 2.20 displays developing osteoporosis in the distal femur of a rat following SCI:

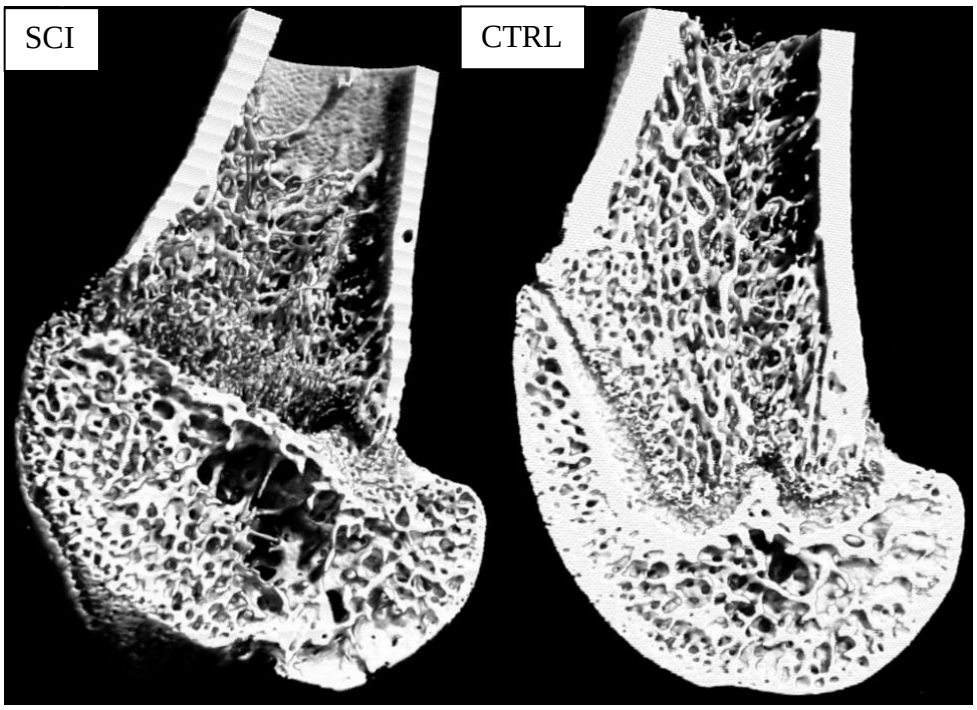

Figure 2. 20: SCI effects on the distal femur. SCI: Spinal Cord Injured. CTRL: Age-matched control.

Clinical studies have found an almost immediate commencement of bone loss following SCI in trabecular bone. In SCI patients, the usual rate of decrease is 2-4% total bone mass per month during acute SCI, with homeostasis (unchanging bone mass) returning at around 30-40% bone loss (Wilmet *et al*. 1995). The time taken for this return to steady state has been reported as 1.5-2 years (Garland *et al*. 1992).

2.7 Rat Models of Osteoporosis

2.7.1 Rat vs. Human Bone

Rats, like most mammals, present a very similar organisation in the long bones. That is to say, compact cortical bone forms the primary component of the midshaft (diaphysis), with widening portions containing more trabeculae and a more porous cortical shell (metaphysis) leading to the most proximal and distal regions in the bone; the epiphyses. Each epiphysis contains a growth plate wherein the instigation of endochondral ossification occurs as a result of the creation and proliferation of chondrocyte scaffolds which grow towards the diaphysis.

One of the notable differences between rat and human bone in this regard is the time into adulthood with which the growth plate closes and endochondral ossification ceases to occur. In humans, this occurs at ages 13-15 in females and 15-17 in males (Ballabriga 2000). In comparison, rat growth plates have been observed to be open as late as 30 months of age in males and 15 months in females (Jee & Yao 2001).

The cortical bone makeup is also different between rats and humans. In humans, the cortical shell is composed of uniformly distributed cylindrical osteons, formed from concentric lamellae surrounding a central canal (the Haversian canal). The space in between each osteon is occupied by lamellar (layered) bone. In small spaces between the lamellae known as lacunae, the osteocytes are located. These osteocytes communicate through minute channels in the bone know as canaliculi. Rats do no possess this structure of uniformly distributed osteons and interstitial lamellae. Instead, the endosteal and periosteal regions of the cortical cross section are composed of circumferential lamellae, with the core of the cortical bone being composed of a disorganised region of mineralised chondrocyte material. Throughout this

disorganised region are interspersed numerous islands of highly mineralised cartilage (Shipov *et al.* 2013). Figure 2.21 depicts human vs. rat cortical bone arrangement:

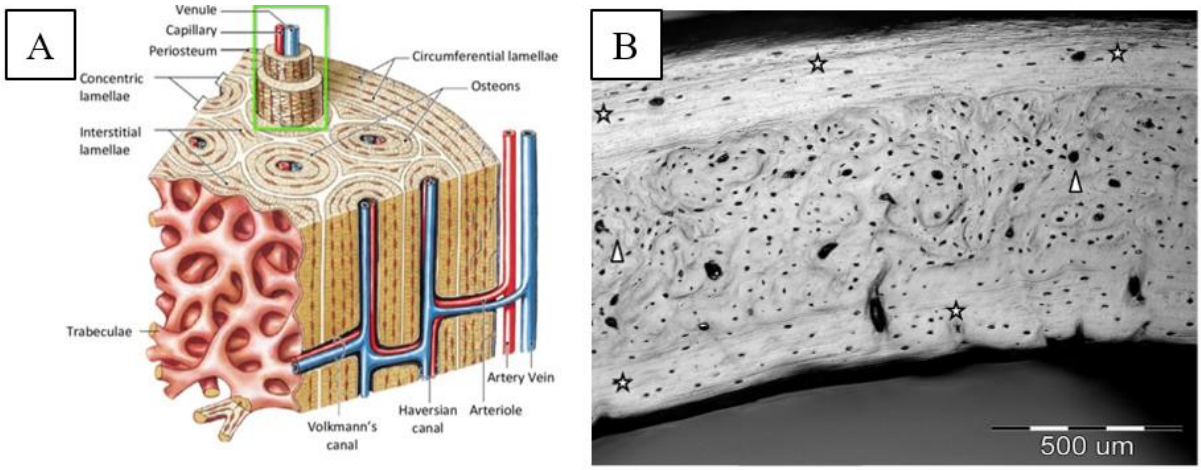

Figure 2. 21: The arrangement of osteons in human (A) and rat (B) cortical bone. Stars distinguish regions of circumferential lamellar bone from the central disorganised region (arrowheads). Reproduced from Ahmed 2021 and Shipov et al. 2013.

The organisation of the human femoral and tibial cortical bone in this regard is in response to the primary loading axis of the bones i.e. in the caudal-cranial direction paralleling the long axis of the bones. This loading leads to a cortical microstructure which is better suited to dealing with axial compression, hence the bundled osteons depicted above. In the rat, as the primary loading axes differ from the more vertical alignment seen in humans, the microstructure deviates understandably as a result. Figure 2.22 contains a diagram of a rat and its femoral and tibial orientation:

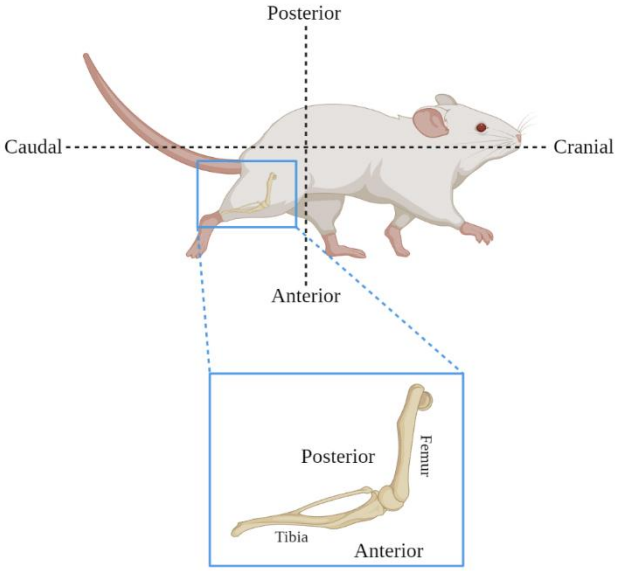

Figure 2. 22: Rat femur and tibia orientation differs from the typical vertically-aligned orientation seen in humans.

This effect of mechanosensitive bone remodelling based on loading direction has been observed *in vivo* using bending stresses. Regions of maximum bending stress in the rat tibia which underwent consistent daily bending stresses initially formed poorly mineralised and organised bone material which then consolidated into well mineralised bone (Turner, Woltmann & Belongia 1992).

2.7.2 Model Selection

There are a variety of murine studies on immobilisation, weight bearing and dOP in the literature. Table 2.1 details these rodent models of disuse:

Model	**Reference(s)**
Hindlimb immobilisation (plaster of Paris / brachial plexus transection)	Allison & Brooks 1921
Hindlimb immobilisation (botulinum toxin)	Brent *et al.* 2020 | Chappard *et al*. 2001b
Hindlimb immobilisation (bandages)	Lindgren 1976
Hindlimb immobilisation (spinal cord transection)	Heimburger 2005
Hindlimb immobilisation (spinal cord contusion)	Ghasemlou, Kerr & David 2005
Hindlimb immobilisation (spinal cord clip compression)	Rivlin & Tator 1978
Hindlimb impedance (SC dislocation without transection)	Choo *et al*. 2009 | Fiford *et al*. 2004
Hindlimb impedance (SC distraction using clips)	Dabney *et al*. 2004
Limb unloading (zero gravity orbital flight)	Morey 1979

Table 2. 1: Rodent models of long bone disuse for assessment of bone mass and architectural changes due to mechanical unloading.

The correct model for a particular study depends on a number of variables, namely the aims, resources and equipment. The method selected for this study, for both microCT and histological analysis, was complete spinal cord transection at the T9 vertebra. This method is easy to administer, with greater sample sizes compared to other animal models. Additionally, due to their rapid reproductive nature and the ability to minimise genetic variability, rats allow a variety of conditions to be reproduced in a repeatable and consistent manner. This is imperative when so many clinical studies contain cohorts of varying age, weight and co-morbidities (Lelovas *et al*. 2008).

The main clinical case of SCI is one in which the patient is adult and has experienced incomplete SCI (Cheriyan *et al.* 2014). The chosen model in this regard would seem initially to be a bad choice in analysing bone post-SCI. However, the complete SCI model presents an advantage over incomplete forms of SCI such as contusion in that the injury is more repeatable and consistent to administer. This model also avoids the growth recovery effects that are common in subjects with partial motor function, as the administered paralysis is total and unrecoverable. A final advantage to using this model is the severity of injury. SCI transection incurs the largest impact on future endochondral ossification (bone growth) in the sublesional bones, meaning that the growth occurring in the analysed rats is minimised and the effects are confounded to a lesser extent when compared to the main clinical case (Williams 2019).

Chapter 3: Characterising SCI-Induced Osteoporosis using MicroCT

3.1 MicroCT Literature Review

3.1.1 Computed Tomography

Tomography is an imaging method that uses penetrating waves (mainly X-rays) to produce cross sections (tomograms) through an object. Computed tomography (CT) is a medical imaging technique that utilises rotating X-ray tube(s) to take multiple X-rays at different angles around the scanned object. In CT, the X-ray source emits to multiple detectors which are aligned radially around the object, creating a 'fanned' image which avoids superimposition. The scanner moves the X-ray source and the detectors in sync around a patient, creating an image cross section at each position. Figure 3.1 shows a modern CT scanner:

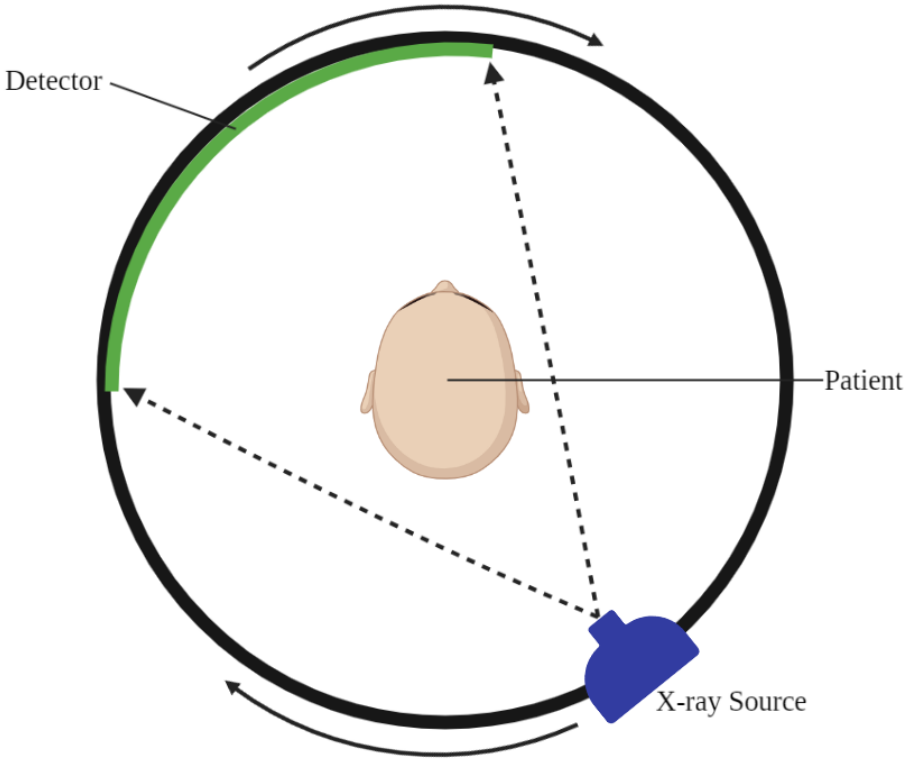

Figure 3. 1: CT scanner diagram.

Clinical CT scans can be repeated at regular intervals along the object (patient), and the series of slices that are captured can be processed in reconstruction software to create a 3D structures from a sequence of 2D projections (Parks 1986).

3.1.2 MicroCT Fundamentals

MicroCT is a further development to CT scanning. It was devised in 1989 (Feldkamp *et al*. 1989) and utilises a different type of scanner in which the X-ray source and detector remain stationary whilst a small object (such as a rodent bone) is rotated in discrete steps at the centre of the scanner. Figure 3.2 displays a schematic of the principal of operation:

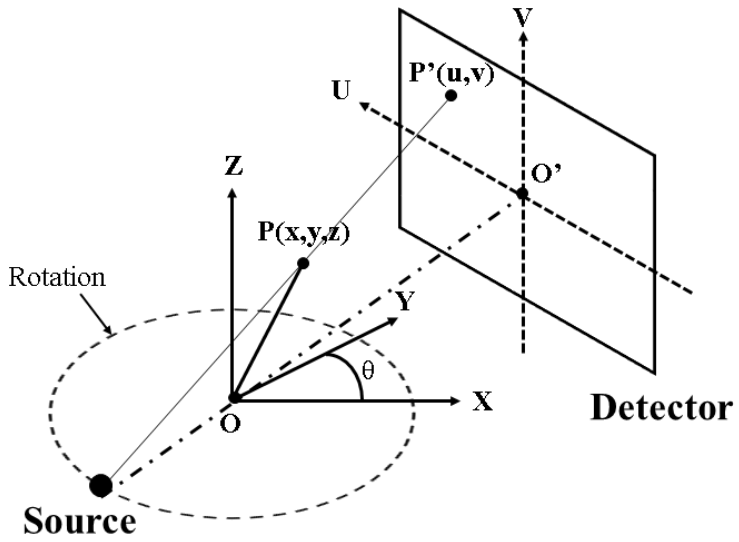

Figure 3. 2: MicroCT scanner diagram. With a rotation of Θ, the points O and P in the object remain in the same locations, but their resulting projections on the 2D detector (O' and P') change. The exact 3D coordinates of O and P can be determined once reconstruction has been completed using the values of O' and P' at all values of Θ. Reproduced from Williams 2019.

MicroCT scanners capture planar 2D images in a radial pattern. The working concept is as follows. First, many 2D projection images of an object are captured at a regular interval, usually a fraction of a degree (known as the rotation step). These 2D projections are then computed into cross-sectional images and grouped into a z-stack of sequential slices, in a process known as reconstruction. The resulting z-stack of cross-sectional 2D slices can be used to make 3D models for subsequent analysis.

As the name suggests, microCT provides a much higher resolution (μm compared to mm) than clinical CT (Kuhn *et al*. 1990). Clinical CT scanners are hence limited in

their analysis potential for bone. More detailed, microarchitectural bone analyses (discussed later in this chapter) are only available when utilising higher resolutions.

3.1.3 DXA and MicroCT

The clinical standard for measuring bone mineral density (BMD) to diagnose osteoporosis is a technique known as dual energy X-ray absorptiometry (DXA). The main reasons for this are the low X-ray dose and fast scanning time when compared to other non-invasive imaging techniques such as microCT. However, DXA can only express BMD as an area (2D) measurement (g/cm^2), limiting its ability to fully characterise the bone quality (Li *et al*. 2013). This is due to the setup of a DXA scan; put simply there are two X-ray beams (high and low energy) passed through the patient simultaneously, with two detectors for either energy level sandwiched on top of one another. Attenuation coefficients are calculated for either X-ray and the resulting absorption levels of each beam used to calculate the amount of bone mass per cm^2. The subject is moved in the XY plane during this process in order to generate average aBMD values for entire regions, commonly the hip and lower spine for osteoporosis diagnosis (Kanis 2002). Figure 3.3 is provided for understanding of the DXA method:

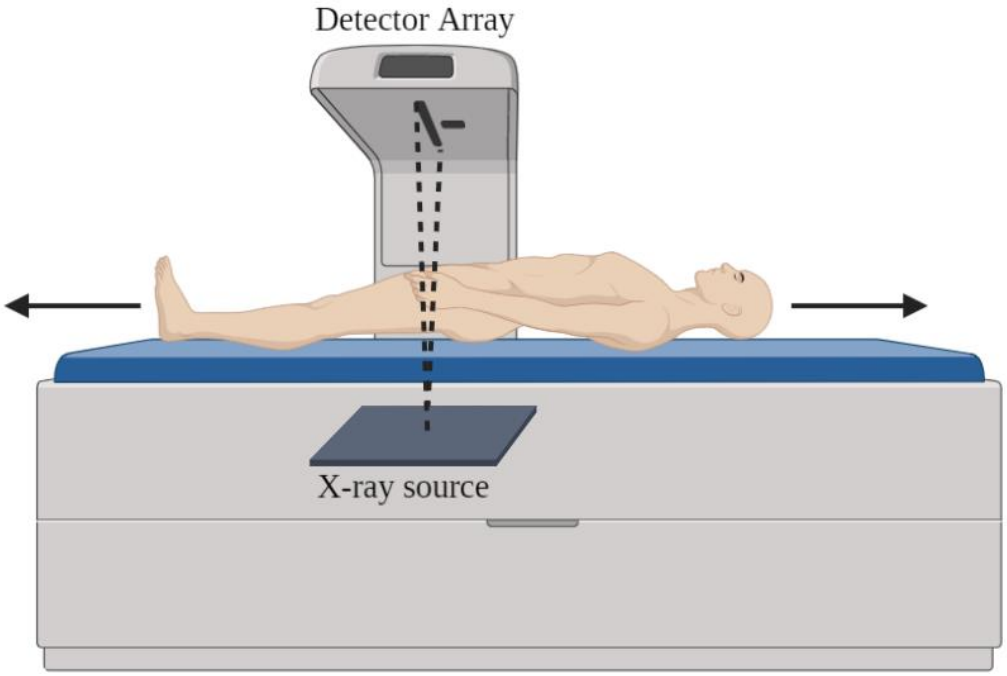

Figure 3. 3: DXA scanner diagram.

As a stepping stone to the resolutions and step sizes obtainable with microCT, another imaging technique known as peripheral Quantitative Computed-Tomography (pQCT) is available for imaging of the appendicular skeleton. It has clinical applications, as the radiation dose is sufficiently low to be used on living subjects, and provides step sizes of as low as 1mm, with resolutions as fine as 100μm. Additionally, pQCT allows for distinctions to be made between different tissues present in the limbs scanned i.e. it allows for separate measurements on bone, muscle and fat in the VOI obtained. A final benefit to using pQCT is the same as that obtained with microCT; a true volumetric assessment of BMD is obtainable as the attenuation measured throughout different slices of the VOI is calibrated to known attenuations due to different hydroxyapatite densities (Stagi *et al*. 2016).

In comparison, microCT scans are performed at multiple angles around the object, either through a 180^{o} or full rotation of the specimen (in the case of a denser object like bone which might fully absorb all X-rays depending on the X-ray energy level set). This results in a map of X-ray attenuation values for each voxel in the 3D reconstruction. With this information, an assumption is made that 'the X-ray attenuation within mineralised tissues such as bone is dominated by, and can be approximated as, the X-ray attenuation of the mineral compound calcium hydroxyapatite' (Bruker 2011b). Using this assumption, phantoms (blocks with known concentrations of calcium hydroxyapatite) can be scanned prior to the bone sample and their attenuation profiles used to calibrate the readings. This gives a volumetric BMD measurement in g/cm^3, as opposed to the 2D result (g/cm^2) from DXA.

3.1.4 MicroCT Morphology and Topology Analysis

When analysing bone's microarchitecture, morphology refers to the assessment of bone's three dimensional structure including shape and distribution of material at a surface. Standard morphological properties of a trabecular network include the thickness (diameter) of trabeculae, the separation between them, the linear density (trabecular number) and the volume of trabecular bone in a given region (Bouxsein *et al.* 2010). These assessments were initially performed via direct 2D measurement on stained histomorphometric bone sections, with stereology then employed to derive information for entire 3D volumes by taking multiple consecutive 2D slices.

MicroCT presents multiple advantages over 2D histomorphometry by employing direct 3D measurements on the trabecular bone. This results in shorter analysis times, and larger VOIs can be studied. This technique is also non-destructive, leaving potential for additional analyses like tension or torsion mechanical testing.

As well as the standard morphological parameters like trabecular thickness and number, recently developed morphological assessments are now in use in the literature for advanced insights into pathologies such as SCI. Ellipsoid factor (EF) is one such morphological analysis which is employed in this study to give additional, detailed information into the effects of SCI on sublesional trabecular bone (Doube 2015).

Topology is defined as the properties of an object which remain invariant through elastic shape transformations like stretching and twisting. Topological parameters such as connectivity density and inter-trabecular angle (Reznikov *et al.* 2016) are included in the analysis in the current study, with a view to providing the most complete characterisation of the bone quality through combining mineral density, morphological and topological assessments.

3.2 Methodology

3.2.1 Rat Model of SCI

The chosen model of spinal cord injury (SCI) for this study was spinal cord transection, specifically at the thoracic-9 (T9) vertebra. Transection is a complete form of SCI, as the cord is severed and a small section is removed. This model avoids the effects of partial functional recovery that incomplete SCI models frequently encounter, as some motor function recovery is common following injuries such as contusions. The experimental and surgical procedures were all undertaken by Dr John Riddell and Dr Jonathan Williams in compliance with the Animals (Scientific Procedures) Act 1986. The Ethical Review Panel of the University of Glasgow, UK gave approval for the study.

6 male SD rats were acquired from Charles River Laboratories, Tranent, UK at 200-225g, around 7 weeks of age. They were then allowed to acclimatise for one week before being split into two groups (n=3) and given either a spinal cord transection surgery at the T9 vertebra or no spinal cord surgery (naïve controls), wherein the spinal cord was exposed but not transected. This sham operation allowed for a more accurate control which eliminated the effects of surgery from the results.

The rats were allowed to live in their SCI state for 11 weeks post-surgery before sacrifice. Contralateral hindlimb pairs (left and right femora and tibiae) were extracted for analysis. Left hindlimb bones were selected for microCT analysis of the bone architecture changes during SCI. Right hindlimb bones were used for analysis of the bone remodelling (TRAP staining) and blood network (CD34 immunohistochemistry) impact of SCI, via histology and immunohistochemistry.

3.2.2 Acute SCI Dataset

Complications due to COVID-19 had initially reduced this project to a single cross-sectional study, at 11 weeks post-injury i.e. chronic SCI and n=3 for SCI and CTRL groups. In an effort to provide more datapoints for correlation analysis, to provide additional information on time course effects of complete SCI, and to increase the results available for the chosen growing rat model of complete SCI, an additional acute SCI proximal tibia dataset was included for analysis.

The model selected for this acute dataset was almost identical to the chronic SCI model. The only difference was the species of rat and the timepoint post-injury. 11 male Wistar rats (n=5 SCI and n=6 CTRL) were operated on at 7 weeks of age, ~225g bodyweight. They were given either a T9 SC transection or a sham operation as before. Right tibiae were acquired following sacrifice at 2 weeks post-injury. The bones were processed, microCT scanned, reconstructed and analysed at exactly the same parameters and settings as the chronic dataset.

For clarity, the addition of the acute dataset resulted in the following:

1. Distal femur and proximal tibia chronic (11 weeks) microCT and histology analysis.
2. Proximal tibia acute (2 weeks) microCT analysis.
3. No histology was performed on the acute dataset.

3.2.3 MicroCT Scanning

The rats were sacrificed and their bones were excised, cleaned and stored at -20^{o}C. To prevent samples from drying out, they were wrapped in gauze soaked in phosphate-buffered saline (PBS) before freezing.

The bones were thawed at 4^{o}C overnight and scanned in a microCT scanner (Bruker Skyscan 1172, Kontich, Belgium). In order to minimize image artefacts, the bones were placed in as secure a position as possible, rotating as close as possible to the rotation axis (isocentre) of the scanner platform. This was achieved through placing the gauze-wrapped bones in plastic Bijou tubes and securing each Bijou tube in a screw-tightening mount at the centre of the platform.

The scanner settings used were as follows: X-ray tube voltage 70kVp, X-ray tube current 100µA, Isotropic voxel size 10µm, Camera resolution medium 2k, Rotation step 0.4°, Frame averaging 2, Total rotation 180°. A 0.5mm thick aluminium filter was placed in front of the X-ray source in order to pre-harden the beam. Beam hardening is explained in section 3.2.6.

3.2.4 Image Reconstruction

The microCT images were reconstructed using Bruker NRecon software (Version 1.6.9.18, Kontich, Belgium). The projection images were reconstructed into 8-bit (256 grey levels) greyscale image slices using the Feldkamp-David-Kress (FDK) cone beam algorithm (Feldkamp, Davis & Kress 1984).

The isocentre of the X-ray scanner does not align exactly with the rotation axis of the scanned long bone in practice. This is because rat femora and tibiae are not perfect cylinders; they bend slightly towards the lateral and anterior directions. Because of this, the first and last projection images captured i.e. the 0° and 180° projections are often misaligned following scanning. This produces streak artefacts, detailed in Figure 3.4:

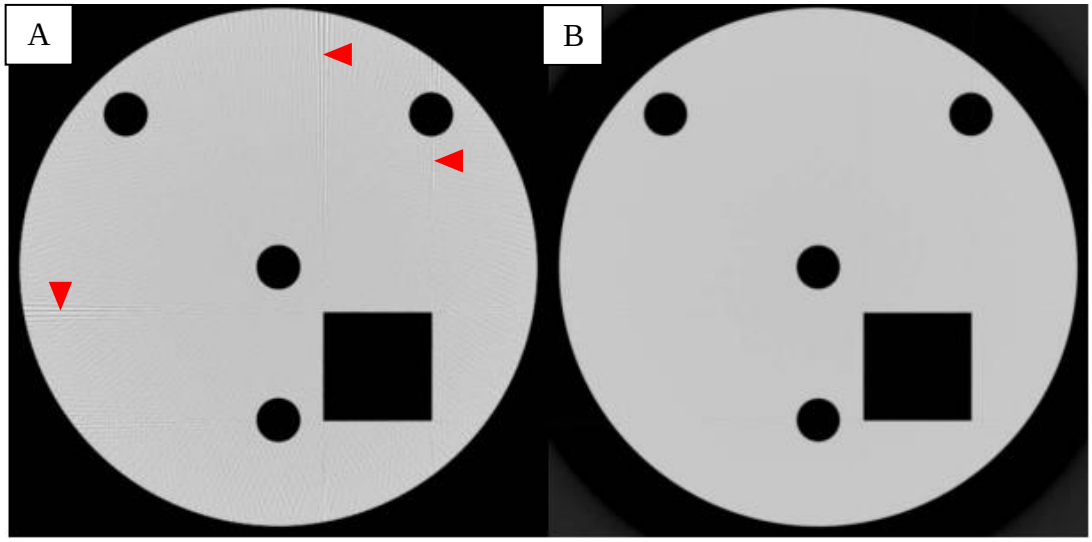

Figure 3. 4: Misalignment compensation in example test phantom. A: Projection image taken with a total rotation of 180°, requiring misalignment compensation as evidenced by the streak artefacts (red arrowheads). B: Perfectly reconstructed image of the same phantom. Reproduced from Davis & Elliott 2006.

As the microCT scan was designated at 180^{o} rotation range, the realignment compensation was checked against the 0 and 180^{o} attenuation profiles for each bone. Manual adjustment of the alignment of the two profiles was required in ~10% of cases to remove streaking and blurring artefacts.

3.2.5 Gaussian Smoothing

MicroCT scanners experience a problem known as mottle, so called as it presents as a mottled appearance on zoomed-in images. This is due to the discrete grid-pattern of the charged couple devices (CCDs) on the X-ray detector being struck by a stochastic distribution of photons from the source beam. Smoothing operations are usually performed on the X-ray projection images during reconstruction to account for this artefact. The smoothing operation used here was a 2D Gaussian smoothing filter.

A Gaussian filter (or Gaussian smoothing operator) is a 2D convolution operator similar to a mean filter. A mean filter uses identical scaling values in each pixel of a kernel, moves the kernel through the image, and multiplies the corresponding underlying pixels together before summing to create an average pixel value for each kernel position. A Gaussian filter uses the same kernel but the scaling values are altered so that the smallest are on the outside edges and the largest at the centre. Figure 3.5 displays the result of discretising the 2D Gaussian distribution into a square kernel comprised of multiple pixels:

A

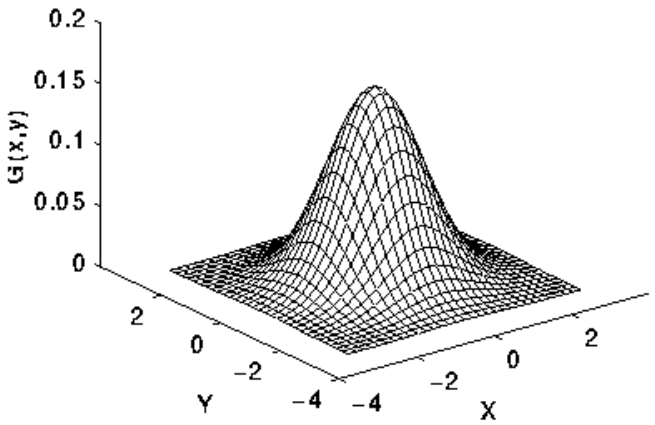

B

1	4	7	4	1
4	16	26	16	4
7	26	41	26	7
4	16	26	16	4
1	4	7	4	1

Figure 3. 5: A: 2D Gaussian distribution. B: A discretised representation of a smoothing filter kernel with values approximating a Gaussian distribution. Adapted from Fisher et al. 2004.

The kernel slides through each position in the image in which the kernel can be fully contained, producing an output pixel value for each kernel position by multiplying together the relevant pixels at that position and summing, as displayed in Figure 3.6:

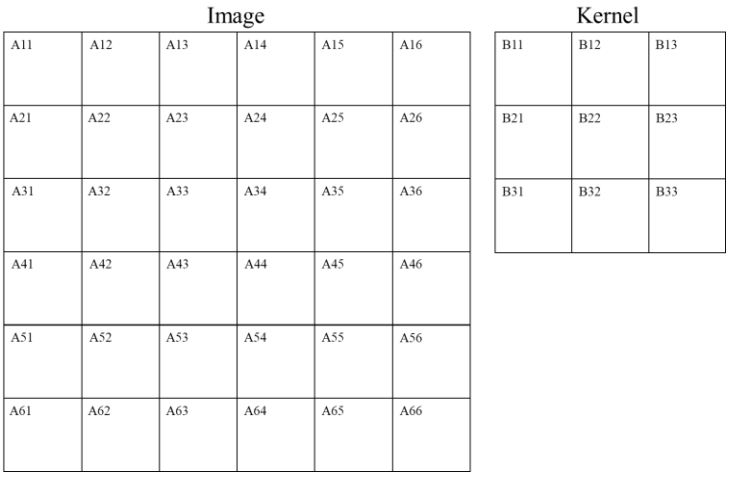

Figure 3. 6: Convolution operator diagram. The kernel is slid along each position in the image to be filtered which allows the kernel to be fully contained.

If the image is composed of 'A' rows and 'B' columns, and the kernel contains 'a' rows and 'b' columns, the output image will contain A-(a+1) rows and B-(b+1) columns. The output image in the this case would have values in the top left position equating to $A_{11}B_{11}+A_{12}B_{12}+A_{13}B_{13}+A_{21}B_{21}+A_{22}B_{22}+A_{23}B_{23}+A_{31}B_{31}+A_{32}B_{32}+A_{33}B_{33}$.

This Gaussian method of smoothing produces a weighted average pixel value for each pixel's neighbourhood (defined by the kernel size), with the larger values at the centre. This leads to less effect at the edges, which means it is a more effective smoothing operation for preserving the edges of a given object. In order to account for mottle, Gaussian smoothing was applied to the projection images with a 4x4 square kernel during reconstruction. The inner pixels of the kernel had a weight of 1, whilst the outer pixels had a weight of 0.5 (Bruker 2011c).

3.2.6 Beam Hardening

The X-ray source used in microCT is polychromatic. That is to say, it is composed of a spectrum of different energies.

Beam hardening occurs when the low energy components of a polychromatic X-ray beam are attenuated more than the high energy components when moving through a

scanned object (a femur or tibia in this case). The beam is said to 'harden' as it passes through the object, leaving only the higher energy photons of the X-ray source being absorbed by the detector. The FDK algorithm uses the assumption that every point along the X-ray source path experiences the same attenuation through the sample. Beam hardening makes this untrue in practice. The X-ray beam will be attenuated to a greater extent at the first point of contact it makes with the object, and to a lesser extent at the exit side. This results in a contrasting appearance at the edges of the bone. Figure 3.7 illustrates this:

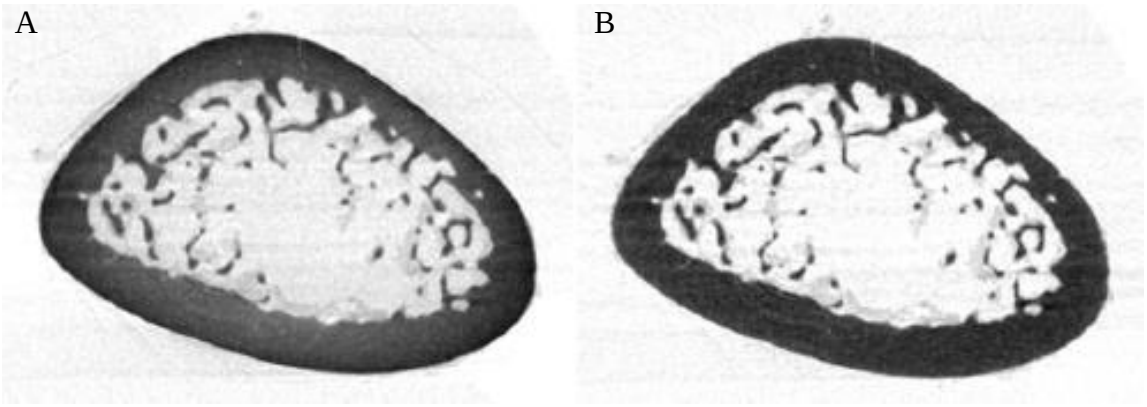

Figure 3. 7: Beam hardening artefact in microCT reconstructed cross section of rat femur. A: no beam hardening correction applied. B: same cross section following beam hardening correction. Reproduced from Bruker 2011a.

For monochromatic X-ray sources, Beer's law applies when assuming bone is of approximately uniform density (X-ray absorption), as displayed in equation 3.1:

$$\frac{I}{I_0} = e^{(-\mu t)} \tag{3.1}$$

Where I is the intensity of the transmitted X-ray, I_0 is the intensity of the X-ray incident on the detector, e is Euler's number, μ is the linear attenuation coefficient of the bone and t is the thickness through which the X-ray has travelled.

For polychromatic X-ray sources, however, the attenuation of a homogeneous density material is not proportional to the thickness, as the attenuation coefficients are lower for higher energy components of the X-ray beam. This produces a curved (instead of linear) relationship between the attenuation given by $\log_e(I/I_0)$ and t, which is corrected through application of a 2nd order polynomial equation. This correction aims to restore the linear relationship, and can be altered in NRecon as a percentage value (Bruker

2011c). The percentage value here defines the weighting of the quadratic term in the 2nd order polynomial. Through a process of manual trial and error whilst examining the resulting images at different percentages, beam hardening correction in NRecon was set at 20% for all reconstructions.

3.2.7 Ring Artefacts

On each CCD comprising a X-ray detector, varying numbers of electrons from the X-ray beam are incident. The gain of a detector system is specified by the user, and it determines the number of incident electrons necessary for one 'count' of an analogue to digital unit (ADU) to occur for that CCD. More ADUs at a CCD correspond to a higher pixel value at that location. The calculation of gain for digitized X-ray images in given in equation 3.2:

$$Gain = \frac{Incident\ electrons\ per\ pixel}{Counts\ per\ pixel} \tag{3.2}$$

Ring artefacts are caused by imperfections in the detector array like gain errors due to defective CCDs at specific positions. Once the X-ray source has completed a full rotation, this presents as a bright ring on the object being scanned. Figure 3.8 illustrates ring artefact correction:

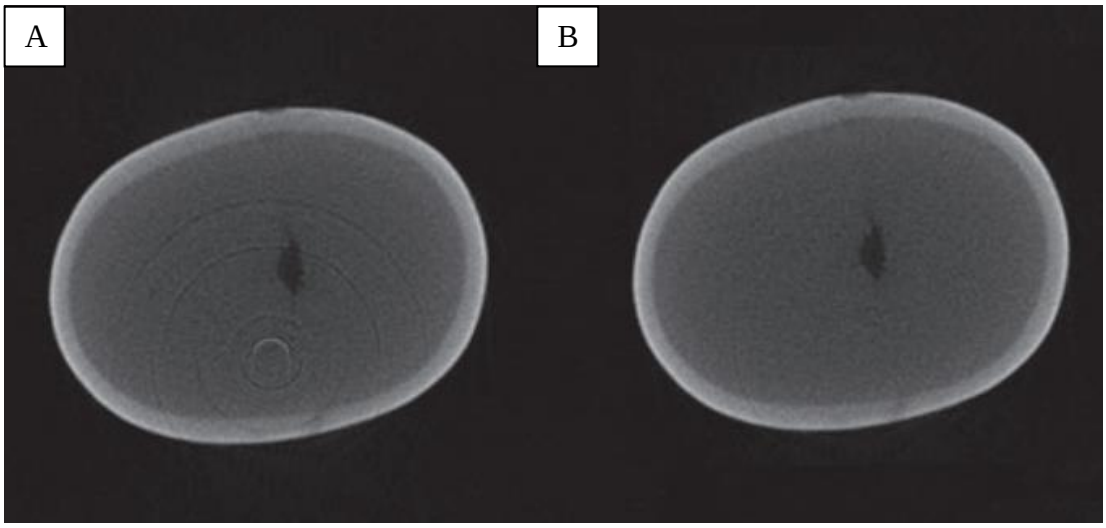

Figure 3. 8: Ring artefact correction in a microCT scan of a rat tooth crown. A: Raw projection image presenting ring artefacts. B: Image after correction. Reproduced from Adapted from Orhan, de Faria Vasconcelos & Gaeta-Araujo 2020.

Before reconstruction, ring artifacts present as vertical lines on the collection of 2D projections acquired from the microCT scanner; the sinogram. The sum of every grey value in each column of the sinogram is computed. This produces troughs in the grey value graph at the same x-positions as the artefacts, as displayed in Figure 3.9:

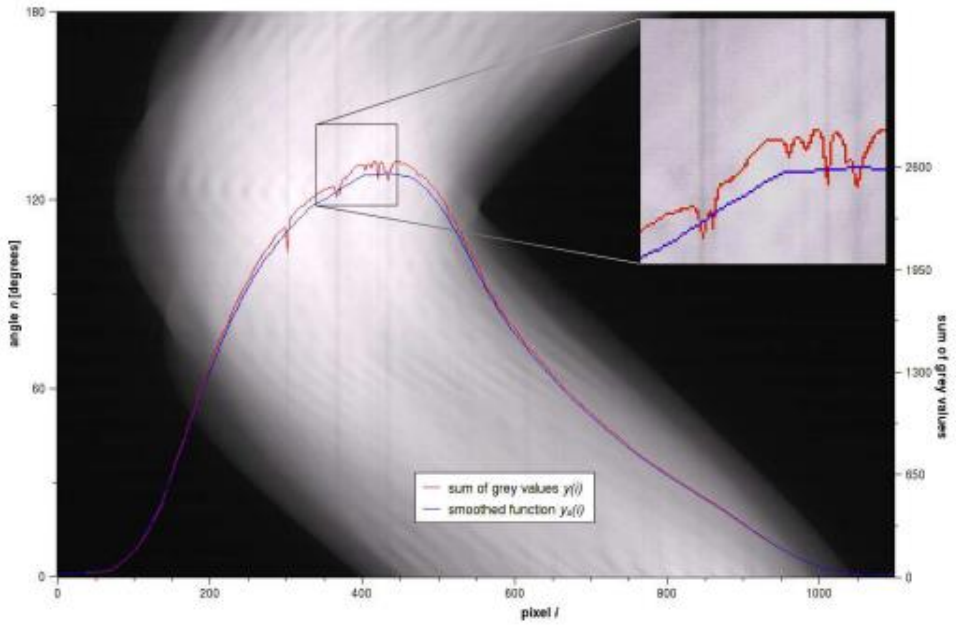

Figure 3. 9: Ring artefacts correction in the sinogram. Grey value summations for each column present as troughs (red line on top-right graph) at the same locations as each artefact. Reproduced from Boin & Haibel 2006.

The troughs in the function of grey value vs x-position are reduced via application of a smoothing function, displayed in equation 3.3:

$$y_s(i) = \frac{1}{2N+1}[y(i+N) + y(i+N-1) + \cdots + y(i-N)] \qquad (3.3)$$

Where y_s is the smoothed grey value of the original y, N is the span factor which ranges from 1 to 20 in NRecon and i is the x-position of the column of pixels being smoothed. It follows that a greater value of N results in a broader neighbourhood of grey values included in the smoothing, reducing the artefact to a greater extent (Boin & Haibel 2006). As with the beam hardening correction, the ring artefacts correction (N value) was set in NRecon via an iterative process, analysing the resulting image at each value. It was set to 13 for all reconstructions. Values higher than this resulted in blurring of the images.

Once reconstructed using the appropriate artefact corrections, the datasets were loaded into Bruker Dataviewer software (Version 1.5.1.9, Kontich, Belgium) for minor adjustment of the orientation of each bone scan. This was to ensure that each slice in the final dataset for analysis was displaced primarily in the z-axis from its neighbour, with minimal XY displacement between slices. This arrangement was necessary for correct definition of the reference height for each trabecular volume of interest (VOI) for analysis. The term 'reference height' is explained in the following section.

3.2.8 CTan Metaphyseal VOI Segmentation

The reconstructed 2D image stacks were loaded into Bruker's CTan software (Version 1.18.8, Kontich, Belgium) and a metaphyseal VOI was selected using the following protocol adapted from the method note supplied with the CTan software (Bruker 2016). This metaphyseal VOI was for trabecular and cortical porosity analysis. Cortical tissue mineral density (TMD) analysis was performed in a diaphyseal VOI which is defined in the next section.

Metaphyseal VOI:

- Moving slice by slice from the epiphyseal (proximal tibia or distal femur) end of the bone, a region begins to appear in which the epiphyseal trabecular bone gives way to an appearing band of low-density cartilaginous tissue. This cartilaginous tissue lies adjacent to the primary spongiosa emanating towards the diaphysis from the growth plate.
- The chondrocyte seam can be seen emerging in Figure 3.10:

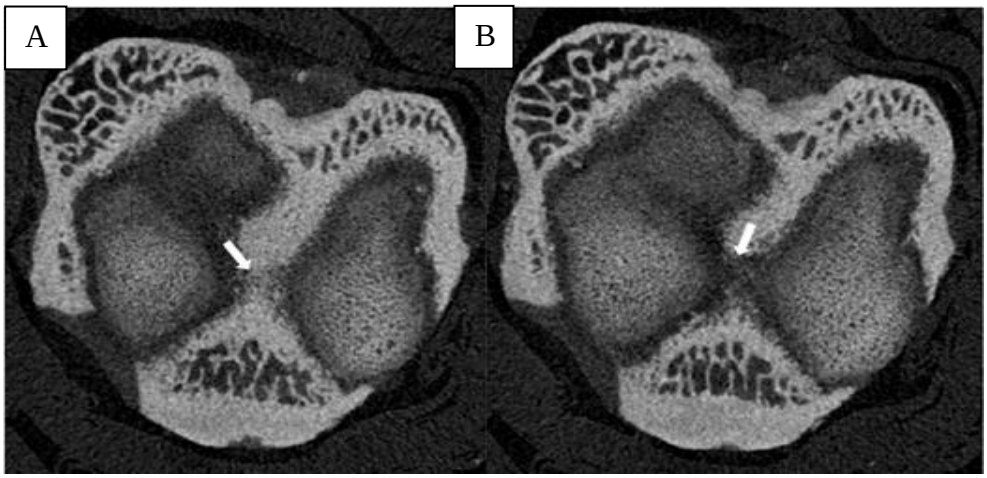

Figure 3. 10: Emerging chondrocyte seam in metaphyseal proximal tibia. As the last bone segment of the primary spongiosa disappears (Image A arrow), the low-density cartilage first joins at a distinct bridge (Image B arrow).

- The slice at which the cartilage bridge is first considered to be clearly connected is designated as the reference slice, designated in blue in Figure 3.11.

- The metaphyseal volumes of interest can now be defined relative to this reference level, as displayed in the CTan bone overview in Figure 3.11:

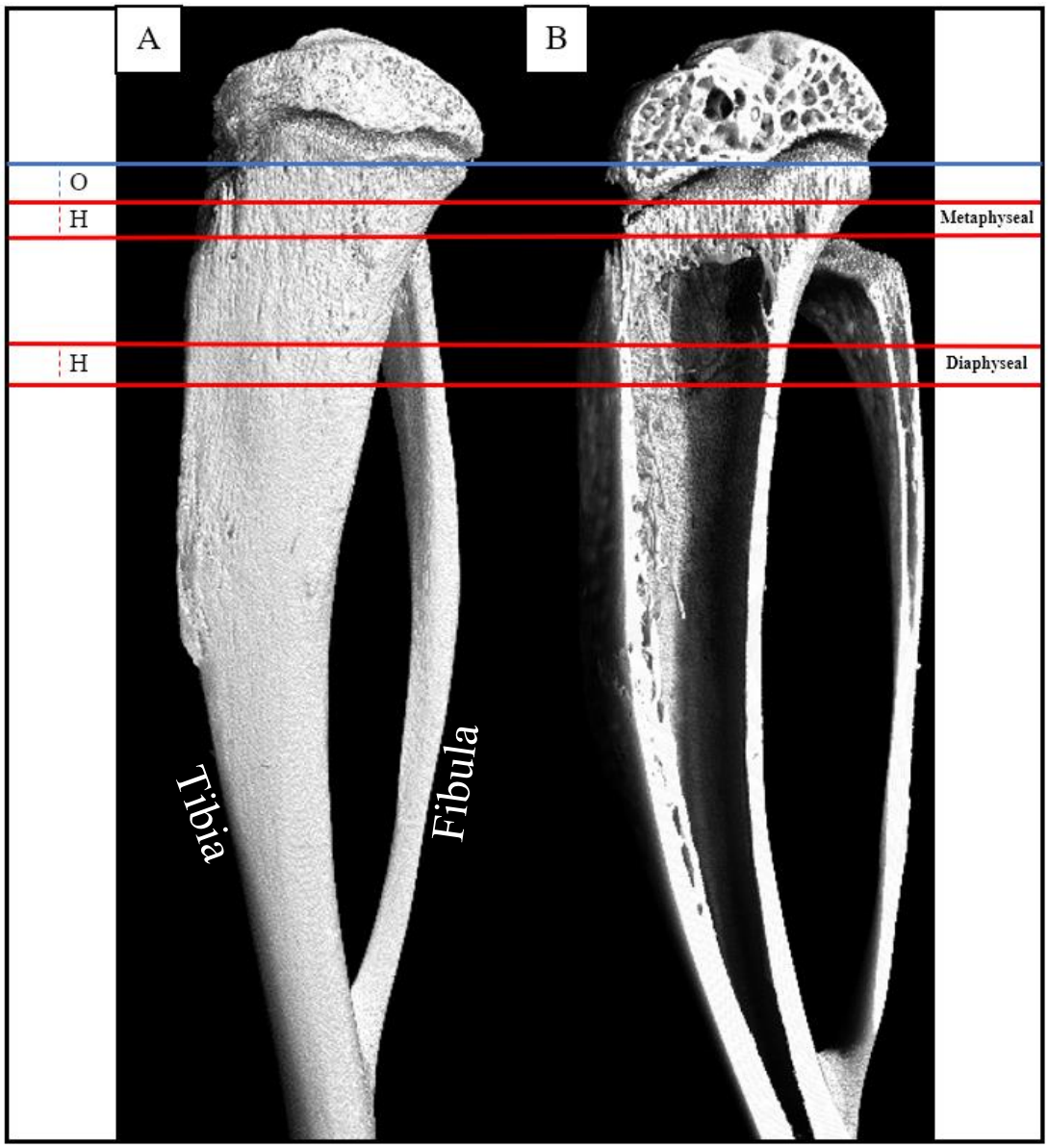

Figure 3. 11: VOI selection diagram. Rat left tibia. Blue line: Reference slice. O: Offset. H: Height. A: Proximal tibia. B: Cutaway showing trabecular rich (metaphyseal) and sparse (diaphyseal) VOIs.

- Bone length was measured using digital calipers prior to X-ray scanning. The offsets and heights of each trabecular VOI were calculated as 2.5% and 5% bone length respectively.

- When drawing the trabecular region of interest (ROI), the boundary was placed as close as possible to the endosteal (inner) surface of the bone marrow cavity, whilst still excluding the cortical shell.

- The cortical ROI delineation was similar, excluding the trabecular bone and ensuring the entire periosteal perimeter was included.
- For the proximal tibia, it was ensured that the fibula was excluded from the ROI. Figure 3.12 displays the two different ROI definitions for the metaphyseal region:

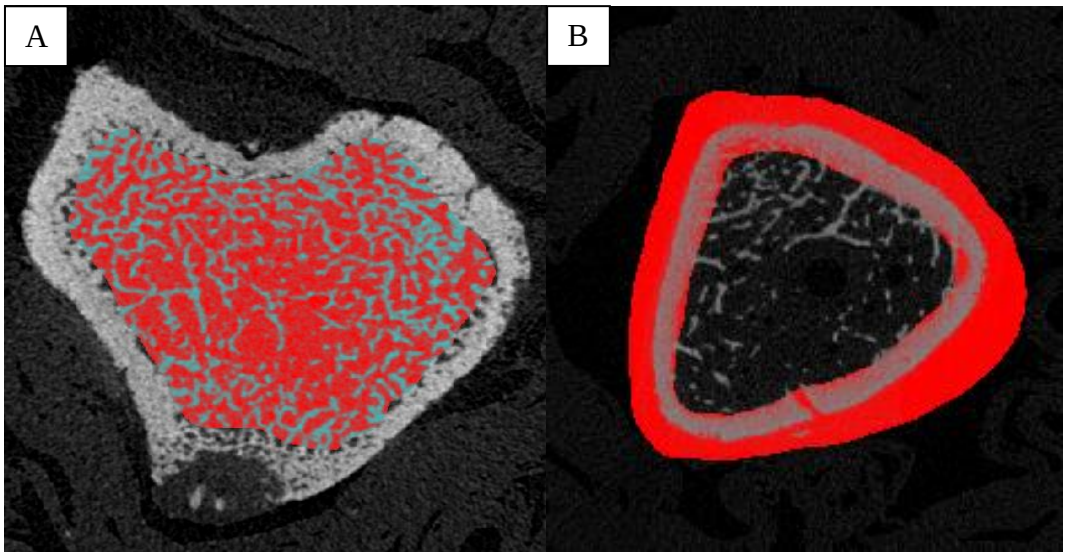

Figure 3. 12: Trabecular and cortical ROI delineation in the metaphysis. A: Trabecular ROI. B: Cortical ROI.

- Trabecular and cortical (porosity) ROIs were then drawn by hand at the first and final slices of the VOI (the slices at the red lines in Figure 3.11), as well as at semi-regular intervals in between where required.
- The built-in feature 'interpolate ROI' was then utilised in CTan to complete the ROIs for all remaining slices in each VOI.

Example metaphyseal trabecular and cortical VOIs are displayed in Figure 3.13:

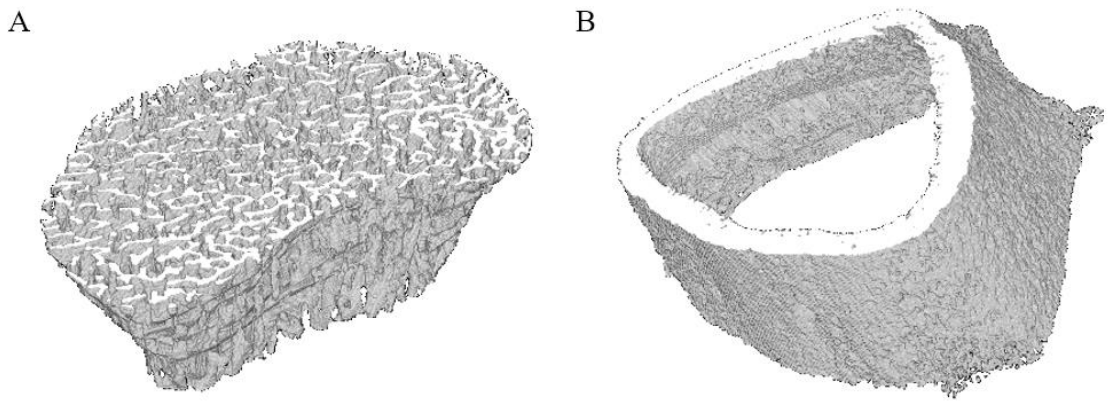

Figure 3. 13: Metaphyseal volumes of interest. A: Trabecular VOI. B: Cortical VOI.

Once a VOI had been defined in this manner, a new and much smaller dataset was created. This new dataset enabled a significantly faster level of manipulation in digital image processing software for the various analyses.

3.2.9 CTan Diaphyseal VOI Segmentation

During microCT scanning, each femur and tibia was designated with a proximal scanning region and a distal scanning region following a scout scan. This removed the mid-diaphysis from each bone, significantly reducing scanning time whilst allowing an adequate portion of diaphysis to remain in each. Figure 3.14 displays the scanned regions:

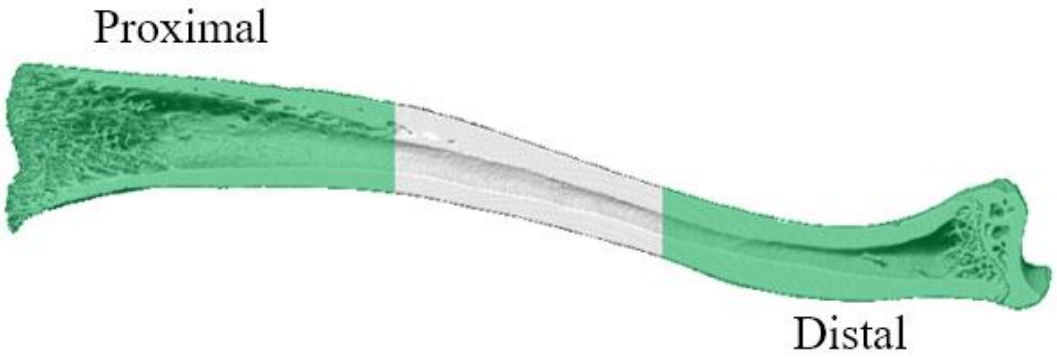

Figure 3. 14: Example rat tibia showing proximal and distal scanning regions, omitting the midshaft in order to decrease scanning times.

As with the metaphyseal VOI selection, the reconstructed 3D bone volumes were loaded into Bruker's CTan software and cortical VOIs selected according to the following protocol. The protocol was adapted from the method note supplied with

CTan software and assumed that the bone volume was split into a z-stack of multiple image slices:

- Moving slice by slice from the diaphyseal end slice in each VOI, a depth of 100 slices (1mm) was designated for the cortical VOIs (Figure 3.11). Bruker recommends at minimum of 50 slices for VOI height, as the direct 3D cortical measurements are divided by the VOI height in order to produce the 2D cortical results. A smaller VOI height would therefore incur a greater likelihood of failing to represent a true average result for the bone in question.
- A cortical ROI was then drawn by hand at the first and final slices of the VOI (Figure 3.11).
- The cortical 'halo' shaped ROI was defined by first drawing a circular region around the diaphyseal cross section, and then using the 'remove' function in CTan to exclude the medullary cavity. Figure 3.15 displays the method for creating a cortical ROI:

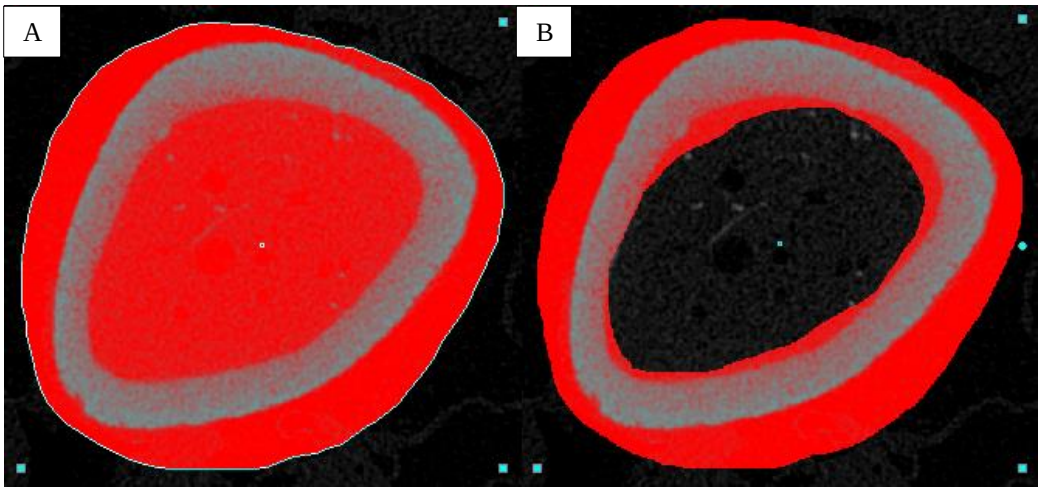

Figure 3. 15: Cortical ROI delineation in CTan software. A: The initial ring is hand-drawn around the periosteal surface. B: A subtraction is made from the ROI, removing the medullary cavity region from analysis without overlapping the endosteal cortical surface.

- When drawing the cortical ROIs for both the metaphyseal and diaphyseal regions, the initial outer ring was not required to be particularly accurate, as a shrink-wrap operation would later be performed to assign the ROI to the cortical bone (see Appendix entries 1 and 2). The inner, subtractive ring, however, was ensured to be placed as close to the cortical endosteal surface as

possible. This ensured that any trabecular fragments in each slice would be removed from analysis, leaving just the cortical ‘halo’ shape.

An example diaphyseal cortical VOI can be seen in Figure 3.16:

Figure 3. 16: Binarised cortical VOI.

This diaphyseal cortical VOI was used for all cortical analyses except for porosity. The reasons for analysing porosity at the metaphyseal region instead were twofold:

1. The accompanying histology (see pages 149-152). As metaphyseal cortical blood vessel density was analysed using histology, it was more suitable to compare the cortical porosity at the same metaphyseal region as the vascularization quantification.
2. Diaphyseal cortical pores are too small in the rat to quantify using a resolution of 10µm.

3.2.10 CTan Trabecular Analysis

Once each trabecular metaphyseal VOI had been reconstructed in NRecon, aligned in Dataviewer and segmented in CTan, trabecular bone morphometric analysis was performed using the recommended CTan method note trabecular analysis macro (Bruker 2016).

Each trabecular parameter analysed in CTan for this study is explained below, with a final section on structure model index (SMI), the validity of which has been disputed in recent times (Salmon *et al.* 2015). As a replacement, ellipsoid factor (EF) (Doube 2015) has been developed to provide a description of the plate-to-rod transition in trabecular bone during osteoporosis, which is independent of bone volume fraction (unlike SMI). This parameter was analysed using the ImageJ (Version 1.53q, Bethesda, USA) plugin BoneJ2 (Version 7.0.13, London, UK). Also analysed using BoneJ2, inter-trabecular angle (ITA) (Reznikov *et al.* 2016) was used to gain topological insights into the effects of complete SCI on trabecular bone. EF and ITA are explained in their own succeeding sections.

The exact settings used in CTan were tweaked slightly from the method note:

- Load delineated trabecular VOI.
- Apply global threshold to binarise 8-bit greyscale image. Limits 65-255.
- Despeckle. Type: Remove white speckles in 2D space | Area: Less than 2px | Apply to: Image.
- 3D Analysis: All parameters selected.

In brief, the 8-bit greyscale VOI was binarised by setting a global threshold 65→255, including most of the fine trabeculae in the analysis. Any noise still remaining in the volume was then removed using the despeckle tool in CTan. The despeckle operation in this case was remove white speckles in 2D (slice by slice). A 2x2 pixel kernel was passed systematically over each binarised slice, and if a white segment was fully encapsulated (i.e. any speckles which were smaller than 2x2 pixels), the speckle was removed from the image. The same settings were used for all bones processed for trabecular microCT analysis.

Figure 3.17 displays the results of thresholding and despeckling in CTan:

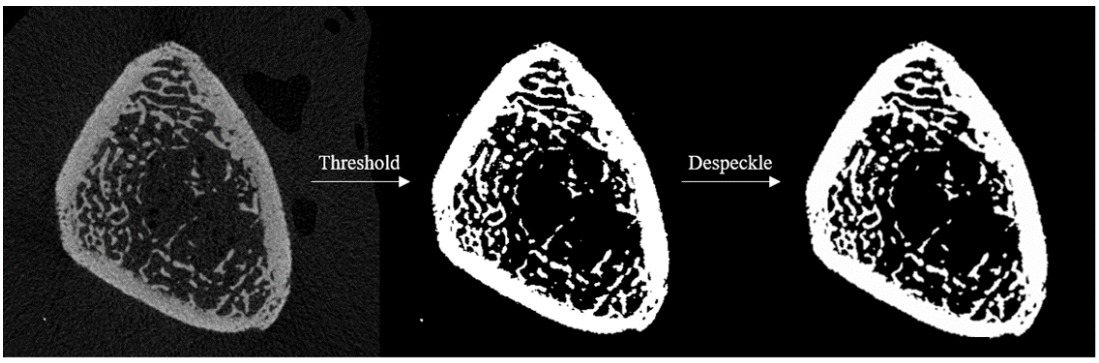

Figure 3. 17: Distal femur trabecular section following thresholding and despeckling operations.

Standard Parameters

3D morphometric analysis was performed on the binarised trabecular datasets. A published list exists of the minimum set of parameters which should be analysed when conducting a microCT study on bone (Bouxsein *et al*. 2010). Table 3.1 details the required trabecular parameters:

Parameter	**Abbreviation (units)**	**Explanation**
Bone volume fraction	BV/TV (%)	Bone volume (BV) is calculated using the volumetric marching cubes algorithm (Müller & Rüegsegger 1995). The trabecular 3D structure is surface rendered and then infilled with tetrahedrons, and their combined volume is the result for BV. Total volume (TV) is simply the volume of the VOI which contains the analysed trabeculae.
Trabecular number	Tb.N (1/mm)	The average number of trabeculae per unit length in the sample. Calculated as the inverse of the number of trabecular junctions by determining first the trabecular thickness and separation.
Trabecular thickness	Tb.Th (mm)	Directly measured average thickness of each trabecula in the sample. Determined using maximal sphere-fitting, wherein the local Tb.Th is defined as the diameter of the largest sphere which can fit inside the trabecula at that point. Average Tb.Th is simply the volume-weighted average throughout the entire 3D volume.
Trabecular separation	Tb.Sp (mm)	Calculated in a near-identical manner to Tb.Th, with the only difference being that spheres are fitted to the negative spaces between trabeculae, instead of the trabeculae themselves.

Table 3. 1: Minimal parameters required for microCT trabecular bone studies. Reproduced from Bouxsein et al. 2010.

Some trabecular parameters like connectivity density, specific surface and fractal dimension are commonly utilised but are not included in the above list of minimal parameters. There are also additional parameters developed in the last ≤6 years which allow a different view of the changing bone morphology following SCI. It is essential to conduct numerous studies involving these more novel microCT analyses (such as ellipsoid factor and inter-trabecular angle – explained later in this chapter) so that potential correlations can be uncovered and SCI effects on bone can be further understood.

Connectivity Density

Connectivity density (Conn.D) in trabecular analysis is a measure of the highest number of connected junctions which can be removed before a trabecular (branching) network splits into 2 pieces. It is normalised to volume, hence it is in units of $1/mm^3$. The Euler number X is determined using equation 3.4:

$$X = \beta_0 - \beta_1 - \beta_2 \tag{3.4}$$

Where β_0, β_1 and β_2 are the Betti numbers for 0, 1 and 2 dimensional complexes i.e. β_0 is the number of separated bone parts (1 if the structure is not split), β_1 is the connectivity (the number of one-dimensional holes) and β_2 is the number of fully enclosed cavities, respectively. As an example, consider a sphere which has β_0, β_1 and β_2 of 1, 0 and 1 i.e. the structure is not split into two parts, it contains no holes and it's surface encompasses a single enclosed cavity.

Once X is calculated, Conn.D is then determined using equation 3.5:

$$Conn.D = \frac{1-X}{V} \tag{3.5}$$

Where V is the volume in mm^3 of the trabecular VOI (Kabel *et al*. 1999).

Specific Surface

Specific surface is calculated using the same surface rendering and tetrahedron infilling as with bone volume fraction (Table 3.1). It is the surface (mm^2) to volume (mm^3) ratio of the trabecular bone, and so it is in units of 1/mm. A higher specific bone

surface indicates that the average trabecula is thinning, typical in osteoporosis (Chappard, Marchadier & Benhamou 2008).

Fractal Dimension

Fractal dimension (FD) is a measure of the simplicity or complexity of an irregular 3D structure, such as trabecular bone, which presents repeating features in its geometry i.e. can be termed self-similar. The FD analysis in this study is performed via the Kolmogorov box-counting method wherein (Bruker 2016):

- The trabecular bone is binarised.
- A digital grid of boxes of equal side length ε is superimposed over the trabecular network.
- The number of boxes intersecting trabeculae (i.e. the number of boxes containing foreground pixels in the binarised image) is counted. This number is termed N.
- The process is repeated varying ε along a reasonable range, in this case 2 to 100 pixels. Reasonable here means not too small or too large, as bone (like most biological materials) does not exhibit fractal characteristics at extremely small or large scales.
- N is recorded for each value of ε.

Figure 3.18 displays the box counting method in 2D. In 3D, the boxes are simply replaced with cubes of side length ε, but the process is essentially identical:

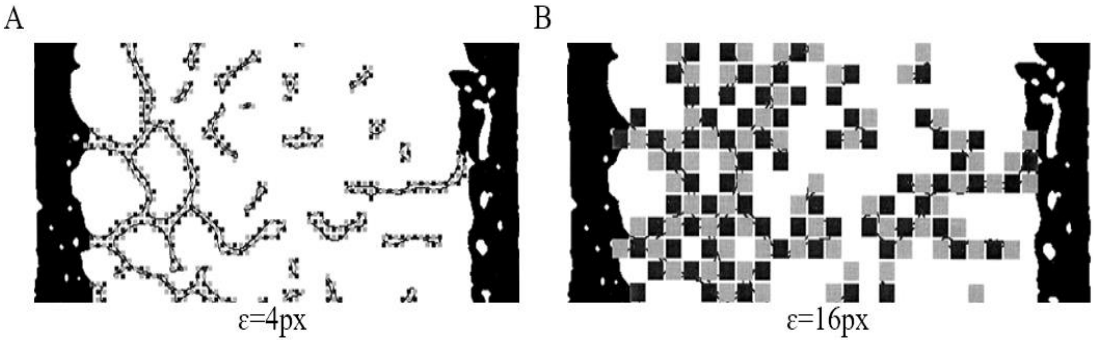

Figure 3. 18: Kolmogorov box-counting method for fractal dimension analysis. Differing numbers N of trabecula-intersecting boxes (black squares) result from lower (A) and higher (B) side lengths. Reproduced from Chappard et al. 2001a.

Once every pair of N and ε value is recorded, a log-log chart of N vs. ε is produced. The slope of its linear regression line gives the value of FD (Chappard *et al*. 2001a). An increased FD means that the trabecular network in the VOI is more complex, that is to say the trabeculae are greater in number, with smaller separation, and are organised in a less regular manner (Gaêta-Araujo *et al*. 2019). Figure 3.19 displays an example log-log FD plot:

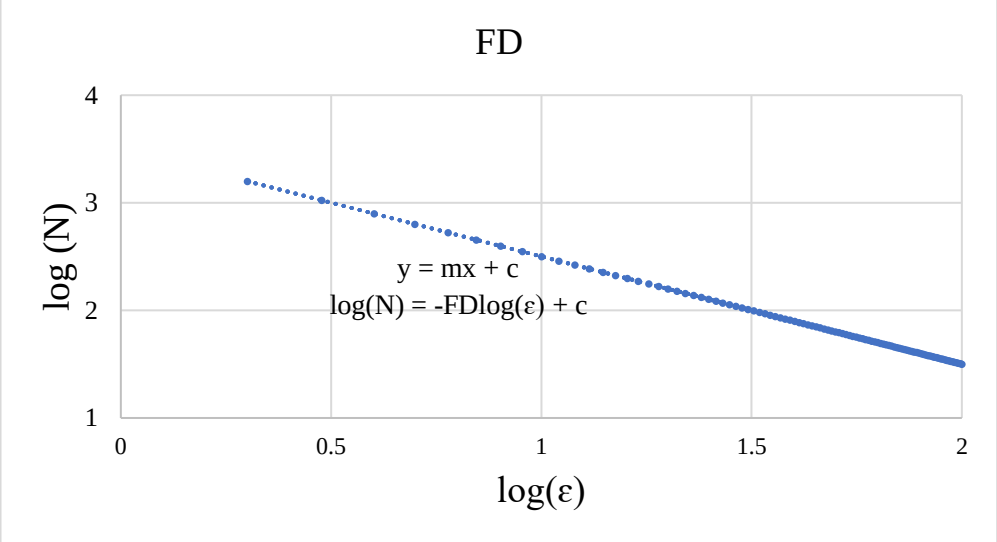

Figure 3. 19: Fractal Dimension calculation using linear regression line slope. Input values are log(ε) from cube side length ε=2 to ε=100, and the log of N; the resulting number of cubes to span the VOI.

Structure Model Index

Structure Model Index (SMI) was the standard for measuring rod-like and plate-like geometries in trabecular bone since its inception. SMI assigns a value varying non-linearly between 0 and 4 to the measured trabecula, basing the value on the change in surface area following a dilation. SMI is 0 for flat planes, 3 for perfect cylinders, and 4 for perfect spheres (Hildebrand & Rüegsegger 1997a). Figure 3.20 illustrates this:

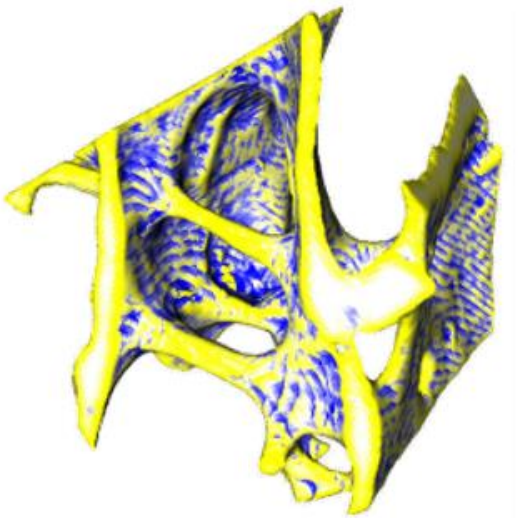

Figure 3. 20: Structure model index uses triangulated meshes on trabecular bone and assesses whether each triangle grows (yellow), shrinks (blue) or remains unchanged (white) following a dilation of the mesh. Reproduced from Salmon et al. 2015.

In recent times, SMI has been shown to be invalid as a measurement of rod-like and plate-like geometries in trabecular bone. This is because the SMI calculation assumes that the analysed structure is entirely convex. In trabecular bone, however, numerous concave geometries exist. Equation 3.6 contains the SMI calculation:

$$SMI = 6 * \frac{\frac{S'}{r} * V}{S^2} \tag{3.6}$$

Where S' is the change in surface area of the entire mesh being dilated, S is the original area of the mesh, r is the dilation distance and V is the bone volume. The concave triangles in the mesh shrink when is it dilated, resulting in a negative value for S'. These SMI^- values alter the overall SMI so that it no longer provides an accurate depiction of the average plate or rod like geometries in each trabecular VOI (Salmon *et al.* 2015).

Additionally, SMI has been previously shown to be dependent on BV/TV (Doube 2015). As a useful replacement, ellipsoid factor (EF) is a more robust and reliable method for analysing local trabecular geometries in a volume. More detail is provided in section 3.2.12. SMI analysis is included in this study to test the correlation with BV/TV and with EF in order to add to the validity of EF as an indicator of the plate-to-rod transition following SCI.

3.2.11 Inter-Trabecular Angle Analysis

Inter-trabecular angle (ITA) utilises the Skeletonize3D algorithm to obtain the skeleton of a trabecular bone region (Reznikov *et al*. 2016). Skeletonize3D is a thinning algorithm which removes a one-voxel layer from the outermost surface of an object, and then repeats this process until the object is only one voxel thick. This one-voxel-thick line (known as a skeleton) therefore runs along the medial axis of the 3D structure which has been skeletonised.

The 'Analyze Skeleton' algorithm is then used to create a node-branch network out of the largest possible skeleton, based on the number of nodes (trabecular junctions). The branches between nodes represent the trabeculae themselves. Figure 3.21 illustrates this:

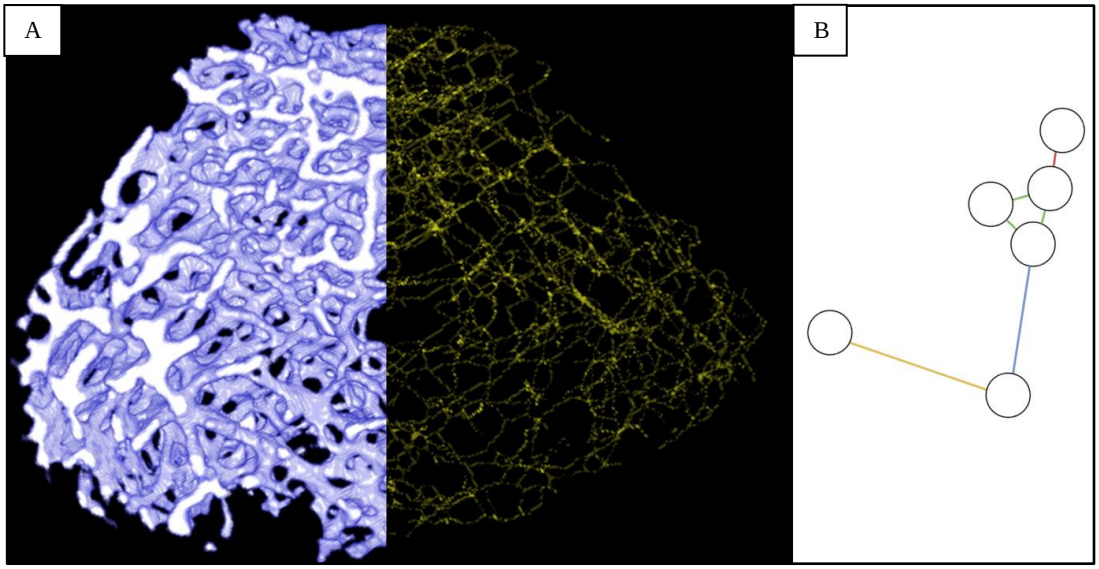

Figure 3. 21: A: Blue left hand side: Original trabecular VOI. Yellow right hand side: Result of skeletonization. B: ITA node-branch network. Red: Dead end. Yellow: Outer branch. Blue: Inner branch. Green: Short branch.

There are four different types of branches defined in the node-branch network (Figure 3.21). An 'outer' branch does not inter-connect any other parts of the graph; only one of its end points connects to only one branch. An 'inner' branch connects to nodes with more than one branch. A 'dead-end' branch is just an outer branch whose length is smaller than the minimum length for a trabecula to be deemed as such (set by the user). Similarly, a 'short' branch is just an inner branch whose length is smaller than the minimum trabecular length.

The node-branch network is not initially the most ideal representation of the trabecular network in the bone VOI. Numerous branches exist (e.g. dead-ends and short branches) which are not representative of trabeculae in reality. The ITA plugin includes a number of options to alter the topology of the graph in order to obtain a more accurate node-branch network. This process of alteration is known as pruning.

Pruning a dead-end branch simply removes it along with its 'lonely' end node from the graph. Pruning a short branch removes it and its end points, then places a new node at the midpoint of the former branch. The surrounding nodes are then connected by new branches to this newly formed node.

Sometimes, due to the varying topology of node-branch networks, pruning will remove short branches and dead-ends but will also create new ones. The 'iteration' parameter for pruning sets whether or not the pruning process will continue until no short branches and dead-ends are left. Selecting iterative pruning therefore changes the topology to a greater extent.

The final option for pruning is clustering. Clustering searches for all nodes connected by short edges, without pruning them. Once all of the nodes have been found, they are all pruned at once. This leads to a different topology compared to pruning the short ends one by one and creating new node-branch connections each time. Using clustering leads to the same topology each time from the same original dataset.

Loops (branches connected to the same node as a start and end point) and parallel branches (branches connected to the same start and end nodes as another branch) are automatically removed during pruning, as these cause erroneous results in determining node type (Figure 3.21) and ITAs.

The parameters used for the ITA analysis were:

- Minimum / maximum valence: The minimum / maximum number of branch connections for a node to be considered a node.
- Minimum trabecular length (px): The minimum length for a branch to be preserved during pruning.

- Margin (px): The minimum distance of a node in the graph from the edge of the original image to be included in the analysis.
- Iterate pruning: Repeat pruning until no short branches are created.
- Use clusters: Remove all short-branched nodes simultaneously as opposed to sequentially.
- The parameters used for the ITA analysis are outlined in Table 3.2, in conjunction with a binarizing threshold of 90-255 and the application of the despeckle operation to reduce noise:

Parameter	**Value**
Minimum Valence	3
Maximum Valence	5
Minimum Trabecular Length (px)	6
Margin (px)	20
Iterate Pruning	No
Use Clusters	Yes

Table 3. 2: Inter-trabecular angle analysis parameters for trabecular bone.

3N nodes were set as the minimum valence instead of 2N nodes because real 2N nodes (two trabecular struts meeting at an angular offset) could not be distinguished from single, curved trabeculae by the skeletonization algorithm. 5N nodes were set as the maximum valence as the relative abundance of 6N+ nodes in each sample was <2%. As they represented such a small fraction of the total nodes in each VOI, the likelihood that a large portion of high N nodes were artifacts was high. For example, some bones returned node types as high as 11N. In reality, a trabecular junction where 11 struts intersect would be virtually impossible given any reasonable trabecular thickness. It is more likely that these nodes were large, platelike trabeculae containing small pores which were recognized as individual trabeculae. Such structures are also present at the boundaries of the VOI due to manual delineation of the cortical shell during pre-processing, despite the use of the margin parameter in BoneJ's ITA tool. Visually searching 3D VOIs for high N nodes also returned very few 6N+ node observations.

The results output from the ITA analysis were:

- Inter-trabecular angles: The angle between each branch of each different node type.
- Centroids: The coordinates for the end nodes of each branch.

ITAs for each node type were determined in BoneJ2 automatically. For node abundance, the centroids output was utilised. This output is simply a list of the x,y,z coordinates for each node in a given VOI. The coordinates are provided for the nodes at either end of each branch in the node-branch network. Therefore, multiple mentions of the same coordinate combination occur when that node provides an endpoint to multiple branches. For example, the same coordinate combination appearing 4 times in the centroids output means that there is a 4N node at those coordinates. The absolute counts of each 3N, 4N and 5N node type were performed by counting these coordinate combinations. They were then normalised to the total count of all nodes in each VOI, in order to produce the data seen in the relative node abundance graphs (Figures 3.41, 3.43 and 3.59). The centroids output was also used to plot the locations of each 3N, 4N and 5N node in each VOI, with a colour-coding system used to differentiate between them (Figures 3.40, 3.42, 3.57 and 3.58).

The mechanical efficiency of a trabecular structure improves as the nodes approach the idealized ITAs for each node type i.e. as the angles between each branch approach 120^{o} for 3N nodes and 109.5^{o} for 4N nodes. Figure 3.22 displays the example idealized motifs for each node type:

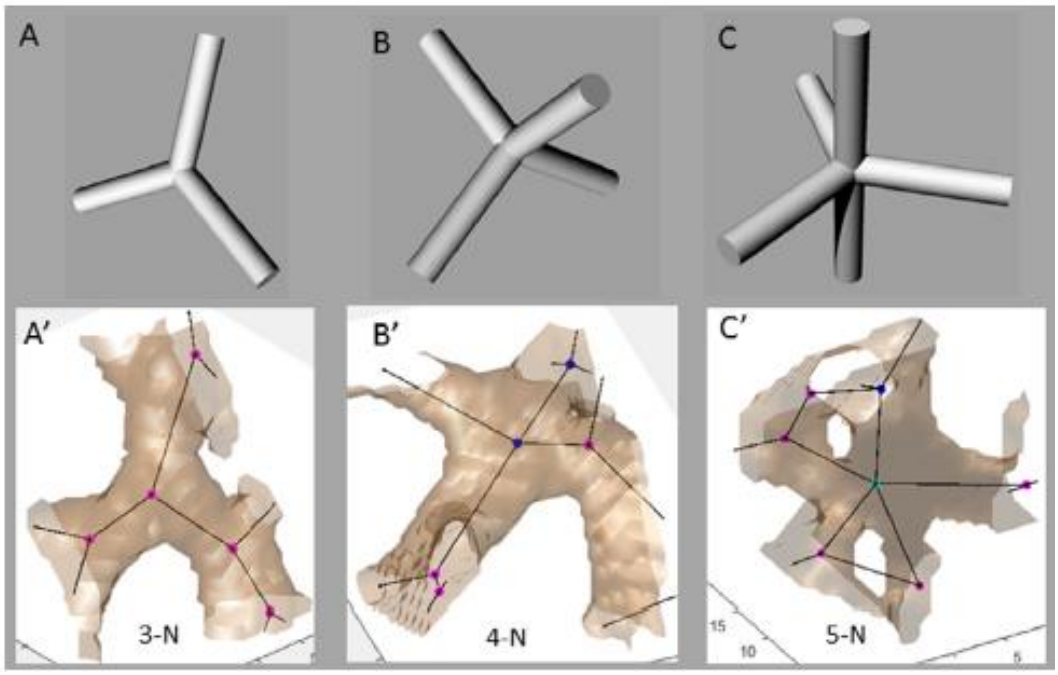

Figure 3. 22: Ideal geometries for A:3N, B:4N and C:5N nodes. Reproduced from Reznikov et al. 2016.

For 5N nodes, there is no perfect equal angular offset for all branches; a combination always exists e.g. 90^{o} and 120^{o} (Figure 3.22C). This results in a mean idealized ITA for 5N nodes of 100^{o}. As the angular offsets approach 120^{o} (as in a triangle) for 3N nodes and 109.5^{o} (as in a tetrahedron) for 4N nodes, the structures primarily fail in compression or tension, as opposed to shear or bending. This produces a stronger 3D network, as the numerous columns (trabeculae) in each network perform better under axial loads. The importance of the maximal space-spanning / angular offset arrangement of the nodes in a trabecular network was highlighted in the seminal ITA study by Reznikov *et al.* (2016), wherein it was shown in the human proximal femur that ~1/3 of all ITAs in 3N/4N/5N nodes fell within a 20 degree range around the idealised (120^{o}/109.5^{o}/100^{o}) value. Hence, the maximally space-filling topological arrangement of the constituent nodes is thought to be key in determining the mechanical integrity and fracture risk of trabecular bone.

3.2.12 Ellipsoid Factor Analysis

Ellipsoid factor (EF) is an analytical tool for the digital image processing software ImageJ (Rueden *et al*. 2017), available as part of the BoneJ2 plugin (Doube *et al*. 2010). It follows similar principles to the sphere-fitting method commonly used to measure trabecular thickness. Trabecular thickness here is defined as the diameter of the largest possible sphere wholly contained within a trabecula at a given location (Bouxsein *et al*. 2010). EF employs maximally fitted ellipsoids in place of spheres, utilizing the lengths of the perpendicular axes for prolate (rod-like), oblate (plate-like) and intermediate 3D ellipsoids to determine how prolate or oblate the trabecular space is at a particular point. Figure 3.23 displays prolate and oblate ellipsoids:

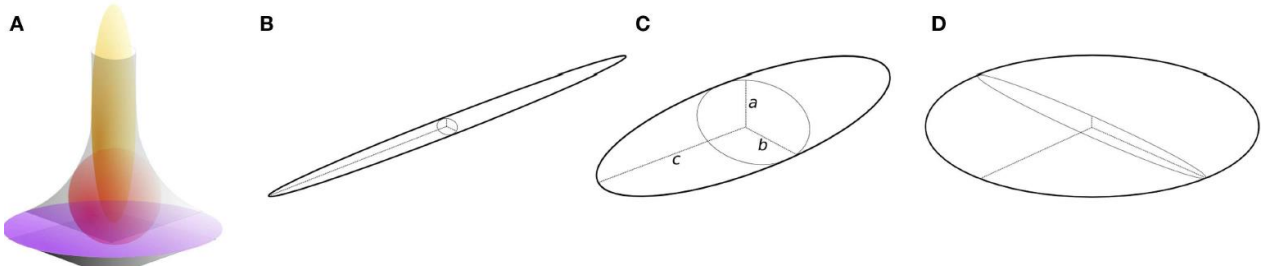

Figure 3. 23: Ellipsoid definitions. A: All different types of ellipsoids. B: Highly prolate ellipsoid. C: Less prolate ellipsoid approaching intermediate status. D: Highly oblate ellipsoid. Reproduced from Doube et al. 2015.

For prolate ellipsoids, there is one longer axis (c) and two shorter axes (a and b), as described by equation 3.7:

$$a < b \ll c \tag{3.7}$$

Whilst for oblate ellipsoids, there are two longer axes (b and c) and one shorter axis (a), as defined by equation 3.8:

$$a \ll b < c \tag{3.8}$$

EF is calculated as the difference of the two axis ratios, summarised in equation 3.9:

$$EF = \left[\frac{a}{b}\right] - \left[\frac{b}{c}\right] \tag{3.9}$$

So, for prolate ellipsoids (large c and equal a and b): EF ~ 1.

For oblate ellipsoids (equally large b and c and small a): EF ~ -1.

For ellipsoids of axis length ‘a’ satisfying the axis ratio a:qa:q^2a (intermediate) or a:a:a (totally spherical): EF=0.

Prior to EF analysis, some preparation is required. First, the background is distinguished from the bone in the volume by binarisation. As a result, all bone voxels register as values of 1 (white) and all voxels in the negative space register as a value of 0 (black).

As in ITA analysis, EF utilises the Skeletonize3D plugin to create a skeleton of the 3D trabecular VOI. Once BoneJ has the skeleton of the trabecular bone, the original, thicker 3D model is superimposed over the skeletonised model. An ellipsoid is created at each voxel in the skeleton (known as a seed point) and increased in size along one of its vectors (the number of vectors used to create each ellipsoid is user defined) until it contacts the background i.e. until an axis of the ellipsoid exceeds the radius of the trabecula in that orientation. The ellipsoid is then rotated about this contact point’s vector and increased in size again until another contact point is reached. This process continues iteratively until every vector in the ellipsoid has undergone this elongation step.

Once all vectors have been maximally fitted, the orthogonal primary axis dimensions (a, b and c dimensions in Figure 3.23) of the resulting ellipsoid are recorded. EF is then calculated using the above formula with the maximally-fitted axis lengths as inputs. The EF at any point in a structure can therefore be defined as the EF of the most voluminous ellipsoid which contains that point.

The parameters used for the EF analysis are as follows:

- Sampling increment: How large the increment is for increasing the size of the ellipsoid e.g. a sampling increment of 2 voxels grows the ellipsoid by 2 pixels each time before reporting on a potential contact point being reached. A smaller sampling increment therefore leads to longer computation times, with more accurate results. This value should be set to a smaller distance than the edge length of the voxels in the 3D image, in order to avoid missing out the first contact point on any particular ellipsoid axis growth operation.

- Vectors: How smooth / detailed the surface is for each ellipsoid. An ellipsoid created with 1000 vectors projecting from its centroid to form its outer rim will be more detailed than an ellipsoid created with only 10 vectors. A higher number of vectors renders an ellipsoid more closely aligned to the maximal fit in reality, but this can lead to increased computation times if analysing multiple samples.

- Skeleton points per ellipsoid: How large the gap is between each ellipsoid along the skeleton. A value of 1 for this parameter would give the most detail, as it would attempt to size an ellipsoid at every single voxel of the skeleton i.e. every single seed point.

- Contact sensitivity: How many contact points need to be reported as touching the background before the ellipsoid is rotated and resized. 1 is the norm.

- Maximum iterations: How many times after completion that the maximal fitting process will be repeated from a different orientation in 3D about the centroid, in an attempt to find the largest possible ellipsoid at that point. This can lead to more ellipsoids achieving a virtually 'true to life' maximal fit, but impacts computation time significantly.

- Maximum drift: How far in pixels the centroid of the seed point will be allowed to move upon commencing a new iteration. This is usually maintained at 1 pixel as a maximum, so as to ensure that smaller cross-sectional geometries are not removed from the attempted representation of the bone volume. If the seed point for each ellipsoid sizing were allowed to drift to whatever voxel in a large range returned the largest ellipsoid, this would lead to an overestimation in the average volume and 3D aspect ratios of the trabecular cross sections in the volumes i.e. it would bring the fitting algorithm further from reality.

The outputs used for the EF analysis are as follows:

- Median EF: the median value of EF for all ellipsoids seeded in the VOI.

- EF image: An image stack (3D model made out of slices) which is colour coded according to the EF at each voxel. Figure 3.24 contains an EF image from a proximal tibia trabecular VOI:

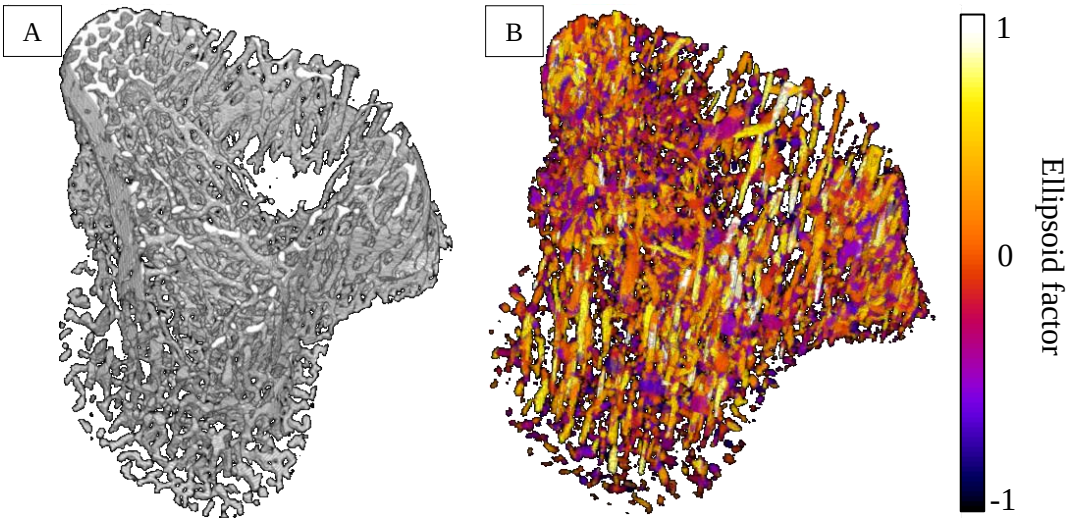

Figure 3. 24: EF diagram of proximal tibia trabecular VOI. A: Trabecular VOI imaged using 3D viewer ImageJ tool. B: EF image of the same volume.

Each 8-bit trabecular dataset was binarised in ImageJ prior to EF analysis, at a threshold range of 65→255. The lower threshold had the effect of increasing the diameter of the trabeculae to reduce skeletonization artefacts, at the cost of increasing partial volume effects. Noise was reduced using the despeckle plugin in ImageJ. This particular despeckle operation was of the median type; replacing each pixel with the median value in its 3x3 vicinity. Although this type of filtering can be performed in CTan, it was performed in ImageJ for consistency and ease of post-processing for ellipsoid factor and inter-trabecular angle.

The log which reports at the conclusion of each EF analysis states the fill percentage of the algorithm along with any unsuccessful seed points. The fill percentage is the percentage of seed points with a successfully seeded ellipsoid. Seed points are omitted from the analysis if the volume of the ellipsoid seeded from them lies more than 50% in the background of the image, as this would lead to ellipsoids being formed which were not sufficiently representative of the local volumes encapsulating them.

An ideal EF analysis would have a fill percentage of 100%, meaning that the bone sample was 100% represented by the ellipsoid data. In practice, a fill percentage >90% is recommended in order for results to be valid (Doube *et al*., 2015).

The EF analysis was performed on a sample DF metaphyseal VOI initially with the default parameters and then optimised to obtain a fill percentage above 90% whilst maintaining a practical computation time. The optimisation parameters are displayed in Table 3.3:

Parameter	**Default**	**Optimised**
Sampling Increment (px)	0.43	0.1
Vectors	100	80
Skeleton Points / Ellipsoid	1	1
Contact Sensitivity	1	1
Max. Iterations	200	800
Max. Drift (px)	4	2
Fill Percentage	~78%	90→94%

Table 3. 3: Ellipsoid factor parameters for optimisation.

The above parameters were used in combination with the previously mentioned VOI selection, thresholding and despeckling operations in order to return the final results. BoneJ2 returns the following set of EF results for each analysis: median EF, max. EF, min. EF, fill % and total number of seeded ellipsoids. Median EF was compared between SCI and CTRL groups as a quantitative measure of changing bone microarchitecture following chronic SCI.

EF images (3D colour volumes displaying local EF values) were presented for qualitative assessment, and EF histograms enabled a broader understanding of the median EF values for each VOI.

3.2.13 CTan Cortical Analysis

The analysis protocols for cortical measurements were once again based on the software method notes (Bruker 2016). The specifics can be found in Appendix entries 1 and 2. First, a global threshold was applied in order to remove all material apart from bone from the VOI. The minimum limit for the threshold here could be higher than that used for trabecular assessment, as the trabecular bone was desired to be removed (as opposed to included) as much as possible prior to analysis. The global threshold was set at 90→255.

Similar to the trabecular analysis, a despeckle operation was then applied to remove noise (Figure 3.17). This was following by a 3D pore closing operation to ensure that no small gaps remained inside the cortical shell. Removing the pores in this way means that the average cortical thickness measurement will be valid. Without removing the pores, there is a risk to accidentally measure the distance from the endosteal surface to a pore as the cortical thickness, as opposed to the actual distance; that from the endosteal surface to the periosteal surface. If the pores were included, a different method for averaging cortical thickness would be adopted, wherein the thickness would be defined as the mean of all local thicknesses in the sample.

Figure 3.25 highlights the two different methods of measuring mean cortical thickness:

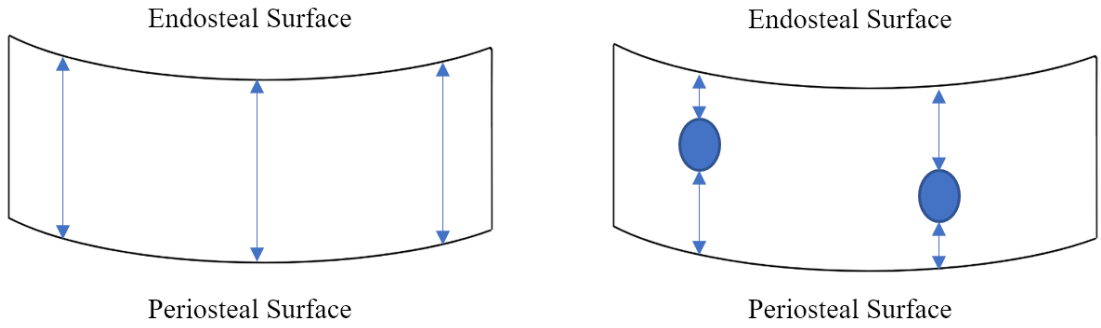

Figure 3. 25: Clarification of the mean cortical thickness measurement taken in CTan. Blue ellipses: cortical pores. Blue arrows: Measurement lines for mean cortical thickness.

In line with standard protocol, the method used here was one in which the pores were removed, and cortical thickness was measured across the entire span from endosteum to periosteum.

Once the closing operation had removed the pores, a region of interest (ROI) shrink-wrap operation was applied. This adhered the ROI flush to the outer (periosteal) cortical surface. The ROI was now perfectly defined, with 3D and 2D analyses both performed on the same region. Figure 3.26 displays the results of the pore closing and ROI shrink-wrap operations on an already thresholded and despeckled cortical volume:

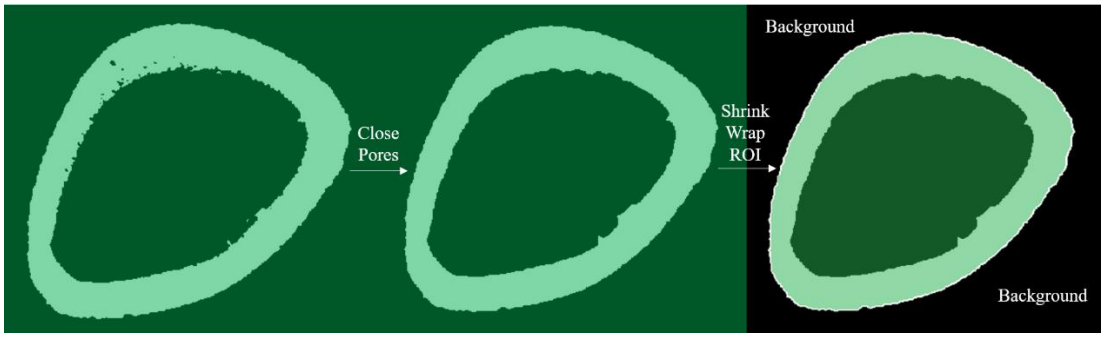

Figure 3. 26: Distal femur cortical section following thresholding, despeckling, pore closing and applying a shrink-wrapped ROI. Image in black and white. ROI in green.

The shrink-wrap ROI is necessary so that the analysis is contained to the black (0) or white (1) pixels within the periosteal perimeter only. The black pixels in the background (Figure 3.26) would obscure the total area measurement, and the medullary area can be calculated simply as the difference between total and cortical areas (Table 3.4 and Figure 3.27).

Like the trabecular parameters in Table 3.1, Bouxsein *et al.* (2010) provide a minimal list of parameters for assessment of cortical bone, outlined in Table 3.4:

Parameter	**Abbreviation (units)**	**Explanation**
Total cross-sectional area	Tt.Ar (mm^2)	A measure of the total area inside the cortical bone region, including the medullary void (termed the 'periosteal envelope'). Calculated in 3D by counting the number of binarised pixels in a given VOI. This value is then divided by the height of the VOI to give the averaged 2D result.
Cortical bone area	Ct.Ar (mm^2)	The average area of the cortical shell between the periosteal and endosteal surfaces. Calculated in the same manner as Tt.Ar.
Mean cortical thickness	Ct.Th (mm)	The average thickness of the cortical shell. Calculated via the same sphere-fitting algorithm used for Tb.Th.

Table 3. 4: Minimal parameters required for microCT cortical bone studies. Reproduced from Bouxsein et al. 2010.

3D and 2D cortical parameters were both assessed in CTan. These included cortical thickness, total area (periosteal area), cortical area, medullary area (calculated separately), polar second moment of area, specific surface and eccentricity.

Total area in the context of cortical analysis refers to the cross-sectional area of a long bone transverse cross section which is encompassed by the periosteal perimeter i.e. including the cortical and medullary areas. Cortical area is the annular area between the periosteal and endosteal surfaces, and medullary area is calculated as total area - cortical area. Figure 3.27 displays these cortical parameters:

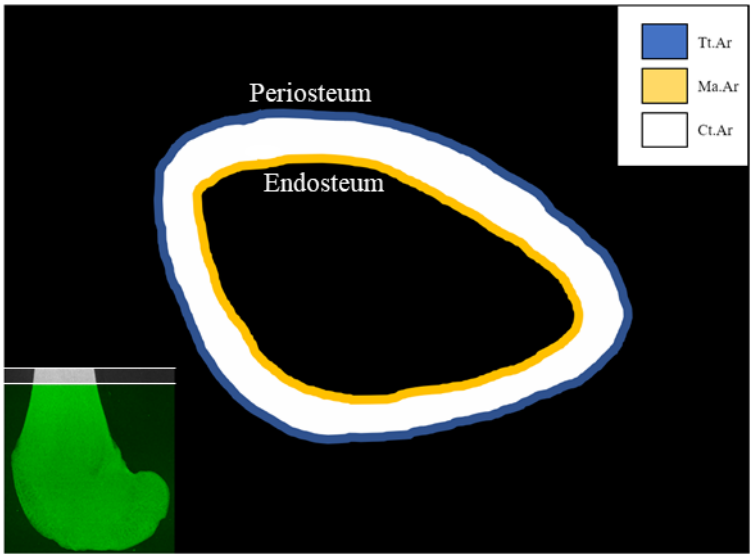

Figure 3. 27: Cortical area measurements in CTan. Bottom left insert: example distal femur VOI. Tt.Ar: Total Area. Ma.Ar: Medullary Area. Ct.Ar: Cortical Area.

The polar second moment of area (J) is a 2D measurement of the distribution of material about an object's rotational axis i.e. it provides insight into the object's resistance to torsional loads. It is calculated using the following equation:

$$J = I_{max} + I_{min} \tag{3.10}$$

Where I_{max} and I_{min} are maximum and minimum second moments of area, calculated by:

$$I_{max} = \frac{I_{xx}-I_{yy}}{2} + \sqrt{(\frac{I_{xx}-I_{yy}}{2})^2 + {I_{xy}}^2} \tag{3.11}$$

$$I_{min} = \frac{I_{xx}-I_{yy}}{2} - \sqrt{(\frac{I_{xx}-I_{yy}}{2})^2 + {I_{xy}}^2} \tag{3.12}$$

Where I_{xx}, I_{yy} and I_{xy} are the second moments of area calculated by the following summation for all bone pixels in the digitized image:

$$I_{xx} = \sum_{i=1}^{N}(Area\ of\ pixel\ \times (y_i - y_c)^2 + MA_{pixel}) \quad (3.13)$$

$$I_{yy} = \sum_{i=1}^{N}(Area\ of\ pixel\ \times (x_i - x_c)^2 + MA_{pixel}) \quad (3.14)$$

$$I_{xy} = \sum_{i=1}^{N}(Area\ of\ pixel\ \times (x_i - x_c)(y_i - y_c) + MA_{pixel}) \quad (3.15)$$

Where the area of the square pixel is just the side length squared, x_i,y_i are the xy coordinates of the i^{th} pixel, x_c,y_c are the xy coordinates of the centre of rotation, and the moment of area (MA) of the pixel is that of a square about its centre: MA = side length^4 / 12. Figure 3.28 illustrates the parameters in the above equations:

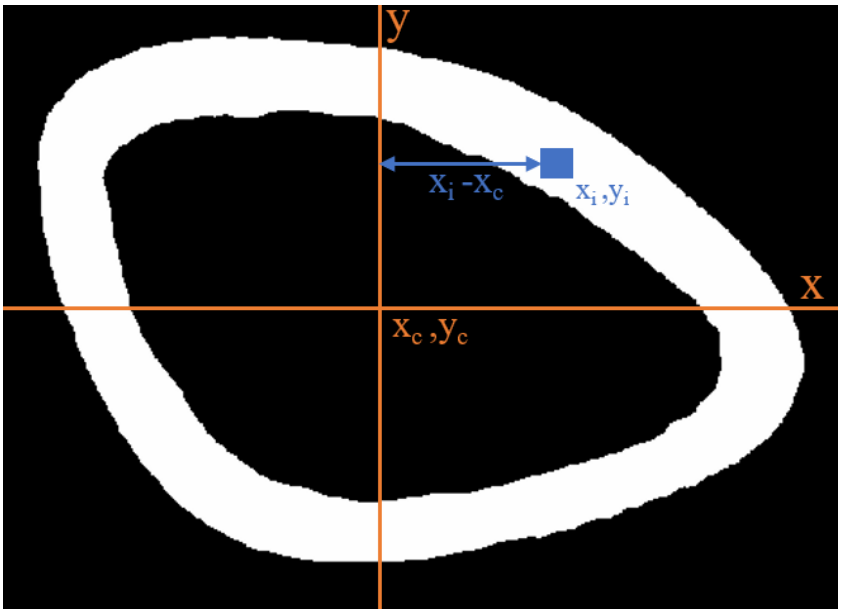

Figure 3. 28: Cortical second polar moment of area calculation.

Eccentricity is another 2D analysis used for cortical bone. It categorises ellipses according to their 'departure' from a perfectly circular shape. Consider an ellipse which has been elongated slightly from a circle. The major and minor axes of the ellipse can be labelled as 2a and 2b, such that a and b are the 'semi-axes' equal to half the relevant axis length. Eccentricity is calculated using these values:

$$Eccentricity = \sqrt{1 - \frac{b^2}{a^2}} \quad (3.16)$$

Figure 3.29 displays the parameters for eccentricity calculation.

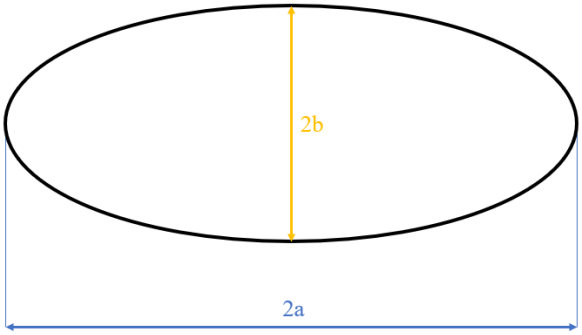

Figure 3. 29: Eccentricity calculation for elliptic geometries.

A greater eccentricity value (~1) means a greater degree of elongation, whilst a value of 0 indicates a perfect circle i.e. no elongation.

3.2.14 Cortical Porosity Analysis

The cortical porosity macro was similar to that for the general cortical analysis. The main difference here was that the threshold minimum limit was set higher, in order to more accurately define the pores in the cortical bone as opposed to closing them over. Additionally, the 3D closing operation was not utilised here in order to preserve the pores for analysis. The exact details of the cortical porosity analysis macro can be found in Appendix entry 2.

Once the ROI had been defined using a shrink-wrap operation, the pores were selected for analysis by using the bitwise operation ‘exclusive or’ (XOR). XOR removes any white pixels from the image that are overlapping the ROI. As the ROI has been defined as a non-porous halo via the shrink-wrap operation, XOR here removes all of the bone in the cortical shell, leaving the voids (pores) as the new image for analysis. Figure 3.30 displays the selection of the cortical pores using XOR:

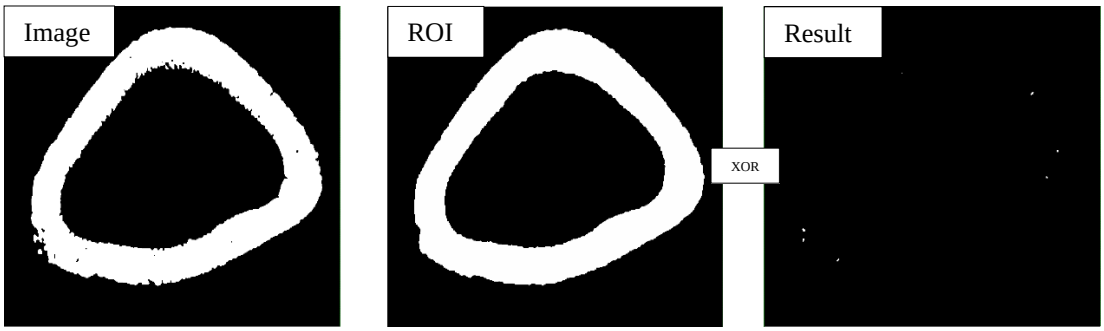

Figure 3. 30: Cortical pore selection from a porous input image and non-porous ROI using XOR in CTan software.

The pores can then be measured using mean local thickness as explained prior. This allows for measurements such as mean pore diameter and mean pore separation, using the same in-built trabecular bone measurement capabilities in CTan. The trabeculae in this case are instead the highlighted cortical pores.

As a reminder, cortical porosity in this study was measured at the metaphysis, and not the diaphysis as with all other cortical analyses. The main reason was for comparisons with the metaphyseal cortical blood vessel density analysis via histology (Figures 4.20C and 4.20D). Additionally, the diaphyseal cortical pores in the rats used were too small for accurate quantification at 10µm resolution without incurring significant partial volume effects.

3.2.15 Cortical Tissue Mineral Density Analysis

Areal bone mineral density (aBMD) is a standardized parameter for definition of osteoporosis. It is clinically assessed as a measurement of bone strength using DXA (Liu *et al*. 2017). In microCT analysis, volumetric BMD (vBMD) is a measure of the average mass content of calcium hydroxyapatite (CaHA) per unit volume, most commonly expressed in g/cm^3.

As the X-ray source incident on the detector is measured in units of X-ray attenuation per unit length (1/mm), and not in g/cm^3 of CaHA, a calibration is necessary using phantom blocks (the size of which are selected as specific to the type of bones being scanned – rat femora and tibiae in this case) of known CaHA density. With this calibration information, and assuming that the bone's attenuation effect is dominated by CaHA (its most abundant constituent), a measurement can be made of the vBMD.

The vBMD parameter is not analysed in this project. Instead, volumetric tissue mineral density (vTMD) is used. TMD is a separate parameter to BMD. Where BMD measures the CaHA density of the whole contents (bone, muscle, cartilage etc.) of a given VOI, TMD measures it solely in the bone content of the region. For trabecular vTMD to be accurate, the resolution must be fine enough such that mean trabecular thickness is at least 10 pixels (Bruker 2011). As the resolution for all bones was 10µm/px and mean Tb.Th was as low as 60µm in some VOIs, trabecular TMD was not analysed. All vTMD results in this study are obtained solely from cortical bone analysis.

Two 4mm diameter phantom cylinders with densities of 0.25g/cm^3 and 0.75g/cm^3 both were scanned at the same settings and parameters as the bones for analysis, and the average X-ray attenuation coefficients (ACs) recorded. The ACs were measured across 100-slice VOIs which excluded the ends and edges of the phantoms (Figure 3.31) in order to minimise partial volume effects:

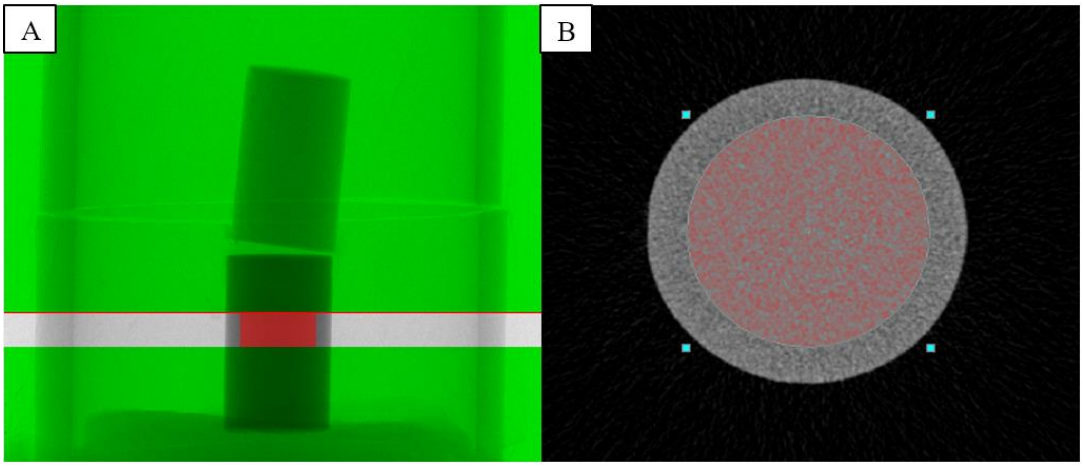

Figure 3. 31: CaHA phantom VOI delineation. A: Vertical ROI bounds. B: Cross-sectional ROI bounds. ROI in red.

The average AC and CaHA density for both VOIs was used to produce a linear calibration, explained in Figure 3.32. The resulting calibration equation was used to obtain the TMD results:

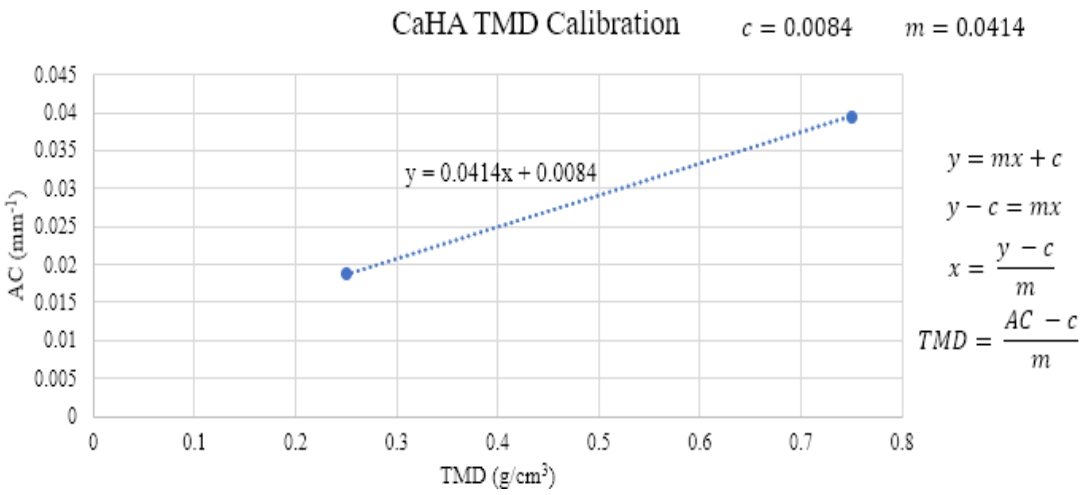

Figure 3. 32: Calibration of TMD using two known concentrations of calcium hydroxyapatite. TMD: Tissue mineral density. AC: Measured attenuation coefficient. c: Y-intercept. m: Gradient.

3.2.16 Statistical Analysis

The data was organised into the results for either bone region; distal femur and proximal tibia. A standard protocol to test normality, variance and mean differences in the data was devised, specifically making use of the Shapiro-Wilks test, Levene's test, Student's t-test and the Welch Two Sample t-test, and finally the Mann-Whitney U test. This relies on the values in each group being sufficient in number so as to enable tests of their approximation to a perfect normal distribution. As the sample size in the acute and chronic datasets were n=3 and n=5 respectively, the Shapiro-Wilks test to check for normal distribution was omitted from the statistical analysis. Similarly, the Levene's test for equal variance between groups was omitted prior to the analysis, as the p value varies significantly with sample size. That is to say, larger sample sizes are much more likely to return a significant different in variances between two groups. As the sample sizes here were so small, undertaking the Levene's test in R always returned a nonsignificant result, and so Student's t-test (for assumed equal variance between two independent groups) was selected as the basis for comparing mean differences between groups, instead of the Welch Two Sample t-test for unequal variances. Solely utilising the Student's t-test meant that any non-parametric tests such as the Mann-Whitney U test would not be used for analysis, as these tests are only used in cases where the data cannot be assumed to be normally distributed.

For significance, $p<0.05$ was designated as the first level of statistical significance, with the next two thresholds at $p<0.01$ and $p<0.001$. Data was presented comparing between SCI and control groups as the group mean ±1 standard deviation, calculated and graphed in R (Version 1.3.1093). Asterisks (*) denoting statistical significance were manually added after generating each figure. For correlations, linear regression lines were plotted using the least-squares fitting method, and the proportion of the variance in the response variable which could be predicted by the variance in the independent variable (R^2) was calculated using equation 3.17:

$$R^2 = \frac{Var(mean) - Var(fit)}{Var(mean)} \tag{3.17}$$

Where the variance of the data around the mean was calculated as the sum of the squared residuals around the mean divided by the sample size, and the variance of the data around the fitted line from the least squares fit was calculated as the sum of the squared residuals around the fitted line divided by the sample size.

3.3 Results - MicroCT Chronic SCI

The following results are all concerning the chronic (11 week post-injury) dataset. Both the distal femur (DF) and proximal tibia (PT) were analysed here. The acute (2 week) PT results are summarised in their own succeeding section.

3.3.1 Trabecular Analysis

Figure 3.33 displays the bone loss effects of SCI on DF and PT metaphyseal trabecular bone:

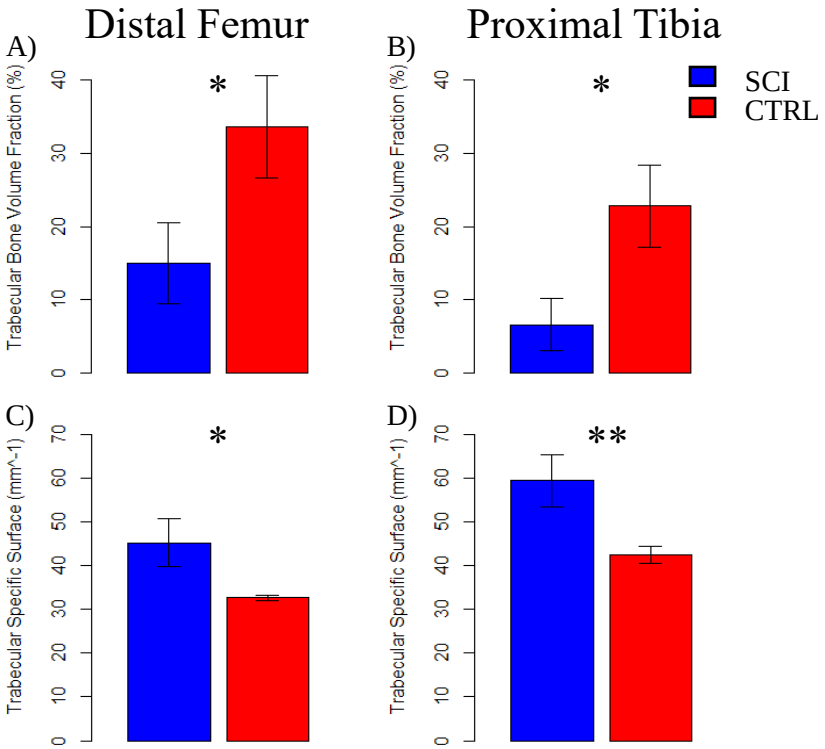

*Figure 3. 33: Trabecular bone volume fraction and specific surface changes following chronic SCI. SCI: spinal cord injured. CTRL: control. * indicates significant difference between SCI and CTRL at p<0.05. ** indicates p<0.01. Data presented as mean ±1SD.*

The trabecular bone volume fraction exhibited a significant difference in both the DF and PT following SCI, with percentage reductions of 55% and 71%, respectively (p=0.0227 and 0.0135) (Figures 3.33A and 3.33B). This was also the case for trabecular specific surface, with both bone regions showing significant differences. The percentage increases due to SCI in BS/BV were 28% (p=0.0168) for DF and 29% (p=0.0089) for PT (Figures 3.33C and 3.33D).

In Figure 3.34, trabecular thickness, separation and number results are displayed:

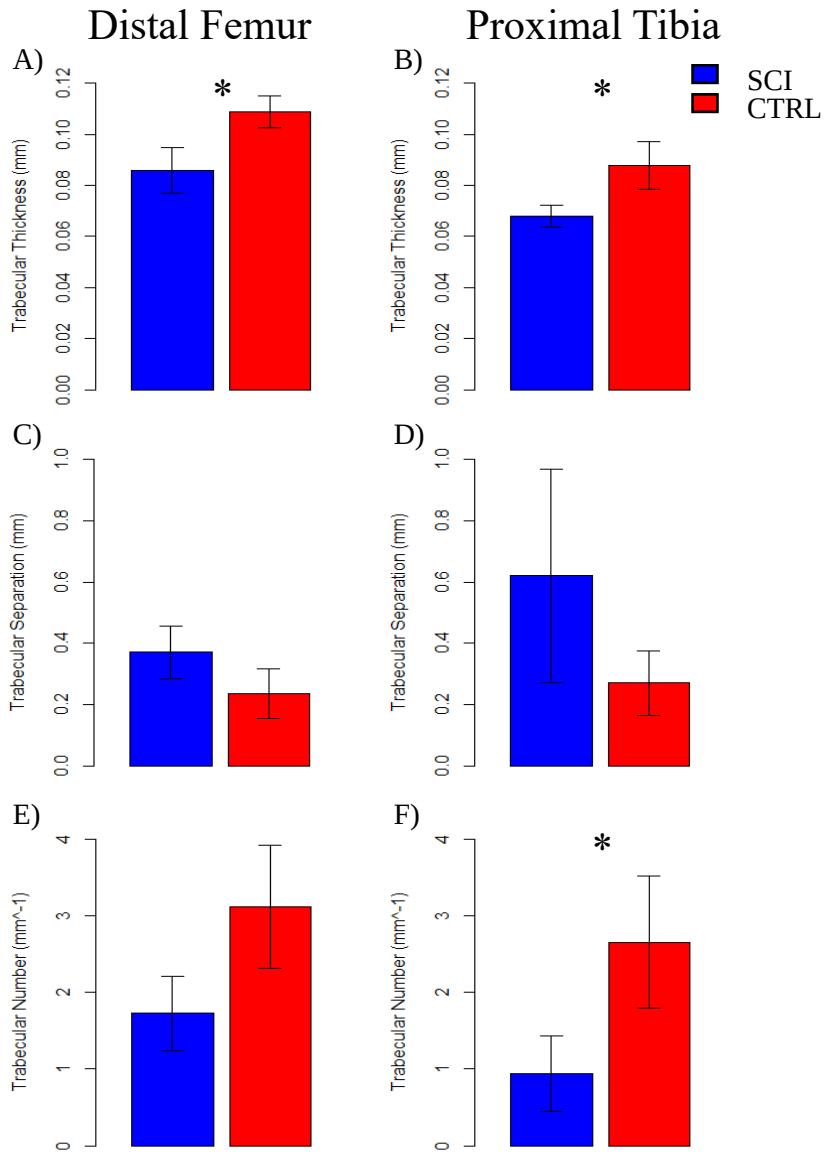

*Figure 3. 34: Trabecular thickness, separation and number changes following chronic SCI. SCI: spinal cord injured. CTRL: control. * indicates significant difference between SCI and CTRL at p<0.05. Data presented as mean ±1SD.*

The average trabecular thickness was found to significantly decrease in SCI compared to CTRL in both the DF and PT metaphyseal VOIs, with percentage reductions of 21% and 23%, respectively (p=0.0223 and 0.0290) (Figures 3.34A and 3.34B). No significant difference was detected in the trabecular separation for either bone region (Figures 3.34C and 3.34D). For trabecular number, only the PT presented a significant difference following chronic SCI; a percentage decrease of 64% (p=0.0405) (Figure 3.24F).

The effects of SCI on the fractal dimension and connectivity density in the DF and PT are displayed in Figure 3.35:

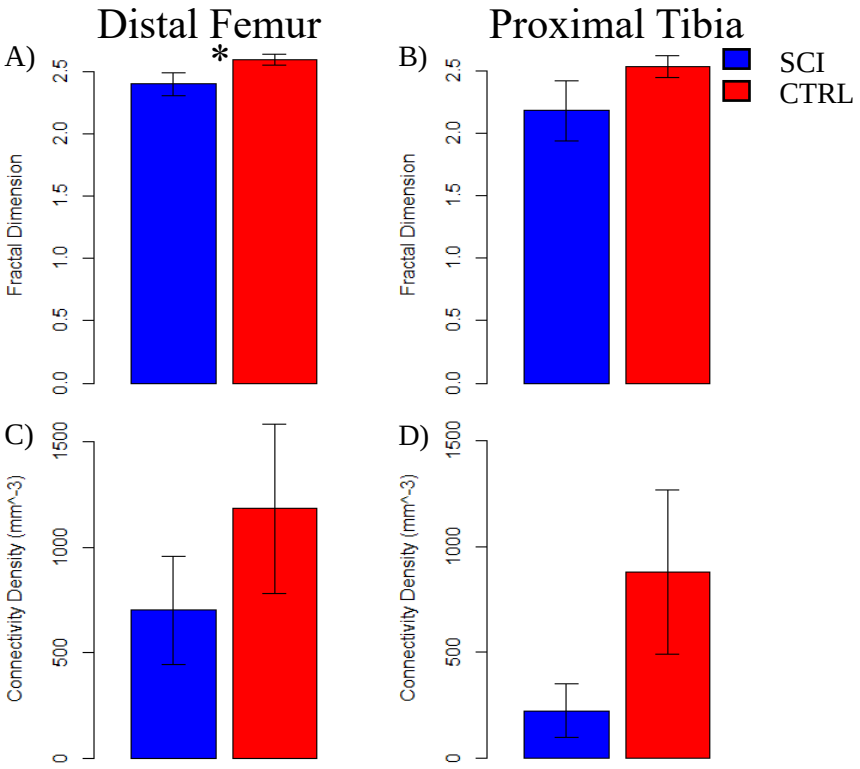

*Figure 3. 35: Trabecular fractal dimension and connectivity density changes following chronic SCI. SCI: spinal cord injured. CTRL: control. * indicates significant difference between SCI and CTRL at p<0.05. Data presented as mean ±1SD.*

Only the DF exhibited a 8% (p=0.0269) significant decrease in fractal dimension in SCI compared to CTRL (Figure 3.35A). Neither bone region VOI presented a significant difference in connectivity density (Figures 3.35C and 3.35D).

3.3.2 Ellipsoid Factor

Additional EF data can be found in Appendix Entry 8. Figure 3.36 contains the quantitative data resulting from the chronic EF and SMI analysis:

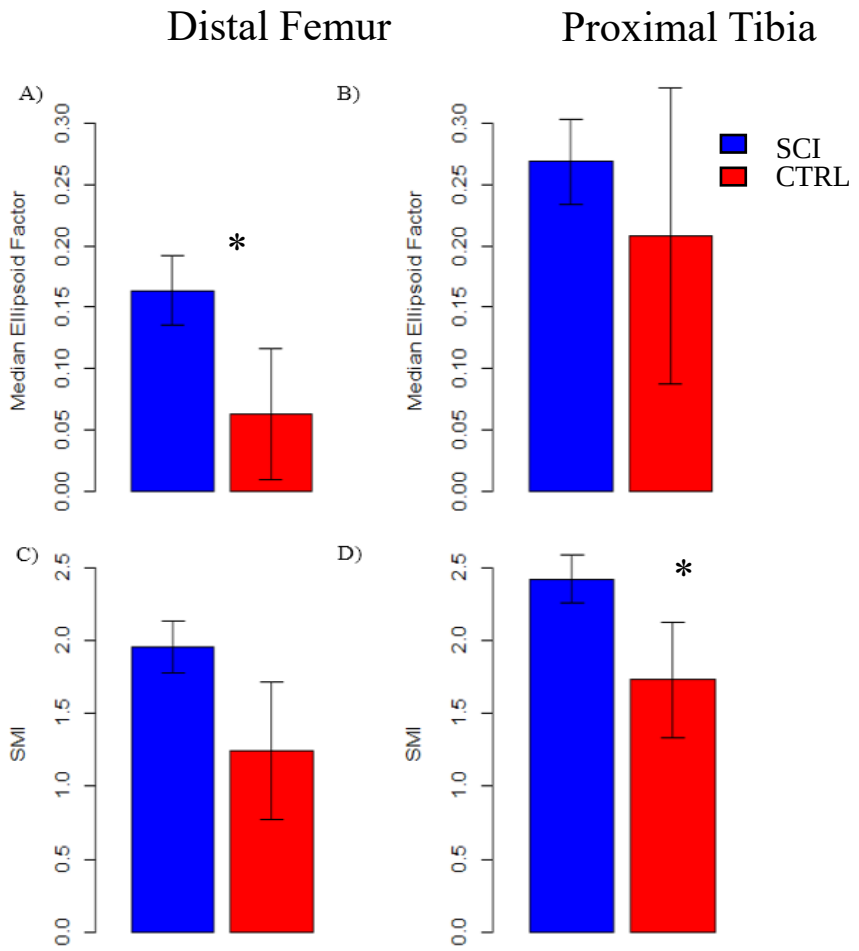

*Figure 3. 36: Median EF and SMI changes following chronic SCI. DF: distal femur. PT: proximal tibia. SCI: Spinal cord injured. CTRL: Control. * indicates significant difference between SCI and CTRL at p<0.05. Data presented as mean ±1SD.*

The predominant rod-like or plate-like geometries in trabecular bone can be generalised by analysing the median EF value for each VOI. In the DF, median EF was seen to be significantly affected by SCI (p=0.045), increasing by 163% in SCI compared to CTRL following 11 weeks of SCI (Figure 3.36A). For the PT, SCI was found to have no significant effect on changing median EF (Figure 3.36B).

SMI was not found to be significantly different in the DF after 11 weeks of SCI, however in the PT there was a significant effect, as SMI increased by 39.96% (p=0.049) (Figures 3.36C and 3.36D).

Figure 3.37 contains the EF histograms for the chronic DF and PT:

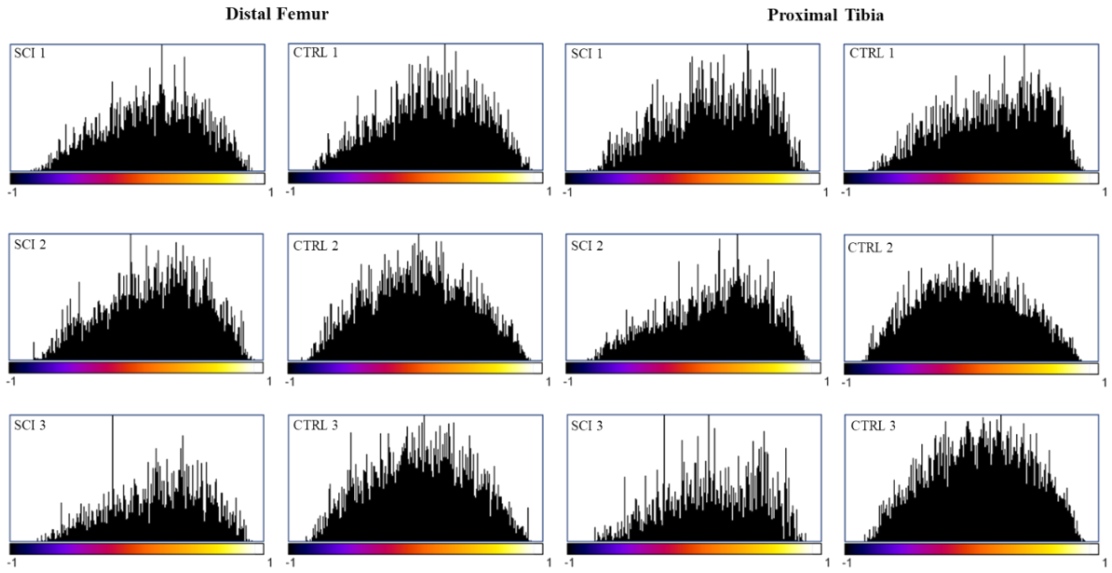

Figure 3. 37: EF histograms of DF and PT metaphyseal trabeculae following chronic SCI.

Distributions of EF values in each DF and PT bone were unimodal. Most distributions skewed left (indicating a rod-like average trabecular morphology) with the exception of some CTRL bones, which presented either none or a mild right skew (Figure 3.37).

Figures 3.38 and 3.39 display the EF images for each bone in the DF and PT datasets:

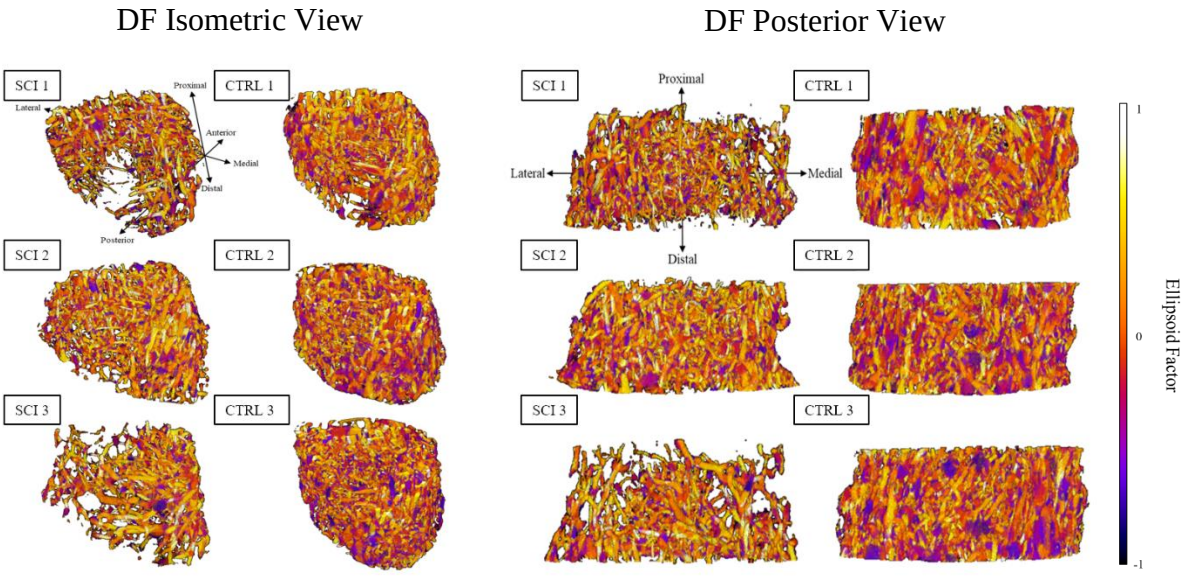

Figure 3. 38: Ellipsoid factor (EF) 3D models for SD rat DF metaphyseal trabecular VOIs following chronic SCI. SCI: Spinal cord injured. CTRL: Control.

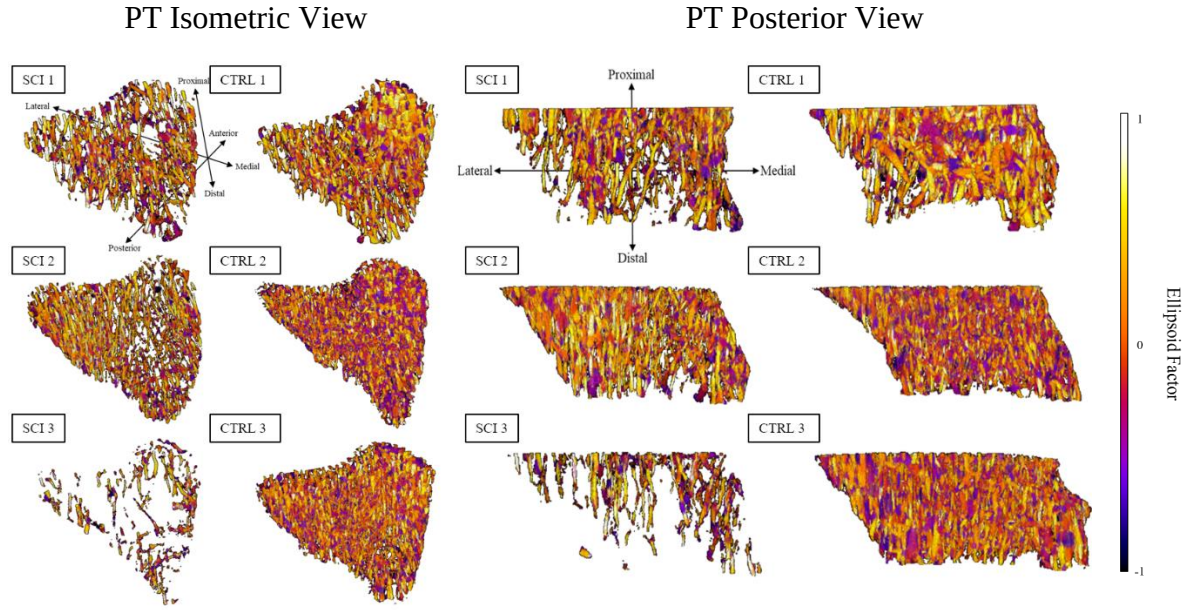

Figure 3. 39: Ellipsoid factor 3D models for SD rat PT metaphyseal trabecular VOIs following chronic SCI. SCI: Spinal cord injured. CTRL: Control.

The distribution of rod-like (yellow) or plate-like (purple-black) geometries was observed to be different between the SCI and CTRL VOIs for both bone regions. CTRL bones exhibited the most plate-like trabeculae, with a uniform spread throughout both the medullary and endosteal regions. The SCI VOIs presented less plate-like struts in the medullary region, and less plate-like geometries overall. The

orientations of the rod-like trabeculae in the SCI bones were predominantly along the loading axis of each long bone (proximal-distal), whilst the plate-like geometries were composed of a mix of orientations (Figures 3.38 and 3.39).

3.3.3 Inter-Trabecular Angle

As mentioned previously (page 78), one of the main outputs of the ITA analysis is a list of the centroid coordinates of each node. These were used to create the following figures on node type abundance and location. The results of the node type distribution analyses are displayed in Figures 3.40, 3.41, 3.42 and 3.43:

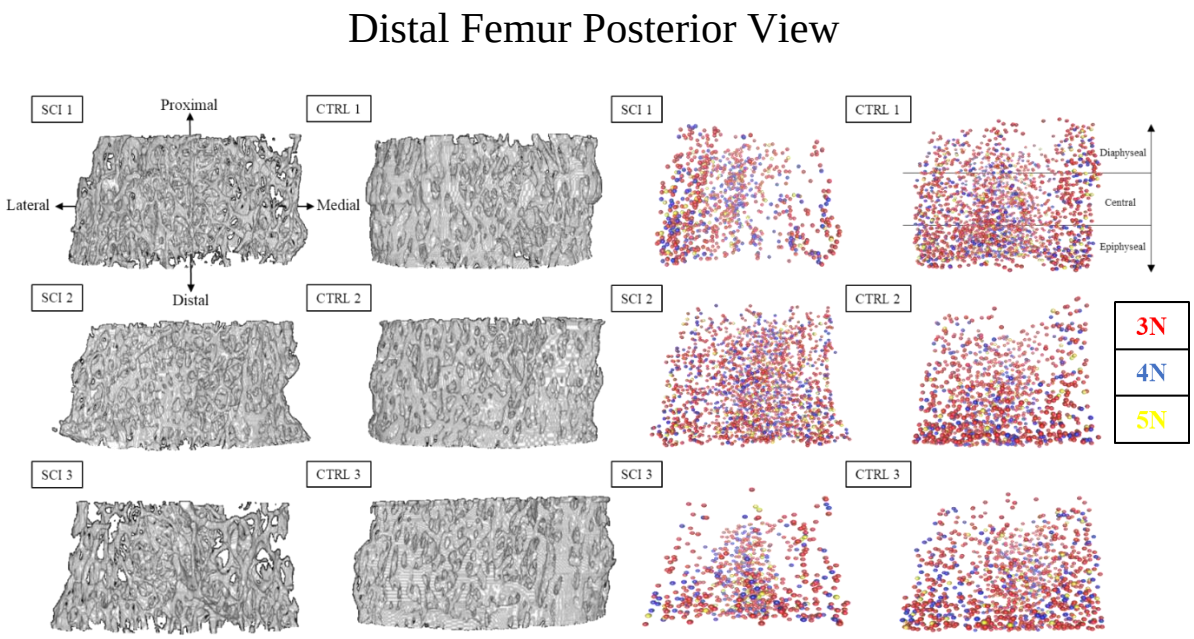

Figure 3. 40: 3D colour plots of 3N, 4N and 5N nodes in the distal femur following chronic SCI. SCI: Spinal cord injured. CTRL: Control.

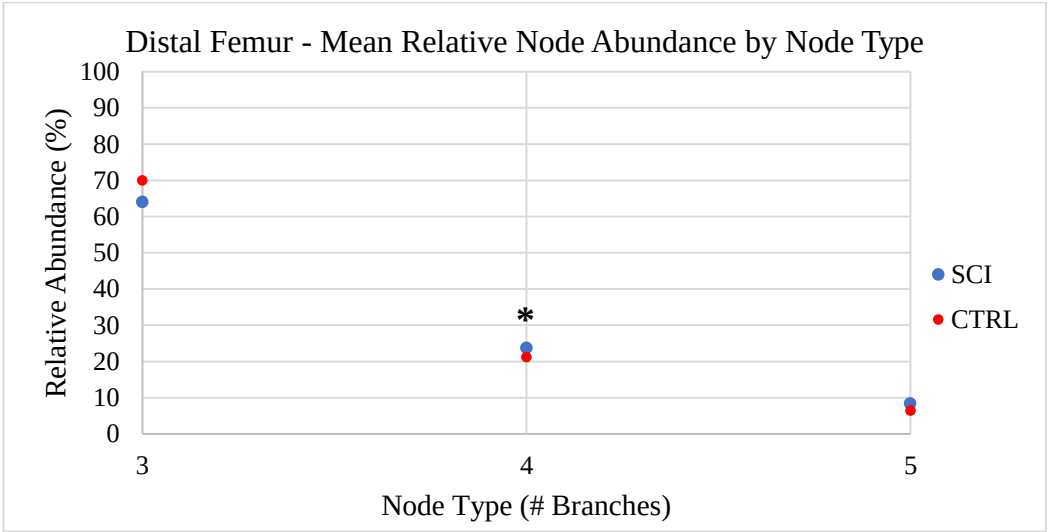

*Figure 3. 41: Effects of chronic SCI on node type relative abundance in the distal femur. * indicates significant difference between SCI and CTRL at p<0.05*

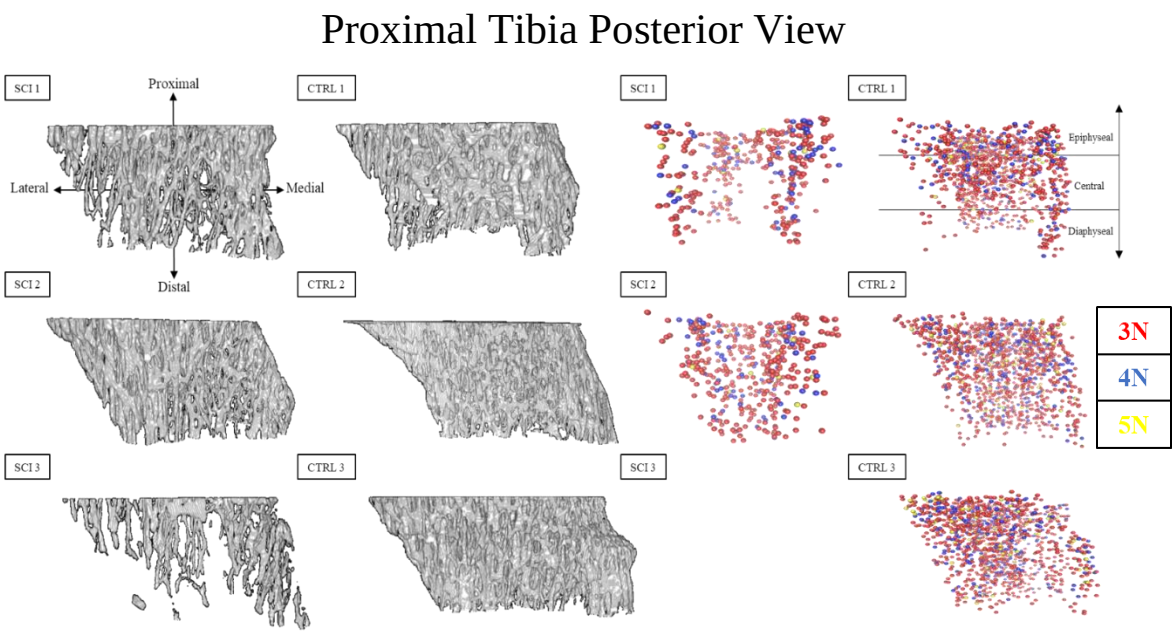

Figure 3. 42: 3D colour plots of 3N, 4N and 5N nodes in the proximal tibia following chronic SCI. SCI: Spinal cord injured. CTRL: Control.

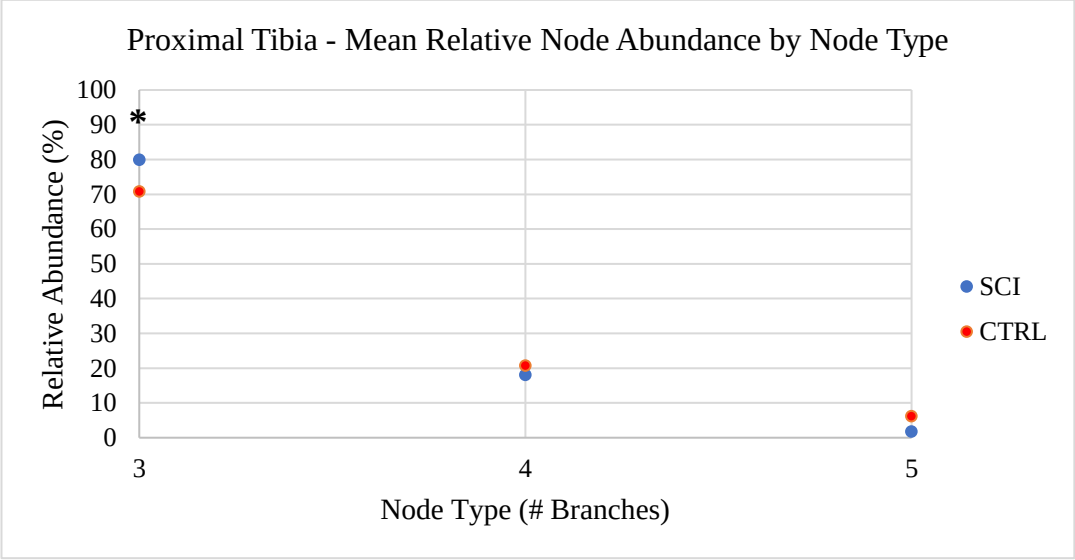

*Figure 3. 43: Effects of chronic SCI on node type relative abundance in the proximal tibia. * indicates significant difference between SCI and CTRL at $p<0.05$.*

In the DF, the SCI bones were observed to contain comparatively less 5N nodes in their diaphyseal regions than in the central or epiphyseal regions. The CTRL bones did not show such a pattern (Figure 3.40). The PT showed the same pattern as the DF in this case, with sparse populations of 5N nodes in the SCI diaphyseal regions (Figure 3.42).

The normalised node abundances were the same in both CTRL and SCI bones in the DF for 3N and 5N nodes. For 4N nodes, a significant difference (p=0.0457) was observed following chronic SCI, increasing from 21% to 24% following SCI (Figure 3.41). The node abundance ratio for 3N, 4N and 5N nodes in the DF CTRL was 11:3:1, whilst the DF SCI presented a ratio of 7:3:1. The PT presented one significant difference in relative node abundance between 3N, 4N and 5N nodes. In this case, the 3N relative node abundance increased from 71% to 80% following SCI (p=0.0376) (Figure 3.43). The node abundance ratio for 3N, 4N and 5N nodes in the PT CTRL was 12:3:1, with the PT SCI exhibiting a ratio of 46:10:1.

One rat (CTRL 3) was a considerable outlier compared to the rest of the PT CTRL group. This was due to an infection prior to the SCI surgery. The trabecular number, spacing and volume fraction were all considerably more affected following SCI in this rat (see Appendix entry 6). These effects likely caused the node-branch network creation to be based on a skeleton which did not cover the entire dimensions of the VOI. As stated in the documentation, ITA uses the largest possible single skeleton for analysis (Reznikov *et al*. 2016). A VOI with such a low trabecular connectivity would likely result in a discontinuous network, resulting in ITA analysis based on a much smaller skeleton which would give inaccurate results in the node abundances recorded there. As the effects were so severe, this bone is omitted from the ITA analysis.

Figures 3.44 and 3.45 display the mean ITAs for each node type:

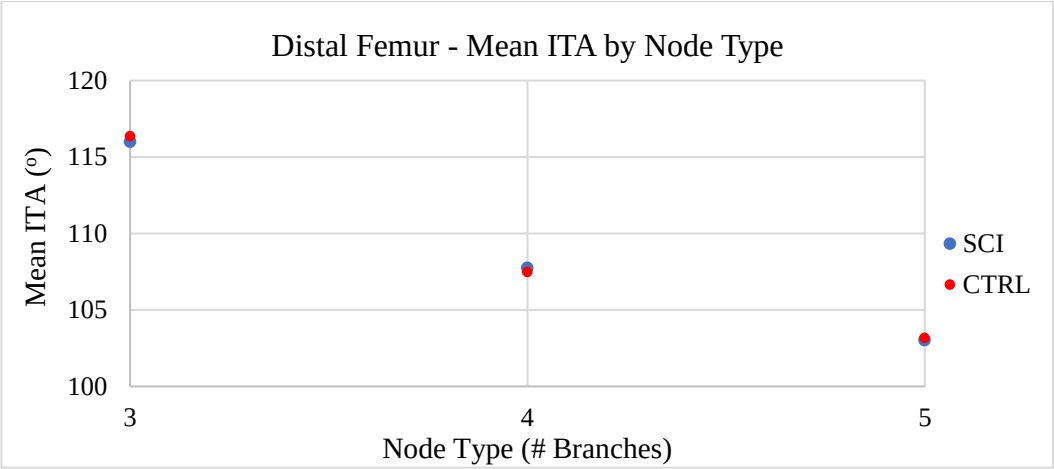

Figure 3. 44: Effects of chronic SCI on mean ITA for 3N, 4N and 5N nodes in the distal femur.

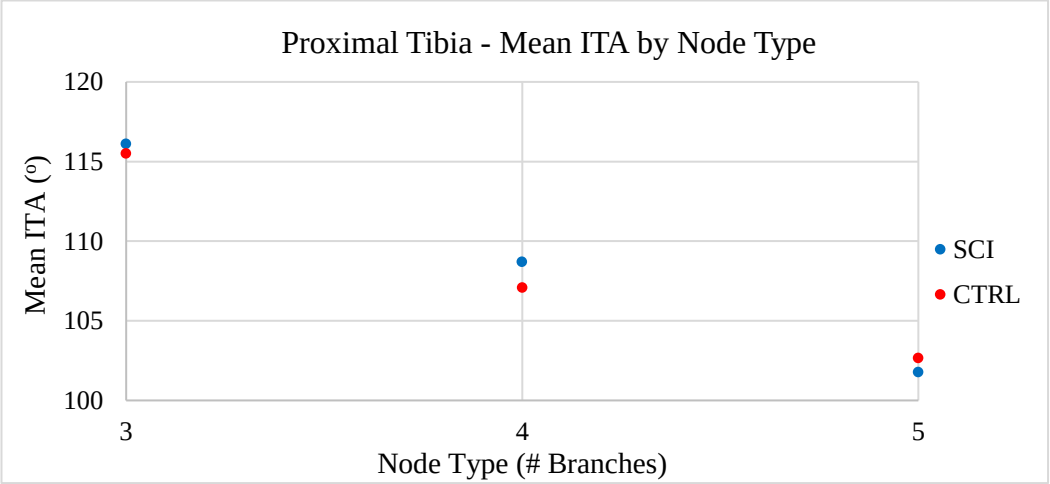

Figure 3. 45: Effects of chronic SCI on mean ITA for 3N, 4N and 5N nodes in the proximal tibia.

For the DF group, no significant difference in mean ITA was detected between SCI and CTRL bones at the chronic timepoint in any of the 3N, 4N or 5N groups (Figure 3.44).

In the PT group, a noticeable difference in mean ITA was observed between control and SCI in the 4N nodes, however it was likely not significant due to the small sample size with the CTRL 3 bone omitted (Figure 3.45).

Figures 3.46 and 3.47 display the ITA distributions in each bone region for each 10 degree ITA bin, from 10 to 180 degrees:

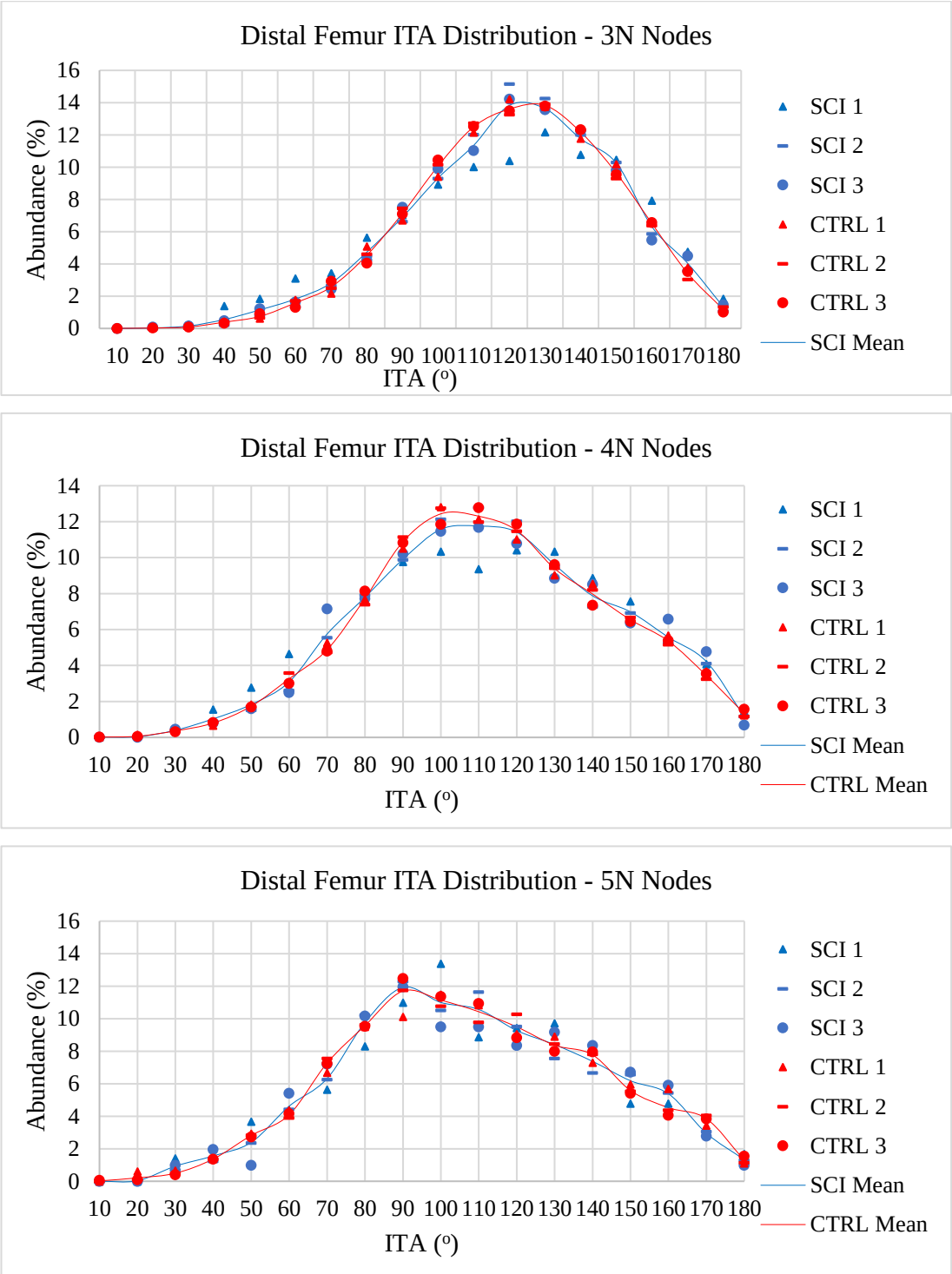

Figure 3. 46: ITA distributions of chronic DF dataset. Individual values for each SCI and CTRL bone presented alongside group means.

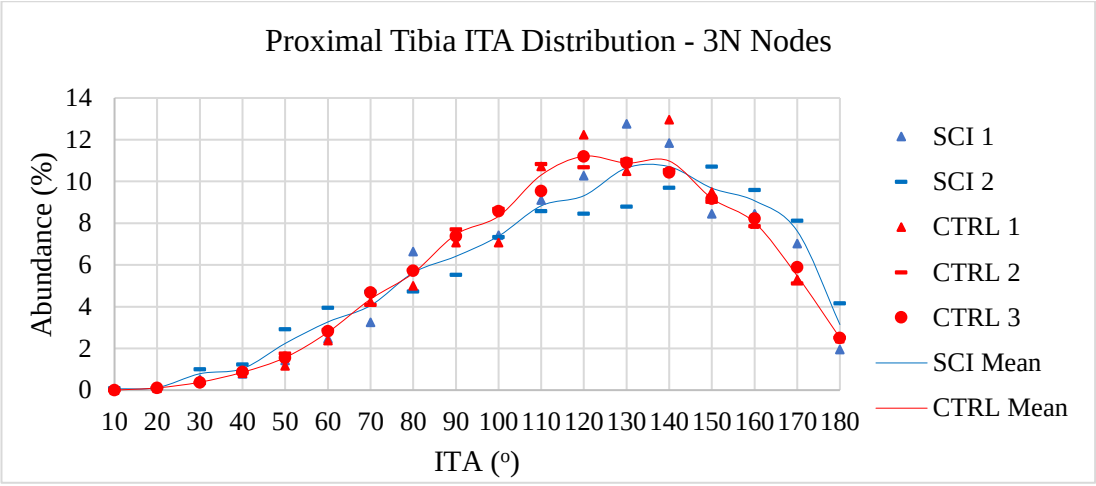

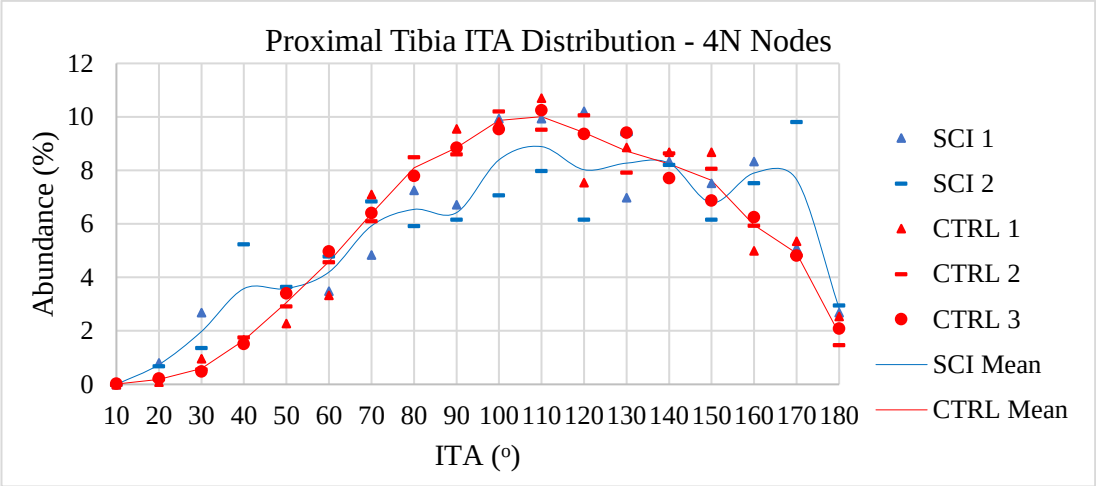

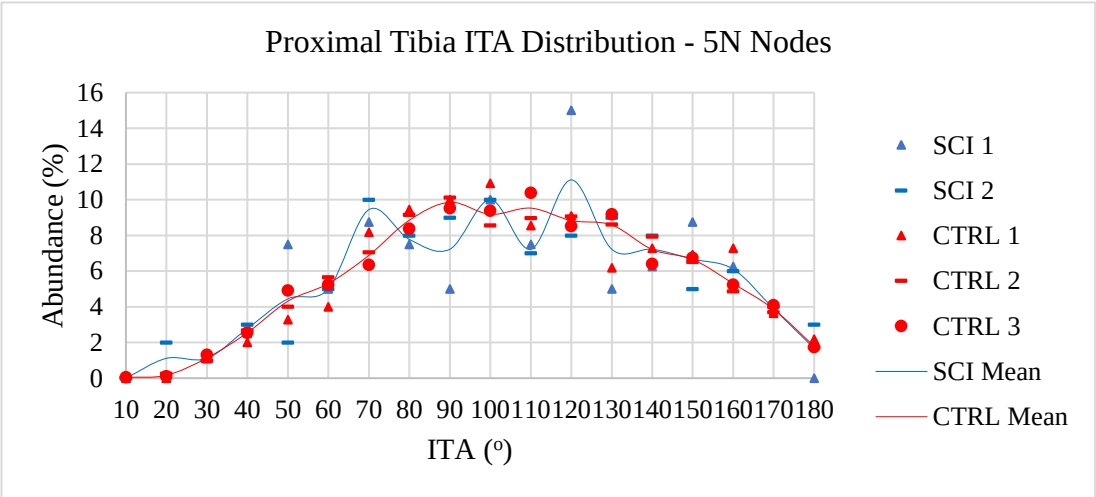

Figure 3. 47: ITA distributions of chronic PT dataset. Individual values for each SCI and CTRL bone presented alongside group means.

3.3.4 Cortical Analysis

Figure 3.48 displays the effects on diaphyseal cortical bone average thickness (Ct.Th) and area (Ct.Ar) following SCI:

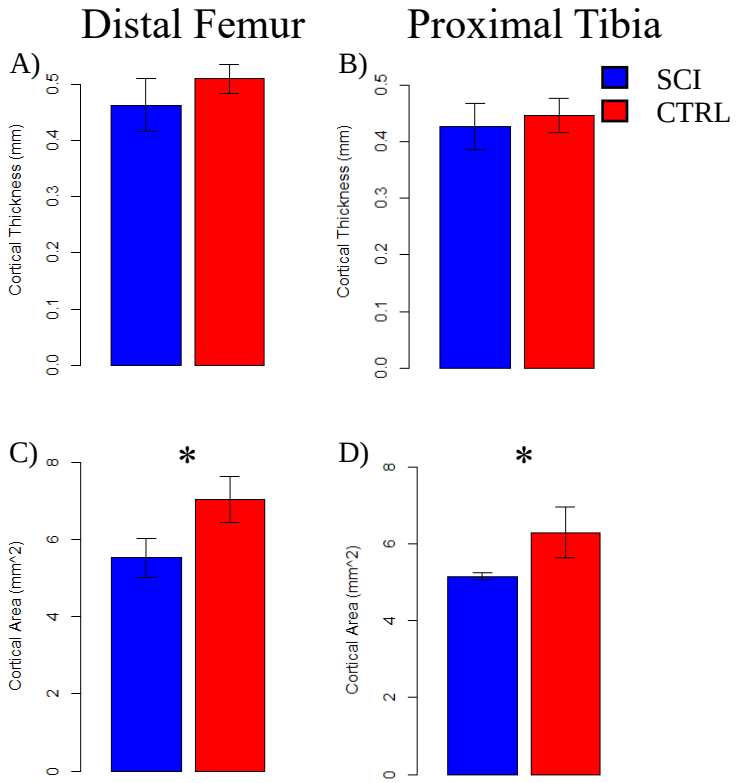

*Figure 3. 48: Average cortical thickness and area changes following chronic SCI. SCI: spinal cord injured. CTRL: control. * indicates significant difference between SCI and CTRL at p<0.05. Data presented as mean ±1SD.*

Cortical thickness was observed to remain unchanged following SCI (Figures 3.48A and 3.48B). However, significant differences were detected in cortical area in both the DF and PT, with percentage decreases of 22% (p=0.028) and 18% (p=0.0419) respectively (Figures 3.48C and 3.48D).

Figure 3.49 displays the effects of SCI on the total area enclosed by the periosteal envelope (Tt.Ar) and medullary area (Ma.Ar):

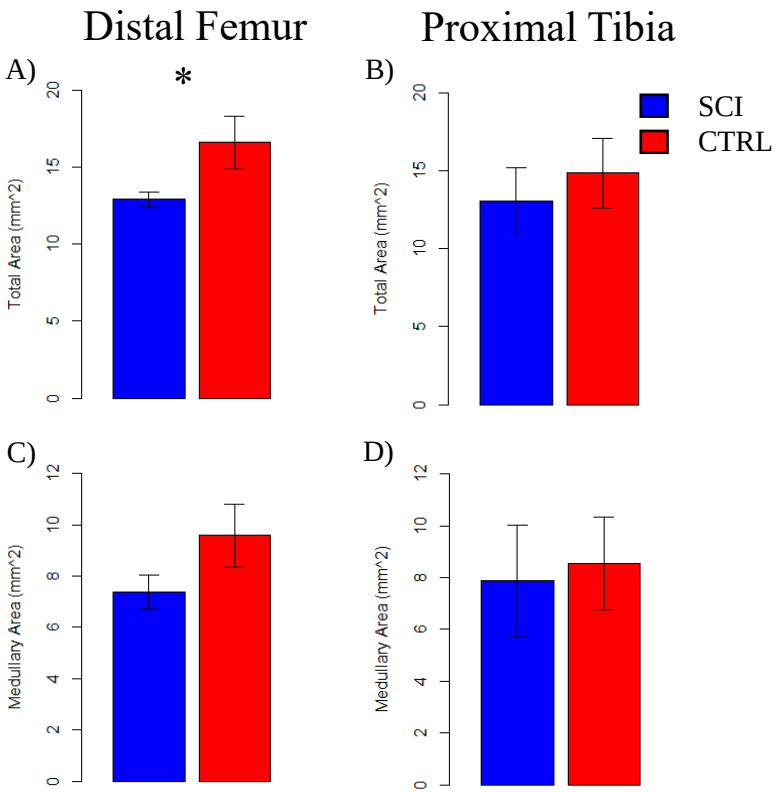

*Figure 3. 49: Total area (periosteal envelope area) and medullary area changes following chronic SCI. SCI: spinal cord injured. CTRL: control. * indicates significant difference between SCI and CTRL at p<0.05. Data presented as mean ±1SD.*

The DF presented a significant difference following SCI in Tt.Ar i.e. the area of the periosteal envelope reduced significantly by 22.35% (p=0.023) (Figure 3.49A), while the PT did not (Figure 3.49B). Ma.Ar was not significantly affected by SCI (Figures 3.49C and 3.49D).

Figure 3.50 contains the results of the polar second moment of area (J), cortical specific surface (Ct.BS/BV) and eccentricity (Ecc) analyses:

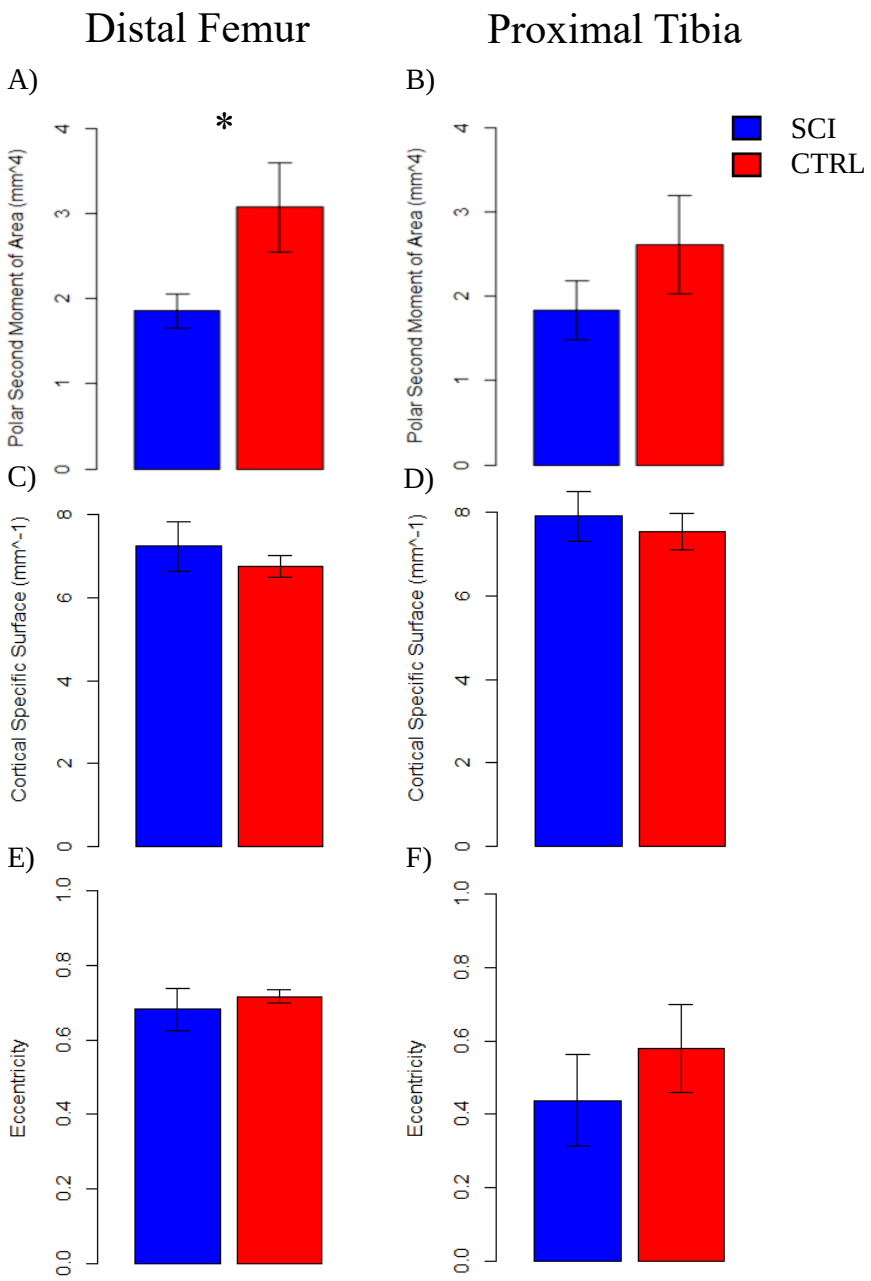

*Figure 3. 50: Cortical polar second moment of area, specific surface and eccentricity changes following chronic SCI. SCI: spinal cord injured. CTRL: control. * indicates significant difference between SCI and CTRL at $p<0.05$. Data presented as mean ±1SD.*

The effect of chronic SCI on polar second moment of area was observed to be significant in the DF, with a percentage reduction of 39.62% ($p=0.01977$) (Figure 3.50A). No such significance was detected in the proximal tibia (Figure 3.50B).

For both cortical specific bone surface and eccentricity, neither bone region exhibited any notable differences (Figures 3.50C, 3.50D, 3.50E and 3.50F).

Figure 3.51 details the effects of chronic SCI on cortical diaphyseal tissue mineral density:

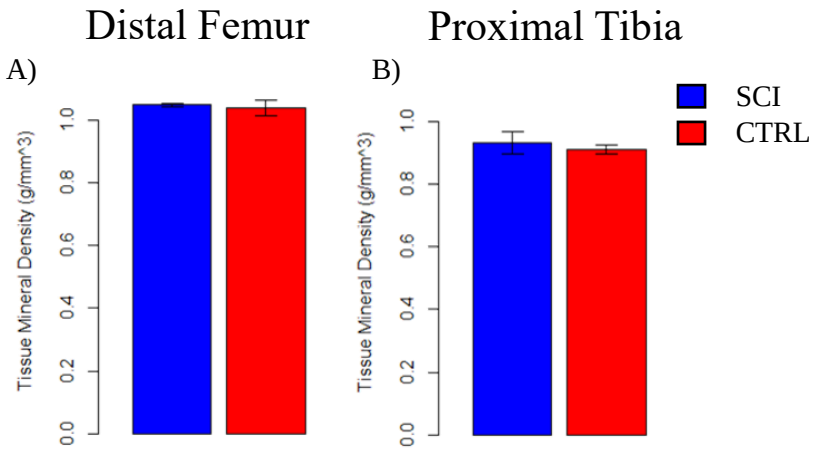

Figure 3. 51: Cortical TMD changes following chronic SCI. SCI: spinal cord injured. CTRL: control. Data presented as mean ±1SD.

The mean cortical tissue mineral density (TMD) of both the DF and PT was found to be unaffected by chronic SCI (Figure 3.51).

Figure 3.52 displays the effects of chronic SCI on the metaphyseal cortical bone porosity:

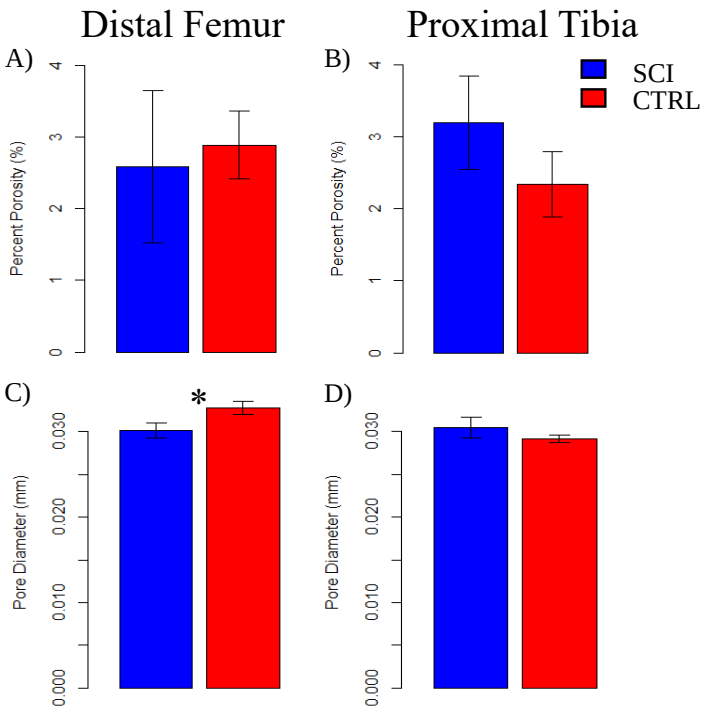

*Figure 3. 52: Cortical porosity changes following chronic SCI. SCI: spinal cord injured. CTRL: control. * indicates significant difference between SCI and CTRL at $p<0.05$. Data presented as mean ±1SD.*

For both the DF and PT, no significant change was observed in cortical porosity following chronic SCI (Figures 3.52A and 3.52B).

When examining pore diameter, a significant decrease of 8.09% was observed in the DF metaphysis ($p=0.01761$) (Figure 3.52C). No such significance was observed in the PT (Figure 3.52D).

3.4 Results - MicroCT Acute SCI

As the chronic (11 week) dataset contained a small sample size n=3, a previous dataset was utilised in order to add to the correlation data for EF and SMI, as well as to provide additional information into the time course effects of SCI-induced osteoporosis. This acute dataset contained n=5 SCI and n=6 CTRL (age-matched sham operated) bones from male Wistar rats ~225g (7 weeks of age), with acute SCI at 2 weeks post-injury following a T9 transection. Only the proximal tibiae were examined.

3.4.1 Trabecular Analysis

Table 3.5 displays the standard 3D trabecular results from CTan for the acute dataset.

Means	**BV/TV (%)**	**BS/BV (mm-1)**	**Tb.Th (mm)**	**Tb.Sp (mm)**
SCI	12.031±2.68***	50.944±2.99***	0.070±0.003***	0.777±0.22***
CTRL	30.919±6.69	42.916±2.47	0.080±0.002	0.223±0.07
Means	**Tb.N (mm-1)**	**FD (-)**	**Conn.D (mm-3)**	
SCI	1.706±0.35***	2.350±0.09***	2509±931***	
CTRL	3.841±0.76	2.595±0.04	5224±1517	

*Table 3. 5: Standard 3D trabecular parameter effects following 2 weeks of SCI. SCI: spinal cord injured. CTRL: control. *** indicates significant difference between SCI and CTRL at p<0.001. Data presented as mean ±1SD.*

The acute dataset exhibited significant differences in all standard trabecular parameters analysed. BV/TV, Tb.Th, Tb.N, FD and Conn.D reduced by 61%, 12%, 55%, 9% and 51% respectively following 2 weeks of SCI. BS/BV and Tb.Sp increased by 19% and 249% (Table 3.5).

3.4.2 Ellipsoid Factor

Table 3.6 displays the EF and SMI effects for the acute SCI PT dataset:

Means	**Median EF**	**SMI**
SCI	0.146±0.04	1.446±0.43
CTRL	0.168±0.03	1.1836±0.47

Table 3. 6: EF and SMI effects following 2 weeks of SCI. SCI: spinal cord injured. CTRL: control. Data presented as mean ±1SD.

Neither EF or SMI detected a significant difference between SCI and CTRL bones by 2 weeks of SCI (Table 3.6).

Figure 3.53 displays isometric views of the PT bones in the 2 week dataset:

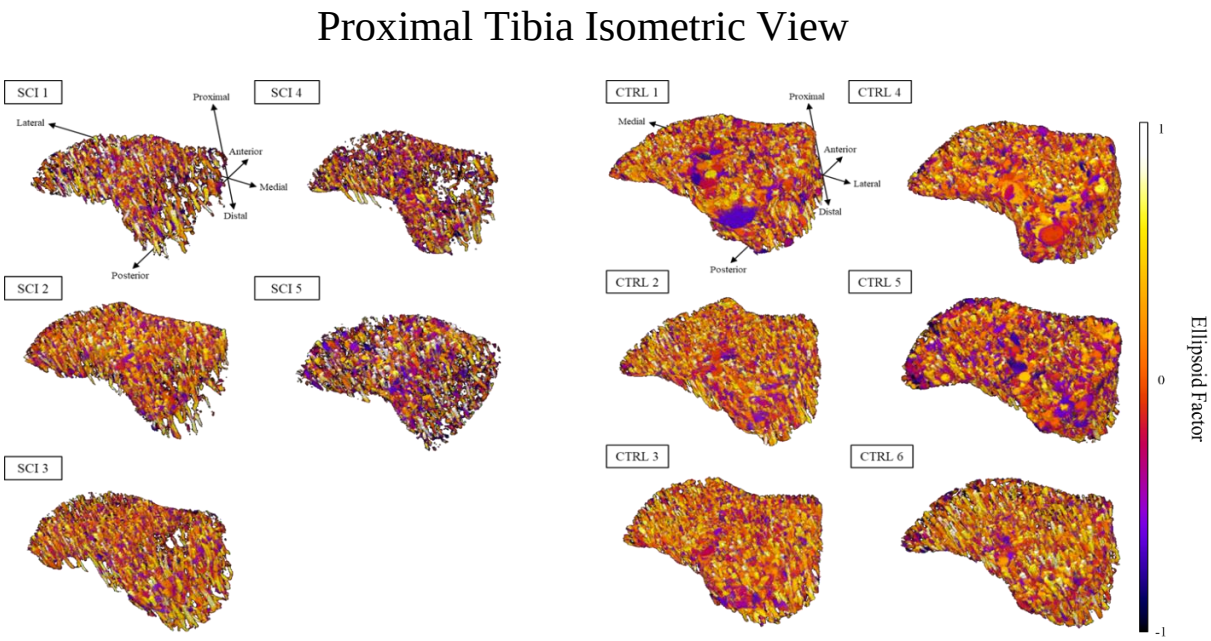

Figure 3. 53: Ellipsoid factor 3D models for SD rat right proximal tibiae. Isometric view. SCI: Spinal cord injured. CTRL: Control.

Unlike the chronic dataset, the acute bones did not appear to differ between SCI and CTRL when observing the numbers and locations of rod-like and plate-like trabeculae in each volume. Instead, each VOI exhibited a relatively uniform distribution of different EF values (Figure 3.53).

Figure 3.54 contains the same bones viewed from the posterior:

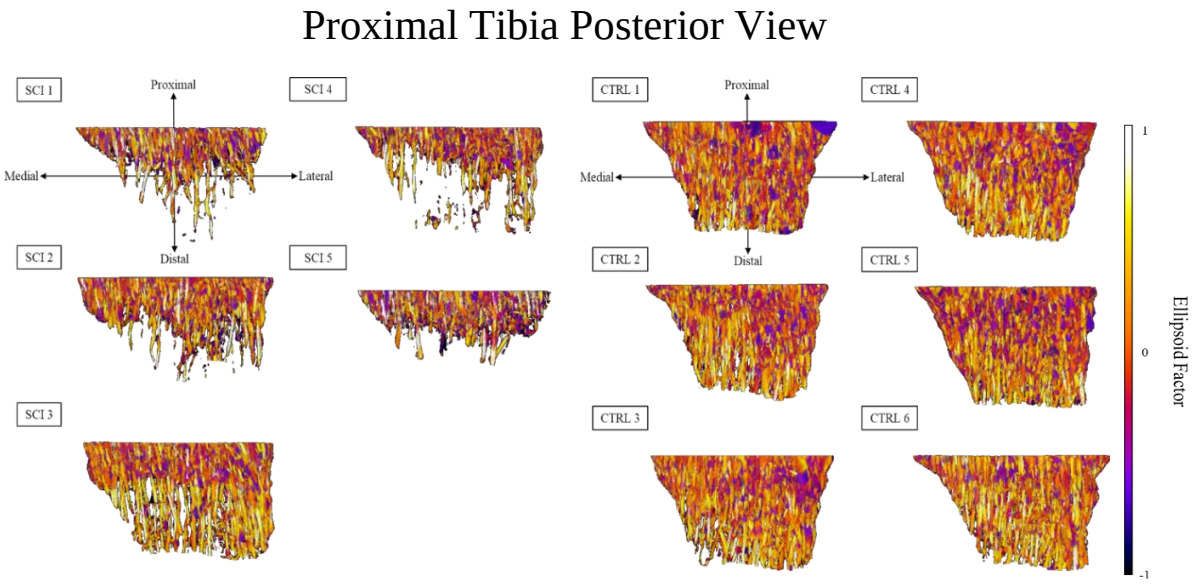

Figure 3. 54: Ellipsoid factor 3D models for SD rat right proximal tibiae. Posterior view. SCI: Spinal cord injured. CTRL: Control.

Observing the acute PT dataset in the posterior view clearly displayed how diaphyseal trabeculae are lost to a greater extent than those in the more proximal regions during SCI-induced osteoporosis. Extensive diaphyseal losses were observed in the SCI bones, whereas the CTRL bones exhibited no distinct regions of bone loss (Figure 3.54).

Figure 3.55 displays the EF histograms for the acute dataset:

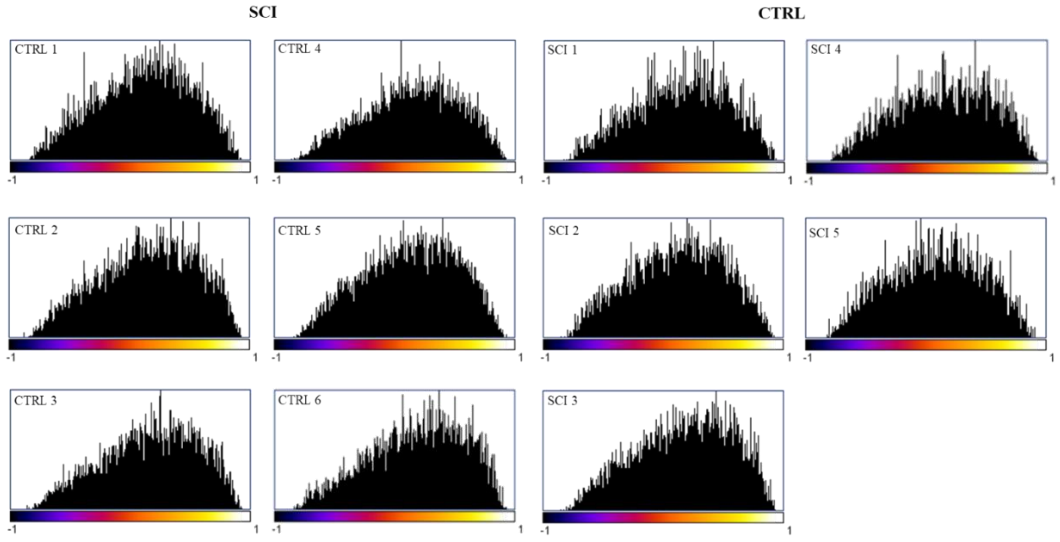

Figure 3. 55: EF histograms of acute dataset PT metaphyseal secondary spongiosa.

The EF histograms of the acute dataset were all observed to skew left. Each distribution was unimodal, with most EF modes lying at 0.2→0.4 (Figure 3.55).

Figure 3.56 contains the correlations of median EF, EF mode and SMI with BV/TV:

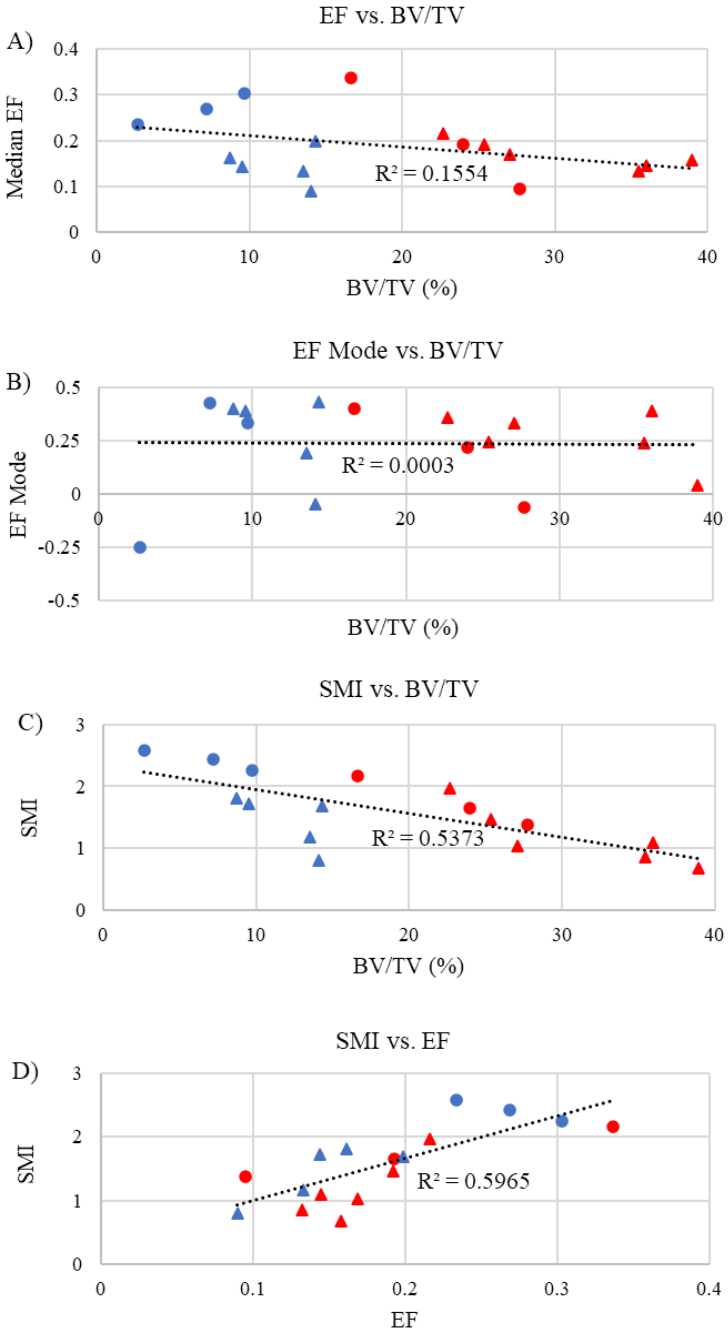

Figure 3. 56: Correlation of EF median / mode and SMI with BV/TV. Combined results from acute 2 week and chronic 11 week datasets. Circles: Chronic datapoints. Triangles: Acute datapoints.

Median EF was not observed to depend on BV/TV at any significant level, with a R^2 value of 0.1554 (p=0.117) (Figure 3.56A). SMI, however, could be predicted by BV/TV in over 50% of cases, with a R^2 value of 0.5373 (p=0.0008) (Figure 3.56C). EF mode had the weakest correlation with BV/TV, with a R^2 value of 0.0003 (p=0.94) (Figure 3.56B). SMI and EF were not found to be independent, as the R^2 value was 0.5965 (p=0.00028) (Figure 3.56D).

3.4.3 Inter-Trabecular Angle

Figures 3.57 and 3.58 contain the node type distribution diagrams, plotting the locations of each 3N, 4N and 5N node in the SCI and CTRL acute PT volumes:

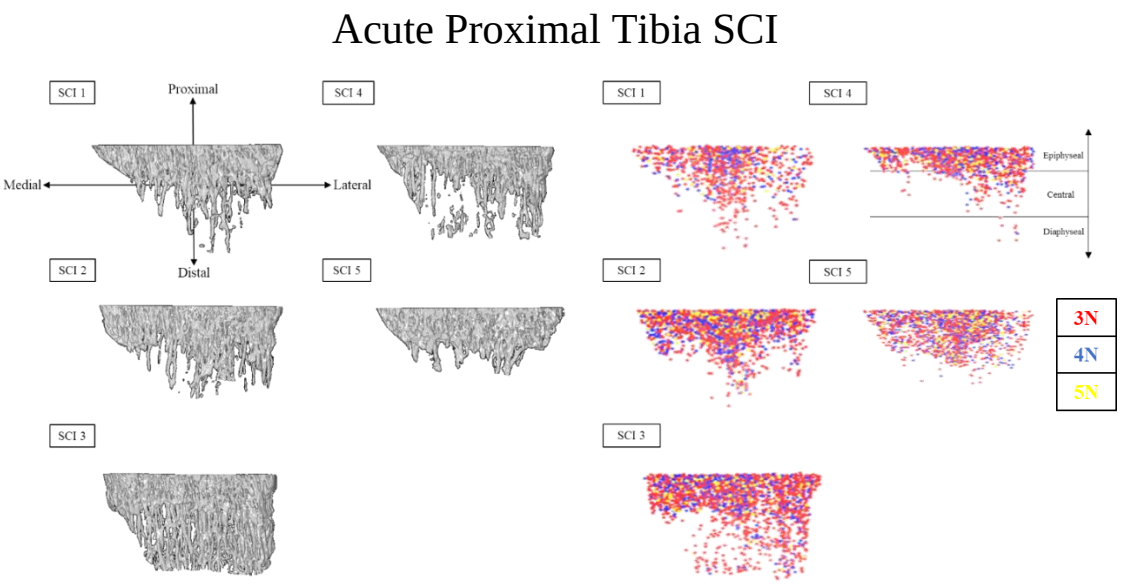

Figure 3. 57: 3D colour plots of 3N, 4N and 5N nodes in the acute PT. SCI: Spinal cord injured bones.

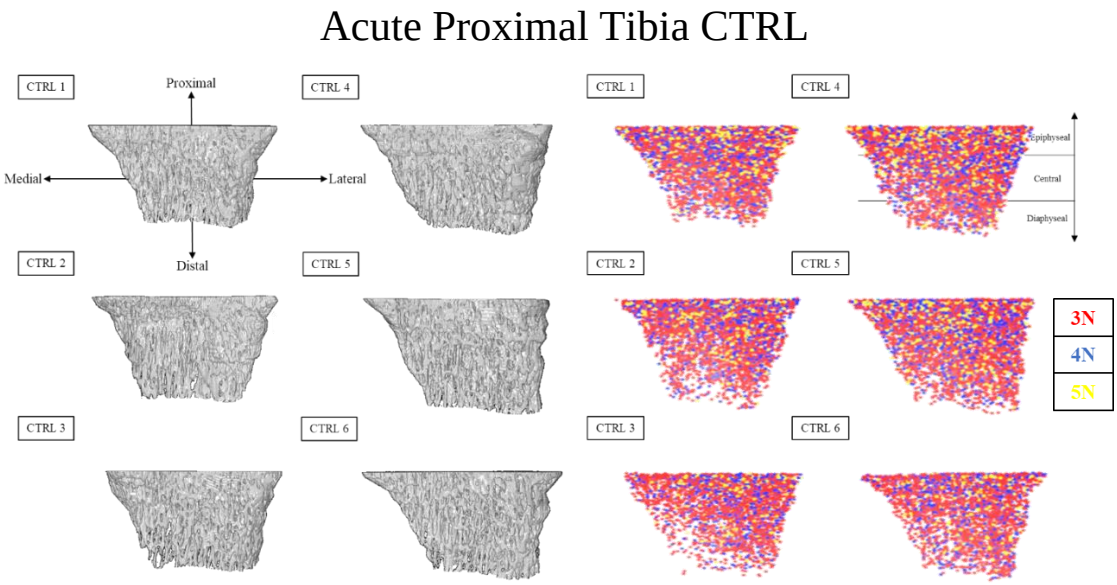

Figure 3. 58: 3D colour plots of 3N, 4N and 5N nodes in the acute PT. CTRL: Age-matched sham control bones.

Unlike the chronic (11 week) PT, the acute (2 week) PT did not present any notable regional clustering of 3N, 4N or 5N nodes. In every acute VOI, the spatial distribution

of 3N nodes remained unchanged by lowering trabecular density due to SCI. This was also the case for 4N and 5N nodes (Figures 3.57 and 3.58).

Figure 3.59 contains the mean relative node abundances for the SCI and CTRL acute bones:

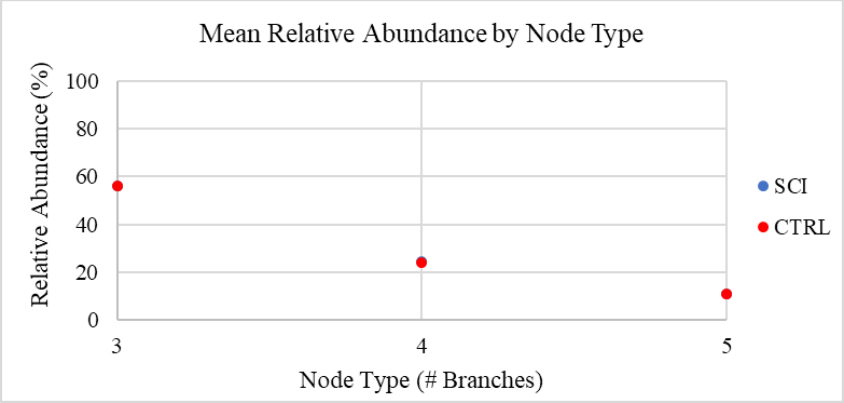

Figure 3. 59: Effects of acute SCI on node type relative abundance in the proximal tibia.

No effects due to SCI were observed in any node type of the acute PT bones. The ratios of 3N:4N:5N nodes in both SCI and CTRL acute PT datasets was ~6:2:1. (Figure 3.59).

Figure 3.60 displays the mean ITA by node type for the acute bones:

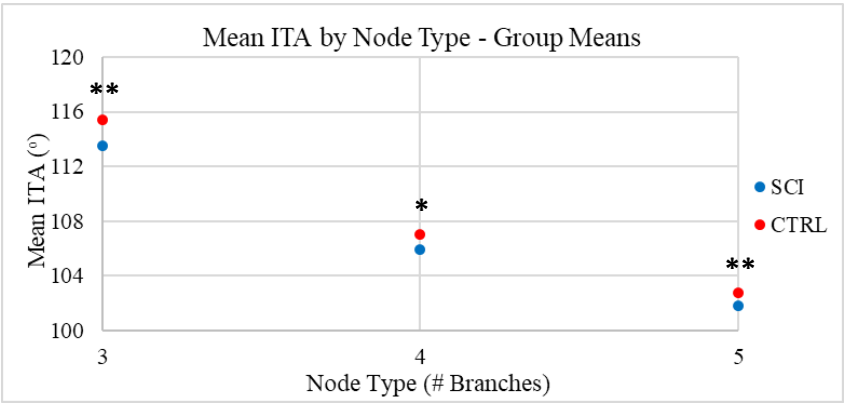

*Figure 3. 60: Effects of acute SCI on mean ITA for 3N, 4N and 5N nodes in the proximal tibia. * indicates significant difference between SCI and CTRL at $p<0.05$. ** $p<0.01$.*

SCI was found to effect a significant difference in mean ITA in the acute stages of SCI-induced osteoporosis. After 2 weeks of SCI, mean ITA decreased from 115° to

113º (p= 0.0067), 107º to 106º (p=0.0238) and 103º to 102º (p=0.0016) in 3N, 4N and 5N nodes respectively in the acute PT (Figure 3.60).

Figure 3.61 contains the ITA distributions for 3N, 4N and 5N nodes in the acute PT dataset:

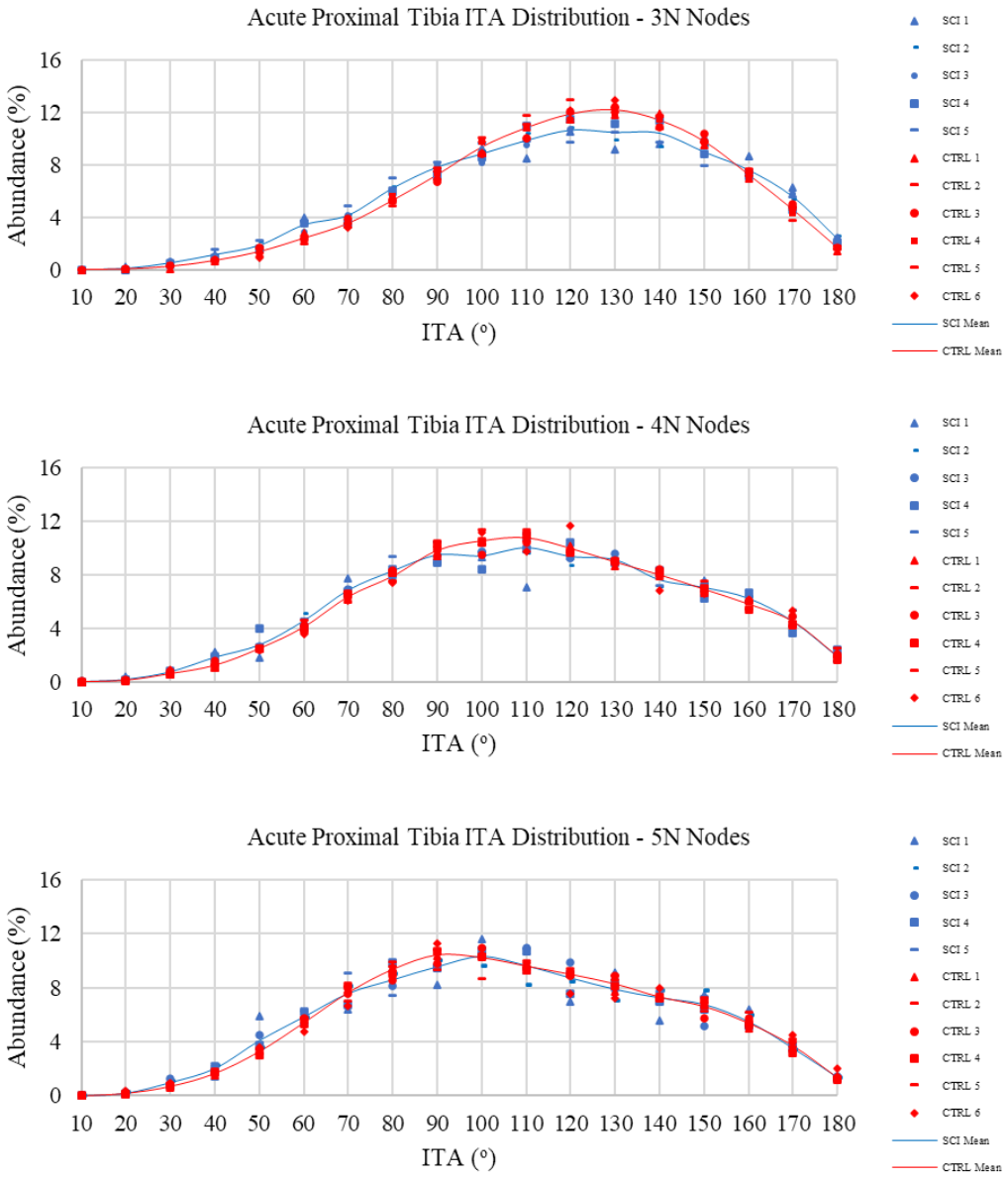

Figure 3. 61: ITA distributions of the acute PT dataset. Individual values for each SCI and CTRL bone presented alongside group means.

3.4.4 Cortical Analysis

Table 3.7 contains the results of the cortical analysis performed mainly on the diaphyseal cortex of the acute PT VOIs. The only VOIs which were altered were those selected for the porosity analysis. As previously stated, this designation was to enable comparisons between the cortical porosity (microCT) and cortical blood vessel density (IHC) results at the same region.

	Tt.Ar (mm^2)	**Ct.Ar (mm^2)**	**Ma.Ar (mm^2)**	**Ct.Th (mm)**	**J (mm^4)**
SCI	4.1853 ±0.1572	3.2336 ±0.1195*	0.9517 ±0.1435	0.6402 ±0.0311	2.6897 ±0.1854
CTRL	4.3874 ±0.2215	3.4437 ±0.1531	0.9437 ±0.1174	0.6708 ±0.0271	2.9976 ±0.2848
	Ct.BS/BV (mm^{-1})	**Eccentricity (-)**	**Ct.TMD (g/cm^3)**	**Porosity (%)**	**Po.Dm (mm)**
SCI	4.8554 ±0.2063	0.5405 ±0.0540	1.3196 ±0.0062	7.6191 ±0.9698**	0.0320 ±0.0002
CTRL	4.7281 ±0.1387	0.5783 ±0.0622	1.3223 ±0.0128	5.0470 ±0.9697	0.0325 ±0.0009

*Table 3. 7: Cortical 3D, 2D, TMD and porosity effects following 2 weeks of SCI. SCI: spinal cord injured. CTRL: control. * indicates significant difference between SCI and CTRL at $p<0.05$. **$p<0.01$. Data presented as mean ±1SD.*

The cortical effects were observed to be different between the acute and chronic PT datasets only when analysing percent porosity. In the chronic PT, porosity was not observed to change (Figure 3.52B). In the acute PT, a significant increase of 50.96% ($p=0.0018$) in cortical porosity was observed following 2 weeks of SCI (Table 3.7). The significant decrease in cortical area which was observed in the chronic PT (Figure 3.48D) was also observed in the acute bones, with a 6% reduction ($p=0.034$) observed following 2 weeks of SCI (Table 3.7). No significant differences were detected at the acute timepoint between SCI and CTRL PT bones in the following parameters: total area, medullary area, cortical thickness, polar second moment of area, cortical specific surface, eccentricity, tissue mineral density or pore diameter (Table 3.7).

Chapter 4: Characterising SCI-induced Osteoporosis using Histology

Chapter 4 begins with a literature review providing first a basic overview of the histological and immunohistochemical method. Background on either of the two selected stains is provided, with justifications for their selection at the end of the relevant sections.

Following the literature review, the methodology outlines the preparation of rat long bones for histology. The preparation includes the techniques used for fixation, decalcification, paraffin embedding, microtoming, staining and mounting. The rat model of chronic spinal cord injury used is identical to that described in the methodology in Chapter 3.

Following the staining methodology, the methodology for quantifying the obtained images is described. The results obtained are displayed and discussed to complete the chapter.

4.1 Histology Literature Review

4.1.1 Histology Fundamentals

The process of identifying structures and pathologies at the microscale in biological tissues is commonly agreed to stem from the 17th century work of the Italian physician Marcelo Malpighi (Reveron 2011). Since then, advancements in understanding of cell structures, chemical binding and imaging equipment have brought about the modern histology we understand today (Saikia, Gupta & Saikia 2008).

The main concept behind histology is simple: biological tissues are examined at the microscale, usually through the use of a light or electron microscope. The tissues to be examined are often prepared with chemical stains prior to imaging in order to highlight the cells or structures of interest (Titford 2006). The information garnered from such images can be of great utility for pathological and anatomical studies. An example of this is seen in Figure 4.1, using a stain specific to osteoclasts:

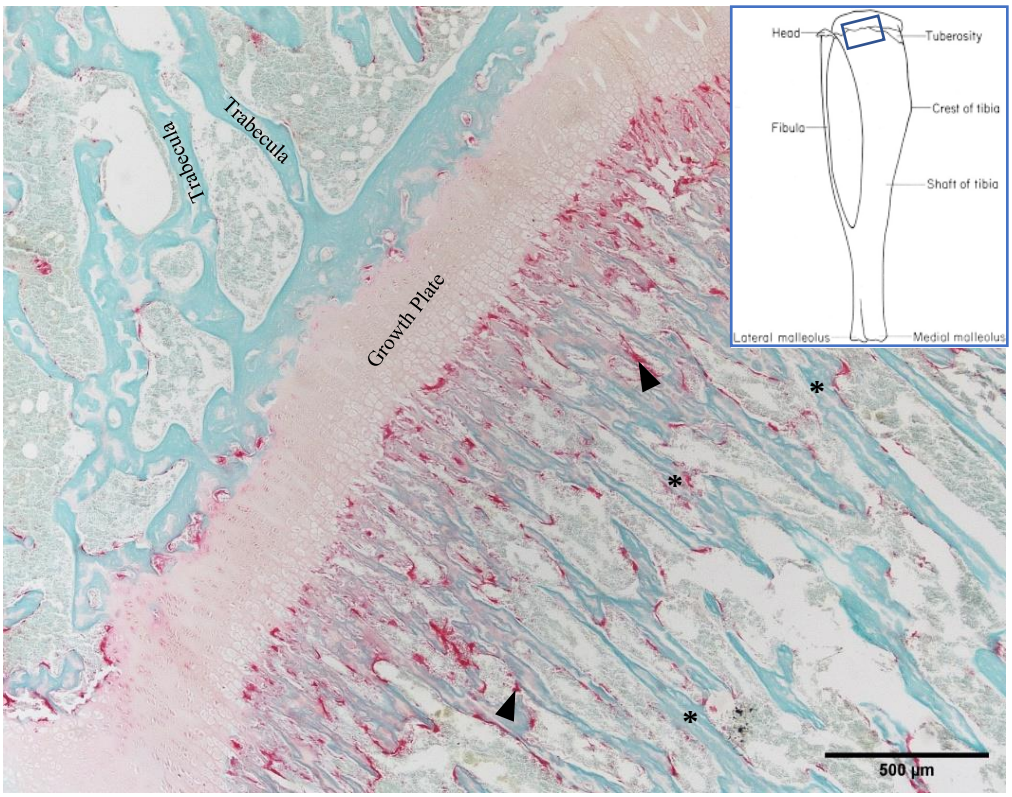

Figure 4. 1: Tartrate-resistant acid phosphatase (TRAP) staining in the epiphyseal growth plate region of the rat proximal tibia. Counterstained with Fast Green FCF. TRAP stains osteoclastic cells (arrowheads), macrophages and dendritic cells. Fast Green FCF is a general protein stain that can be used on osteochondral tissues like the mineralising cartilage scaffolds seen here (asterisks), as well as fully developed trabeculae.

4.1.2 Immunohistochemistry Fundamentals

The technique of immunohistochemistry (IHC) is based in histology. IHC staining exploits the binding properties of antibodies to antigens in order to produce a specific stain. It was invented in 1941 by using fluorescent dye to label antibodies and subsequently identify antigens in pneumococcal tissue sections (Coons *et al*. 1941). The number of studies using IHC began to accelerate rapidly following the development of horseradish peroxidase (HRP)-conjugated antibodies in 1966 (Nakane, Ram & Pierce 1966). This method of using enzymes to catalyse reactions with chromogenic substances is still in widespread use today. Incubating HRP-treated samples in a solution of 3-3 diaminobenzidine (DAB) leads to the colour reaction; the HRP enzyme catalyses the oxidation of DAB by hydrogen peroxide, producing a brown coloured product which is clearly visible under the microscope (Graham &

Karnovsky 1966). An example of IHC using HRP and DAB as the chromogen can be seen in Figure 4.2:

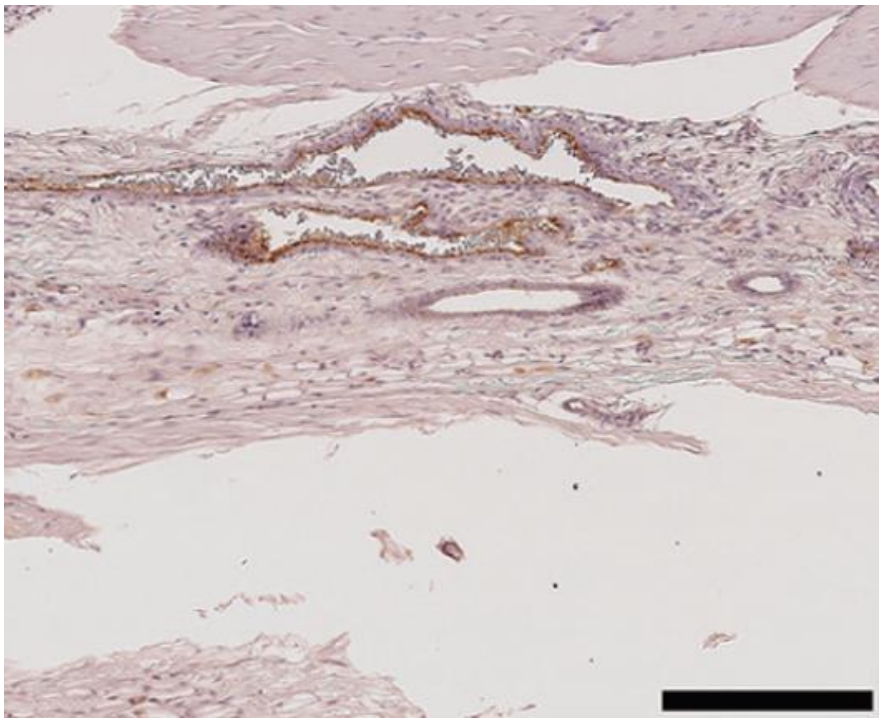

Figure 4. 2: IHC staining for von Willebrand Factor (vWF) in anterior rat mandible. vWF stains endothelial cells of blood vessels brown. The counterstain is haematoxylin-eosin (H&E) which highlights nuclei, cell cytoplasm and extracellular matrix in purple. Reproduced from Savi et al. 2007. Scale bar: 200μm.

The two most common methods for preparing biological tissues for IHC are:

1) Formalin fixed, paraffin embedded (IHC-FFPE)
2) Frozen (IHC-Fr)

The method used in this thesis is IHC-FFPE for rat femurs and tibiae. In FFPE preparation of bone, samples are immediately fixed in formalin (saturated formaldehyde solution) following excision from a sacrificed animal. Formaldehyde readily forms covalent bonds with a wide variety of proteins, amino acids and DNA bases. This results in many of the proteins in the tissue being cross-linked with formaldehyde via certain amino groups. This cross-linking both preserves and blocks the antigens of the tissue's cells, rendering it biologically inert and hence fixing it for the rest of IHC preparation (Hoffman *et al*. 2015).

Once fixed, the tissue is decalcified. Decalcification enables sections (slices) to be taken from the otherwise hard and brittle bone material. It is important to ensure the decalcification procedure (choice of agent, decalcification time, number of solution refreshes, temperature, pH) is chosen for the optimal balance of section structural integrity, time efficiency and antigen preservation.

The bone is then dehydrated in a graded series of alcohol solutions. The alcohol in the bone is then removed by immersion with a clearing agent such as xylene. Clearing is necessary as alcohol is immiscible with paraffin (Metgud *et al*. 2013). The fixed, dehydrated and cleared bone is then immersed in molten paraffin wax, placed in a histology cassette mould and cooled. The result is a well-preserved specimen which is embedded in a paraffin wax block, ready for sectioning. Sectioning in this case refers to cutting the tissue block into very thin slices, usually around 5µm depending on the type of tissue (CAP 2012).

Once FFPE preparation is complete, the general process of IHC staining using the HRP / DAB reaction is as follows:

The bone section is pre-treated to remove the paraffin, remove the formalin cross-links (to uncover or 'retrieve' the cell antigens), and finally to rehydrate the tissue. Rehydration is performed in a graded series of alcohol solutions in order for the section to be incubated with a variety of aqueous staining reagents without osmotic lysis occurring in the cells.

Once all paraffin is removed, antigens are retrieved and cells rehydrated, the sections are incubated in a hydrogen peroxide solution in order to block the endogenous peroxidase enzymes in the bone, so that the only peroxidase activity comes from the HRP.

The section is then incubated in a solution containing the primary antibody. This solution also contains a mixture of antibodies which bind to nonspecific (i.e. not the antigen being stained) sites and block unwanted staining in the section. A common source of these blocking antibodies is serum albumin from animals such as cows, goats and donkeys (Majorek *et al*. 2012).

Once the primary antibodies have bound on to the antigens of interest, the section is incubated with secondary antibodies. These secondary antibodies are specific to the same species as the primary antibodies were raised in. For example, a CD34 IHC protocol for rats could use rabbit-raised anti-CD34 primary antibodies in combination with goat-raised anti-rabbit secondary antibodies. It is important to avoid selecting a primary antibody raised in the same species as the animal being studied, as this would lead to the secondary antibodies cross-reacting with endogenous immunoglobulins in the section instead of the artificially-introduced primary antibodies.

Signal amplification is improved by utilising the binding properties of avidin (or streptavidin) to biotin. This method of improving the staining intensity is known as the Avidin-Biotin Complex (ABC) method. When utilising the ABC method, the secondary antibodies are conjugated to biotin (Vitamin B_7). The avidin molecule is a tetramer; it can bind four biotin molecules as each subunit can bind one. By combining avidin with a biotinylated enzyme like HRP, large complexes are formed made up of avidin molecules bound to the biotinylated enzymes. These complexes can then bind to the biotinylated secondary antibodies, resulting in numerous HRP enzymes at each site of primary antibody binding. This leads to a more intense stain due to an increased catalysation of the DAB-oxidation reaction (Adams 1992).

Figure 4.3 illustrates this signal amplification step:

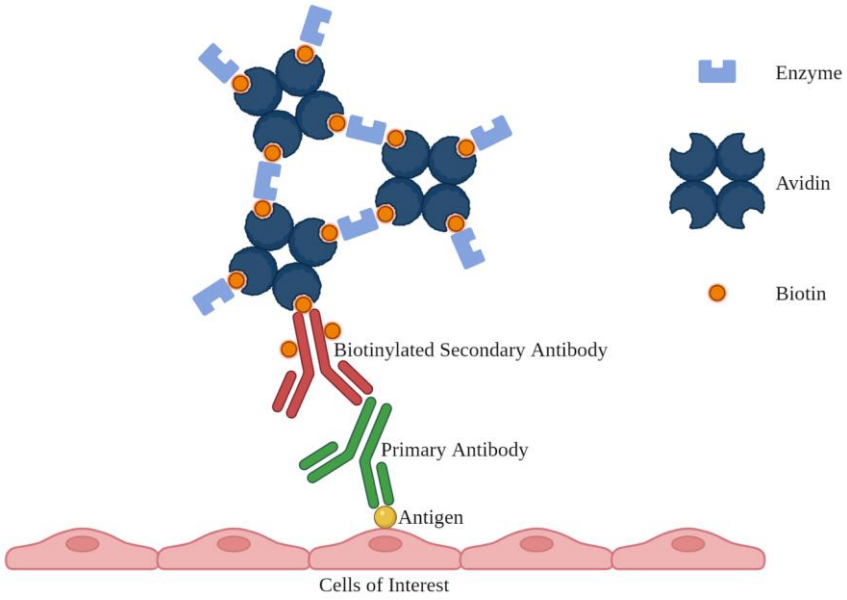

Figure 4. 3: ABC (avidin-biotin complex) method for IHC Signal Amplification.

The main difference in using avidin or streptavidin in the signal amplification process is that with avidin, the HRP is introduced in a separate, biotinylated form. The HRP then attaches to the avidin-biotin complexes on each antigen. With streptavidin, the HRP is directly conjugated to the streptavidin, as opposed to being introduced in a separate solution (Esposito 2021).

Once the HRP has aggregated around the primary antibody by utilising ABC, the chromogen (DAB) is introduced to allow the colour reaction to develop. The section is then incubated with a counterstain to further increase the contrast between the DAB positive sites and the tissue background. Additionally, the counterstain allows visualisation of the extraneous tissue contents and hence puts everything in context for the observer.

Once sections have been stained using this IHC-FFPE + HRP / DAB method, coverslips are mounted onto slides using a non-reactive, xylene based mounting media such as DPX (Saify & Tiwari 2020). This preserves the sections indefinitely.

4.1.3 IHC Controls

The following information is from the same source (Hewitt *et al*. 2014).

No Primary Control

A no primary control is a type of negative control that confirms that any observed staining is appearing only because the specific primary antibody has been introduced. For a no primary control, a solution is created which is identical to the diluent in the primary antibody solution, just without the primary antibodies themselves. The sections are then incubated in this diluent in the same conditions (time, temperature etc.) as the primary antibody sections, followed by “normal” incubation with the secondary used in the main staining. Negative staining (a lack of staining) here indicates that without the relevant primary antibody, the observed staining does not occur. This validates the use of the selected primary antibody for its staining application and confirms that the secondary antibody itself does not bind to the samples.

Isotype Control

An isotype control must be created in the same species as that in which the primary antibodies were raised. For example, a rabbit-raised anti-CD34 antibody solution would require a rabbit-raised isotype control. For an isotype control, the control solution is incubated in place of the primary antibody in the same conditions and concentration. For polyclonal antibodies, the control solution contains a multitude of different IgG subclasses which all react with varying antigens in the species they were raised in. Incubating with this control proves that the tissue being stained (rat in this case) does not contain significant numbers of antigens which will be bound to by rabbit-targeting antibodies, and the only reason the primary antibody stain is showing is because the primary antibody recognized the specific protein that is was raised against.

Positive Tissue Control

A positive tissue control ensures that the selected primary antibody is working as it should be i.e. is staining the cells / proteins defined for its purpose. A positive tissue control is performed using a tissue type known to express the antigen of interest in abundance. For example, a positive tissue control for an endothelial cell marker like CD34 would be lung tissue, as the vast multitude of alveoli in the lungs are all located beside endothelial-lined blood capillaries.

4.1.4 Histological Stains for Bone Analysis

Examples of stains specific to different cells in bone are given in Table 4.1. All entries except TRAP (highlighted in blue) are stained using immunohistochemistry. That is to say, they are proteins expressed by their respective cell types in bone for which commercial primary antibody solutions are available.

Research Area	Stain	Cell	Source
Bone Vasculature	von Willebrand Factor (vWF)	Endothelial cells	Stark *et al*. 2011
	Platelet and endothelial cell adhesion molecule (CD31 / PECAM-1)	Endothelial cells	Stockinger *et al*. 1990
	CD34	Endothelial cells	Lanza, Healy & Sutherland 2001
	Endomucin (Emcn)	Endothelial cells	Liu *et al*. 2001
Bone Formation	Osterix (Osx)	Osteoblasts	Harada *et al*. 2001
	Runx2	Osteoblasts	Franceschi & Xiao 2003
	Osteocalcin	Osteoblasts	Ducy *et al*. 1996
	Procollagen type 1 extension peptides (P1NP)	Osteoblasts	Hlaing & Compston 2014
	Sclerostin	Osteocytes	Winkler *et al*. 2001
Bone Resorption	Tartrate-resistant Acid Phosphatase (TRAP)	Osteoclasts	Minkin 1982
	Cathepsin K	Osteoclasts	Drake *et al*. 1996

Table 4. 1: Histological targets for the analysis of different cell types in bone.

The two histological stains utilised to characterise SCI-induced osteoporosis in this study are TRAP staining and CD34 immunohistochemistry (IHC).

4.1.5 TRAP

There are at least five different isoforms of the enzyme acid phosphatase. It acts to hydrolyse organic phosphates such as ATP in acidic pH conditions (Henneberry, Engel & Grayhack 1979). Every isoform has been found to be inhibited by L(+)- tartaric acid, except band 5 (Seibel 2005). This band 5 acid phosphatase is referred to as Tartrate-resistant acid phosphatase type (TRAP5). Of the two isoforms of TRAP5 (a and b), TRAP5b is the type commonly found in osteoclasts. TRAP5b is referred to simply as TRAP for the remainder of this thesis.

TRAP acts alongside enzymes such as Cathepsin K to break down bone mineral at the resorption surface. It also acts to deactivate osteopontin following resorption, causing the osteoclast to release from the bone surface (Mira-Pascual 2019). It is thought to be found in cell lysosomes, although evidence has suggested that TRAP is located in vesicles which bond to transcytotic vesicles responsible for removing waste bone material to the basolateral surface of the osteoclast (Hayman 2008). TRAP is found

abundantly in alveolar macrophages, dendritic cells and the ruffled border (bone resorbing side) of the osteoclast (Galvao *et al*. 2011). Figure 4.4 displays an active resorbing osteoclast:

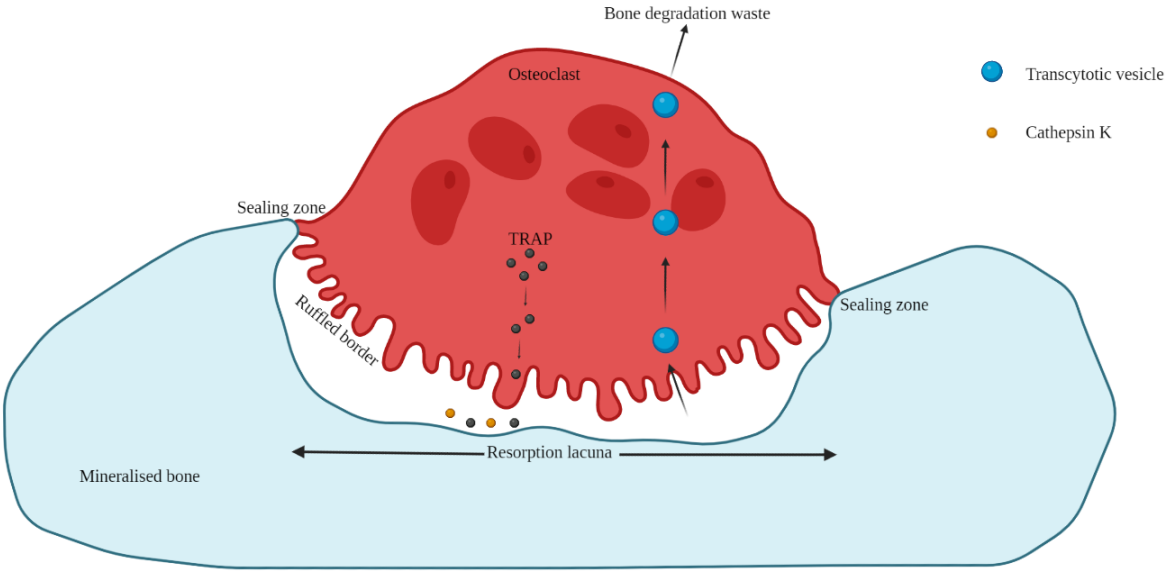

Figure 4. 4: Osteoclast structure and cell constituents.

TRAP staining was first utilised as a marker of osteoclast presence (Burstone 1959) and then confirmed to be a marker of osteoclast activity (Minkin 1982).

Figure 4.5 shows an example of a TRAP positive region in rat trabecular bone:

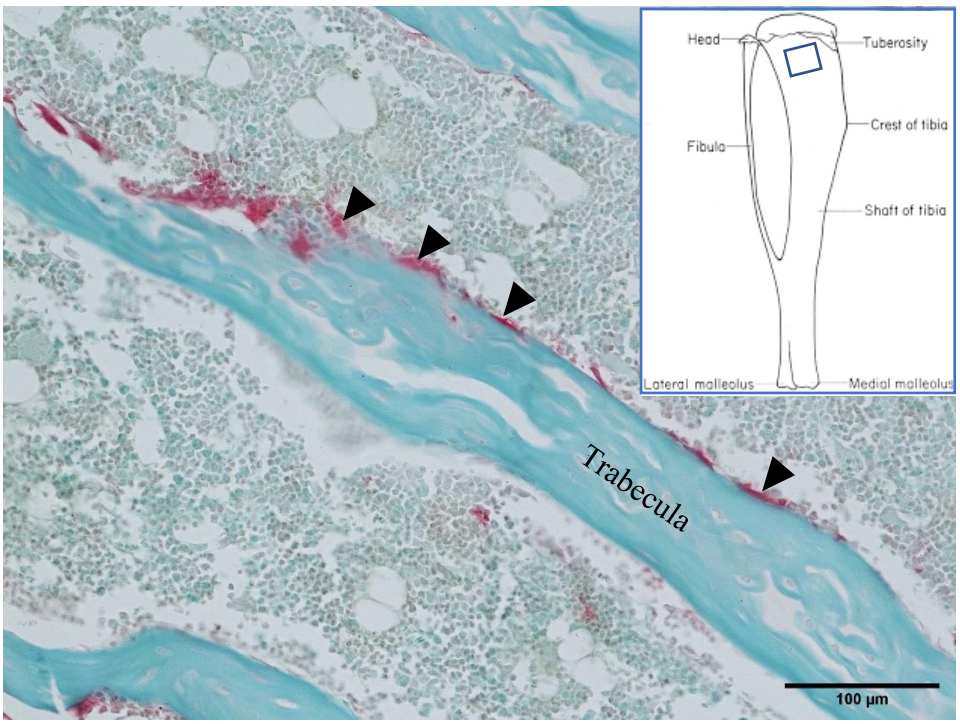

Figure 4. 5: TRAP staining in the metaphyseal marrow trabeculae of the rat proximal tibia. Arrowheads: osteoclastic surface. Counterstained with Fast Green FCF.

4.1.6 TRAP Staining in SCI-induced Osteoporosis

TRAP staining has been used in various different studies involving disuse. The current study (to the best of the author's knowledge) presents the first time TRAP has been used for quantitative histology in a model of complete SCI.

Severe osteopenia was induced in 5-month-old rats using a combination of orchidectomy and disuse via muscular application of botulinum toxin. TRAP staining was used to observe osteoclast numbers in the femoral secondary spongiosa increasing during acute disuse (1 month), and then decreasing towards control values in more chronic situations (2 and 3 months disuse) (Blouin *et al*. 2007).

TRAP staining of samples from 4-month-old F1 hybrid rats showed a positive correlation of osteoclast surface percentage (Oc.S/BS) increase with a decrease in trabecular bone volume (Tb.BV/TV) following 21 days of disuse by hindlimb suspension (Squire *et al*. 2008).

TRAP staining was used in an ovariectomised (estrogen deficient) rat model of disuse osteoporosis (dOP) to quantify recovery in bone resorption activity following

administration of the sex hormone estradiol. This was visualised as a reduction in the number of TRAP-positive cells in the estradiol treated sections following acute osteopenia at 14 days disuse (Sun *et al*. 2015). Similarly, TRAP staining was used in rats to investigate the benefits of testosterone treatment on osteoclast surface increase following orchidectomy (Laurent *et al*. 2016).

A novel calcium treatment for dOP was developed and used TRAP staining to assess its effectiveness over traditional calcium carbonate medications for disuse (Qu *et al*. 2019).

Finally, TRAP staining has also been used to investigate the involvement of αβ T cells in maintaining bone density following SCI (Sahbani *et al*. 2021).

In summary, TRAP staining is a commonly utilised osteoclastic stain for characterising various bone pathologies. It has been utilised for assessment of dOP, however to date has not been employed in a model of complete SCI, which incurs different effects than models such as BTX and hindlimb suspension due to the severing of the spinal cord. This results in additional complications such as cardiovascular, circulatory and hematologic problems which can all affect the remodelling state of the subject's bone (Guertin 2011). Therefore, the TRAP analysis in the current study is a novel assessment of the osteoclastic activity in sublesional long bones during complete SCI.

4.1.7 CD34

CD34 is the name given to the protein that is encoded by the CD34 gene in mammals. The CD34 antigen was first defined in 1984 (Civin *et al*. 1984) from haematopoietic progenitor cells, but it was not until 1992 that is was discovered to be expressed by small vessel (capillaries, arterioles and venules) endothelial cells (Simmons *et al*. 1992).

CD34 is a transmembrane phosphoglycoprotein. As a cell surface protein, its primary role in the endothelium is to enable cell to cell adhesion. Its most common ligand is the cell adhesion factor L-Selectin (Sidney *et al*. 2014).

Although cell adhesion is the primary function of CD34, it has also been suggested that CD34 effects haematopoetic stem cell recruitment to specific niches in the bone marrow of humans (Nielsen & McNagny 2009).

As haematopoetic progenitor cell expression of CD34 is much lower in mice and rats than in humans (Okuno *et al*. 2002), but endothelial expression is largely the same, CD34 is an effective blood vessel stain for use in murine studies of microvasculature. This is confirmed by multiple studies, for example:

- Analysis of glomeruli development in the mouse kidney, from embryonic to postnatal development (Zhang *et al*. 2018).
- Staining of the hepatic arteries and veins in diabetic Wistar rats (Tchokonte-Nana *et al*. 2017).

See Figure 4.6:

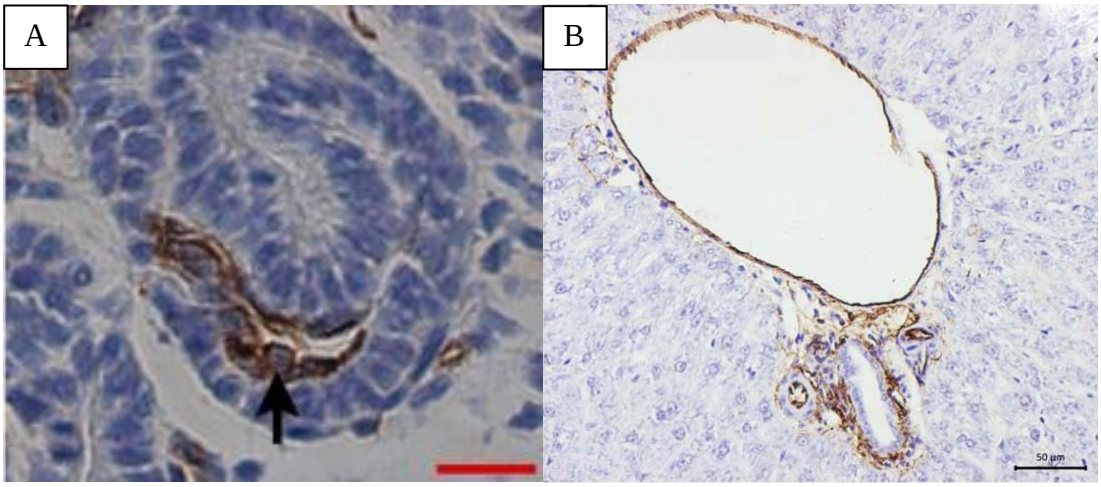

Figure 4. 6: A: CD34+ immunostaining of kidney glomerulus (black arrow) in 21-day-old Kunming mouse. Scale bar: 25µm. Reproduced from Zhang et al. 2018. B: CD34+ immunostaining of hepatic blood vessels in diabetic adult Wistar rat kidneys. Reproduced from Tchokonte-Nana et al. 2017.

In addition to the previously mentioned murine kidney and liver studies using CD34, the blood vessel marker has also been used in bone. CD34 immunostaining was used to show the recruitment of CD34 positive stromal cells to a surgically-created defect in the jaw bone of Wistar rats, as a marker of tissue regeneration following parathyroid hormone therapy (Wang, Du & Ge 2016).

CD34 staining was used in 2004 to identify human umbilical cord cells which were implanted into rat spinal cord areas of transection, in an attempt to promote functional motor recovery following spinal cord injury in adult Wistar rats (Zhao *et al*. 2004).

To summarize, CD34 has been used in numerous studies to highlight vasculature, stem cells and stromal cells in murine models. CD34 staining has been used to assess pathologies in almost every region of the mammalian body, including the spinal cord and in bone. To date, however, there are no studies using CD34 staining to identify microscale blood vessels in murine trabecular bone, nor has there been any characterization of any type of dOP via assessment of the vasculature using CD34. Therefore, CD34 represents a novel staining target for characterization of the blood network effects due to complete SCI.

4.2 Methodology – TRAP Staining and CD34 Immunohistochemistry

The protocols described herein were optimised by the author via iterative staining runs. See Appendix entry 5 for details.

4.2.1 Excision, Fixation and Decalcification

As previously described, bones were excised at the 11-week post-injury timepoint, from 10 week old male SD rats. Contralateral femur and tibia pairs were selected, and as much excess tissue (cartilage, skin, muscle etc.) was removed without damaging the bones.

Bones were immediately placed into 10% neutral buffered formalin (NBF) for 48 hours at 4^{o}C, in order for protein-cross links to form sufficiently.

Following fixation, the bones were washed in 10mM phosphate-buffered saline (PBS) for 30 minutes. Decalcification was then performed in 10% ethylenediaminetetraacetic acid (EDTA) pH 7.4 at 4^{o}C for 28 days. The EDTA solution was provisioned at 50ml per bone, in individual histology pots. Each pot was refreshed 3x weekly during the 28-day decalcification.

4.2.2 Dehydration and Paraffin Immersion

Once decalcified, bones were rinsed in 10mM PBS for 30 minutes before being cut in half using bone snips at the mid-diaphysis and placed into an auto-processor (Shandon Citadel 1000, Thermo Scientific, UK) for FFPE preparation. During this step, the bones were subjected to the following protocol.

First, samples were incubated in a graded ethanol (EtOH) series to dehydrate fully without causing any cell damage. After this, a clearing agent (Histoclear, Advanced Applications Institute, Charlotte, USA) was utilised to remove any ethanol from the bones, as ethanol is immiscible with paraffin. The final incubation was in molten paraffin wax to fully permeate the bone with the same material it would subsequently

be embedded in. A step-by-step summary of the concentrations and incubation times used is as follows:

1. 50% EtOH 1 hour
2. 70% EtOH 1 hour
3. 95% EtOH 1 hour
4. 100% EtOH 1 hour
5. 100% EtOH 1 hour
6. 100% EtOH 1 hour
7. Histoclear 1 hour
8. Histoclear 1 hour
9. Paraffin 3 hours
10. Paraffin 3 hours

Multiple changes of each solution were used in order to increase the effectiveness of dehydration, clearing and paraffin invasion. The volume of solution in each tank of the auto-processor was 1.2L.

4.2.3 Wax Embedding and Microtome Sectioning

Once the bones had been retrieved from the auto-processor, they were removed from their histology cassettes and embedded into paraffin wax blocks using a wax embedding machine (EG 1140H, Leica Biosystems, UK) and plastic block moulds.

The paraffin blocks were sectioned using hard-tissue microtome blades (MX35, VWR, UK) and cut to 7μm thickness on a rotary microtome (RM2125RTF, Leica Biosystems, UK). This selection of 7μm was made to give the thinnest possible slice thickness without compromising the structures (trabeculae, blood vessels) in each section. Sections were mounted onto poly-l-lysine (Sigma-Aldrich, Gillingham, UK) coated Superfrost glass slides (Thermo Fisher Scientific, Waltham, USA), and dried in an oven at 55^{o}C for 2 hours prior to clearing, rehydration and staining.

Alignment of the different bones in the wax moulds was selected to be as consistent and repeatable as possible, whilst still allowing for quality metaphyseal trabecular bone volumes to be imaged. This meant that each bone was placed either with the anterior or lateral side facing downwards, so the orientation of each slice would remain

as close as possible to perfect alignment with the sagittal or coronal plane. Before sections were taken, bones were sliced past the cortical bone and close to halfway through, so as to take the medullary portion of sections from each bone for consistency. Before taking sections from the region of interest, each cut face was immersed in ice water for 10 minutes.

The sectioning plane for the proximal tibiae was sagittal. As a result, the posterior and anterior metaphyseal trabeculae are present in each section, as displayed in Figure 4.7:

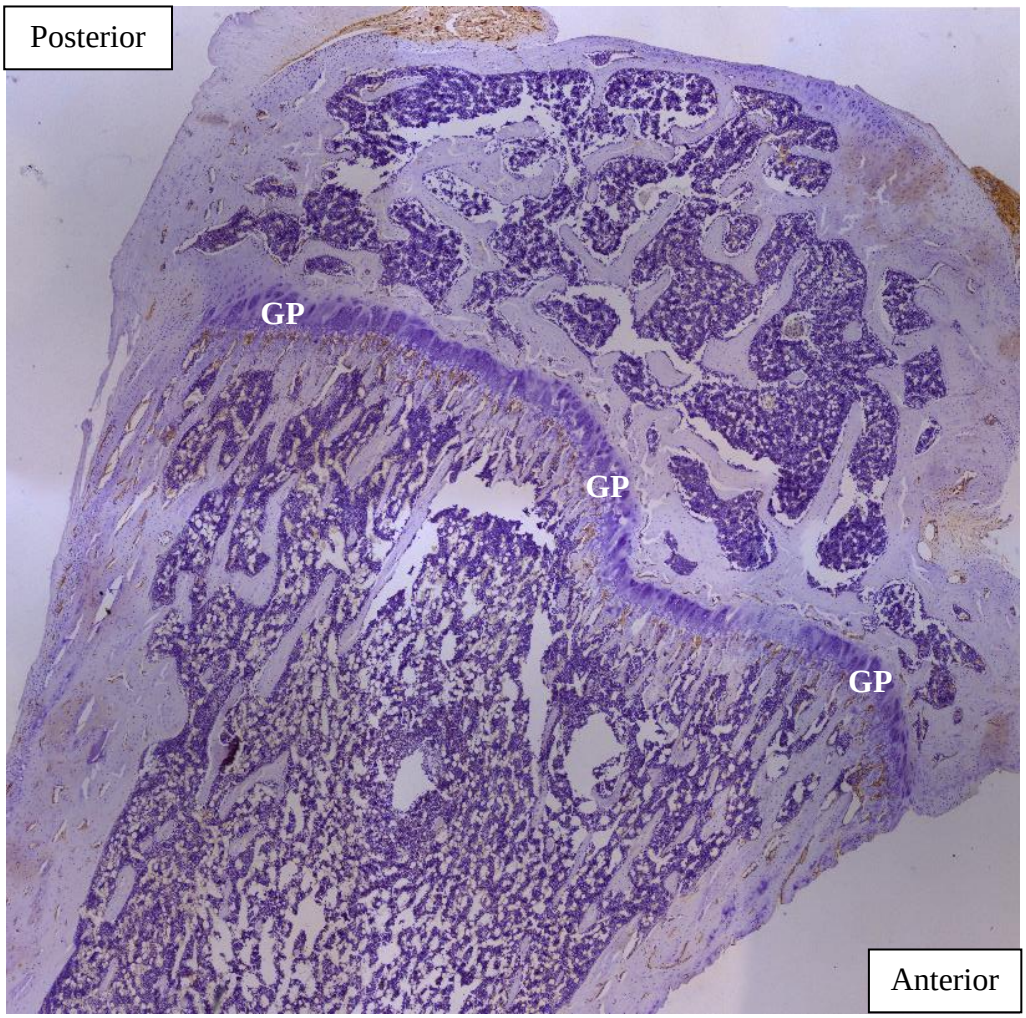

Figure 4. 7: Example proximal tibia sagittal section. Stained using HRP-streptavidin / DAB detection for anti-CD34 primaries. Counterstained with Mayer's haematoxylin. GP: growth plate.

The above image is a composite, created by stitching together 6 images of x40 magnification in ImageJ. In brief, multiple images were manually aligned under the

microscope and then captured in a defined pattern before being uploaded into the software for use with the stitching tool. See Appendix entry 7 for details.

The sectioning plane for the distal femora was coronal, meaning that lateral and medial trabeculae were included in each section. This is shown in Figure 4.8:

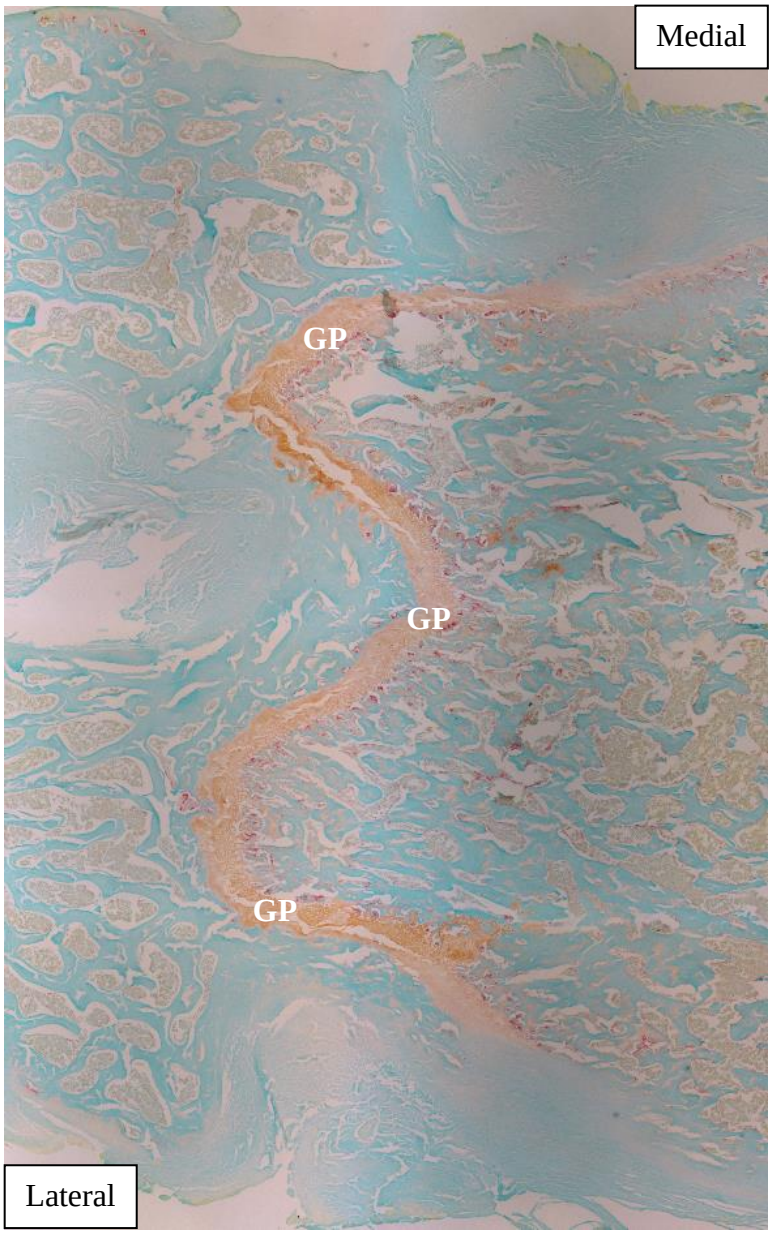

Figure 4. 8: Example distal femur coronal section stained for osteoclastic activity using TRAP, counterstained with Fast Green FCF. GP: growth plate.

4.2.4 Staining: TRAP

The exact staining protocol for TRAP can be found in Appendix entry 3.

TRAP staining is performed by incubating bone tissue with naphthol-AS-BI-phosphate, allowing the endogenous TRAP enzymes to hydrolyse the substrate and produce naphthol++. In the next incubation, an unstable brown dye (pararosaniline mixed with sodium nitrite) attaches to the napthol++ to create a stable, pinkish red staining at the site of TRAP activity (Lamp & Drexler 2000).

To begin, slides were dried in an oven at 55^{o}C for two hours and then cleared in Histoclear, before rehydration through a graded alcohol series to water.

Basic incubation medium (BIM) was produced to the following concentrations: 250ml dH20 + 0.7ml glacial acetic acid + 2.9g L-(+) tartaric acid + 2.3g anhydrous sodium acetate.

Pararosaniline dye was produced as follows: 1g pararosaniline chloride + 20ml 2N hydrochloric acid.

Aqueous sodium nitrite was also produced: 1g sodium nitrite + 25ml dH20.

Finally, the naphthol solution was created: 100mg naphthol AS-BI phosphate + 5ml 2-ethoxyethanol.

The first staining incubation was at 37^{o}C for 30 minutes in a solution of 250ml BIM and 2.5ml naphthol solution, followed by the colour reaction incubation for 8 minutes at room temperature in a solution of 250ml BIM, 5ml pararosaniline dye and 5ml sodium nitrite. The TRAP staining protocol used was supplied and adapted from Dr Brendan Boyce at the University of Rochester Medical Center, Rochester, New York, USA. As TRAP staining produces a vibrant red/pink colour, 0.08% Fast Green FCF (Sigma-Aldrich, Gillingham, UK) was selected as an effective counterstain for good contrast when quantifying the obtained images.

4.2.5 Staining: CD34

The exact staining protocol for CD34 can be found in Appendix entry 4.

Similar to the preparation for TRAP staining, slides were first dried at room temperature for five hours, before one hour in an oven at 55^{o}C. Clearing was performed in xylene instead of Histoclear for CD34 IHC, as it was found experimentally to produce a 'cleaner' stain with less nonspecific staining. Rehydration to was performed through the same graded alcohol series as that used for TRAP staining.

Prior to incubation with the rabbit anti-CD34 primary antibodies, antigen retrieval was performed at 60^{o}C overnight in citrate buffer pH6, in order to undo some formalin-induced protein crosslinks and unmask the epitopes on the trabecular blood vessel endothelial cells (ECs).

Once antigen retrieval had been performed, the endogenous peroxidase enzymes were blocked using a hydrogen peroxide solution in water.

This was followed by blocking of the undesired antigens in each section through incubation with a protein block containing casein and bovine serum albumin in a saline solution.

Once the undesired endogenous peroxidases and antigens had been blocked, the primary antibodies were bound to the ECs. This particular protocol used the streptavidin-biotin complex (ABC) method to amplify the staining intensity. Primary antibodies were allowed to bind to the protein of interest in an overnight incubation at 4^{o}C, before a second peroxidase block was performed to minimise nonspecific staining.

Following this, the sections were incubated with biotinylated secondary antibodies, and then with streptavidin-conjugated HRP enzymes.

With the ABC complex now in place, the DAB was added, and a brown colour allowed to develop for eight minutes. This DAB reaction time was optimised experimentally.

With the primary staining now produced, the counterstain was added. The selected counterstain for all CD34 runs was Mayer's haematoxylin which produced a purplish-blue colour on the all nuclei CD34 negative cell cytoplasm.

A bluing reagent (ammonia solution in distilled water) was added to the sections in order to change the counterstain from a reddish-brown to a purplish-blue, followed by dehydration back through the graded alcohol series and clearing in Histoclear.

In between every incubation in the above protocol, multiple 350ml rinses were performed in phosphate-buffered saline (PBS).

Once stained, dehydrated and cleared, all slides were mounted using DPX and glass coverslips and allowed to set overnight before images were obtained.

4.2.6 Controls

In order to validate the anti-CD34 antibodies and TRAP reagents, three different controls were used: isotype, no primary and positive tissue. Figure 4.9 contains an example of a stained section from the study for purposes of comparisons with the controls shown in the subsequent figures:

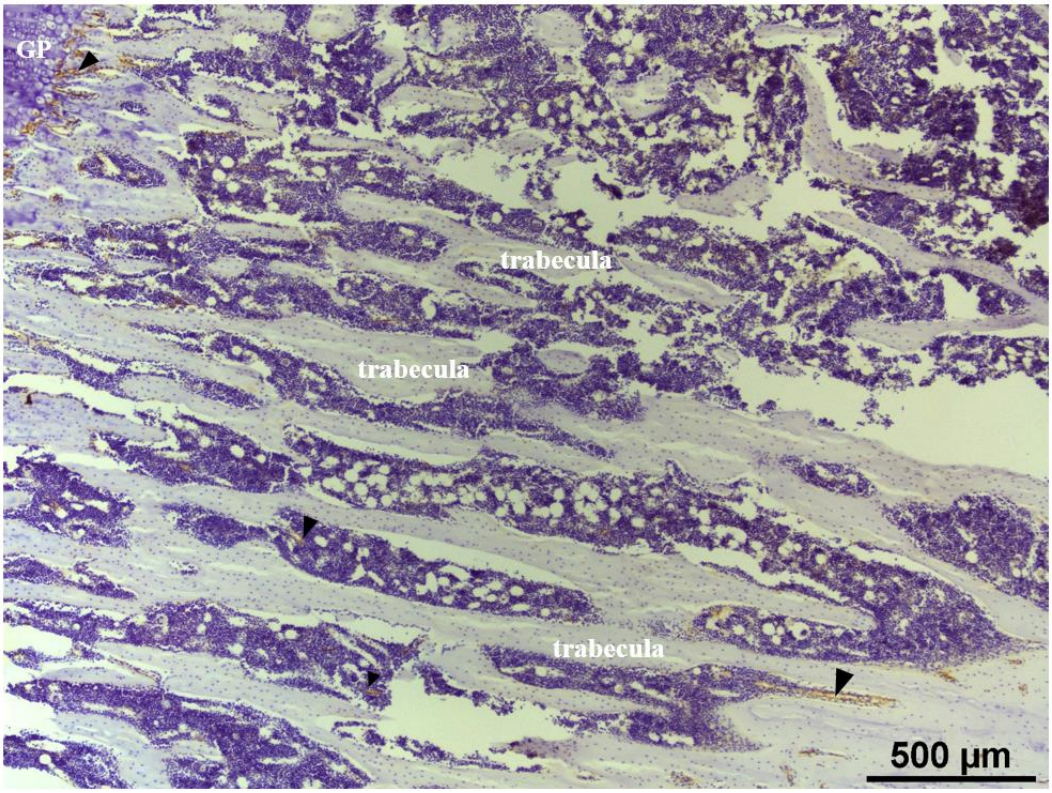

Figure 4. 9: Proximal tibia spongiosa. Stained for CD34 using HRP/DAB detection with Mayer's haematoxylin counterstain. GP: growth plate. Note the lack of positive staining on the trabeculae and the specific, strong staining on the blood vessels between them, as well as the significant staining around the developing chondrocytes from the growth plate. (arrowheads).

The isotype control for the chosen anti-CD34 antibody was purified rabbit serum polyclonal IgG (2BScientific, Upper Heyford, UK). It was incubated with the regular CD34 antibody solution in the same buffer at the same concentration (1% bovine serum albumin in 50mM PBS) as used in regular anti-CD34 staining. Figure 4.10 displays the results of the isotype control:

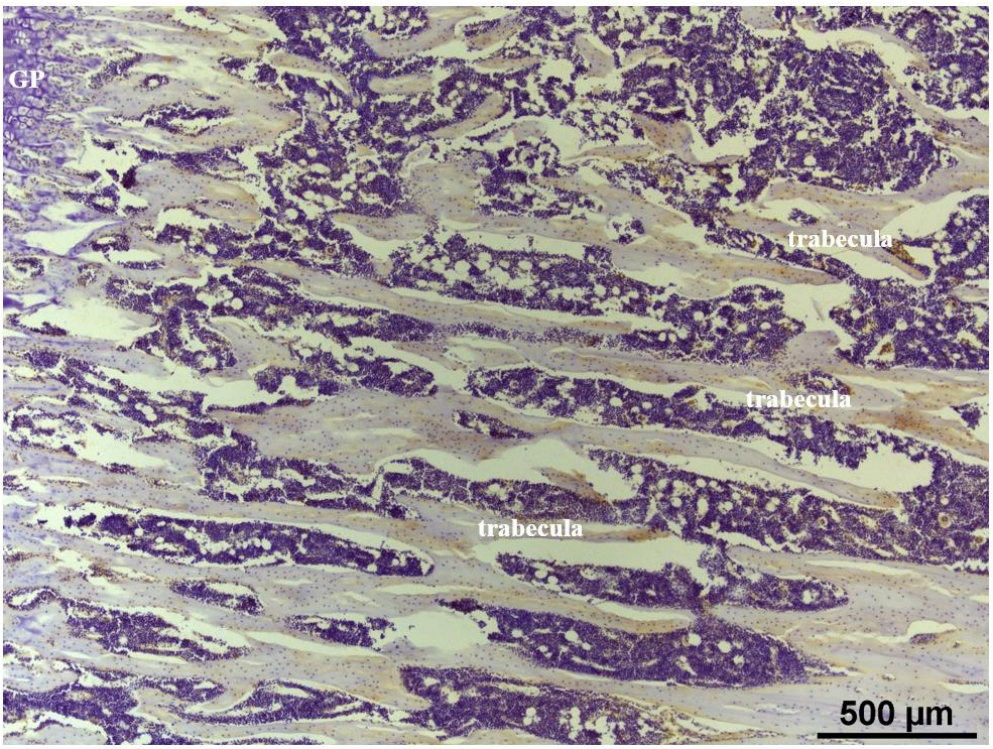

Figure 4. 10: Isotype control. Stained with rabbit serum IgG using HRP/DAB detection with Mayer's haematoxylin counterstain. GP: growth plate. Note the unspecific, weak staining especially in the bodies of the trabeculae. Also note the lack of positive staining in the chondrocytes proliferating from the growth plate.

The combination of weak, unspecific staining with the lack of any noticeable positive region in the growth plate chondrocytes validated the efficacy of the anti-CD34 monoclonal antibodies in their use for blood vessel IHC in trabecular bone. When comparing the images in Figures 4.9 and 4.10, it is clear to see that the specificity and intensity of the staining in the trabecular blood vessels was due to the use of the anti-CD34 antibodies chosen for this study.

Further validation was obtained via a 'no primary' control. This control was performed using only the antibody diluent, specifically 1% normal goat serum (v/v) in 50mM

PBS, in place of the primary antibody solution. The diluent did not contain any quantity of antibodies. Figure 4.11 displays the result of the ‘no primary’ control:

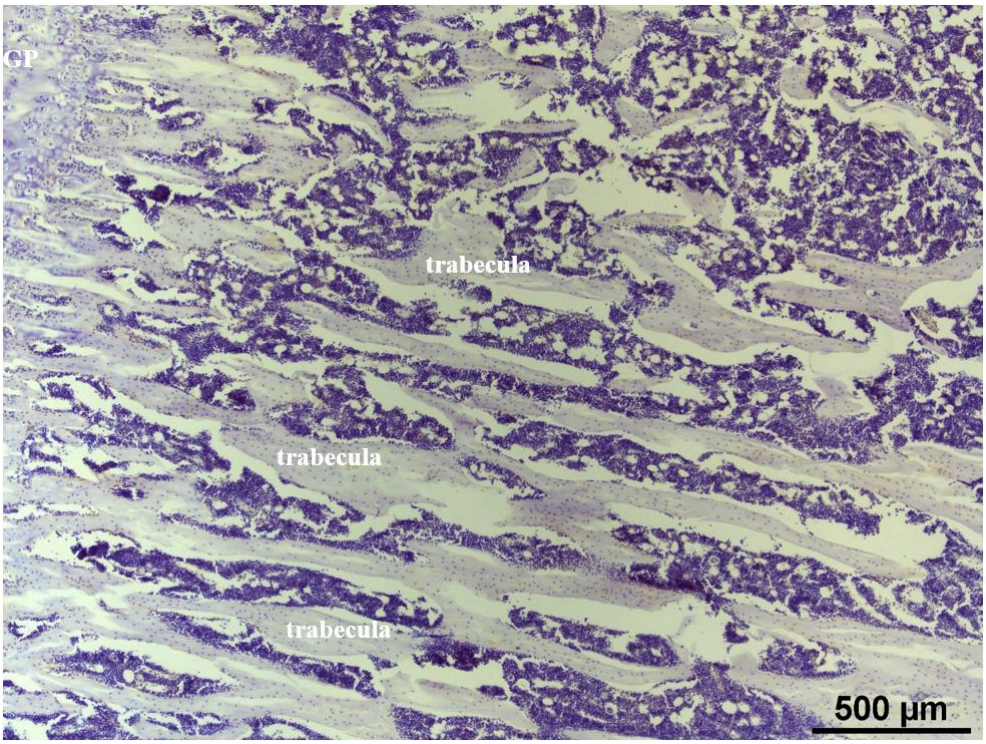

Figure 4. 11: ‘No primary’ control. Stained without primary antibodies using HRP/DAB detection with Mayer’s haematoxylin counterstain. GP: growth plate. Note the lack of any brown CD34 positive regions anywhere in the section.

The ‘no primary’ control predictably yielded a section without any discernible staining at all, proving that the brown-stained blood vessels in the regular sections were indeed due to the introduction of the anti-CD34 antibodies. Without primary antibody binding and subsequent HRP-conjugated secondary antibody binding and catalysation, no significant oxidation of the DAB could occur and hence no noticeable staining would be produced.

The positive control tissue for CD34 staining was supplied from a different study on rat lung, provided by Margaret Nilsen (University of Glasgow, UK). The rats in question were ~300g male Wistar rats, raised in normoxic conditions, as they were controls for Sugen5416-hypoxic rats. The endothelium of the bronchioles and alveoli in these samples presented a rich source of positive staining for antibody validation. Figure 4.12 displays the strong endothelial staining of the lung tissue by the anti-CD34 antibody:

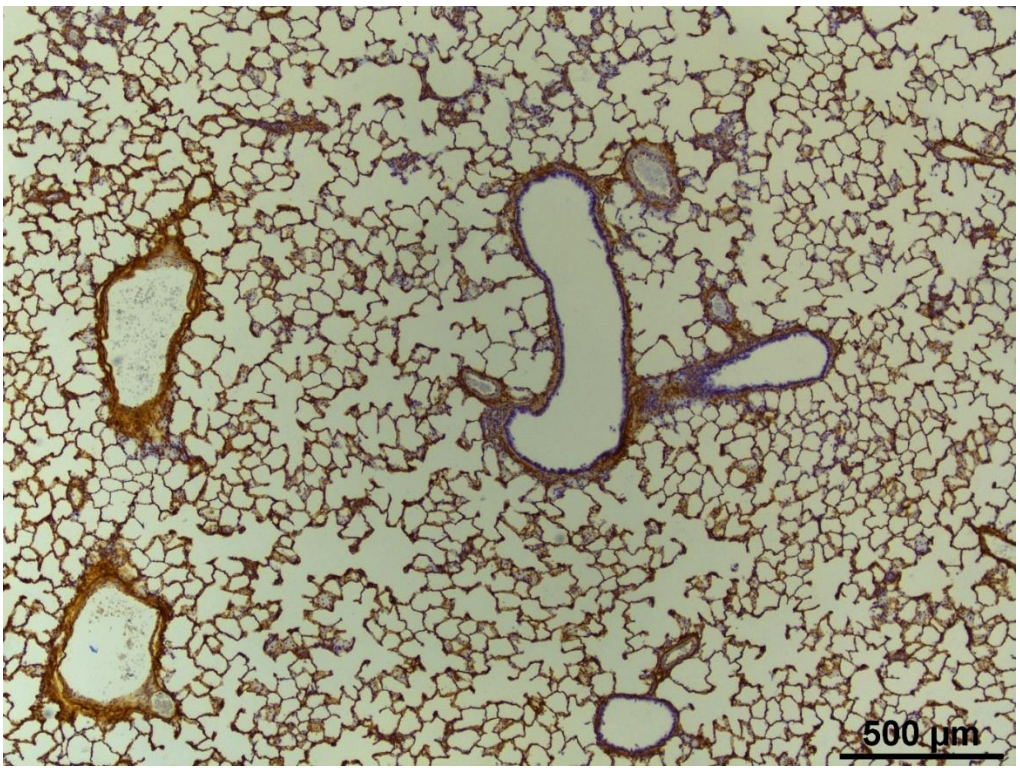

Figure 4. 12: Positive tissue control section of rat lung. Stained for CD34 using HRP/DAB detection with Mayer's haematoxylin counterstain. Note the widespread positive endothelial staining of the alveoli.

The final control for this study was a positive tissue control for the TRAP staining of trabecular bone. The sections for this were taken from the bones of the control rats, at the proximal femur femoral head. This region is known to undergo endochondral ossification as late as 30 months into the lifetime of rats (Dawson 1925) and is therefore a suitable choice for a region which is rich in osteoclasts and bone remodelling activity. Figure 4.13 contains the femoral head positive tissue control for osteoclastic staining with TRAP:

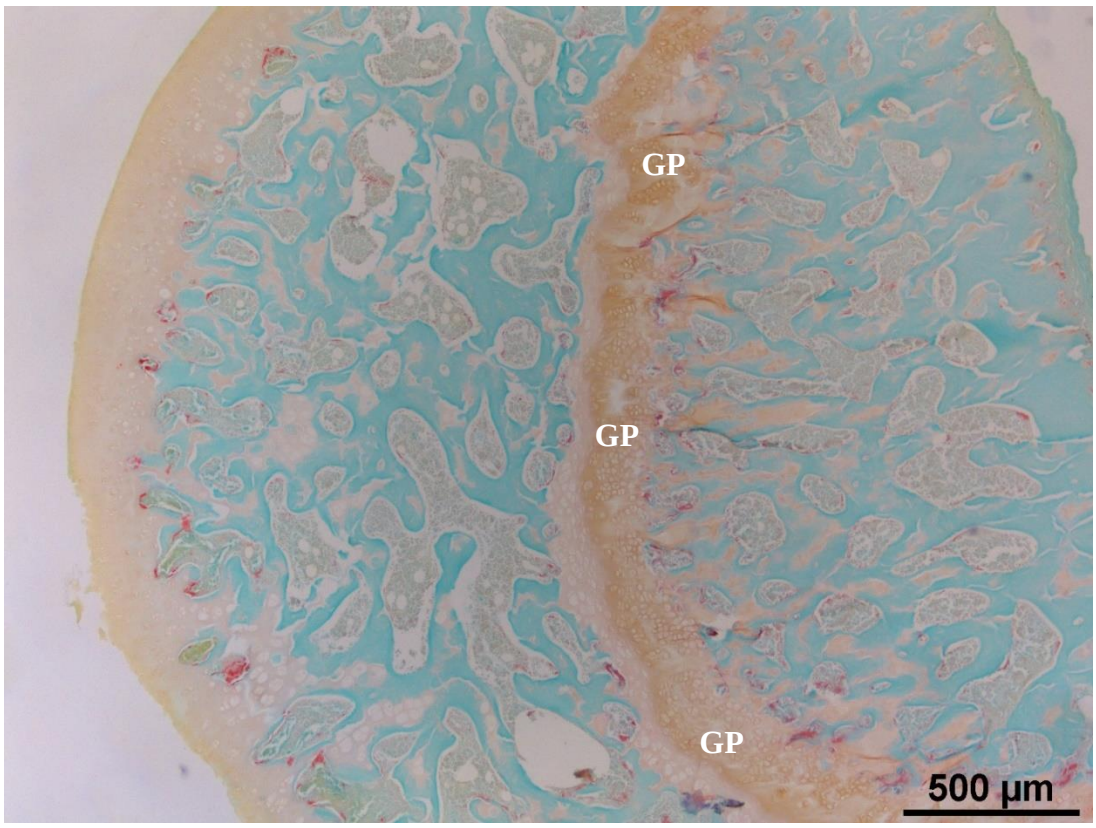

Figure 4. 13: TRAP positive tissue control on SD rat femoral head. Stained for TRAP with Fast Green FCF (turquoise) counterstain. GP: growth plate. Note the positive (purple/red) staining around the developing bone near the GP.

Significant staining of osteoclastic activity around the growth plate was observed in the TRAP positive tissue control. The newly forming chondrocyte scaffolds for endochondral ossification require extensive bone modelling activity in order for mineralisation to occur, and so are an excellent place to check for osteoclasts when confirming the efficacy of a TRAP staining protocol.

4.2.7 Region of Interest Selection

The ROI selection method for quantification of both the proximal tibia and distal femur osteoclasts and blood vessels was very similar. The key structure was the mature (secondary) spongiosa below the growth plate. The secondary spongiosa analysed was in the posterior metaphysis for the proximal tibia, and on the lateral condyle for the distal femur. As the primary spongiosa in any section are still undergoing the initial mineralisation stage of endochondral ossification, any osteoclastic activity observed on their surface is a confounding factor for studies of osteoporosis and bone

remodelling. This reasoning is confirmed by Jee and Yao (2001) in the literature. The aim of this study was to examine the changes to bone and its related cells during SCI-induced osteoporosis, not during bone growth. The immature primary spongiosa observed still containing their unmineralised collagen core were therefore excluded from the ROI for analysis. Figure 4.14 illustrates this ROI selection:

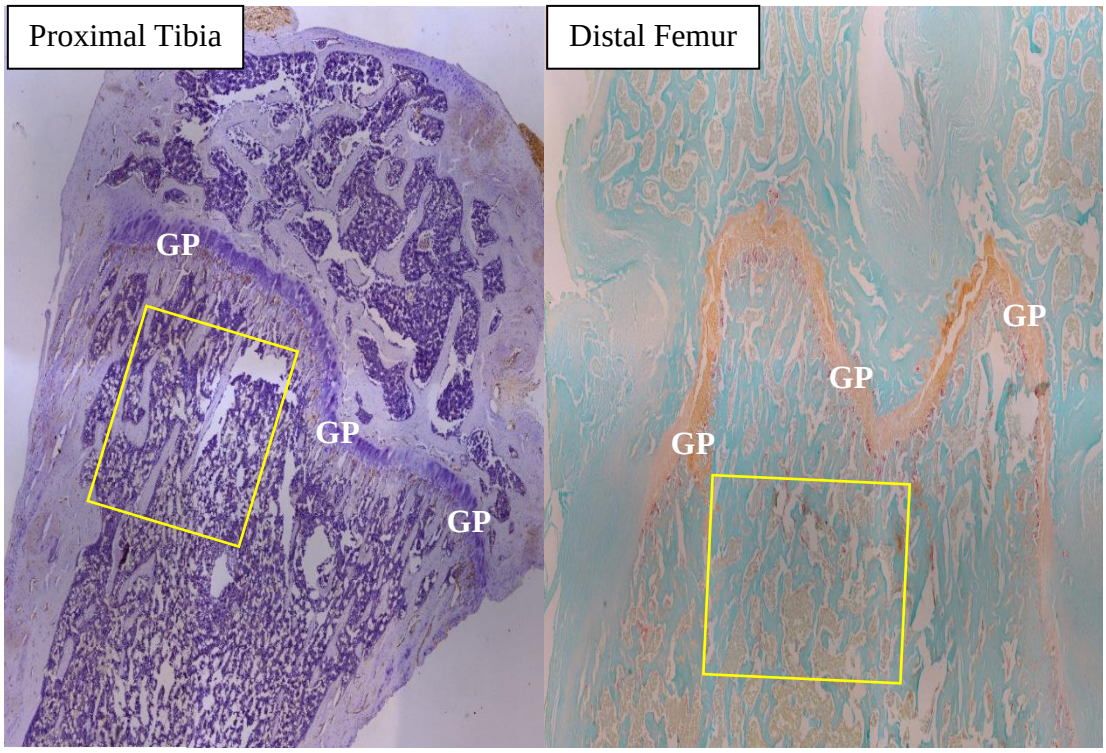

Figure 4. 14: TRAP and CD34 analysis example ROIs. Yellow boxes: Trabecular ROIs.

4.2.8 Quantifying Histological Images

Once stained, histological images are often quantified using a variety of different software and counting methods. The software and methods selected for this study are detailed below.

The quantifying software used for the TRAP staining is the product of an open-source project from the University of Liverpool titled TrapHisto (Van't Hof *et al*. 2017).

The method used to quantify the microvessel density (Mv.D) in trabecular bone was devised by the author using ImageJ software and the plugin BoneJ2 (Doube *et al*. 2010).

4.2.9 Quantification: TRAP

The following is an outline of a typical TrapHisto workflow for analysing osteoclastic parameters in rat trabecular bone.

First, square-shaped digital images were captured at 40x magnification using a compound light microscope (Eclipse 50i, Nikon, Japan) attached to a digital camera (DS-U3, Nikon, Japan) and software (NIS Elements, Nikon, Japan).

The image captures from the microscope were calibrated using a graticule at 1.19μm/px (0.84px/μm). This value was input into TrapHisto prior to region of interest selection.

The region of interest (ROI) was selected within each x40 magnification capture of the proximal tibiae and distal femora using the supplied tool in TrapHisto. For the distal femora, the lateral and medullary regions of the metaphysis were captured in the coronal plane. For the proximal tibiae, the ROI was selected within the posterior and medullary regions of the metaphyseal secondary spongiosa in the sagittal plane.

Figure 4.15 illustrates the method with a description of each stage. The example workflow overleaf uses the distal femur coronal section, with the bounds of each image being the bounds of the x40 magnification capture from the digital camera.

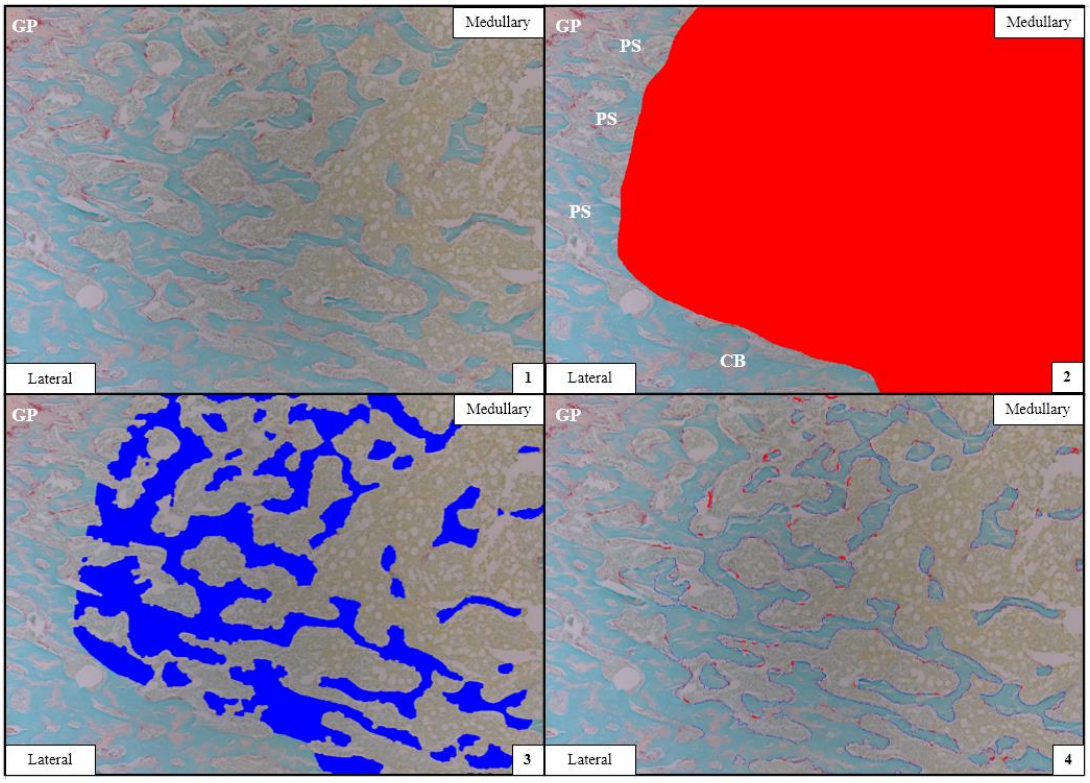

Figure 4. 15: Analysis using TrapHisto software. GP: growth plate. PS: primary spongiosa. CB: cortical bone. 1: Example ROI selection for trabecular osteoclasts. 2: Red region: ROI manually selected to exclude primary spongiosa (with noticeable unmineralised collagen cores) and cortical bone from analysis. 3: Blue region: resulting trabeculae highlighted for analysis using user-defined HSB thresholding and fine tuning parameters for cracks / edges / holes. 4: Blue surface: trabecular perimeter calculated from thresholding in previous step. Red dots: osteoclasts defined via a combination of HSB thresholding and limiting parameters.

1) In the first step, an image was loaded into the TrapHisto software ready for ROI segmentation.

2) The next step was to select a suitable trabecular ROI. The ROI selection was performed by manually drawing on the desired trabecular bone area using a freehand or polygon tool in the software. In the case of this project, care was taken to ensure that no primary spongiosa (those close to the growth plate with a visible unmineralised collagen core) were included in the ROI, and that the ROI was drawn as close to the cortical boundary (endosteal surface of the metaphysis) as possible without including any cortical bone.

3) Once the ROI was satisfactory, the thresholding of the trabeculae was performed via a 3-way threshold, using a hue-saturation-brightness (HSB) colour model with

ranges of 0-360 for each input. Trabeculae were observed to be stained turquoise by the Fast Green FCF counterstain. Therefore, only hues of turquoise / light blue were selected by setting the H-value to 360-160. Some hues of this range were still being included in a comparatively weak manner by undesirable portions of the image (mainly intraosseous bone marrow cells), and so the S-value for saturation was set to 360-50 to eliminate these 'weak-turquoise' regions. The B-value for brightness was left unchanged at 360-0. Once the HSB threshold had been applied, the trabeculae were still not sufficiently represented in the software. There remained some small particles which were not trabeculae, and in the trabeculae themselves there were some small gaps and cracks. The software accounts for this, however, and the 'remove small particles', 'close cracks' and 'fill small holes' tools were all utilised at values of 9, 8 and 34 respectively.

4) With the trabecular volume now defined in the software, standard histomorphometric measurements like total volume (volume of the ROI in mm^2), bone volume (volume of all combined trabeculae in the ROI in mm^2) and trabecular surface (combined perimeter of all trabeculae in mm) were automatically calculated in TrapHisto. The final step was to utilise another HSB threshold, this time for the osteoclasts in the image. In order to specify the vivid reddish-pink of the TRAP-positive osteoclastic regions in the ROI, a H-value of 360-291, S-value of 360-48 and B-value of 360-0 was input. This left for a nicely thresholded image, again with a few remaining issues. Many of the positive regions remaining were nowhere reasonably close to the trabecular surface. As defined in the literature, osteoclasts develop and adhere to the bone matrix (Boyle, Simonet and Lacey 2003). Consequently, the 'max. distance from bone' tool was used at a value of 3 to remove any floating positive regions in the bone marrow. This tool is enabled by the software's automatic definition of the trabecular surface being the perimeter of the trabecular volumes defined in step 2. The final fine-tuning tool utilised was the 'merge-fragments' tool, at a value of 3. This ensured that only osteoclasts of reasonable size were included in the analysis.

4.2.10 Quantification: CD34

As with TRAP quantification, digital images were captured at 40x magnification using a compound light microscope attached to the same digital camera. They were then loaded into ImageJ software.

The calibration of the captured images was input into ImageJ using 'Analyse>Set Scale' at 1.19µm/px.

The workflow for quantifying microvessel density (Mv.D) in the CD34 sections is detailed in the following pages.

As with TRAP, the distal femora was captured at the lateral / medullary region in the coronal plane. The proximal tibia was imaged at the posterior / medullary region in the sagittal plane.

The region of interest (ROI) was defined in ImageJ using the polygon selection tool. See Figure 4.16:

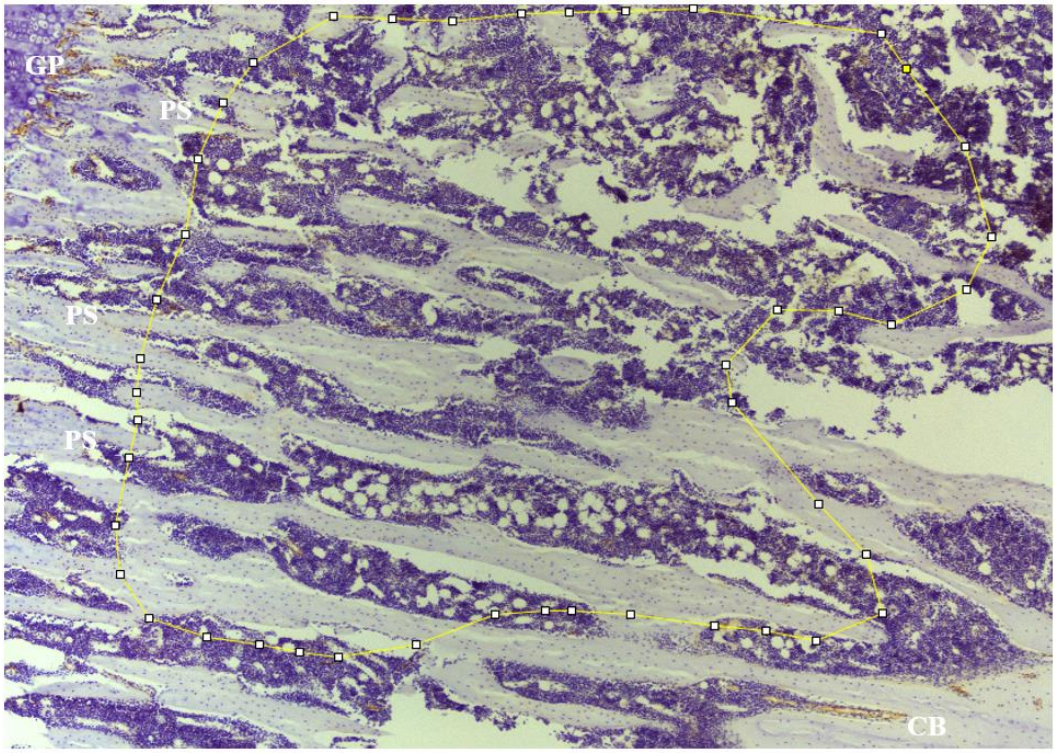

Figure 4. 16: ROI selection for CD34 trabecular microvessel density analysis using ImageJ software. Yellow polygon: ROI. ROI selected to exclude undesirable primary spongiosa (PS) around the growth plate (GP), as well as cortical bone (CB) in the image.

Following the definition of the ROI bounds and the calibration of the pixel size in μm, 'Analyse>Measure' was used to return the area of the ROI in μm^2.

With the ROI area now recorded, the number of microvessels in that area AKA the microvessel density (Mv.D in $1/\mu m^2$) could be assessed through counting the number of microvessels in the ROI. In order to perform this count, the surrounding bone constituents were removed from the image by the following method.

First, the part of each image outside the ROI was removed by using 'Edit>Clear Outside'. This ensured that any brown vessels identified in the following stages were those inside the ROI.

The ImageJ plugin 'IHC Toolbox' was then utilised in order to perform a colour threshold of the blood vessels which had been stained brown by the CD34 IHC staining. IHC Toolbox is a useful plugin which allows users of DAB IHC to train ImageJ to recognise a certain saturation range for the brown hue (which DAB oxidisation produces) in HSB colour space, and then remove all parts of the image which do not lie in this hue or saturation range. For training, rectangular areas were defined in the ROI using the rectangle tool in ImageJ. Three rectangles for each image were placed above suitable blood vessels in the sample. Figure 4.17 displays an example:

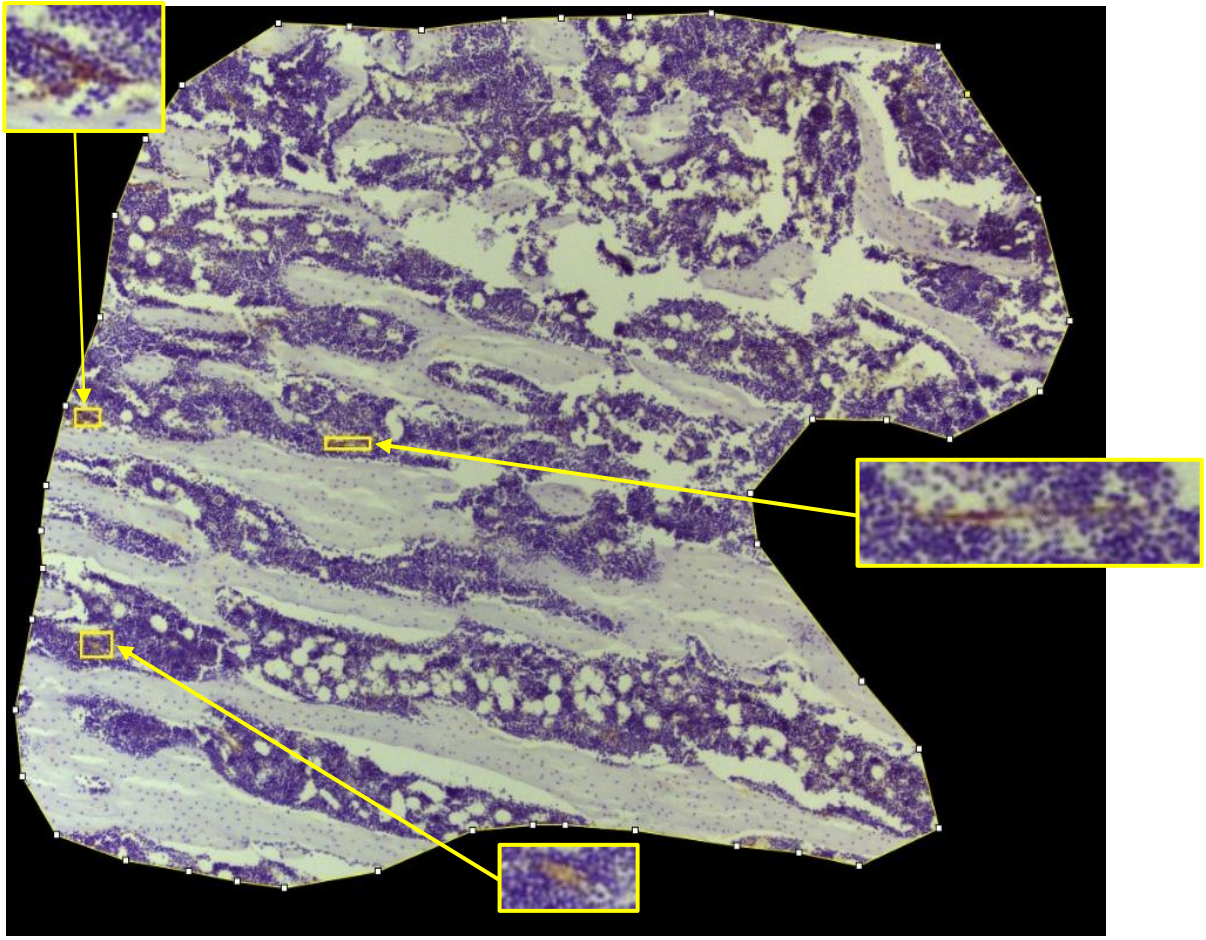

Figure 4. 17: Colour threshold training in ImageJ plugin 'IHC Toolbox'. Yellow rectangles: regions of brown CD34 positive staining (microvessels). Region outside ROI removed via 'clear outside' function.

With the brown regions now selected and the plugin trained, a colour threshold was performed, resulting in the blood vessels being segmented out from the background staining. The final step was to count the number of microvessels.

A median filter (4x4 square) was utilised in order to remove the smallest BVs and noise from the ROI. Anything larger than 16px (22.65μm^2) was deemed a valid blood vessel for this method.

Finally, a binary (black and white) threshold was performed on the ROI to prepare it for the ImageJ tool 'Analyse Particles'.

As the pre-processing had in theory removed anything from the image that was not a valid blood vessel, no limitations were set in the Analyse Particles parameters. The resulting number of particles was deemed the number of microvessels in the ROI. This

number was then normalised against the pre-recorded ROI area to give the final Mv.D measurement. Figure 4.18 displays example outlines recognised by Analyse Particles:

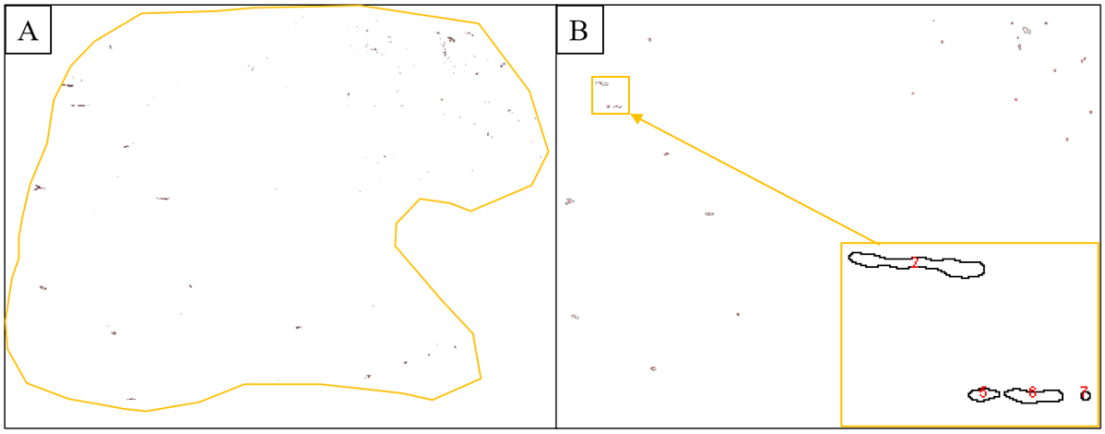

Figure 4. 18: Microvessel Density quantification in ImageJ. A: Colour thresholding segmenting out the CD34 positive microvessels from the bone constituents by their brown staining product. B: Result of ImageJ 'analyze particles' tool. Outlines created to define each trabecular microvessel. Magnified insert showing numbered particles during counting.

4.3 Results - Histology Chronic SCI

One of the samples from the PT bones was damaged during processing, and so was removed from the results. As n=2 for the PT groups, no statistical tests were performed on their data.

4.3.1 TRAP Staining

To analyse the remodelling state in sublesional trabecular bone after chronic SCI, Figure 4.19 displays the effects on osteoclast number and osteoclast surface percentage at 11 weeks post-injury:

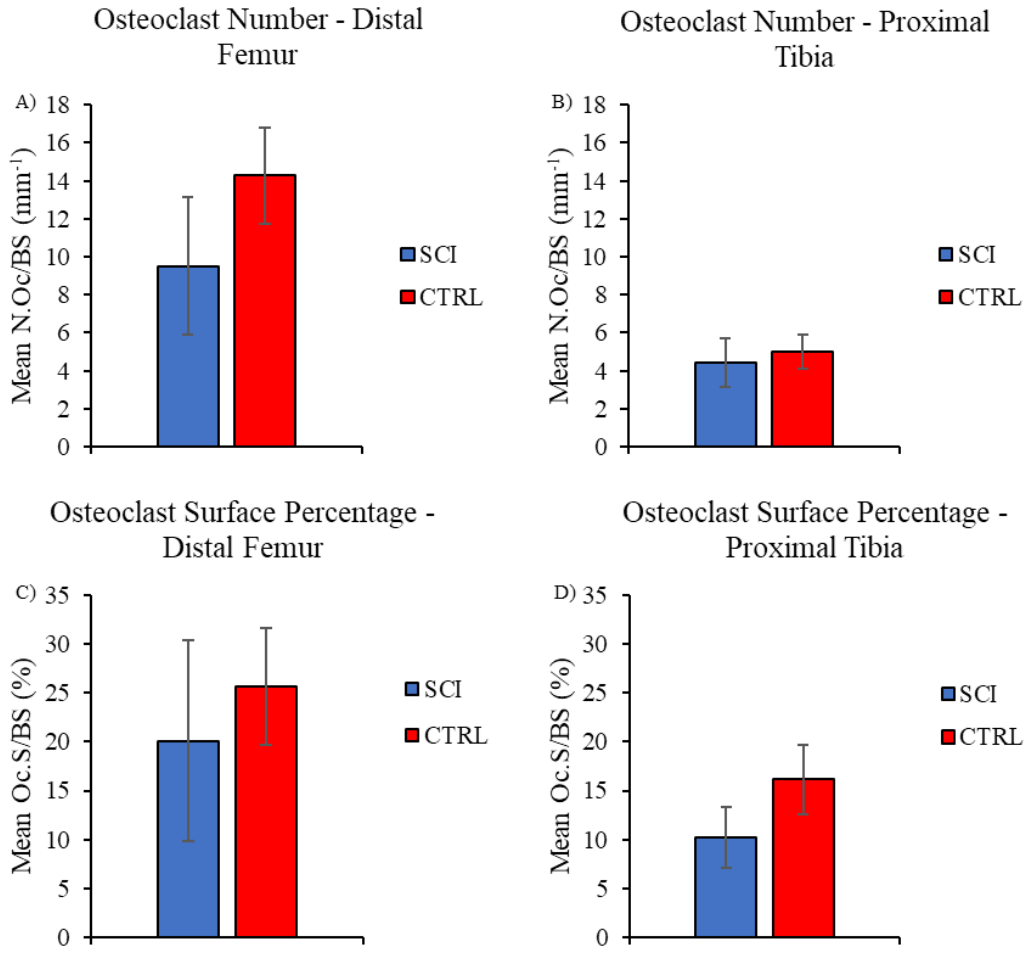

Figure 4. 19: A&B: Number of osteoclasts normalised to bone surface. C&D: Percent of trabecular surface covered by osteoclasts, as determined by TRAP staining. SCI: Spinal cord injured. CTRL: Control. Data presented as mean ±1SD.

Using a student's t-test for equal variance and normally distributed groups, the TRAP staining results returned no significant differences in the DF for either osteoclast number or surface percentage (Figures 4.19A and 4.19C). As one of the 3 samples in the PT group was damaged during processing, no statistical tests were performed on the PT (Figures 4.19B and 4.19D). The group means for both bone regions in both osteoclast parameters were observed to reduce following 11 weeks of SCI. Additionally, the DF exhibited a higher mean N.Oc/BS in both CTRL and SCI groups.

4.3.2 CD34 Immunostaining

Figure 4.20 contains the results of the trabecular and cortical blood vessel analysis:

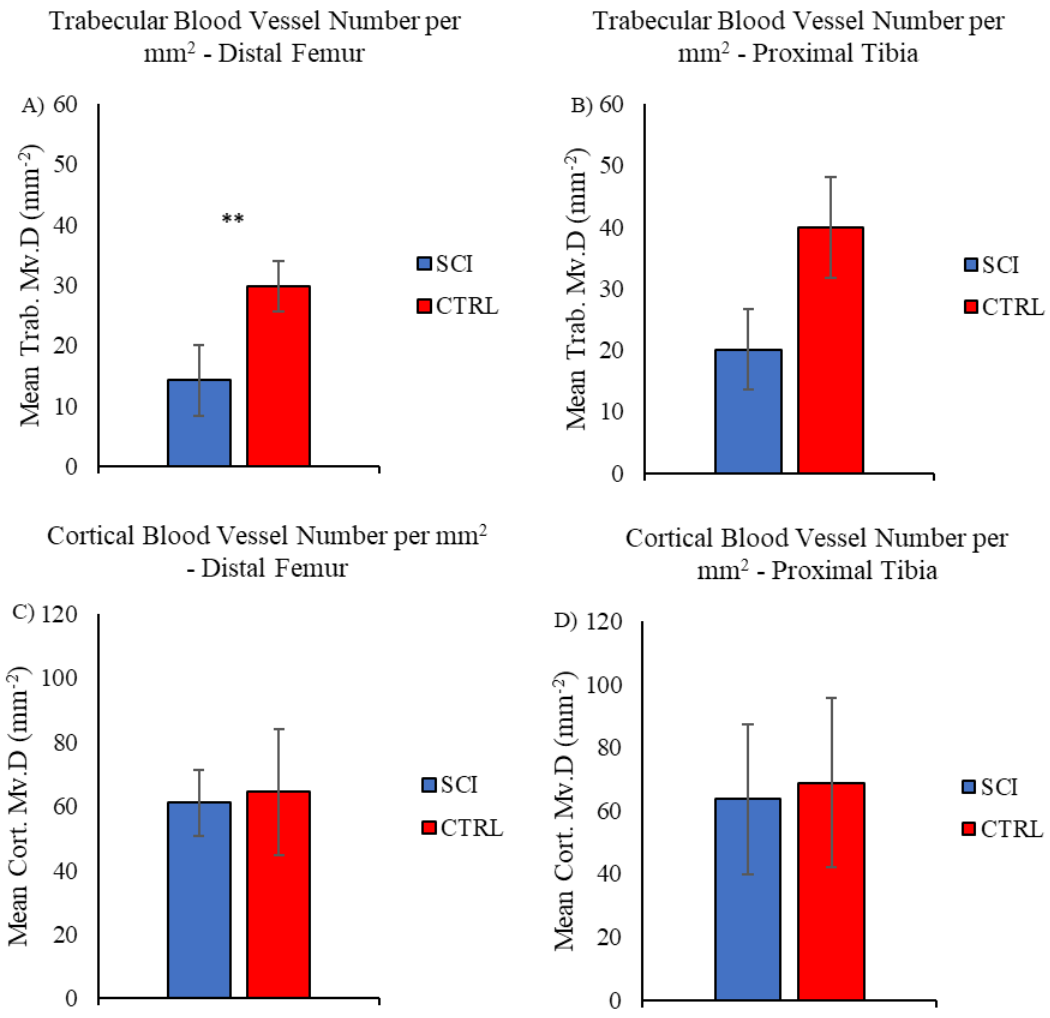

*Figure 4. 20: Bone microvessel density results via CD34 staining. SCI: Spinal cord injured. CTRL: Control. Data presented as mean ±1SD. ** indicates significant difference between SCI and CTRL at p<0.01.*

In the DF, a significant change in trabecular microvessel density was observed, with Mv.D decreasing by 52.1% following chronic SCI (p=0.00168) (Figure 4.20A). The DF cortical bone exhibited no such significant difference (Figure 4.20C). The n=2 sample size in the PT group rendered statistical tests invalid (Figures 4.20B and 4.20D), however the PT trabecular Mv.D exhibited a nonsignificant mean reduction of 49.5% following chronic SCI.

Chapter 5: Discussion, Future Work & Conclusions

5.1 Discussion

This study characterised the effects of complete SCI at the acute and chronic stages on the bone quality, distribution, resorption activity and blood supply in rat sublesional (below the site of injury) long bones, namely the distal femur (DF) and proximal tibia (PT) regions. For microarchitectural insights, microCT was employed to obtain both the standardised set of results (Bouxsein *et al*. 2010) and more novel outcome parameters ellipsoid factor (EF) and inter-trabecular angle (ITA) (Doube *et al*. 2015, Reznikov *et al*. 2016). Through histology, the bone resorption effects were analysed using a standard TRAP staining protocol (van't Hof *et al*. 2017), as well as a CD34 quantification protocol for blood microvessel density.

Where possible, comparisons have been made individually for acute and chronic SCI results in accordance with the relevant literature for each. Comparisons have also been made between the acute and chronic results from the current study.

5.1.1 Standard Trabecular Parameters

Current Study - Chronic SCI

The DF and PT metaphyseal secondary spongiosa (MSS) VOIs exhibited significant trabecular bone volume fraction (BV/TV) reductions following chronic SCI, with percentage reductions of 55% and 71%, respectively (Figures 3.33A and 3.33B). This brought about associated increases in trabecular specific surface (BS/BV) of 28% and 29% (Figures 3.33C and 3.33D). The DF and PT exhibited trabecular thickness (Tb.Th) reductions of 21% and 23% (Figures 3.34A and 3.34B), respectively. Trabecular separation (Tb.Sp) did not increase in either the DF or PT (Figures 3.34C and 3.34D). Trabecular number (Tb.N) was not affected in the DF, but the PT returned a decrease of 64% (Figures 3.34E and 3.34F).

As the BS/BV increases were similar but the BV/TV reduction was less in the DF, these results suggest that the mechanism of trabecular bone loss in the DF was dominated by trabecular thinning, as opposed to more trabeculae being completely resorbed in the PT, causing the PT BV/TV reduction to be comparatively higher (Figure 3.33).

The fractal dimension (FD) decreased significantly in the DF following chronic SCI, but did not change in the PT (Figures 3.35A and 3.35B). This result suggests that structural complexity is likely to be higher in VOIs with a greater trabecular density. Once the trabeculae are thinned or resorbed, the complexity reduces. The reason why the PT did not show a significant difference in FD may be because the PT presented a significantly lower initial (CTRL) trabecular volume than the DF, as displayed in Figure 5.1:

Bone Region	**Trab. BV SCI (mm^3)**	**Trab. BV CTRL (mm^3)**
DF	3.08 ± 1.55	9.11 ± 1.19
PT	1.52 ± 1.09 (p=0.2257)	5.68 ± 1.48 * (p=0.0356)

*Figure 5. 1: Chronic DF and PT bone volume. * indicates significant difference between DF and PT at p<0.05.*

Although the percentage decreases in connectivity density (Conn.D) between CTRL and SCI were 41% and 75% for the DF and PT respectively, the variation in results within each group meant that the result was non-significant (Figures 3.35C and 3.35D). This inconsistent result is likely due to a small sample size, as the aforementioned PT Tb.N results indicate.

Trabecular Bone Steady State

Williams (2019) found that by the 16 weeks of SCI, the BV/TV of SCI rats had risen from 9.04% (at 10 weeks) to 12.35%, indicating that a lower bone mass steady-state had not yet been reached. This is likely due to the effects of growth on the results, with rat long bone growth thought to end at around 26 weeks of age (Walker & Kember 1972). Human low bone mineral density (BMD) steady state following SCI has been shown to occur at around the 3 year timepoint post-injury (Eser *et al*. 2004). Therefore, confounding effects exist in the current study due to the effects of adolescent long bone growth alongside opposing SCI effects.

Clinical Literature - Chronic SCI

Taking trabecular aBMD (measured by DXA) as analogous to trabecular BV/TV (measured here by microCT), the results on the DF and PT MSS are in accordance with the clinical literature on the chronic stages of SCI-induced osteoporosis >1 year post-injury. Dauty *et al*. (2000) performed DF and PT trabecular BMD measurements on chronic SCI human patients. Subjects were male aged 18 to 60, and were analysed at 1 year post-injury. The DF and PT BMD measurements were found to have decreased by 52% and 70% respectively compared to age-matched controls. These results are similar to the 55% and 71% decreases reported herein.

Dudley-Javoroski & Shields (2012) used pQCT to examine the trabecular BMD at the DF and PT MSS in patients both male and female with complete SCI, ranging from 16 to 72 years of age. They found BMD reductions of 24% (DF) and 22% (PT) following 1 year of SCI. These results indicate a more mild rate of trabecular bone loss than the BV/TV reductions observed in the current study.

Analysing the human trabecular architecture at a more detailed level is difficult, as the X-ray techniques which can obtain sufficiently fine resolutions (e.g. microCT) involve comparatively greater radiation doses than less detailed techniques such as DXA (Li *et al.* 2013). Magnetic resonance imaging (MRI) has been employed to address this issue, as there is no ionizing radiation involved in the imaging process.

Modlesky *et al.* (2004) assessed the trabecular networks of ten SCI male patients at >2 years post-injury. Both the distal femur and proximal tibia were analysed, with apparent BV/TV reductions of 27% and 20% respectively, compared to able-bodied controls.

Magnetic resonance spectroscopy was utilised by Fanucci *et al*. (2006) to image the lumbar vertebrae in ten patients with osteoporotic vertebral fractures and an additional ten with osteoporosis but no OP-fractures. It was found that morphological change to the vertebral trabecular bone (the bone appearing more hyperintense) was a reliable indicator of vertebral fracture. Additionally, using spectroscopy to compare the fat content of the analysed regions, it was found that osteoporotic patients had a significant increase in fat tissue in their vertebrae when compared to healthy controls.

Developments to high resolution pQCT (HR-pQCT) systems have allowed for the first direct (independent of bone density) measurements of trabeculae to be performed in the appendicular skeleton of humans (Manske *et al.* 2015). Resolutions as fine as 61μm have allowed for a sufficiently small voxel to enable measurements of human trabecular thickness in radii samples from cadaveric tissue. This is an improvement of the previous achievable resolution of 82μm, which due to its size could only produce derived trabecular thickness measurements. This 'derived trabecular thickness' is calculated by dividing the trabecular vBMD for a given VOI by its directly measured Tb.N value (MacNeil & Boyd 2007). There is promise in future for utilising HR-pQCT in analysing of SCI-OP, as the first generation (82μm) accuracy has already been utilised in humans to show a significant decrease in derived Tb.Th following 6 weeks of non-weight bearing activity (Kazakia *et al*. 2014).

Rat Literature - Chronic SCI

In rat studies of SCI (contusion or transection), microCT and DXA densitometry have been used to assess the MSS site in the DF or PT at the chronic timepoint >8weeks post-injury (Lin *et al*. 2015, Williams 2019, Williams *et al*. 2020, Otzel *et al*. 2019, Jiang *et al*. 2007a). Every study found a significant reducing effect on trabecular bone volume and / or density following chronic SCI.

The effects of the chosen model of disuse are apparent in the literature. For example, Otzel *et al*. (2019) used a T9 contusion model on 16 week old male SD rats and found a 39% BV/TV drop in the DF metaphysis after 8 weeks of disuse, whilst a similar study (16 weeks old, 8 weeks of disuse) using a different model (botulinum toxin injection on quadriceps of female Wistar rats) found no discernible change in the same bone region (Vegger, Bruel & Thomsen 2015). For this reason, only immobilisation models via SCI transection or contusion are considered for comparison in Table 5.1:

Study	Disuse Model	Type of Rat	Age at SCI	Timepoint Post-Injury	VOI	Findings
Lin *et al*. 2015	T13 Contusion	Fischer 344	4 months	16 weeks	DF MSS	vBMD ↓54% BV/TV ↓65%
Williams 2019	T9 Transection	Wistar	10-12 weeks	10 / 16 weeks	DF / PT MSS	BV/TV ↓65% / 48%
Williams *et al*. 2020	T9 Transection	Wistar	10-12 weeks	10 weeks	DF MSS	BV/TV ↓57%
Otzel *et al*. 2019	T9 Contusion	SD	16 weeks	8 / 12 weeks	DF MSS	BV/TV ↓39% / 26%
Jiang *et al*. 2007a	T11 Transection	SD	6 weeks	6 months	PT	vBMD ↓42%
Current Study	T9 Transection	SD	8 weeks	11 weeks	DF / PT MSS	BV/TV ↓55% / 71%

Table 5. 1: Rat models of chronic SCI assessing trabecular bone density.

The number of confounding factors amongst the studies in Table 5.1 means that any links identified between different study datasets are somewhat tenuous. The most affecting parameters are the age of the rats at time of injury (as it incurs growth effects on bone loss data) and the time spent post-injury. The literature has not yet determined the age in rats at which bone loss due to SCI reaches a steady state (Williams 2019, Jiang *et al*. 2007a). This highlights the importance of the current study; adding to the knowledgebase of SCI-induced bone loss at a different timepoint and aiding in determination of the most effective rat model of disuse, whilst examining as many effects at each timepoint as possible.

For the standard trabecular parameters, a number of the most analysed microCT results were found to be in line with the literature, with some exceptions. Lin *et al*. (2015) found that as BV/TV reduced significantly by 65% in the DF following 16 weeks of SCI, Tb.Th and Tb.N concomitantly reduced as Tb.Sp was found to increase significantly. These findings suggest that the DF experienced a mode of bone loss more dominated by complete trabecular resorption than partial thinning, which is in line with the comparatively higher BV/TV reduction. This result follows the same pattern as that observed in the PT in the current study. The comparatively greater time post-injury

here (16 weeks compared to 11 in the current study) could also explain these greater bone volume losses.

Williams (2019) found as BV/TV reduced significantly in the DF by 65% and 48% by 10 and 16 weeks post-injury that Tb.N concomitantly reduced whilst Tb.Sp significantly increased. Tb.Th was found to be significantly affected at the 10 week timepoint, but not at 16 weeks. These results suggest that the DF initially experienced a combination bone loss mode of trabecular thinning and resorption, but by the most chronic timepoint, Tb.Th had recovered in order to account for the lower Tb.N. This is likely due to growth effects overcoming the SCI-induced trabecular loss as the rate had slowed by the chronic timepoint. This study found that Conn.D and FD were significantly affected at both timepoints. This highlights that recovery of trabecular bone mass in chronic SCI is more commonly achieved via morphological adaptation of the remaining trabeculae, as opposed to broken trabecular junctions (or entire trabeculae themselves) reforming. These results are consistent with the Tb.Th data in the current study DF at 11 weeks post-injury (Figure 3.34A), as well as the node densities observed in Figure 3.40.

Williams *et al*. (2020) found that as DF BV/TV and Tb.N were significantly affected by 57% and 52% respectively following 10 weeks of SCI, Tb.Th was only reduced by 10%. These results suggest that the bone loss due to chronic SCI was dominated trabecular removal rather than trabecular thinning. This is in contrast to the current study (BV/TV ↓55% and Tb.Th ↓21% with no change in Tb.N), which suggests that the DF experiences primarily trabecular thinning-associated bone loss during similar conditions. The current study analysed 8 week old rats at the 11 week post-injury timepoint, whilst Williams *et al*. (2020) analysed 10-12 week old rats at the 10 week timepoint. Therefore, effects of bone growth or time spent post-injury are minimal for this specific comparison, in relation to other studies in the literature.

Otzel *et al*. (2019) found that the 8 and 12 week timepoints post-injury both resulted in significant effects on DF MSS BV/TV, Tb.N and Tb.Sp, however Tb.Th was not affected at either timepoint. These results agree with those found by Williams *et al*. (2020), suggesting that Tb.Th is recovered during long periods of SCI. It is interesting to compare the Tb.Th results in the current study (DF ↓20.98% and PT ↓22.65%), as

both regions did not appear to have recovered by 11 weeks of SCI. One reason for this larger impact on Tb.Th is the age of the rats in the current study. As they are comparatively younger, more thin trabeculae are present which exhibit a higher BS/BV, resulting in greater resorption effects on adolescent bone.

Current Study - Acute SCI

As the analysis timepoint for the acute dataset was 2 weeks instead of 11 weeks post-injury, the confounding effects of growth were comparatively less. The mode of bone loss in the acute PT bones was predicted to be characterised by the near-immediate increased resorption response which is widely understood in the literature (Chantraine, Nusgens & Lapiere 1986, Williams *et al*. 2022a).

The standard trabecular results from the acute dataset were all found to be significantly different in SCI than CTRL groups. In fact, the p value for every t-test performed was below 0.001. Significant reductions in BV/TV, Tb.Th, Tb.N, FD and Conn.D occurred alongside significant increases in BS/BV and Tb.Sp (Table 3.5). In comparison, the chronic PT bones were only found to be significantly different in BV/TV, BS/BV, Tb.Th and Tb.N (Figures 3.33B, 3.33D, 3.34B and 3.34F). As an indicator of the speed of the resorption response, BV/TV was found to have decreased by 61% in the PT by 2 weeks (Table 3.5), whilst after 11 weeks it had reduced by 71% (Figure 3.33B). These results highlight the rapid increase in osteoclastic cell numbers and activity as an acute response to complete SCI. The findings of no significant change in Tb.Sp, FD or Conn.D in the chronic SCI dataset (Figures 3.34D, 3.35B and 3.35D) suggest that growth effects act to recover the initial trabecular losses following SCI. It is possible, however, that the lack of statistical significance in these results is due to the small sample size.

Clinical Literature - Acute SCI

The acute BV/TV results from the current study are inconsistent with those in the clinical literature using DXA to assess aBMD in adult human SCI patients. Comparisons are less accurate with skeletally mature patients as the rats in the current study present growth effects due to their adolescent age. Skeletally developing human patients (≤15 years) only comprise ~4% of the global SCI population (Parent *et al.* 2011). For completeness, comparisons are made with both adult and paediatric clinical SCI studies.

Zehnder *et al.* (2004) assessed males with traumatic SCI of 30±3 years of age. Timepoints post-injury ranged from 3 months to 30 years. Dramatic decreases in aBMD of the femoral neck and distal tibial epiphysis were observed from 3 months to 1 year, levelling off at a z-score of -3→-4 by the 3 year post-injury timepoint. These results indicate a rapid initial bone loss response to SCI. They are consistent with the results from the current study, however they are not directly comparable as the patients were skeletally mature and neither the DF or PT MSS was selected as a VOI for analysis.

In contrast to the results from Zehnder *et al.*, a study on the femoral neck of SCI patients of varying age and gender found no significant decrease in aBMD from 2 to 6 months post-injury (Roberts *et al.* 1998). Subjects ranged in age from 13 to 66 years, however no comparisons were made between growing and skeletally mature patients in the study. These results are inconsistent with those from the current study, which suggest a near-immediate and marked trabecular bone loss following SCI. The clinical results here indicate that the acceleration of trabecular bone loss following SCI occurs at some point after 6 months post-injury. It must be noted that this delay could be largely due to the comparatively slower response to SCI that skeletally mature bone exhibits.

An example of the rapid response of growing bone to SCI is provided in a study by Liu *et al.* (2008). In this study, eight children of different gender and aged 3-15 years were assessed using DXA. Significantly reduced BMD in whole-leg scans, as well as significantly reduced BMD z-scores in the femoral neck were observed at 1 to 4 months post-injury. These reductions were more severe at the 1 year timepoint. There

was no significant difference in either metric between 1 and 2 years post-injury, however. These results indicate a rapid and progressing bone density reduction in growing bone as a response to SCI (consistent with the current study), the effects of which are offset by growth following the 1 year timepoint.

Rat Literature - Acute SCI

The 61% decrease in BV/TV in the 2 week SCI PT bones from the current study (Table 3.5) indicates a fast-acting resorption response to complete SCI. This is highly consistent with the previous literature on the acute timepoint <4 weeks post-injury in growing rat models of complete SCI. A summary of each study is given below:

Jiang, Jiang & Dai (2006) performed a T10 transection on six week old male SD rats, and via microCT examined the trabecular effects at 3 weeks post-injury. BV/TV significantly reduced by 64% compared to sham operated controls in the PT MSS.

In another study using 6 week old male SD rats, Liu *et al.* (2008) performed a T10 transection and analysed the PT MSS at 3 weeks post-injury. BV/TV at this timepoint was found to be significantly lower in the SCI bones, reducing by 57% compared to age-matched controls.

Minematsu *et al*. (2014) observed a 51% and 62% significantly lower BV/TV compared to sham controls in the PT MSS after 1 and 3 weeks of complete SC transection at the T12 vertebra. The rats in this study were male Wistar rats at 8 weeks of age.

Female SD rats at 6 weeks of age were studied by Jiang *et al.* (2007). A T10 transection was given, and the PT MSS analysed at 3 weeks post-injury. BV/TV was found to be significantly reduced by 72% compared to age-matched controls.

Peng *et al.* (2020) investigated the DF MSS of 8 week old male Wistar rats at 2 and 7 days post-injury, following a T4 transection. BV/TV reduced significantly compared to sham controls by 19% and 29% after 2 and 7 days respectively.

5.1.2 Inter-Trabecular Angle

As mentioned previously (page 78), this study utilised the centroids output of the inter-trabecular angle (ITA) analysis in BoneJ2 to plot the coordinates of the endpoints of each trabeculae in a given VOI, based on their number of connections i.e. the coordinate combinations were used to plot the node types whilst differentiating between 3N, 4N and 5N nodes. Additionally, the angles between each branch at each node (the ITAs) were averaged for each 3N, 4N and 5N node type.

Current Study - Chronic SCI

In the CTRL bones of both the DF and PT groups, node type abundance ratios were found to be ~12:3:1 for 3N, 4N and 5N nodes. The SCI bones, however, presented noticeably altered node type ratios (Figures 3.41 and 3.43). These results suggest that healthy trabecular bone is likely to arrange in the same manner topologically in the absence of any pathology, however a condition such as SCI can alter this preferred organisation.

The 3D colour plots of the different node types in the chronic DF and PT showed similar differences in both bone regions between SCI and CTRL bones (Figures 3.40 and 3.42). SCI appeared to bring about a reduction in 5N nodes in the diaphyseal trabeculae of the DF. When compared to this region, the central and epiphyseal regions of the SCI bones tended to contain not only a greater number of nodes, but a greater density of higher-connected 5N nodes. In the DF CTRL bones, however, no distinct localisation of 5N nodes was observed (Figure 3.40). The same pattern was observed in the PT. SCI bones in the PT MSS exhibited a more sparse node density than the CTRL bones, with the majority of 5N nodes in the epiphyseal and central regions (Figure 3.42). These results suggest that the trabecular network loses nodes of higher connectivity preferentially to lower N nodes during significant trabecular bone loss. Either:

1. The node and all of its branches are totally resorbed, or -
2. The node changes from 5N to 4N, 4N to 3N, 5N to 3N etc. as branches are resorbed.

The first case is more likely to occur in low-N nodes, as there are less trabeculae to be completely resorbed. This can potentially explain the node abundance ratio change in the chronic DF (Figure 3.41), as 3N nodes were observed to be removed at a greater rate than 4N or 5N nodes. The 3N, 4N and 5N node abundance ratios changed from (CTRL to SCI) 12:3:1 to 7:3:1 in this instance.

The second case should be more pronounced in cases of greater BV/TV reduction. 5N nodes losing a branch and hence contributing to 4N node counts whilst the same process happens as 4N nodes become 3N nodes should result in the ratio of 3N and 4N (compared to 5N) nodes increasing at the same magnitude as the trabecular bone loss. This is consistent with the BV/TV (Figure 3.33B) and node abundance ratio (Figure 3.43) effects from the chronic PT, as a 71% decrease in BV/TV brought about a concomitant increase in 3N and 4N relative node abundance from a ratio of 12:3:1 in the CTRL bones to a ratio of 46:10:1 in the SCI bones.

The mean ITA results showed no significant differences between CTRL and SCI bones following chronic SCI (Figures 3.44 and 3.45). The mode of geometrical change in the trabecular network during SCI is one of a thinning and breakage of the trabeculae already present, as opposed to the genesis of entirely new, differently oriented structures. The finding of no significant change in mean ITA could therefore be explained by the likelihood of a structure failing at its weakest point. For example, a 4N node losing one trabecula would lose that which was the least optimally aligned in a 3N configuration. Another explanation for the mean ITA results is the ability of the bone to respond to mechanical demand. This theory is commonly discussed in the literature (Frost 2003, Ben-Zvi *et al*. 2017), describing the local osteogenic and resorptive effects on trabeculae initiated by the osteocytes in response to a different load demand, such as SCI. During the course of their lifetimes, it is plausible that some remodelling occurred in the SCI rats to better form their remaining nodes into more optimised angular configurations. This outcome is more likely at later timepoints as it gives time for remodelling to occur. The similar ITA distributions (Figures 3.46 and 3.47) in SCI and CTRL bones in the chronic dataset add weight to the idea that over time, remodelling effects act to maximally span 3D space at each trabecular junction, creating a more mechanically efficient structure.

Current Study - Acute SCI

Both CTRL and SCI bones in the acute dataset presented node abundance ratios of 6:2:1, indicating that 3N node density increases with age (Figure 3.59). The CTRL and SCI acute results were also the same when searching for spatial clustering of different node types. In this case, a uniform distribution of 3N, 4N and 5N nodes was observed in all volumes i.e. no notable clustering of certain node types was found (Figures 3.57 and 3.58). This finding indicates that the pattern observed in chronic SCI (higher-connected 5N nodes being removed at a greater rate in the diaphyseal regions of the MSS and 3N / 4N node abundance increasing as a result) takes some time to develop. The acute SCI bones were found to be significantly different to CTRL bones in mean ITA for all node types, with values of 113^{o}, 106^{o} and 102^{o} following 2 weeks of SCI (Figure 3.60). Although it presented these lower mean ITAs, the acute SCI dataset did not exhibit a noticeably different ITA distribution in 3N, 4N or 5N node ITAs (Figure 3.61). This mild reduction in mean ITAs in the absence of any node type clustering suggests that in the initial stages following SCI, the optimal angular arrangement of nodes in affected trabecular bone is disrupted during the initial rapid bone loss. Once the chronic stages are reached, gradual remodelling effects act to recover these losses, producing nodes of ITA values closer to the optimal alignment (Figures 3.44 and 3.45).

Clinical Literature

To date, there are three studies which have used ITA to characterise human trabecular bone. In the seminal study on ITA, Reznikov *et al*. (2016) examined the human femoral head from human cadaveric tissue age 20-79, with one sample coming from an osteoporotic patient with a femoral neck fracture. They found that node type relative abundances were around 70%, 25% and 6% for 3N, 4N and 5N nodes respectively, a ratio of 12:4:1. This pattern prevailed regardless of bone pathology i.e. it was observed in all samples analysed. The observed ratio here (12:4:1) is consistent with the chronic CTRL bones in the current study (12:3:1). Conversely, the chronic SCI bones presented noticeably different node type abundance ratios (7:3:1 DF / 46:10:1 PT) (Table 5.2). These results indicate that analysing node abundance ratios can potentially uncover subtle morphological changes in trabecular bone following SCI, and that the ratios likely do no remain invariant after injury. The possibility of node clustering in

different locations throughout the femoral head was also investigated by Reznikov *et al*. The metaphyseal secondary spongiosa (MSS), femoral neck and acetabular head of the PF were examined, and no specific clustering of 3N, 4N or 5N nodes was found in any location in any VOI analysed. Consistent with this finding, the chronic CTRL bones exhibited no noticeable regions containing different clustering of any node type. The chronic SCI bones, however, presented a different result. 5N nodes appeared to reduce in number in the diaphyseal portion of the MSS following chronic SCI (Figures 3.40 and 3.42). These results suggest that the healthy spatial organisation of nodes in trabecular bone is affected slowly over time by SCI. In addition to the node type clustering and abundance ratios, the mean ITAs and ITA distributions for each node type were studied by Reznikov *et al*. Mean ITAs for 3N, 4N and 5N nodes were found to be 116^{o}, 107^{o} and 103^{o} respectively. The ITA distributions were highly similar for every femoral head. The mean ITAs in both chronic CTRL and SCI bones from the current study were consistent with 116^{o}, 107^{o} and 103^{o} for 3N, 4N and 5N nodes (Figures 3.44 and 3.45). The ITA distributions in the current study were not seen to be affected by SCI in either the acute or chronic case (Figures 3.46, 3.47 and 3.61). These results indicate that, regardless of pathology, trabecular bone organises itself naturally in the most optimal space-filling manner. This theory is countered by the mean ITA results from the acute PT, however. The 2 week SCI bones exhibited significantly altered mean ITAs for 3N, 4N and 5N nodes, reducing to 113^{o}, 106^{o} and 102^{o} respectively, a drop of 1→2^{o} for each node type (Figure 3.60). This result is interesting. It suggests that the average orientation of trabecular struts is affected to a significant extent following SCI, with the effect reduced continuously as time allows for remodelling corrections in the affected bone.

In another other human study on trabecular bone using ITA, Reznikov *et al*. (2017) examined the changes in the human calcaneus following chronic periods of foot-binding, a historical aesthetic procedure with apparent changes in the trabecular bone along the predominant loading axes of the foot. They found that the anisotropic trabecular characteristic of unbound foot bones (the expected alignment of trabeculae along the primary loading axis) did not develop in the footbound bones. Additionally, they found that despite the different morphological adaptations, the underlying topological characteristics (such as the mean ITAs for different node types and node

abundance ratios) remained invariant following foot binding. These findings suggest that an inconsistent or inadequate mechanical load prevents the formation of useful anisotropic morphology in trabecular bone, whilst the underlying topology seems to follow the same pattern regardless of mechanical demand. Node abundance ratios and ITA distributions were found to be consistent with the previous literature and the current study, reinforcing the idea that trabecular bone naturally optimised itself towards the most space-filling topology (Table 5.2).

The most recent study into human trabecular bone using ITA is of particular importance to the current study, as it was conducted on a large sample of both healthy and osteoporotic (OP) adult bone. Reznikov *et al*. (2020) collected DF and PT trabecular biopsies from 31 patients with total hip arthroplasty immediately following fragility fractures at varying stages of osteoporosis, as well as 10 healthy adult controls. They assessed the potential differences in the underlying topology in each trabecular network, as well as the potential changes in the standard morphometric parameters. It was observed that many common morphological descriptors such as trabecular separation and connectivity density did not detect significant differences between control and OP bone. However, when examining topological effects via the node type distributions, clear and significant differences were detected. These results suggest that the loss of trabecular connections (the reduction of node valence) in the acute stages following osteoporotic fragility fracture is not merely a result of morphological changes but is also affected significantly by an impaired topological arrangement which leads to stress concentrations within the network. The mean node abundance ratios for 3N, 4N and 5N nodes in this study were 79%, 17% and 4% (20:4:1) in the control bone and 84%, 14% and 2% (42:7:1) in the OP bone. These results deviate from the previous literature and the current study, with 3N nodes comprising a much greater proportion of total nodes, even in healthy bone. This increase in 3N node abundance due to osteoporosis suggests that the effects of growth and / or remodelling act to recover the topological changes due to SCI by adopting a more mechanically efficient arrangement. Table 5.2 summarises the clinical literature using ITA:

Study	Bone Examined	Results for 3N / 4N / 5N Nodes
Reznikov *et al*. 2016	Human femoral head CTRL / femoral fracture osteoporotic (FFOP)	• Node abundance ratios 12:4:1 all bones • Mean ITAs 116/107/103º CTRL • Mean ITAs 112/108/99º FFOP
Reznikov *et al*. 2017	Human calcanei CTRL / footbound	• Node abundance ratios 12:4:1 all bones • Mean ITAs 115/107/101º all bones
Reznikov *et al*. 2020	Human distal femur (DF) and proximal tibia (PT) CTRL / osteoporotic (OP)	• Node abundance ratios 20:4:1 CTRL / 36:6:1 OP
Current Study	Rat distal femur (DF) and proximal tibia (PT) CTRL / spinal cord injured (SCI)	• Node abundance ratios 12:3:1 chronic CTRL DF and PT / 7:3:1 chronic SCI DF / 46:10:1 chronic SCI PT / 6:2:1 acute CTRL and SCI PT • Mean ITAs 116/107/103º all bones except acute SCI PT 113/106/102º

Table 5. 2: Clinical studies on trabecular bone using ITA.

Animal Literature

To date, there are two studies which have used ITA to characterise the topology of non-human trabecular bone. Ben-Zvi *et al*. (2017) employed ITA to study the structure-function relationship in the mandible and proximal femur (PF) of the pig. In the PF and condylar neck of the mandible, near identical node type abundance ratios to those found in the human PF were observed. They equated to ratios of around 10:3:1. The condylar head, however, presented slightly different ratios. As it contained more than twice the total nodes of the condylar neck, the ratios of 4N and 5N nodes were also higher, which is intuitive given the higher connectedness of the trabecular network. Unlike the human femoral head, neck and MSS where no clustering of nodes was observed (Reznikov *et al*. 2016), the pig mandible was found to contain greater densities of 3N nodes in the central condylar head, where the principle stress axis aligns. This result suggests that trabecular bone tends to contain a greater proportion of 3N nodes in regions experiencing the greatest forces, in order to provide the most

mechanically efficient trabecular network which can maximally span the occupied space and manage the load in the most effective manner. Mean ITAs for 3N, 4N and 5N nodes were 115^{o}, 106^{o} and 103^{o} in every region analysed. These results for 3N and 4N nodes approach the values of maximally spaced 3N (120^{o}) and 4N (109.5^{o}) branched structures (Reznikov *et al*. 2016), which once again indicates the propensity of mammalian trabecular bone to organise itself in a space-filling, mechanically efficient manner. The observation that node density reduces over time in trabecular regions of lower stress demand (i.e. the condylar neck) is in keeping with the findings in the current study, as the diaphyseal portions of the MSS in both the chronic DF and chronic PT SCI groups were observed to contain less 5N nodes in proportion to total nodes (indicating lower connectedness), and also less nodes overall (Figures 3.40 and 3.42).

The other non-human study into trabecular topology using ITA was conducted by Grun & Nebelsick (2018). In this study, the morphological properties and topological properties of the echinoid (sea urchin) trabecular network were examined. Specifically, trabecular VOIs from the species *Echinocyamus pusillus* were analysed, and the node abundance ratios for 3N, 4N and 5N nodes were found to be 66%, 21% and 6.5% respectively, a 10:3:1 ratio. In contrast to the previous literature on trabecular bone of varying species, the mean ITA values for the echinoid were found to be 106^{o}, 102^{o} and 99^{o} for 3N, 4N and 5N nodes. These results suggest that less optimally-aligned trabecular bone is indicative of reduced mechanical loads (echinoids are subsea dwellers).

The current study represents the first time that ITA has been used to analyse topological changes in osteoporotic / SCI trabecular bone in an animal model. The animal studies in the literature which utilise ITA are summarised in Table 5.3:

Study	Bone Examined	Results for 3N / 4N / 5N Nodes
Ben-Zvi *et al*. 2017	Pig mandible condylar head (CH) / neck (CN) and proximal femur (PF)	• Node abundance ratios 6:3:1 CH / 10:3:1 CN and PF • Mean ITAs 115/106/103º all bones • Node density in CH = 2→2.6x node density in CN
Grun & Nebelsick 2018	Echinoid central / margin trabeculae	• Node abundance ratios 10:3:1 all bones • Mean ITAs 106/102/99º all bones
Current Study	Rat distal femur (DF) and proximal tibia (PT) CTRL / SCI	• Node abundance ratios 12:3:1 chronic CTRL DF and PT / 7:3:1 chronic SCI DF / 46:10:1 chronic SCI PT / 6:2:1 acute CTRL and SCI PT • Mean ITAs ~116/107/103º all bones except acute SCI PT 113/106/102º

Table 5. 3: Animal studies on trabecular bone using ITA.

Why is it useful to characterise trabecular topology in osteoporosis?

In certain instances, patterns of anisotropy (large scale orientation) in the struts of a given trabecular network are observable at the macroscale. Such observations are often made using 2D images of planes through a trabecular VOI. Solely relying on these analyses to determine the overall 3D topological changes in a VOI is likely to exclude crucial information on parameters such as node clustering or connectedness (Reznikov *et al*. 2016).

Results from morphological analyses in 3D are essential for determining the trabecular bone microarchitecture, but do not complete the picture for examining the potential effects of a given pathology. Analyses such as ITA abundance distribution, mean ITA and node type abundance ratio do not include overlying morphological attributes, revealing data on the core topology which can uncover significant differences between control and affected samples.

Reznikov *et al*. (2017) illustrated that despite exhibiting significantly different mean trabecular thickness from the talocalcaneal joint (proximal end) to the tuberosity (distal end) of the human calcaneus following foot binding, the underlying topological characteristics analysed via ITA showed no change. This highlights that the morphological and topological responses in the bone remodelling process are distinct, with both providing useful information when characterising a condition such as osteoporosis.

Reznikov *et al*. (2020) showed that despite morphological analyses detecting no significant effects on trabecular bone following fragility fracture, the underlying topology was altered in a subtle but consistent manner. This points towards the utility of topological analyses for SCI / osteoporotic trabecular bone. It is vital when characterising a condition that the complete picture is provided via the selection of relevant analyses. These results show that morphological changes are only one mode in which the trabecular bone remodelling cycle responds to pathologies like SCI. There is a more consistent effect on the ‘covert’ topological blueprint in the acute stages which is not immediately evident.

What is the significance of the effects of SCI on the node type abundances of affected trabecular bone?

Interestingly, the DF and PT node type abundance ratios were both noticeably affected by chronic SCI. The DF experienced a greater relative reduction in 3N nodes than 4N or 5N nodes, resulting in a ratio of 7:3:1 i.e. a mild effect on 3N node relative abundance. Conversely, the PT experienced a significant reduction in both 4N and 5N nodes, resulting in a ratio of 46:10:1, a considerable change in node abundance ratio (Table 5.3).

The chronic DF node abundance results are interesting (Figure 3.41). As the BV/TV reduction in the chronic DF was less than that in the PT, the fact that mainly 3N nodes were lost suggests that trabecular bone primarily maintains connectedness of the network following SCI, however if the losses are severe (as in the PT), the connections in the higher N nodes fail, creating larger abundances of lower N nodes as a consequence. Another reason why the 3N nodes might be lost in the less severe cases of SCI-induced trabecular bone loss is that thinner trabeculae are more likely to be resorbed first. 5N nodes would likely take longer to form than 3N nodes, with this time taken resulting in thicker trabeculae on average at each 5N node. As the ITA analysis negates trabecular morphology via the skeletonization algorithm, it remains unclear whether this is the case.

The chronic PT node abundance results (Figure 3.43) suggest that, when experiencing a large enough reduction in trabecular bone density, the affected region loses its most connected nodes at a greater rate than their lower-N counterparts. This result is to be expected. As 2N nodes were discounted from analysis, any breakages in 5N nodes would result in 4N nodes, any breakages in 4N nodes would result in 3N nodes, and any further breakages would simply discount that node from consideration. It is therefore expected that following significant trabecular bone density reductions, the 3N node relative abundance will increase significantly up until the point of total resorption of all nodes.

The node abundance ratios for both CTRL and SCI bones in the acute dataset was 6:2:1. This finding is understood when considering the effects of growth and the adolescent age of the rats used in the current study. This finding of a lower 3N node

abundance in adolescent rats which grows to become consistent with the 12:4:1 ratios in the literature (Reznikov *et al*. 2016, Reznikov *et al.* 2017, Ben-Zvi *et al.* 2017) highlights that adolescent mammalian trabecular bone has not yet reached the stage of optimal arrangement which better prepares it for everyday loads. The fact that SCI did not cause a significant change in node abundance ratio after just 2 weeks (Figure 3.59) suggests that complete resorption of trabeculae in the initial stages following SCI occurs primarily on the higher N nodes, transforming them into lower N nodes as branches are removed which are understandably less optimally arranged than pre-existing lower N nodes.

Does a use exist for topological analysis to be utilised as a indicator of osteoporosis?

If data is acquired on the trabecular topological blueprint of different skeletal sites (spine, long bones, ribs, skull), it will inform whether or not the local functional loads on each bone in the body impose a different trabecular topology according to the applied forces, or whether the skeleton possesses a more global trabecular topology which is reflective of the pathological state of the individual. If the latter is the case, this underlying, subtle aspect of the trabecular bone remodelling response can be examined in order to provide insight into a given patient's bone quality (Reznikov *et al*. 2020).

5.1.3 Ellipsoid Factor

As described on page 80, ellipsoid factor (EF) is a measure of rod-like and plate-like geometries in the trabecular continuum. Plate-like trabeculae are considered mechanically superior to their rod-like counterparts, and so a trabecular region which is predominantly composed of plate-like geometries will perform better under load and pose a lower fracture risk (Salmon *et al*. 2015).

Current Study - Chronic SCI

The highest densities of plate-like structures were observed to be in the control bones of both the DF and PT metaphyses. As the plate-like structures reduced in number following SCI, the medullary regions in the SCI bones appeared to lose more plate-like geometries and undergo greater topological changes than the endosteal region (Figures 3.38 and 3.39). This change from a plate-like to rod-like predominant local morphology was confirmed by a higher median EF in the DF SCI bones. The PT, however, did not follow this expectation and exhibited no significant change in median EF (Figure 3.36). Maximum and minimum EF values were similar in all cases, indicating that extremely rod-like and plate-like geometries persist following chronic SCI (Appendix entry 8).

The EF distribution histograms were skewed left in the majority of cases. Some CTRL bones showed almost zero or a mild right skew in one CTRL case (Figure 3.37). These results suggest that the predominant trabecular morphology is one of a mildly rod-like shape (EF 0→0.4), as confirmed in the EF mode data (Figure 3.56B). Some bones, however, showed a negative value for EF mode, albeit comparatively milder in magnitude (EF ~ -0.2). It is therefore reasonable to assume that the EF mode is not an accurate measure of osteoporosis severity.

Current Study - Acute SCI

The current study represents the first ever comparison of healthy and complete SCI bone in the acute stages of osteoporosis using EF. Neither median EF nor SMI was found to be significantly different between control and SCI in the 2 week SCI PT bones (Table 3.6). This result was expected, given the theory of the mild plate-to-rod

transition in osteoporotic bone being delayed with respect to the initial bone loss (Felder *et al.* 2020). This theory is discussed further on page 183.

When qualitatively assessing the EF volumes in the acute PT dataset, the observations made differed to those in the chronic PT bones. Whereas the chronic SCI PT exhibited less plate-like geometries in the medullary region and overall (Figures 3.39), the acute SCI PTs appeared identical to their CTRL counterparts (Figures 3.53 and 3.54). In the acute PT, no thinning of trabecular density in the medullary regions was observed, and each VOI exhibited a uniform distribution of local EF values throughout. This result is consistent with the aforementioned findings (Table 3.6); no significant difference in median EF is indicative of the overall similarity in local geometries in SCI and CTRL volumes. These findings can be explained by considering that the larger reduction in BV/TV and the longer time spent post-injury in the chronic dataset allowed for more extensive morphological remodelling to occur, and hence could produce noticeably differing CTRL and SCI volumes at this later timepoint.

Clinical Literature

There are a small number of studies to date which have utilised EF to characterise osteoporotic bone in the clinical literature. Using microCT, average EF was found to be -0.03 in osteoporotic human femoral head trabecular biopsies from hip replacement patients (Porelli *et al*. 2022). These patients varied in numerous parameters including age, weight and gender.

Felder *et al*. (2020) used microCT to analyse EF in progressing osteoporosis via selecting 22 female human vertebrae samples from ages 24-88 years. This is the first ever study comparing healthy and osteoporotic bone using EF in humans. They found that whilst EF median did not correlate with BV/TV, SMI was significantly negatively affected by increasing BV/TV. These results are all in accordance with those in the current study. When analysing EF mode, however, Felder *et al*. found a mild negative association (in human vertebrae) between EF mode and increasing BV/TV. This result was not observed in either the DF or PT rat VOIs analysed herein. It remains unclear whether different trabecular regions (DF / PT etc.) present different topological changes when affected by SCI.

Rodent Literature - Chronic SCI

Currently, there are only two studies which have used rodent models of disuse and EF analysis to characterise the changes. Both of these assess the chronic timepoint >6 weeks post-injury. A mild transition is common from plate to rod-like median EF following chronic SCI (Salmon *et al*. 2015, Felder *et al*. 2020). Table 5.4 summarises the literature:

Study	**Osteoporosis Model**	**Rodent**	**Age**	**Timepoint post-surgery**	**VOI**	**Findings**
Salmon *et al*. 2015	Ovariectomy	SD Rat	12 weeks	6 weeks	DF MSS	Median EF ↑0.02
Felder *et al*. 2020	Sciatic Neurectomy	Mouse	12 weeks	9 weeks	PT MSS	Median EF ↑0.1
Current Study	T9 Transection	SD Rat	8 weeks	11 weeks	DF / PT MSS	Median EF ↑0.1 / No change in median EF

Table 5. 4: Rodent studies of osteoporosis using ellipsoid factor.

Salmon *et al*. (2015) found that SMI had a strong, significant dependence on BV/TV (R^2 = 0.985, p<0.001) whilst EF was independent of BV/TV (R^2 = 0.093, p=0.035). These results are consistent with those in the current study (Figure 3.56). They highlight the utility and validity of employing EF in place of SMI to analyse trabecular plate-to-rod transitions in VOIs of varying stages of osteoporosis. Inherent in the SMI calculation is the assumption that the entire trabecular surface is convex. In reality, this is often not the case. Concave geometries in the analysed bone lead to inaccurate results which fail produce a realistic impression of local trabecular shapes, and hence the mechanical performance and fracture risk of the bone.

In addition to the median EF changes following chronic disuse, Felder *et al*. (2020) found that in the proximal tibia of mice, EF histograms were unimodally distributed with a mixture of left and right skews in both control and disuse bones. Minimum and maximum EF values of <|0.85| were found in all bones analysed. SMI was found to be significantly different between control and disuse bones at 1, 7 and 9 weeks post-surgery, whereas EF median was only significantly different at 9 weeks. EF was found to depend on BV/TV to a much lesser extent than SMI (R^2 = 0.25 p<0.05 and R^2 = -

0.81 $p<0.001$ for EF and SMI, respectively). Fill percentages were ~90% for all EF analyses. The results in the current study are almost entirely consistent with these findings; a mild plate-to-rod transition appears to occur at the chronic stages of SCI-induced osteoporosis when measured by EF. When measured by SMI, the effect (erroneously) appears to be greater (Figure 3.36). The results in the current study follow this pattern in the PT SMI results. In the DF, however, no significant difference was detected between SCI and CTRL bone SMI values. It is likely due to the small sample size, however it could also be the case that the comparatively greater BV/TV in both CTRL and SCI bones influenced the SMI results in the DF, leading to results which differed from the PT bones in this study. This is because the influence of concave geometries is greater in trabecular networks of higher bone volume fraction (Salmon *et al*. 2015).

Why is it useful to characterise trabecular morphology in osteoporosis?

Trabecular bone is more sensitive to changes in the bone remodelling process than other bone types of lower specific surface e.g. cortical bone. The larger relative surface area provides a greater region of cell activity, rendering any effects on these cells' genesis and activity comparatively more severe on trabecular bone. Changes in the morphology of trabecular bone therefore present a significant risk of impairing bone quality or the bone remodelling balance in patients affected by conditions such as SCI. Bone remodelling refers to the osteoblast and osteoclast recruitment balance, the integrity of forming bone remodelling compartments, mesenchymal stem cell niches and supplying capillary networks, as well as the instigation and levels of the essential protein signalling cascades behind each process (Brandi 2009). Bone quality refers to mechanical performance indicators like volumetric bone density, 3D architecture and tissue material properties (Connelly 2011). Determining the most effective and reliable characterisation for trabecular morphology is vital for providing the most detailed impression of a given individual's bone quality and remodelling balance.

Why is it useful to characterise trabecular bone using a plate and rod model?

As previously stated, rod-like trabeculae have a long, cylindrical geometry which form open cells in three dimensions. Plate-like trabeculae are flat, being wide in both the X and Y dimension which form predominantly closed cells in three dimensions. For this

reason, plate-like geometries in trabecular bone have long been considered the superior form for bearing the loads of everyday activity. The superior mechanical performance of closed-cell systems results in a reduced fracture risk and hence a lower risk of associated health problems due to impaired bone quality (Hildebrand & Rüegsegger 1997b). The point at which trabecular loss begins to alter the overall load-bearing capacity of the trabecular network from a closed-cell to an open-cell model has been suggested to occur when BV/TV drops below 20% (Gibson 1985). It would therefore be beneficial to analyse comparable trabecular VOIs both above and below this percentage. Previous work on osteoporosis using EF has (to the best of the writer's knowledge) only analysed the plate-to-rod transition at BV/TV values of 2-18% (Felder *et al*. 2020). The current study provides insight into trabecular effects of chronic SCI at BV/TV values of 11-38% (DF) and 2-27% (PT).

In a study on the resorption cavities in human vertebrae, Goff *et al.* (2012) provide qualitative descriptions from scanning electron micrographs. They suggest that in osteoporotic vertebral trabeculae, the local morphology is characterised by decoupled resorption and formation. Specifically, resorption cavities were said to be located most often at trabecular junctions, then next most commonly at plate-like trabeculae. They conclude by stating the usefulness of future investigations into osteoporotic bone which would utilise analyses (e.g. EF and ITA) to characterise the plates, rods and nodes in trabecular bone.

Does EF present an advantage over SMI for characterising the plate-to-rod transition?

Previous work using EF has stated that SMI is influenced by concave geometries to such an extent that an overall SMI value for a trabecular network does not give an accurate depiction of local plate and rod-like structures in a given trabecular network. Additionally, the bone volume fraction of a selected VOI significantly predicts the resulting SMI value. This has been proven in multiple studies (Doube *et al*. 2015, Salmon *et al*. 2015, Felder *et al*. 2020). The results in the current study add weight to this idea. In the chronic SCI dataset, SMI exhibited a significant difference in the PT (Figure 3.36D), which is the same bone region analysed in the previous studies. In the DF, no significant difference in SMI was observed (Figure 3.36C), with the DF appearing to be affected either by a small sample size or by greater BV/TV values. In

either case, correlations for SMI and BV/TV were strong and significant (Figures 3.56A and 3.56C).

Felder *et al*. (2020) reported that SMI values reached <3 in some cases, a geometry which is more convex than a perfect rod. This added to the case against SMI, as it can produce erroneous results at both ends of its scale. Such SMI values were not detected in the current study, however. SMI ranges were 0.75-2.10 in the DF and 1.38-2.58 in the PT.

EF appeared to present a superior alternative to SMI for characterising osteoporotic bone when assessing dependence of EF mode on BV/TV, as this correlation analysis returned a nonsignificant R^2 value of 0.0003 (Figure 3.56B). Median EF was also found to be independent of trabecular volume fraction, with a nonsignificant R^2 value of 0.1554 (Figure 3.56A). Although SMI showed a significant dependence on BV/TV (Figure 3.56C), it was also found to be predicted by median EF, with a significant R^2 value of 0.5965 (Figure 3.56D). This result was unexpected, as previous work has found no correlation between SMI and EF (Salmon *et al.* 2015). This result indicates that for more rod-like (EF>0) local geometries, SMI could be as accurate as EF for characterising the trabecular morphology. It is understandable that SMI would be closer adhered to EF in cases of higher EF, as trabecular volumes with higher densities of rod-like geometries tend to be found in cases of low BV/TV. Low BV/TV reduces the concave fraction of a given VOI, diminishing the confounding effects on SMI which are now commonly understood to impair its validity.

Koc, Kavut & Ugur (2020) analysed the mandibular condyles of edentulous, unilaterally edentulous and fully dentate human patients and found that all trabecular volumes contained predominantly rod-like mean SMI and EF values. SMI and EF were identical when examining for significant differences between the three groups. These results suggest that towards the positive end of the rod-like / plate-like spectrum, SMI and EF results can be interpreted interchangeably without error.

It must be noted that when analysing mean EF, the value alone does not specify the exact trabecular morphology distribution for a given VOI. VOIs composed of an equal proportion of extremely rod-like (EF 1) and plate-like (EF -1) will return a mean EF of 0, whilst VOIs composed wholly of intermediate or spherical (EF 0) trabeculae will

also return a mean EF of 0. Histograms of the EF distribution for each volume should be examined in order to fully comprehend the acquired median EF value (Doube 2015).

Does the same plate / rod transition pattern happen at higher bone volume fractions?

Analysing the >20% BV/TV bones in the chronic (11 week) dataset showed that the median EF appeared to decrease linearly once the 20% 'tipping point' was reached (Figure 3.56A). The rate at which median EF decreased was similar to that at which it increased from 2→20% BV/TV. The addition of the acute (2 week) datapoints allowed for clearer insight into the dependence of EF on BV/TV values from 2→39%. The negative trend of median EF as BV/TV increased beyond 20% was not confirmed. The relationship between EF and BV/TV was nonsignificant ($p=0.117$) with a R^2 value of 0.1554 for the combined acute and chronic datapoints (Figure 3.56A). It is possible that the 'tipping point' of 20% BV/TV first described by Gibson (1985) could represent the value above which the dependence of EF on BV/TV ceases to exist. Below this value (from 0→20% BV/TV), the results in the current study indicate that chronic SCI EF values are predicted by BV/TV.

Although nonsignificant, the gradual decline in EF with increasing BV/TV (Figure 3.56A) indicates that a larger number of plate-like trabeculae are likely in VOIs of higher BV/TV, consistent with the literature (Gibson 1985). These results are also in line with the qualitative assessments of EF volumes in the chronic dataset (Figures 3.38 and 3.39).

In the chronic dataset, the mild plate-to rod transition observed in lower BV/TV trabecular volumes occurred at the same rate as the initial loss of plate-like local geometries in bones just above 20% BV/TV. Increasing further to 30→40% BV/TV via the acute datapoints, this rod-to-plate transition took place at a similar rate (Figure 3.56A). Analysing both acute and chronic datasets at once garnered results which suggest that the plate-to-rod transition as BV/TV reduces is a gradual one which (at BV/TV values >20%) occurs at much the same rate regardless of trabecular density.

Does the plate-to-rod transition occur as a result of a delayed cellular response to bone volume fraction reduction?

To give insight on this question, the acute and chronic PT results on BV/TV reduction due to SCI were examined (Table 3.5, Figure 3.33B). The same comparisons were made between the acute and chronic PT results for EF (Table 3.6, Figure 3.36B).

In the acute stage of SCI 2 weeks post-injury, BV/TV was seen to significantly decrease by 61% in the PT, whilst no significant difference in median EF was detected (Table 3.5). These results highlight severe trabecular bone loss can occur in the absence of extensive morphological remodelling i.e. the trabeculae themselves are simply resorbed whilst maintaining much the same geometrical organisation as before. This is confirmed by the significant reductions in Tb.Th and Conn.D (Table 3.5) and the lack of change in node abundance ratios in the acute PT bones (Figure 3.59). These results suggest that the initial trabecular losses due to SCI happen in a uniformly distributed manner without any influence from bone remodelling or evidence of adaptation to the altered load demand.

In the chronic PT bones, a significant reduction of 71% in BV/TV was found at 11 weeks post-injury (Figure 3.33B). The expectation for median EF here was one of a significant increase, but no such change was observed in the chronic SCI PT bones (Figure 3.36B). Although unexpected, the small sample size in this dataset meant that any subtle variations in median EF would be unlikely to uncover. The significant increase in SMI (Figure 3.36D) lends weight to this idea that an increase in median EF at this timepoint was likely. Evaluating the DF chronic dataset (which contained n=3 samples compared to n=2 in the chronic PT) showed a significant increase in median EF (Figure 3.36A).

The findings in murine trabeculae from Felder *et al.* (2020) which showed a significant BV/TV reduction in the proximal tibia after 5 days of disuse, followed by a significant increase in median EF at 65 days post-injury suggest that there is a delayed rod-to-plate transition as remodelling effects begin to act following SCI-induced trabecular bone loss. The results in the current study confirm the initial loss of trabecular bone in the absence of EF change, but at the chronic stage no significant difference in EF is detected.

Outlier

In the current study, the PT exhibited no significant change in median EF following chronic SCI. Due to an infection during housing of one of the animals, a single member of the PT bones scanned was a significant outlier, as displayed in Appendix entry 6. Once again, the small sample size rendered this study more sensitive to outliers. It was predicted in the case of a larger sample size that the same mild plate-to-rod transition would occur in the proximal tibia at the chronic stage post-SCI.

5.1.4 Standard Cortical Parameters

Current Study – Chronic SCI

In both the DF and PT, the cortical area (Ct.Ar) was seen to decrease significantly following chronic SCI (Figures 3.48C and 3.48D). A significant decrease in DF total area (area of the periosteal envelope (Tt.Ar)) was also observed, however this change in Tt.Ar was not observed in the PT (Figures 3.49A and 3.49B). Additionally, no change was detected in either bone region in medullary area (Ma.Ar) (Figures 3.49C and 3.49D). For circular cortical cross-sections experiencing a significant decrease in cortical area (Ct.Ar), the cortical thickness (Ct.Th) is expected to follow the same pattern in the affected bone. This was not the case, however, as both the DF and PT presented no significant difference in Ct.Th (Figures 3.48A and 3.48B).

The difference in total area results can be explained by the age of the rats prior to surgery. At 8 weeks of age, some growth is still occurring in the long bones of SD rats. A maturity of at least 7 months before surgery is required in order to be sure that zero growth is happening in the long bones (Ringler *et al.* 1979). An absence of significant change in Tt.Ar can be understood when considering the age of the rats is sufficiently young enough such that growth effects could be counteracting the effects of disuse in the PT, whilst in the DF appositional growth was arrested to an extent sufficient to produce a significant reduction in Tt.Ar.

The fact that mean Ct.Th did not reduce in line with Ct.Ar can be explained in the DF by considering that the DF polar second moment of area (J) significantly reduced following chronic SCI. This result indicates a spatial redistribution; the cortical shell was altered from a relatively uniform thickness to one of thinner and thicker areas, resulting in a similar mean thickness but a significantly different Ct.Ar and J. The discrepancy between Ct.Ar and Ct.Th can also be explained by considering the measurement method for analysing cortical thickness in 3D. Similarly to ellipsoid factor analysis, maximally-fitted spheres are ‘grown’ inside the cortical volume, and the mean diameter of these spheres is taken as the cortical thickness for a given VOI (Hildebrand & Rüegsegger 1997c). Any pores in the cortical shell therefore alter mean thickness measurements. These are accounted for via filtering steps such as closing and sweep operations, however the endosteal surface maintains some ruffled edges

due to pores on the endosteal and periosteal surfaces, even after filtering. This can result in some spheres taking measurements on ruffled edges which are not representative of the true cortical thickness at that point.

Cortical bone presents a considerably lower surface to volume ratio (Ct.BS/BV) than trabecular bone, causing osteoporotic effects to be smaller in comparison. This was highlighted in the results. No significant differences in Ct.BS/BV were detected following chronic SCI in either bone region (Figures 3.50C and 3.50D). This finding emphasises the significance of available resorption surface area on osteoporosis severity. If the specific surface is initially low, the resorptive effects are also likely to follow suit and take a longer time to accumulate.

In the same manner as Ct.BS/BV, cortical eccentricity (Ecc) was not seen to be significantly affected by SCI in either bone region (Figures 3.50E and 3.50F). This result suggests that the change in mechanical load did not cause a significant alteration to the circularity of the diaphyseal cross section. When analysing the cross-sectional geometry via polar second moment of area (J), the DF exhibited a significant difference after 11 weeks of SCI, whilst the PT did not (Figures 3.50A and 3.50B), indicating that the DF (although remaining relatively circular) experienced a comparatively greater deviation from uniform cortical thickness due to chronic SCI.

Despite the aforementioned changes in Ct.Ar, neither bone region presented a significant difference in cortical tissue mineral density (Ct.TMD) due to SCI (Figures 3.51A and 3.51B). This result suggests that diaphyseal cortical mineral density is maintained during osteoporosis, with the impairment in mechanical performance due to the morphological and topological effects instead.

Analysing the cortical bone at the metaphyseal secondary spongiosa (MSS), percent porosity was not seen to be significantly affected by SCI in either the DF or PT (Figures 3.52A and 3.52B). Pore diameter (Po.Dm) was seen to decrease in the DF, but not in the PT. If the pore diameter were seen to increase, this would suggest that the existing pores were increasing in size as resorption effects increased due to osteoporosis. The finding that average Po.Dm decreased implies that the DF experience a notable increase in new, small pores forming in the metaphyseal cortical bone.

Although the aim of the cortical analysis pre-processing was to remove the pores from the ROIs prior to assessing parameters like Ct.Ar, some pores were still observable in the diaphyseal cortex.. As described on pages 45, 46, 47 and 48, the rat long bone structure differs from the human e.g. the cortical bone contains less Volkmann's canals and no clear definition of organised, uniformly distributed Haversian canals due to the less axial and less uniform arrangement of the concentric lamellar bone formed in the rat femur / tibia. Although possessing a different cortical bone microstructure, the rat femoral and tibial cortex still requires vascular invasion to provide nutrients, precursor cells and signal factors to the cortical remodelling regions, and so the pores observed in the cortical bone which were deemed too small (less than the 10μm resolution of the microCT scans) to be included in the analysis, but were present in the VOIs when assessed qualitatively, were most likely the larger channels in the lamellar bone which allow for vascular invasion of the cortex from the endosteal (marrow) or periosteal blood networks e.g. the nutrient foramen (Shipov *et al.* 2013).

Current Study – Acute SCI

As cortical bone is known to react much slower to SCI than trabecular bone due to the lower specific surface (Osterhoff *et al.* 2016), it was expected that most of the cortical parameters assessed at the 2 week post-injury timepoint in the PT would return no significant differences. This was indeed the case. Tt.Ar, Ma.Ar, Ct.Th, J, Ct.BS/BV, Ecc, Ct.TMD and metaphyseal pore diameter (Po.Dm) were all found to exhibit no significant difference following 2 weeks of SCI (Table 3.7). These results indicate that the cortical bone remains relatively unchanged in the acute stages of SCI, with the aforementioned rapid resorption response primarily affected the trabecular regions.

There were two results, however, which were not consistent with this notion. Cortical porosity (in the metaphyseal cortex) was seen to increase significantly by 51% and diaphyseal cortical area reduced by 6% following acute SCI (Table 3.7). The cortical porosity results highlight the increase in bone remodelling activity of bones with a higher specific surface. As the metaphyseal cortex is understood to be more porous than the diaphyseal cortex in humans (Shim, Pitto & Anderson 2012), this comparatively higher severity of bone loss in response to SCI was expected (Table 3.7). The mild cortical area reduction in the absence of medullary area increase

(endocortical resorption) or total area reduction (periosteal resorption) indicates either that the cortical effects of acute SCI are slow and gradual, or that the initial rapid resorptive effects are quickly recovered by periosteal appositional growth.

Clinical Literature – Acute & Chronic SCI

Assessments of bone in rodent models are most commonly performed via *in vitro* studies from sacrificed animals. Human studies on SCI revolve around *in vivo* solutions which are easy to perform in the clinic, such as peripheral quantitative computed tomography (pQCT). Although different to microCT, pQCT enables measurement of volumetric bone mineral density on the cortical bone. As hydroxyapatite phantoms were utilised in combination with microCT scanning in the current study (see pages 90-91), cortical tissue mineral density (Ct.TMD) results were obtained which enabled further comparisons with the outcomes acquired in clinical studies. Only studies which assess the femoral and tibial diaphyses following complete SCI (as in the current study) are discussed.

A number of clinical studies report reductions in the thickness or diameter of the cortical cross section following chronic SCI. The only clinical investigation on growing bone which describes SCI cortical effects therefore presents as a useful source of comparison to the results presented herein. A study on the tibial diaphysis of male and female children (analogous to the growing rats used here) found that SCI periods of 7 to 10 years resulted in no change in Ct.BMD (Biggin *et al*. 2013). Although the cortical density did not reduce in the growing bone, the total area, cortical area and medullary area z-scores (z-score is a diagnostic measurement used by the NHS which analyses a single measurement against the relevant group mean e.g. a z-score of -2.5 in BMD is the diagnosis threshold for osteoporosis) were -1.8, -3.9 and -0.3 respectively. These results indicate that the cortical thinning effects of SCI on growing long bones are effected predominantly via periosteal resorption as opposed to endocortical resorption. It is important to note that resorption effects happen in tandem with appositional growth arrest in growing bone, and so the total, cortical and medullary area results are a combination of potentially increased resorption and reduced growth. The findings of no change in Ct.BMD and a mild reduction in Ct.Ar are consistent with those observed in the femur bones from the current study.

Eser *et al*. (2004) detected a significant difference in diaphyseal Ct.Th between SCI and age-matched control VOIs from the femur and tibia. The subjects were adult men and varied in time post-injury from 2 months to 50 years. The cortical thickness losses were observed to reduce in severity as time post-injury increased. Although cortical thickness was reduced, no such change in Tt.Ar was found, indicating that the mode of cortical bone thinning was one of endocortical resorption. This was confirmed by a significant 30% increase in Ma.Ar which was maintained once the cortical parameters had reached a steady state. These results indicate a mode of bone loss dominated by endocortical resorption in adults with chronic SCI. In contrast, the current study (no change in Ma.Ar but a reduction in Tt.Ar) highlights the likelihood of growing bone to experience SCI-induced bone loss mainly via periosteal resorption compounded by the impedance of appositional growth due to SCI.

In a study performed on adult men ranging from 9 to 32 years post-injury, Rittweger *et al*. (2010) analysed cortical effects of SCI on the tibial diaphysis. Unlike any other clinical studies into SCI effects on cortical bone, a group difference in Ct.BMD between SCI and CTRL of around -4% occurred when analysing various pairs of patients at different time-points and their age-matched controls. This could potentially be due to increased cortical porosity, which was not examined. Increasing cortical porosity can affect BMD (as the entire VOI attenuation is averaged and so pores would reduce this average) but not TMD (as only the cortical bone attenuation is considered). Tt.Ar was also seen to be significantly reduced in the SCI diaphyses. These results suggest that it is not only the morphological effects which enact the increase fracture risk in cortical bone following chronic SCI. The results from the current study are consistent with the reduction in Tt.Ar, however they show no such reduction in tibial Ct.TMD. This was expected, as the rats in the current study were skeletally immature, and so Ct.TMD would be significantly increasing over time post-injury.

Coupaud *et al*. (2015) observed a significant reduction in Tt.Ar, Ct.BMD and Ct.Th in both the femoral and tibial diaphyses following 12 months of disuse in both men and women. The patients in this study varied from 16 to 76 years of age, highlighting that cortical losses likely occur in the same fashion regardless of the remodelling activity of the individual. These effects have been previously observed to be reduced once steady-state (3→8 years post-injury) is reached (Eser *et al*. 2004).

The same research group (Coupaud *et al*. 2017) analysed the tibial diaphysis in adult patients from both the male (16 years+) and female (post-menopausal 55 years+) populations. The patients were organised into early (<4 years SCI) and chronic (>4 years SCI) groups, and matched with similar aged able-bodied controls. For both groups, Ct.BMD reduced consistently with time post-injury and was significantly different to the able-bodied controls, whilst Ct.Ar was not altered. These results are inconsistent with those in the current study. They suggest that morphological effects of disuse are minimal in cortical bone, and that the main impact of SCI is a reduction in bone density.

McCarthy *et al*. (2012) conducted an investigation into the effects of SCI (1 month→11 years post-injury) on the tibial diaphysis of adult men 21→51 years of age. The patients were split into an acute (<6 months) and a chronic (4.5→11 years) group. It was found that the chronic SCI group exhibited significantly reduced J (resistance to torsion) whilst Ct.Ar and Ct.BMD were not altered. In the acute group, no change in any material or structural parameter was observed. These results suggest that a mild redistribution of cortical material occurs during long-term SCI, however the results do not manifest in adult human bone in acute time spans. The lack of cortical effects in the acute group here is consistent with those from the PT in the current study.

A summary of clinical investigations into SCI effects on diaphyseal cortical bone is presented in Table 5.5:

Study	Scan Type | Age & Species | VOI | Timepoint(s) Post-SCI	Significant Cortical Effects due to SCI | Other Results of Note
Eser *et al.* 2004	pQCT | Varying age adult men | Femoral and tibial diaphysis | 2 months → 50 years	Exponential losses (effects getting less severe with time) in Ct.Th over 5-7 years, with steady state around 8 years | No change in Tt.Ar | Ma.Ar ↑30% and maintained during steady state | No change in Ct.BMD
Biggin *et al.* 2013	pQCT | Male and female children | Tibial diaphysis | 7→10 years	No change in Ct.BMD | Tt.Ar z-score -1.8 | Ct.Ar z-score -3.9 | Ma.Ar z-score -0.3
Rittweger *et al.* 2010	pQCT | Varying age men | Tibial diaphysis | 9→32 years	Ct.BMD ↓4% (mild reduction) | Tt.Ar and Ma.Ar strongly predicted ΔCt.BMD (R^2~0.98) whilst total Ct.BMD did not (R^2=0.58) | Tt.Ar ↓
Coupaud *et al.* 2015	pQCT | Adult men and women 16-76 | Femoral and tibial diaphysis | 4, 8 & 12 months	At 12 months, Tt.Ar, Ct.BMD and Ct.Th all ↓
Coupaud *et al.* 2017	pQCT | Adult men and women | Tibial diaphysis | 6 months → 27 years	Ct.BMD ↓ consistently with time post-injury | No change in Ct.Ar
McCarthy *et al.* 2012	pQCT | Adult men | Tibial diaphysis | 1 month → 11 years	No change in any acute SCI cortical parameters | Ct.BMD and J ↓ in chronic group | No change in Ct.Ar in chronic group
Current Study	uCT | 8 week SD rats | Femoral and tibial diaphysis (metaphyses for porosity) | 2 & 11 weeks	At 11 weeks: Ct.Ar, Tt.Ar, J ↓ in femur | No change in Ct.Th, Ma.Ar, Ct.BS/BV, Eccentricity or Ct.TMD in femur | No change in any cortical parameter in tibia At 2 weeks: Ct.Ar ↓ in tibial diaphysis | %Po ↓ in tibial metaphysis | No change in Tt.Ar, Ma.Ar, Ct.Th, J, Ct.BS/BV, Eccentricity, Ct.TMD or Po.Dm in tibia | Femur not examined at 2 weeks, only 11

Table 5. 5: Clinical studies on diaphyseal cortical bone assessing SCI effects.

Rat Literature – Acute & Chronic SCI

More information is available from growing bone when considering rat models of SCI assessing cortical effects. The results from the current study are largely consistent in the DF for growing rats at the chronic stage, however the chronic PT presented a different response to SCI, as no change in any cortical parameter was detected. The acute DF and PT results followed much the same pattern, however one significant effect was observed in the acute PT, as the metaphyseal porosity significantly increased at 2 weeks post-injury. Only models of complete spinal cord transection are considered here for discussion.

The most acute effects of SCI on cortical bone which have been analysed in the literature were assessed by Peng *et al*. (2020). They observed the femoral diaphysis of 8 week old Wistar rats at 2 and 7 days following transection of the spinal cord at the T3 vertebra. Although no effects were detected in the cortical bone at 2 days, significant decreases in Ct.Ar and Tt.Ar were observed as early as 7 days post-injury, with Ma.Ar also increasing. These results suggest that the immediate response of cortical bone to SCI is bone loss via both endocortical resorption and the arrest of periosteal appositional growth. In the current study by two weeks post-injury, Ct.Ar was significantly reduced, however Tt.Ar and Ma.Ar were not (Table 3.7). This result indicates that (although slower than trabecular) the cortical bone response to SCI is not as slow and gradual as it may appear. Initial significant losses in cortical bone can be cancelled out by growth effects in growing rat models of SCI.

Jiang *et al*. (2007b) studied the effects of T10 transection on the tibial diaphysis in 6 week old SD rats. It was observed at the 3 weeks post-injury timepoint that cortical thickness and polar second moment of area were significantly reduced in SCI bones when compared to age-matched controls. Both total and medullary area had also significantly reduced, indicating that cortical bone loss in the acute stages of SCI on growing bone occurs via a relatively balanced combination of periosteal and endosteal resorption. The results from the current study (two weeks post-injury) are somewhat consistent with these findings as Ct.Ar was seen to reduce significantly in the SCI rats, although no similar reductions in Tt.Ar or Ma.Ar were observed (Table 3.7).

Significant reductions in Ct.Ar, Ma.Ar and a 10% decrease in diaphyseal BMD were observed in the tibial diaphysis of 6 week old SD rats at 4 weeks post-injury. Liu *et al*. (2008) selected T10 transection as the model of SCI here. These results indicate that cortical effects due to SCI are more severe than those observed in the current study chronic PT (Table 5.5).

Williams (2019) performed an in-depth cross sectional study into the effects of SCI on the femoral diaphysis. The rats in question were 12 weeks of age and assessed 2, 6, 10 and 16 weeks post-injury then compared to sham-operated, age-matched controls. Tt.Ar and Ma.Ar were significantly different between SCI and CTRL groups at 6 and 10 weeks post-injury. Decreases in Ecc and J were also found at 10 & 16 and 6, 10 & 16 weeks respectively. Ct.Ar was significantly reduced at all timepoints, whilst Ct.TMD was not altered at any timepoint. These results suggest that the diaphysis in sublesional bones adopts a more slender configuration following chronic SCI, with immediate effects on cortical thinning followed by more gradual changes in material distribution towards a more circular cross section. The results from the current study are mostly consistent with this pattern, although some material redistribution effects (eccentricity) were not observed in the femoral diaphysis at 11 weeks post-injury (Table 5.5). Interestingly Ct.Ar and J both increased as time progressed, although Ct.Ar only followed this pattern in the CTRL bones. These findings highlight the effects of appositional growth which are present in studies utilising adolescent rats <4 months of age (Sengupta 2013). The DF acute results from this investigation are consistent with those in the current study. Cortical porosity increased significantly between SCI and CTRL groups at 2 weeks post-injury, and then recovered to exhibit no difference at any succeeding timepoint. Ct.Ar decreased significantly by 2 weeks, and deteriorated further by the 10 week chronic stage (Table 5.5).

In a similar study on 12 week old Wistar rats, Williams *et al*. (2020) investigated the effects of T9 SC transection at 10 weeks post-injury on the femoral diaphysis, observing significant reductions in Ct.Th, Ct.Ar, Tt.Ar, Ecc and J. The same research group (Williams *et al*. 2022a) conducted a study using 8 week old Wistar rats, assessing the 2, 6, 10 and 16 week post-injury timepoints in the femoral diaphysis following a T9 transection. The parameters were found to be affected in much the same way, with significant differences across all main cortical morphological metrics.

Material redistribution (eccentricity) was once again observed to occur in a delayed fashion with regards to faster-changing parameters like Ct.Ar. These results are similar to those in the current study. They suggest that periosteal expansion is still present in rat bone as old as 12 weeks, and so models utilising older rats >4 months of age should be considered as options to reduce appositional growth effects from results.

In light of this, Williams *et al*. (2022b) investigated the femoral diaphysis of 5 month old (adult) Wistar rats following 1, 2 and 4 weeks of SCI. They observed no significant differences in any of Ct.Th, Ct.TMD, Ct.Ar, Tt.Ar, Ma.Ar, Ecc or J at any timepoint. These results indicate that mature bone in rats responds at a noticeably different rate than growing bone. This seems to happen by a combination of a lower rate of appositional growth but also a slower bone remodelling response.

The fact that mean pore diameter was seen to significantly decrease in the DF following SCI is in contrast to a 2013 study on Haversian remodelling in the Wistar rat femur (Bach-Gansmo *et al*. 2013). This study indicates that Haversian remodelling is virtually absent in the rat femoral cortical bone. The work in this study would need to be repeated and expanded to ensure that the percentage porosity was indeed significantly decreasing with disuse.

Studies which have used rat models of complete SCI to assess cortical parameters at the diaphysis are summarised in Table 5.6:

Study	Scan Type | Age & Species | VOI | Timepoint(s) Post-Injury	Significant Cortical Effects due to SCI | Other Results of Note
Williams 2019	µCT | 12 week Wistar rats | Femoral diaphysis | 2, 6, 10 & 16 weeks	Ct.Ar ↓all timepoints, worst at 6&10 weeks | Tt.Ar ↓6&10 weeks | Ma.Ar ↓6&10 weeks | Ecc ↓10&16 weeks | J ↓6,10&16 weeks | Ct.Ar ↑ in CTRL bones | %Po ↑ at 2 weeks then recovers to same as CTRL | No change in Ct.TMD at any timepoint
Williams *et al.* 2020	µCT | 12 week Wistar rats | Femoral diaphysis | 10 weeks	Ct.Th, Ct.Ar, Tt.Ar, Ecc & J all ↓
Williams *et al.* 2022a	µCT | 8 week Wistar rats | Femoral diaphysis | 2, 6, 10 & 16 weeks	Ct.Ar ↓ at 2,6&10 weeks then recovered by 16 weeks | No change in Ct.TMD at any timepoint | Tt.Ar and Ma.Ar both ↓ at 6&10 weeks then recovered by 16 weeks | Ct.Th ↓ at all timepoints but increased over time in CTRL and SCI | J ↓ at 2,6&16 weeks but recovered with time | Ecc ↓ at 10&16 weeks
Williams *et al.* 2022b	µCT | 5 month SD rats | Femoral diaphysis | 1, 2 & 4 weeks	No change in Ct.Th or Ct.BMD | No change in any morphological or densitometric parameter
Otzel *et al*. 2019	µCT | 4 month SD rats | Femoral diaphysis | 2, 4, 8 & 12 weeks	Ct.Ar and Ct.Th ↓ at 8&12 weeks | Ct.TMD ↓ slightly(2-3%) | No transient increase in SCI parameters but notable increases in CTRL | No change in Oc.S/BS at any timepoint | TRAP serum levels ↑ at 2 weeks
Peng *et al*. 2020	µCT | 8 week Wistar rats | Femoral diaphysis | 2 & 7 days	Ct.Ar, Ct.Th and Tt.Ar ↓ at 7 days | Ma.Ar ↑ at 7 days | No change at 2 days
Liu *et al*. 2008	µCT | 6 week SD rats | Tibial diaphysis | 4 weeks	Ct.Th, Ma.Ar, Ct.Ar and Ct.BMD all ↓
Jiang *et al*. 2007b	µCT | 6 week SD rats | Tibial diaphysis | 3 weeks	Ct.Th, Tt.Ar, Ma.Ar and J all ↓
Current Study	µCT | 8 week SD rats | Femoral and tibial diaphysis (metaphyses for porosity) | 2&11 weeks	At 11 weeks: Ct.Ar, Tt.Ar, J ↓ in femur | No change in Ct.Th, Ma.Ar, Ct.BS/BV, Eccentricity or Ct.TMD in femur | No change in any cortical parameter in tibia At 2 weeks: Ct.Ar ↓ in tibial diaphysis | %Po ↓ in tibial metaphysis | No change in Tt.Ar, Ma.Ar, Ct.Th, J, Ct.BS/BV, Eccentricity, Ct.TMD or Po.Dm in tibia | Femur not examined at 2 weeks, only 11

Table 5. 6: Rat studies on diaphyseal cortical bone assessing SCI effects.

5.1.5 Resorption Activity

Current Study

The results from the TRAP analysis did not return any significant differences in the DF. As mentioned previously, the n=2 sample size in the PT meant that no statistical tests were performed for TRAP quantification in this bone region (Figure 4.19). The finding that osteoclast number and surface percentage did not alter in the chronic stage post-SCI suggests that osteoclast recruitment is unaffected, however the activity of the pre-existing osteoclasts is increased in response to SCI. Further studies on the same rat model of SCI using the same quantification and staining techniques would be insightful, as the analysis in the current study only provides information at a single, chronic timepoint. Acute disuse is commonly understood to evoke a rapid resorption response in bone (Chappard *et al.* 1995, Liu *et al.* 2008), and so histological analysis at this stage would be beneficial to understanding SCI-induced bone loss.

Acute timepoints have been assessed previously in the literature using TRAP staining and quantification. TRAP staining is one of the most widely utilised standard histological stains for analysing osteoclasts and their activity (Hayman 2008). In many of these cases, however, it is restricted to serum level analyses, as opposed to TRAP staining followed by computer-based counting. Only studies which utilise TRAP staining and subsequent digitised quantification to investigate the femur and tibia in disuse are discussed below.

Clinical Literature

The only study (to the author's knowledge) currently in the literature which employs TRAP staining to quantify osteoclasts in human trabeculae following SCI was performed by Chappard *et al*. (1995). The study included 6 female and 14 male adult patients, and assessed their trabecular bone in transiliac biopsies 3 months following traumatic SCI. TRAP staining exhibited a significant increase in osteoclast number per bone area following the period of 3 months post-injury. These results suggest that acute SCI instigates an initial increase in bone resorption via increasing osteoclast recruitment to affected bone sites.

No clinical studies are known to the author which align with the current study's timepoint i.e. which perform osteoclast number or surface quantification in chronic SCI human patients.

Rat Literature

The current study represents (to the author's knowledge) the first time that osteoclasts have been quantified via TRAP staining in a growing rat model of complete SCI. One study has employed TRAP staining to quantify osteoclastic parameters in adult rat trabeculae following complete SCI. Studies involving contusion SCI are presented for additional comparisons.

Zhao *et al*. (2021) investigated 13 month old Wistar rats at 6 weeks post-injury from a T4 spinal cord transection. They observed no significant change in osteoclast surface percentage or normalised osteoclast number in the trabecular bone of the DF MSS. These results are consistent with the current study; they indicate that osteoclast numbers are unchanged by the chronic stages of SCI. Additional points at the more extreme acute and chronic stages would be useful for understanding the time course effects on osteoclast activity and numbers due to complete SCI.

In a study on seven week old SD rats, Morse *et al*. (2008) used TRAP quantification on the growth plate of the DF 10 days following a T10 contusion injury. A significant 330% increase in the normalised osteoclast number was detected at the growth plate, indicating that growing rats present a rapid and noticeable response to acute disuse in terms of resorption activity.

Lin *et al*. (2015) added a useful study to the literature, performing TRAP quantification on the trabeculae bone of mature 4 month old Fischer 344 rats. The model of SCI in this case was a T13 contusion, and the rats were analysed at 16 weeks post-injury. At the proximal tibia MSS, a significant 300% increase in normalised osteoclast number was observed. These results suggest that chronic SCI results in permanently increased levels of osteoclasts in sublesional trabecular bone, which is in contrast to the study by Zhao *et al.* (2021) and the current study.

A summary of the rat studies into SCI using TRAP quantification on trabecular bone is given in Table 5.7:

Study	**SCI Type | Age & Species | VOI | Timepoint(s) Post-Injury**	**TRAP Quantification Results**
Zhao *et al*. 2021	T4 transection | 13 month Wistar rats | DF MSS | 6 weeks	No change in Oc.S/BS or N.Oc/BS
Morse *et al*. 2008	T10 contusion | 7 week SD rats | DF growth plate | 10 days	N.Oc/BS ↑ 330%
Lin *et al*. 2015	T13 contusion | 4 month Fischer rats | PT MSS | 16 weeks	N.Oc/BS ↑ 300%
Current Study	T9 transection | 8 week SD rats Z | DF and PT MSS | 11 weeks	No change in Oc.S/BS or N.Oc/BS in DF or PT

Table 5. 7: Rat studies using TRAP quantification on trabecular bone during SCI.

5.1.6 Bone Microvessel Density

The current study is the first (to the author's knowledge) attempt at analysing intraosseous microvessels during SCI by using quantitative IHC. Various different methods have been employed in clinical and rodent studies to count the number of blood vessels in trabecular bone.. The limitations and benefits of previous techniques in the literature, as well as those for the current study are discussed here.

One study used a digital grid overlay on IHC images of un-decalcified human femur biopsies from the femoral head (Shabestari *et al*. 2016), with the positive (brown stained by DAB) region intersections counted for vertical gridlines and normalised over the capture area. This method is prone to errors in miscounting any potential microvessels of vertical alignment in the analysed image, but benefits from the ability to average counts from multiple human sources.

Another study used CD34 IHC to identify the local structures in the bone remodelling compartment of the human iliac crest trabecular bone, as well as quantify the number of contacting capillaries. The quantification here was performed in a similar manner to the study above, using a measure of 'hits per orthogonal lines' normalised to the sample area (Kristensen *et al*. 2014).

The software Osteomeasure has been used in combination with VEGF immunohistochemistry to quantify marrow sinusoids in the MSS of mouse proximal tibiae (Singbrant *et al*. 2011). This method relies on assumptions of uniform BV density across the entire metaphysis, as the images analysed were of high magnification and therefore did not encompass the entire MSS region.

The method developed herein attempted to address the above issues, by using a computer based quantification performed on metaphyseal images of x40 magnification, encompassing as much of the secondary spongiosa region as possible. In practicality, this region represented about half of all secondary spongiosa in each sample, as the full length and half-breadth of the section could be imaged at x40 magnification.

The results from this method found that intraosseous trabecular microvessels decreased in number density by 11 weeks post-injury in the DF, with the PT results

being inhibited by a reduced sample size (Figures 4.20A and 4.20B). One specimen in the PT group was lost during IHC preparation, and so the PT group size here was n=2, rendering statistical comparisons invalid. The findings here are interesting. It appears that where the trabecular bone recovers some of its volume fraction to control levels by 11 weeks post-injury, the blood network supplying that same bone does not. This effect could be attributed to the age of the rats at the 11 week post-injury timepoint, as it has been proven that marrow microvessels in humans decrease in number both with age and following post-menopausal osteoporosis (Burkhardt *et al*. 1987, Wang *et al*. 2009). The rats in this study were ~5 months of age at the time of sacrifice.

MicroCT has been used to show a decrease in trabecular blood vessel volume in the tibial metaphyses of male C57 mice immobilised via sciatic neurectomy at 4 weeks post-injury. The same study analysed angiogenic marker levels in the blood sera and found a significant decrease, in line with the microCT findings (Ding *et al*. 2012). These results indicate that trabecular microvessel density effects occur in the acute stages post-SCI. The current study does not contain data to compare with this timepoint.

For the cortical blood vessel analysis, no significant effects were detected in either the DF or PT metaphysis following chronic SCI (Figures 4.20C and 4.20D). For the DF, the mean cortical pore diameter was seen to significantly decrease following 11 weeks of SCI (Figure 3.52C). This leads to the assumption that porosity decreased, with blood vessel density likely to follow suit. This was not the case, however, as blood vessel numbers remained unchanged in the cortical regions. This can be understood when considering that a decreased mean pore diameter can indicate an increased density of new, small pores. The existing networks of larger Haversian and Volkmann's canals in the cortical bone are unlikely to be affected by these, meaning that cortical blood vessel density would remain relatively unaffected.

The cortical blood vessel density showing no change is consistent with previous research into rat cortical bone (Bach-Gansmo *et al*. 2013). This study states that cortical remodelling is virtually absent in rat long bones, and so presumably this would mean the same for the blood network following any changes to the bone remodelling balance due to SCI.

5.2 Future Work

5.2.1 MicroCT

The fractal dimension (FD) and trabecular number (Tb.N) results for the chronic DF and PT are interesting (Figures 3.34 and 3.35):

- DF: FD ↓ with Tb.N no change
- PT: FD no change with Tb.N ↓

This result (as discussed in Chapter 3) seems to show that the mode of bone loss in the DF acts to change the morphology and orientation of the trabeculae, as opposed to reducing their number by a considerable amount. As these differences could be partially explained by growth effects in the adolescent rat model used, a study using a skeletally mature model on the trabecular morphometry changes during different timepoints in the development of SCI-induced osteoporosis would be useful. It would serve to determine whether or not the reduction in BV/TV experienced following SCI comes about simply as a consistent thinning of the trabeculae (leading to breaks and a reduced Tb.N) in every affected region, or whether the remodelling effects occur in a less uniform manner in different locations, resulting in altered local morphologies. This in-depth trabecular morphometry study could be strengthened by analyses like ellipsoid factor.

For a future ITA analysis, an insight to be gained would be one into the exact change in node type as time post-SCI progresses. From this study, we can see that by chronic SCI, the trabecular network in the DF and PT changes not only by the standard parameters such as BV/TV, but also by a noticeable drop in the average connectedness of each node. A multi-timepoint cross sectional study could be performed, focusing on the spatial distribution of the low to high N nodes in the bone, as well as the comparative abundances of each node type at early, progressing and chronic SCI. This would test the theory from this study that the bone responds to SCI by preparing the trabecular network to be better suited to load bearing via reducing the number of high-N nodes thereby producing more structures of mechanical superiority (tetrahedrons and triangular pyramids).

The node type distributions in healthy human (from the literature) and rat (from the current study) trabecular bone are consistent in all but one study. Reznikov *et al*. (2020) observed mean relative abundances of 3N, 4N and 5N nodes to be 79%, 17% and 4% respectively (a ratio of 20:4:1) in healthy adult human DF and PT, whereas every other study reports that this ratio is maintained in human, pig and rat femurs and tibiae at approximately 11:3:1 (Reznikov *et al*. 2016, Ben-Zvi *et al*. 2017, Reznikov *et al*. 2017) (Tables 5.2 and 5.3). This difference can potentially be explained by long term transient effects on the topological arrangement of human trabecular bone, however no studies have been undertaken to investigate this. Additionally, if the node type distribution was found to predictably alter with age, no studies exist currently which determine the reasons for this change, and whether or not such changes imply healthy development into old age or the onset of skeletal decline and pathologies.

5.2.2 Histology

The histological analyses performed in this study serve as a baseline for a myriad of potential questions which could be answered using the same rat model of SCI as the one employed here. By utilising IHC markers of various known bone cells and processes, the onset, progression and late-stage environment of SCI-induced osteoporosis can be more comprehensively understood. The stains on osteoclasts and bone blood microvessels in this study can be repeated at different timepoints to understand the coupling between blood supply density and osteoclastic activity and recruitment following complete SCI.

The fact that microvessel density presented a significant decrease following 11 weeks of SCI is interesting (Figure 4.20). The bone appears to be able to recover some of the effects of SCI, but the blood network does not. A future study into the development of the trabecular blood network diminishing with progressing time post-SCI would be useful, in combination with IHC analysis into the angiogenic markers on the bone cells and blood vessels themselves. The exact combinations and numbers of bone and blood vessel angiogenic and osteogenic factors as the condition worsens have yet to be studied in rodent models. Only the end-results have been shown; what causes them is far more difficult to discern. If the key signal factors turned out to be sufficiently similar in number at each stage of SCI-induced osteoporosis in rodent and human

models, this could enable various treatments to improve the bone microstructure and quality in the affected limbs via inhibition or promotion of the relevant angiogenic ligands and receptors.

5.2.3 microCT and Histology Combined

Provided adequate staffing, laboratory space and equipment, microCT and histology could be employed to give us a comprehensive understanding of the exact times and locations in which the essential signal factors and cells are present as SCI progresses. Using a full spectrum of staining targets to show angiogenic and osteogenic signal factors being secreted in the bone would allow for the exact onset of each change in bone quality reduction to be clearly understood. This would be possible if a large-scale study was carried out at every 1 week post-injury, detailing the trabecular thinning, local geometry alteration (open cell to closed cell 3D network), network topology (node abundance and ITA) and cortical porosity effects following SCI. In tandem with this, the study should provide osteoblastic activity markers like Runx2 and Osterix, to show which bone forming signal factors are affected to the greatest extent by the injury. Mineral apposition rate (MAR) could also be performed using calcein double-label staining to determine which osteogenic factors cause the most severe detriment to bone formation due to their absence. For resorption, a similar quantified stain should be provisioned. TRAP staining is ideal for this, allowing for the osteoclastic numbers and activity to be understood, especially in the well documented rapid response phase at 1-2 weeks post-injury (Williams 2019). The accompanying angiogenic effects would be invaluable in providing understanding of how the angiogenic / osteogenic coupling is affected following SCI. Standard endothelial stains like the CD34 used here would allow quantification of the blood vessel density, however further insight could be garnered by double staining using transgenic animals models with immunofluorescence for the main vasculature, with IHC targets overlaid to show the key blood vessels and their associated signal factor aggregations. An example of this is the Osterix-positive osteoblast precursors observed in abundance in the vicinity of type H vessels (Kusumbe, Ramasamy & Adams 2014). It is possible that there are other specialised blood vessels which would bring about increased numbers of other key bone remodelling factors like PDGF-BB and VEGF, however these stains and

assessments have not yet been undertaken. The vascular invasion of newly developing or size-changing cortical pores could be investigated using quantitative histology (as used in this project) and microCT in tandem, but could also be quantified using synchrotron microCT (Shipov *et al.* 2013). In a large scale microCT and histology combination study such as this, every parameter included would add to the overall understanding of the bone quality reduction following SCI, enabling future pharmacological and mechanical treatments to be developed using the most comprehensive knowledgebase possible and potentially providing reliable, consistent markers for the onset of different stages in SCI-OP progression.

5.3 Conclusions

This study characterised the condition of SCI-induced osteoporosis in a rat model of complete SCI at acute and chronic stages. There are various methods for analysing pathologies in bone, and microCT and histology present two analysis routes with which to describe the condition. Several of the analyses performed herein represent the first time such measurements have been performed in a rat model of complete SCI, or in any animal model of disuse.

Nevertheless, many effects of SCI at the acute and chronic stages have been characterised herein, with the standard trabecular and cortical microarchitecture effects studied in depth, and other trabecular changes assessed for the first time in a rat model of complete SCI. Histology has been utilised to further add to the knowledgebase of the condition. Novel research in this study includes:

- The first assessment of disuse (in any capacity – specifically here due to complete SCI) by ITA and node type distribution in a clinical or animal model.
- The first assessment of complete SCI by EF in a rodent model, and the first assessing the acute stage of disuse in either a clinical or animal model.
- The first histological assessment of osteoclast activity and numbers in a growing rat model of SCI.
- The development of a bone microvessel density analysis technique via digitised quantitative IHC which attempts to address the issues faced by those currently in the literature (Shabestari *et al.* 2016, Kristensen *et al.* 2014, Singbrant *et al.* 2011).

The research herein also provides important data on the time course effects of trabecular bone loss due to SCI, for purposes of determining potential timepoints at which recovery begins and / or trabecular BV/TV steady state is reached. Analysing both the DF and PT in a controlled manner has allowed for comparisons to be made with either bone region in the literature where only a single VOI has been examined (Tables 5.1 and 5.6). The data procured from the acute and chronic groups in EF and SMI has added weight to the previously described notion that SMI is not a valid

measurement of mechanical efficiency in trabecular bone (Salmon *et al.* 2015, Doube 2015) (Figure 3.56).

Some unexpected results have been observed. Examples include the lack of change in osteoclast number or osteoclast surface percentage at the chronic timepoint post-SCI and the fact that a noticeable amount of plate-like trabeculae remain even in bones in the chronic stages.

The methods used in the literature to quantify trabecular and marrow microvessel density all vary greatly. Factors such as computer / human based counting methods and utilising overlays on acquired IHC images lead to inconsistent quantification routes. Whether or not these different methods return the same values in the same conditions has not been examined. The method developed for this study attempted to remove human error from the counting process, as well as increasing the size of the ROI so as to provide a more realistic impression of the blood network in the long bone metaphyses; one which did not rely too heavily on assumptions of consistency of blood vessel counts across varying locations. The correct blood vessel quantification choice is for the scientist to select according to the study specifics. This process could be standardised in the same manner as microCT or other forms of bone histomorphometry (Bouxsein *et al*. 2010, Dempster *et al*. 2012).

With microCT, the most affected sites (the distal femur and proximal tibia) were examined in detail, with the morphometric and recently developed topologic analyses of trabecular bone providing more detailed patterns of microarchitectural changes which currently are not examinable using the standard clinical diagnosing tool - DXA. These patterns were observed to change in accordance with the timepoint post-SCI.

The quantified staining method for bone microvessel density attempted to address the issues in human error and the uniformity of blood vessel distribution faced by those found in the literature (Shabestari *et al*. 2016, Kristensen *et al*. 2014, Singbrant *et al*. 2011). The results from the histology section serve to highlight the importance of the potential studies outlined for the future. If interesting results are achievable at a single timepoint using two standard histological stains then the usefulness of a more advanced, multi-timepoint study targeting osteogenic and angiogenic markers becomes apparent.

The importance of research into SCI-induced osteoporosis remains high, with many of the associated cellular and structural affects remaining unstudied. As time progresses, the condition will become fully characterised with the combined efforts of the scientific community, revealing exactly how SCI causes the bone cells to change in their recruitment and activity, how the blood supply to the bone remodelling sites and other regions changes in response to unloading, and what these changes mean to the structural integrity and fracture risk of SCI-affected bone.

References

Adams, J.C. (1992). Biotin amplification of biotin and horseradish-peroxidase signals in histochemical stains. Journal of Histochemistry & Cytochemistry, 40 (10), 1457-1463.

Ahmed, K. (2021) Clinical outcomes and implant design optimisation using numerical modelling. (Doctoral thesis, University College, London, UK). Available from: https://discovery.ucl.ac.uk/id/eprint/10137265/

Allison, N., Brooks, B. (1921). Bone Atrophy. An experimental and clinical study of the changes in bone which result from non−use. Surgery. Gynecol Obstet 33:250–60

Andersen, T.L., Sondergaard, T.E., Skorzynska, K.E., Dagnaes-Hansen, F., Plesner, T.L., Hauge, E.M., Plesner, T., Delaisse, J.M., (2013). Understanding Coupling between Bone Resorption and Formation Are Reversal Cells the Missing Link?. American Journal of Pathology, 183 (1), 235-246.

Armour, B.S., Courtney-Long, E.A., Fox, M.H., Fredine, H., Cahill, A. (2016). Prevalence and Causes of Paralysis-United States, 2013. American Journal of Public Health, 106 (10), 1855-1857.

Bach-Gansmo, F.L., Irvine, S.C., Brüel, A., Thomsen, J.S., Birkedal, H. (2013). Calcified Cartilage Islands in Rat Cortical Bone. Calcif Tissue Int 92, 330–338. https://doi.org/10.1007/s00223-012-9682-6

Ballabriga, A. (2000). Morphological and physiological changes during growth: an update. European journal of clinical nutrition, 54 Suppl 1, S1–S6. https://doi.org/10.1038/sj.ejcn.1600976

Bauman, W. A., Zhang, R. L., Morrison, N., & Spungen, A. M. (2009). Acute suppression of bone turnover with calcium infusion in persons with spinal cord injury. Journal of Spinal Cord Medicine, 32(4), 398–403. http://doi.org/10.1080/10790268.2009.11754393

Belavy, D.L., Beller, G., Ritter, Z., Felsenberg, D. (2011). Bone structure and density via HR-pQCT in 60d bed-rest, 2-years recovery with and without countermeasures. J Musculoskelet Neuronal Interact 11:215–226

Ben-Zvi, Y., Reznikov, N., Shahar, R. and Weiner, S. (2017). 3D architecture of trabecular bone in the pig mandible and femur: Inter-trabecular angle distributions. Front. Mater. 4, 29. doi:10.3389/fmats.2017.00029

Betts, J.G., Young, K.A., Wise, J.A., Johnson, E., Poe, B., Kruse, D.H., Korol, O., Johnson, J.E., Womble, M., DeSaix, P. (2017). Anatomy and Physiology. 1st edn. Houston: Rice University OpenStax. Available from: https://openstax.org/details/books/anatomy-and-physiology

Birmingham, E., Niebur, G.L., McHugh, P.E., Shaw, G., Barry, F.P., McNamara, L.M. (2012). Osteogenic differentiation of mesenchymal stem cells is regulated by osteocyte and osteoblast cells in a simplified bone niche. European Cells & Materials, 23 13-27.

Blair, H. C., Larrouture, Q. C., Tourkova, I. L., Liu, L., Bian, J. H., Stolz, D. B., Nelson, D. J., & Schlesinger, P. H. (2018). Support of bone mineral deposition by regulation of pH. American journal of physiology. Cell physiology, 315(4), C587–C597. https://doi.org/10.1152/ajpcell.00056.2018

Bliuc, D., Nguyen, N. D., Nguyen, T. V., Eisman, J. A., & Center, J. R. (2013). Compound risk of high mortality following osteoporotic fracture and refracture in elderly women and men. Journal of bone and mineral research : the official journal of the American Society for Bone and Mineral Research, 28(11), 2317–2324. https://doi.org/10.1002/jbmr.1968

Blouin, S., Gallois, Y., Moreau, M. F., Baslé, M. F., & Chappard, D. (2007). Disuse and orchidectomy have additional effects on bone loss in the aged male rat. Osteoporosis international : a journal established as result of cooperation between the European Foundation for Osteoporosis and the National Osteoporosis Foundation of the USA, 18(1), 85–92. https://doi.org/10.1007/s00198-006-0197-8

Boin, M. & Haibel, A. (2006). Compensation of ring artefacts in synchrotron tomographic images. Opt. Express 14, 12071-12075

Bonewald, L.F. (2011). The Amazing Osteocyte. Journal of Bone and Mineral Research, 26 (2), 229-238.

Bouxsein, M. L., Boyd, S. K., Christiansen, B. A., Guldberg, R. E., Jepsen, K. J., & Müller, R. (2010). Guidelines for assessment of bone microstructure in rodents using micro-computed tomography. Journal of bone and mineral research : the official journal of the American Society for Bone and Mineral Research, 25(7), 1468–1486. https://doi.org/10.1002/jbmr.141

Boyle, W.J., Simonet, W.S. and Lacey, D.L. (2003). Osteoclast differentiation and activation. Nature, 423 (6937), 337-342.

Brandi, M.L. & Collin-Osdoby, P. (2006). Vascular biology and the skeleton. Journal of Bone and Mineral Research, 21 (2), 183-192.

Brandi, M.L. (2009). Microarchitecture, the key to bone quality, Rheumatology, Volume 48, Issue 4, Pages iv3–iv8, https://doi.org/10.1093/rheumatology/kep273

Brent, M. B., Lodberg, A., Thomsen, J. S., & Brüel, A. (2020). Rodent model of disuse-induced bone loss by hind limb injection with botulinum toxin A. MethodsX, 7, 101079. https://doi.org/10.1016/j.mex.2020.101079

Bruker. (2011a). Bone mineral density (BMD) and tissue mineral trabecular density (TMD) calibration and measurement by micro-CT using Brucker-MicroCT CT-analyser. Available from: https://medicine.temple.edu/sites/medicine/files/files/ct_analyzer.pdf.

Bruker. (2011b). C.T. Analysis of Bone by Micro-CT- General Information. Available from: http://umanitoba.ca/faculties/medicine/nuits/cacs/sam/media/MN001_Bone_microCT_analysis_general.pdf

Bruker. (2011c). NRecon User Manual. Available from: https://umanitoba.ca/faculties/health_sciences/medicine/units/cacs/sam/media/NReconUserManual.pdf

Bruker (2016). Structural Parameters Measured by the SkyscanTM CT-Analyser Software. Available from: http://www.skyscan.com/next/ctan03.pdf.

Burkhardt, R., Kettner, G., Böhm, W., Schmidmeier, M., Schlag, R., Frisch, B., Mallmann, B., Eisenmenger, W., & Gilg, T. (1987). Changes in trabecular bone, hematopoiesis and bone marrow vessels in aplastic anemia, primary osteoporosis, and old age: a comparative histomorphometric study. Bone, 8(3), 157–164. https://doi.org/10.1016/8756-3282(87)90015-9

Cao, X. (2018). RANKL-RANK signalling regulates osteoblast differentiation and bone formation. Bone Research, 6.

Carmeliet, P. & Jain, R.K. (2011). Molecular mechanisms and clinical applications of angiogenesis. Nature, 473 (7347), 298-307.

Chantraine, A., Nusgens, B., Lapiere, C.M. (1986). Bone remodeling during the development of osteoporosis in paraplegia. Calcif Tissue Int 38:323–327

Chappard, D., Minaire, P., Privat, C., Berard, E., Mendoza-Sarmiento, J., Tournebise, H., Basle, M., Audran, M., Rebel, A., Picot, C. and Gaud, C. (1995). Effects of tiludronate on bone loss in paraplegic patients. J Bone Miner Res, 10: 112-118. https://doi.org/10.1002/jbmr.5650100116

Chappard, D., Legrand, E., Haettich, B., Chalès, G., Auvinet, B., Eschard, J. P., Hamelin, J. P., Baslé, M. F., & Audran, M. (2001a). Fractal dimension of trabecular bone: comparison of three histomorphometric computed techniques for measuring the architectural two-dimensional complexity. The Journal of pathology, 195(4), 515–521. https://doi.org/10.1002/path.970

Chappard, D., Chennebault, A., Moreau, M., Legrand, E., Audran, M., & Basle, M. F. (2001b). Texture analysis of X-ray radiographs is a more reliable descriptor of bone loss than mineral content in a rat model of localized disuse induced by the Clostridium botulinum toxin. Bone, 28(1), 72–79. https://doi.org/10.1016/s8756-3282(00)00438-5

Chappard, C., Marchadier, A., & Benhamou, C. L. (2008). Side-to-side and within-side variability of 3D bone microarchitecture by conventional micro-computed tomography of paired iliac crest biopsies. Bone, 43(1), 203–208. https://doi.org/10.1016/j.bone.2008.02.019

Cheriyan, T., Ryan, D. J., Weinreb, J. H., Cheriyan, J., Paul, J. C., Lafage, V., Kirsch, T., & Errico, T. J. (2014). Spinal cord injury models: a review. Spinal cord, 52(8), 588–595. https://doi.org/10.1038/sc.2014.91

Cheung, W. Y., Liu, C., Tonelli-Zasarsky, R. M., Simmons, C. A., & You, L. (2011). Osteocyte apoptosis is mechanically regulated and induces angiogenesis in vitro. Journal of orthopaedic research : official publication of the Orthopaedic Research Society, 29(4), 523–530. https://doi.org/10.1002/jor.21283

Chim, S. M., Tickner, J., Chow, S. T., Kuek, V., Guo, B., Zhang, G., Rosen, V., Erber, W., & Xu, J. (2013). Angiogenic factors in bone local environment. Cytokine & growth factor reviews, 24(3), 297–310. https://doi.org/10.1016/j.cytogfr.2013.03.008

Choi, I. H., Ahn, J. H., Chung, C. Y., & Cho, T. J. (2000). Vascular proliferation and blood supply during distraction osteogenesis: a scanning electron microscopic observation. Journal of orthopaedic research : official publication of the Orthopaedic Research Society, 18(5), 698–705. https://doi.org/10.1002/jor.1100180504

Choo, A. M., Liu, J., Liu, Z., Dvorak, M., Tetzlaff, W., & Oxland, T. R. (2009). Modeling spinal cord contusion, dislocation, and distraction: characterization of vertebral clamps, injury severities, and node of Ranvier deformations. Journal of neuroscience methods, 181(1), 6–17. https://doi.org/10.1016/j.jneumeth.2009.04.007

Civin, C. I., Strauss, L. C., Brovall, C., Fackler, M. J., Schwartz, J. F., & Shaper, J. H. (1984). Antigenic analysis of hematopoiesis. III. A hematopoietic progenitor cell surface antigen defined by a monoclonal antibody raised against KG-1a cells. Journal of immunology (Baltimore, Md. : 1950), 133(1), 157–165.

CAP College of American Pathologists (2012). Paraffin Microtomy. Anatomic Pathology Checklist. (1): 23.

Collin-Osdoby, P. (1994). Role of vascular endothelial cells in bone biology. Journal of Cellular Biochemistry 55: 304–9.

Colombo, A., Hoogland, M., Coqueugniot, H., Dutour, O., & Waters-Rist, A. (2018). Trabecular bone microarchitecture analysis, a way for an early detection of genetic dwarfism? Case study of a dwarf mother's offspring. International journal of paleopathology, 20, 65–71. https://doi.org/10.1016/j.ij2017.12.002

Coons, A.H., Creech, H.J. & Jones, R.N. (1941) Immunological properties of an antibody containing a fluorescent group. Proceedings of the Society for Experimental Biology and Medicine, 47 (2), 200-202.

Coupaud, S., Jack, L. P., Hunt, K. J., & Allan, D. B. (2009). Muscle and bone adaptations after treadmill training in incomplete Spinal Cord Injury: a case study using peripheral Quantitative Computed Tomography. Journal of musculoskeletal & neuronal interactions, 9(4), 288–297.

Coupaud, S., McLean, A. N., Lloyd, S., & Allan, D. B. (2012). Predicting patient-specific rates of bone loss at fracture-prone sites after spinal cord injury. Disability and rehabilitation, 34(26), 2242–2250. https://doi.org/10.3109/09638288.2012.681831

Dabney, K. W., Ehrenshteyn, M., Agresta, C. A., Twiss, J. L., Stern, G., Tice, L., & Salzman, S. K. (2004). A model of experimental spinal cord trauma based on computer-controlled intervertebral distraction: characterization of graded injury. Spine, 29(21), 2357–2364. https://doi.org/10.1097/01.brs.0000143108.65385.74

Dauty, M., Perrouin Verbe, B., Maugars, Y., Dubois, C., & Mathe, J. F. (2000). Supralesional and sublesional bone mineral density in spinal cord-injured patients. Bone, 27(2), 305–309. https://doi.org/10.1016/s8756-3282(00)00326-4

Davis, G.R. & Elliot, J.C. (2006). Artefacts in X-ray microtomography of materials. Mat. Sci. Eng. 22 [9] 1011-1018.

Dawson, A.B. (1925). The age order of epiphyseal union in the long bones of the albino rat. Anatomical Record, 31 (1), 1-17.

Delaisse, J.M. (2016). The reversal phase of the bone-remodeling cycle: cellular prerequisites for coupling resorption and formation (vol 3, 561, 2016). Bonekey Reports, 5.

Dempster, D. W., Compston, J. E., Drezner, M. K., Glorieux, F. H., Kanis, J. A., Malluche, H., Meunier, P. J., Ott, S. M., Recker, R. R., & Parfitt, A. M. (2012). Standardized nomenclature, symbols, and units for bone histomorphometry: a 2012 update of the report of the ASBMR Histomorphometry Nomenclature Committee. Journal of bone and mineral research : the official journal of the American Society for Bone and Mineral Research, 28(1), 2–17. https://doi.org/10.1002/jbmr.1805

Ding, W. G., Yan, W. H., Wei, Z. X., & Liu, J. B. (2012). Difference in intraosseous blood vessel volume and number in osteoporotic model mice induced by spinal cord injury and sciatic nerve resection. Journal of bone and mineral metabolism, 30(4), 400–407. https://doi.org/10.1007/s00774-011-0328-y

Donahue, H. J., McLeod, K. J., Rubin, C. T., Andersen, J., Grine, E. A., Hertzberg, E. L., & Brink, P. R. (1995). Cell-to-cell communication in osteoblastic networks: cell line-dependent hormonal regulation of gap junction function. Journal of bone and mineral research : the official journal of the American Society for Bone and Mineral Research, 10(6), 881–889. https://doi.org/10.1002/jbmr.5650100609

Doube, M. (2015). The ellipsoid factor for quantification of rods, plates, and intermediate forms in 3D geometries. Frontiers in Endocrinology, 6.

Doube, M., Kłosowski, M. M., Arganda-Carreras, I., Cordelières, F. P., Dougherty, R. P., Jackson, J. S., Schmid, B., Hutchinson, J. R., & Shefelbine, S. J. (2010). BoneJ: Free and extensible bone image analysis in ImageJ. Bone, 47(6), 1076–1079. https://doi.org/10.1016/j.bone.2010.08.023

Downey, P.A. and Siegel, M.I. (2006) Bone biology and the clinical implications for osteoporosis. Physical Therapy, 86 (1), 77-91.

Drake, F. H., Dodds, R. A., James, I. E., Connor, J. R., Debouck, C., Richardson, S., Lee-Rykaczewski, E., Coleman, L., Rieman, D., Barthlow, R., Hastings, G., & Gowen, M. (1996). Cathepsin K, but not cathepsins B, L, or S, is abundantly expressed in human osteoclasts. The Journal of biological chemistry, 271(21), 12511–12516. https://doi.org/10.1074/jbc.271.21.12511

Ducy, P., Desbois, C., Boyce, B., Pinero, G., Story, B., Dunstan, C., Smith, E., Bonadio, J., Goldstein, S., Gundberg, C., Bradley, A., & Karsenty, G. (1996). Increased bone formation in osteocalcin-deficient mice. Nature, 382(6590), 448–452. https://doi.org/10.1038/382448a0

Dudley-Javoroski, S., & Shields, R. K. (2012). Regional cortical and trabecular bone loss after spinal cord injury. Journal of Rehabilitation Research and Development, 49(9), 1365–76. http://doi.org/10.1682/JRRD.2011.12.0245

Eriksen, E. F., Melsen, F., & Mosekilde, L. (1984). Reconstruction of the resorptive site in iliac trabecular bone: a kinetic model for bone resorption in 20 normal individuals. Metabolic bone disease & related research, 5(5), 235–242. https://doi.org/10.1016/0221-8747(84)90065-1

Eser, P., Frotzler, A., Zehnder, Y., Wick, L., Knecht, H., Denoth, J., & Schiessl, H. (2004). Relationship between the duration of paralysis and bone structure: a pQCT study of spinal cord injured individuals. Bone, 34(5), 869–880. https://doi.org/10.1016/j.bone.2004.01.001

Eser, P., Frotzler, A., Zehnder, Y., Schiessl, H., & Denoth, J. (2005). Assessment of anthropometric, systemic, and lifestyle factors influencing bone status in the legs of spinal cord injured individuals. Osteoporosis international : a journal established as result of cooperation between the European Foundation for Osteoporosis and the National Osteoporosis Foundation of the USA, 16(1), 26–34. https://doi.org/10.1007/s00198-004-1638-x

Esposito, R. (2021). Detection Methods for IHC. Available from https://www.enzolifesciences.com/science-center/technotes/2019/august/what-are-the-different-detection-methods-for ihc?/#:~:text=Thus%2C%20the%20LSAB%20method%20reduces,conjugated%20to%20the%20reporter%20enzyme.>.

Everts, V., Delaissé, J. M., Korper, W., Jansen, D. C., Tigchelaar-Gutter, W., Saftig, P., & Beertsen, W. (2002). The bone lining cell: its role in cleaning Howship's lacunae and initiating bone formation. Journal of bone and mineral research : the official journal of the American Society for Bone and Mineral Research, 17(1), 77–90. https://doi.org/10.1359/jbmr.2002.17.1.77

Fang, B., Wang, H., Sun, X. J., Li, X. Q., Ai, C. Y., Tan, W. F., White, P. F., & Ma, H. (2013). Intrathecal transplantation of bone marrow stromal cells attenuates blood-spinal cord barrier disruption induced by spinal cord ischemia-reperfusion injury in rabbits. Journal of vascular surgery, 58(4), 1043–1052. https://doi.org/10.1016/j.jvs.2012.11.087

Fanucci, E., Manenti, G., Masala, S., Laviani, F., Di Costanzo, G., Ludovici, A., Cozzolino, V., Floris, R., & Simonetti, G. (2007). Multiparameter characterisation of vertebral osteoporosis with 3-T MR. La Radiologia medica, 112(2), 208–223. https://doi.org/10.1007/s11547-007-0136-6

Feldkamp, L.A., Davis, L.C., Kress, J.W. (1984). Practical cone-beam algorithm. J. Opt. Soc. Am; 1 (6):612-619.

Feldkamp, L. A., Goldstein, S. A., Parfitt, A. M., Jesion, G., & Kleerekoper, M. (1989). The direct examination of three-dimensional bone architecture in vitro by computed tomography. Journal of Bone and Mineral Research, 4(1), 3–11. http://doi.org/10.1002/jbmr.5650040103

Fiford, R. J., Bilston, L. E., Waite, P., & Lu, J. (2004). A vertebral dislocation model of spinal cord injury in rats. Journal of neurotrauma, 21(4), 451–458. https://doi.org/10.1089/089771504323004593

Fisher, R., Perkins, S., Walker, A. & Wolfart, E. (2004) Hypermedia Image Processing Reference 2 (HIPR2). University of Edinburgh. Available from: https://homepages.inf.ed.ac.uk/rbf/HIPR2/gsmooth.html

Florencio-Silva, R., Sasso, G. R., Sasso-Cerri, E., Simões, M. J., & Cerri, P. S. (2015). Biology of Bone Tissue: Structure, Function, and Factors That Influence Bone Cells. BioMed research international, 2015, 421746. https://doi.org/10.1155/2015/421746

Franceschi, R.T. & Xiao, G.Z. (2003). Regulation of the osteoblast-specific transcription factor, runx2: Responsiveness to multiple signal transduction pathways. Journal of Cellular Biochemistry, 88 (3), 446-454.

Franz-Odendaal, T.A., Hall, B.K. & Witten, P.E. (2006). Buried alive: How osteoblasts become osteocytes. Developmental Dynamics, 235 (1), 176-190.

Frost, H.M. (2003). A 2003 update of bone physiology and Wolff's Law for clinicians. Angle Orthodontist, 74 (1), 3-15.

Frotzler, A., Berger, M., Knecht, H., & Eser, P. (2008). Bone steady-state is established at reduced bone strength after spinal cord injury: a longitudinal study using peripheral quantitative computed tomography (pQCT). Bone, 43(3), 549–555. https://doi.org/10.1016/j.bone.2008.05.006

Fukada, E. & Yasuda, I. (1957). On the piezoelectric effect of bone. Journal of the Physical Society of Japan, 12 (10), 1158-1162.

Gaêta-Araujo, H., Oliveira-Santos, N., Brasil, D. M., do Nascimento, E., Madlum, D. V., Haiter-Neto, F., & Oliveira-Santos, C. (2019). Effect of micro-computed tomography reconstruction protocols on bone fractal dimension analysis. Dento maxillo facial radiology, 48(8), 20190235. https://doi.org/10.1259/dmfr.20190235

Galvão, M. J., Santos, A., Ribeiro, M. D., Ferreira, A., & Nolasco, F. (2011). Optimization of the tartrate-resistant acid phosphatase detection by histochemical method. European journal of histochemistry : EJH, 55(1), e1. https://doi.org/10.4081/ejh.2011.e1

Garland, D. E., Stewart, C. A., Adkins, R. H., Hu, S. S., Rosen, C., Liotta, F. J., & Weinstein, D. A. (1992). Osteoporosis after spinal cord injury. Journal of orthopaedic research : official publication of the Orthopaedic Research Society, 10(3), 371–378. https://doi.org/10.1002/jor.1100100309

Gasser, J. & Kneissel, M. (2017). Bone Physiology and Biology. DOI: 10.1007/978-3-319-56192-9_2.

Ghasemlou, N., Kerr, B. J., & David, S. (2005). Tissue displacement and impact force are important contributors to outcome after spinal cord contusion injury. Experimental neurology, 196(1), 9–17. https://doi.org/10.1016/j.expneurol.2005.05.017

Gibson L. J. (1985). The mechanical behaviour of cancellous bone. Journal of biomechanics, 18(5), 317–328. https://doi.org/10.1016/0021-9290(85)90287-8

Goff, M. G., Slyfield, C. R., Kummari, S. R., Tkachenko, E. V., Fischer, S. E., Yi, Y. H., Jekir, M. G., Keaveny, T. M., & Hernandez, C. J. (2012). Three-dimensional characterization of resorption cavity size and location in human vertebral trabecular bone. Bone, 51(1), 28–37. https://doi.org/10.1016/j.bone.2012.03.028

Gong, J. K., Arnold, J. S., & Cohn, S. H. (1964). Composition of trabecular and cortical bone. The Anatomical record, 149, 325–331. https://doi.org/10.1002/ar.1091490303

Graham, R. C., Jr, & Karnovsky, M. J. (1966). The early stages of absorption of injected horseradish peroxidase in the proximal tubules of mouse kidney: ultrastructural cytochemistry by a new technique. The journal of histochemistry and cytochemistry : official journal of the Histochemistry Society, 14(4), 291–302. https://doi.org/10.1177/14.4.291

Grun, T. B., & Nebelsick, J. H. (2018). Structural design of the echinoid's trabecular system. PloS one, 13(9), e0204432. https://doi.org/10.1371/journal.pone.0204432

Guertin, P. A. (2011). Adaptations of the Motor System in Animal Models of Spinal Cord Injury and Disuse. Biomechanics in Applications. IntechOpen. London. 10.5772/22492.

Harada, T., Nakano, K., Matuda, H., Muraoka, R., Tomoda, M., Yokoi, Y., Yamada, K. & Okafuji, N. (2012). Immunohistochemical Expression of Osterix Appearing in the Mouse Orthodontic Periodontal Tension Sides. Journal of Hard Tissue Biology, 21 (3), 321-328.

Hauge, E. M., Qvesel, D., Eriksen, E. F., Mosekilde, L., & Melsen, F. (2001). Cancellous bone remodeling occurs in specialized compartments lined by cells expressing osteoblastic markers. Journal of bone and mineral research : the official journal of the American Society for Bone and Mineral Research, 16(9), 1575–1582. https://doi.org/10.1359/jbmr.2001.16.9.1575

Hayman A. R. (2008). Tartrate-resistant acid phosphatase (TRAP) and the osteoclast/immune cell dichotomy. Autoimmunity, 41(3), 218–223. https://doi.org/10.1080/08916930701694667

Heimburger R. F. (2005). Return of function after spinal cord transection. Spinal cord, 43(7), 438–440. https://doi.org/10.1038/sj.sc.3101748

Henneberry, M.O., Engel, G. & Grayhack, J.T. (1979). Acid-Phosphatase. Urologic Clinics of North America, 6 (3), 629-641.

Herman, G.T. (2009). Fundamentals of Computerised Tomography: Image Reconstruction from Projections, Second Edition. 1-297. Available from: https://link.springer.com/book/10.1007/978-1-84628-723-7

Hernlund, E., Svedbom, A., Ivergård, M., Compston, J., Cooper, C., Stenmark, J., McCloskey, E. V., Jönsson, B., & Kanis, J. A. (2013). Osteoporosis in the European Union: medical management, epidemiology and economic burden. A report prepared in collaboration with the International Osteoporosis Foundation (IOF) and the European Federation of Pharmaceutical Industry Associations (EFPIA). Archives of osteoporosis, 8(1), 136. https://doi.org/10.1007/s11657-013-0136-1

Hewitt, S. M., Baskin, D. G., Frevert, C. W., Stahl, W. L., & Rosa-Molinar, E. (2014). Controls for immunohistochemistry: the Histochemical Society's standards of practice for validation of immunohistochemical assays. The journal of histochemistry and cytochemistry : official journal of the Histochemistry Society, 62(10), 693–697. https://doi.org/10.1369/0022155414545224

Hildebrand, T., & Rüegsegger, P. (1997a). Quantification of Bone Microarchitecture with the Structure Model Index. Computer methods in biomechanics and biomedical engineering, 1(1), 15–23. https://doi.org/10.1080/01495739708936692

Hildebrand, T., Laib, A., Ulrich, D., Kohlbrenner, A. & Rüegsegger, P. (1997b). Bone structure as revealed by microtomography. Proc. SPIE, 3149, 34-43.

Hildebrand, T. & Rüegsegger, P. (1997c). A new method for the model-independent assessment of thickness in three-dimensional images. J. Microsc., 185, 67–75.

Hildebrand, T., Laib, A., Müller, R., Dequeker, J., & Rüegsegger, P. (1999). Direct three-dimensional morphometric analysis of human cancellous bone: microstructural data from spine, femur, iliac crest, and calcaneus. Journal of bone and mineral research : the official journal of the American Society for Bone and Mineral Research, 14(7), 1167–1174. https://doi.org/10.1359/jbmr.1999.14.7.1167

Hlaing, T. T., & Compston, J. E. (2014). Biochemical markers of bone turnover - uses and limitations. Annals of clinical biochemistry, 51(Pt 2), 189–202. https://doi.org/10.1177/0004563213515190

Hoffman, E. A., Frey, B. L., Smith, L. M., & Auble, D. T. (2015). Formaldehyde crosslinking: a tool for the study of chromatin complexes. The Journal of biological chemistry, 290(44), 26404–26411. https://doi.org/10.1074/jbc.R115.651679

Ide, H., Seligson, D. B., Memarzadeh, S., Xin, L., Horvath, S., Dubey, P., Flick, M. B., Kacinski, B. M., Palotie, A., & Witte, O. N. (2002). Expression of colony-stimulating factor 1 receptor during prostate development and prostate cancer progression. Proceedings of the National Academy of Sciences of the United States of America, 99(22), 14404–14409. https://doi.org/10.1073/pnas.222537099

Kabel, J., Odgaard, A., van Rietbergen, B., & Huiskes, R. (1999). Connectivity and the elastic properties of cancellous bone. Bone, 24(2), 115–120. https://doi.org/10.1016/s8756-3282(98)00164-1

Jiang, S. D., Jiang, L. S., & Dai, L. Y. (2007a). Changes in bone mass, bone structure, bone biomechanical properties, and bone metabolism after spinal cord injury: a 6-month longitudinal study in growing rats. Calcified tissue international, 80(3), 167–175. https://doi.org/10.1007/s00223-006-0085-4

Jiang, S.-D., Shen, C., Jiang, L.-S., & Dai, L.-Y. (2007b). Differences of bone mass and bone structure in osteopenic rat models caused by spinal cord injury and ovariectomy. Osteoporosis International, 18(6), 743–750. http://doi.org/10.1007/s00198-006-0299-3

Jensen-Jarolim, E. (2017). Comparative Medicine: Disorders Linking Humans with their Animals. 1st edn. Springer International Publishing. ISBN 978-3-319-47007-8. DOI 10.1007/978-3-319-47007-8.

Johnell, O., & Kanis, J. A. (2006). An estimate of the worldwide prevalence and disability associated with osteoporotic fractures. Osteoporosis international : a journal established as result of cooperation between the European Foundation for Osteoporosis and the National Osteoporosis Foundation of the USA, 17(12), 1726–1733. https://doi.org/10.1007/s00198-006-0172-4

Kanis J. A. (1994). Assessment of fracture risk and its application to screening for postmenopausal osteoporosis: synopsis of a WHO report. WHO Study Group. Osteoporosis international : a journal established as result of cooperation between the European Foundation for Osteoporosis and the National Osteoporosis Foundation of the USA, 4(6), 368–381. https://doi.org/10.1007/BF01622200

Kanis, J.A. (2002). Diagnosis of osteoporosis and assessment of fracture risk. Lancet, 359(9321):1929-36. doi: 10.1016/S0140-6736(02)08761-5. PMID: 12057569.

Kazakia, G. J., Tjong, W., Nirody, J. A., Burghardt, A. J., Carballido-Gamio, J., Patsch, J. M., Link, T., Feeley, B. T., & Ma, C. B. (2014). The influence of disuse on bone microstructure and mechanics assessed by HR-pQCT. Bone, 63, 132–140. https://doi.org/10.1016/j.bone.2014.02.014

Kiel, M. J., & Morrison, S. J. (2008). Uncertainty in the niches that maintain haematopoietic stem cells. Nature reviews. Immunology, 8(4), 290–301. https://doi.org/10.1038/nri2279

Kim, H. H., Shin, H. S., Kwak, H. J., Ahn, K. Y., Kim, J. H., Lee, H. J., Lee, M. S., Lee, Z. H., & Koh, G. Y. (2003). RANKL regulates endothelial cell survival through the phosphatidylinositol 3'-kinase/Akt signal transduction pathway. FASEB journal : official publication of the Federation of American Societies for Experimental Biology, 17(14), 2163–2165. https://doi.org/10.1096/fj.03-0215fje

Kim, J. N., Lee, J. Y., Shin, K. J., Gil, Y. C., Koh, K. S., & Song, W. C. (2015). Haversian system of compact bone and comparison between endosteal and periosteal sides using three-dimensional reconstruction in rat. Anatomy & cell biology, 48(4), 258–261. https://doi.org/10.5115/acb.2015.48.4.258

Kobayashi, Y., Uehara, S., Udagawa, N., & Takahashi, N. (2016). Regulation of bone metabolism by Wnt signals. Journal of biochemistry, 159(4), 387–392. https://doi.org/10.1093/jb/mvv124

Kreja, L., Brenner, R. E., Tautzenberger, A., Liedert, A., Friemert, B., Ehrnthaller, C., Huber-Lang, M., & Ignatius, A. (2010). Non-resorbing osteoclasts induce migration and osteogenic differentiation of mesenchymal stem cells. Journal of cellular biochemistry, 109(2), 347–355. https://doi.org/10.1002/jcb.22406

Kristensen, H. B., Andersen, T. L., Marcussen, N., Rolighed, L., & Delaisse, J. M. (2013). Increased presence of capillaries next to remodeling sites in adult human cancellous bone. Journal of bone and mineral research : the official journal of the American Society for Bone and Mineral Research, 28(3), 574–585. https://doi.org/10.1002/jbmr.1760

Kristensen, H. B., Andersen, T. L., Marcussen, N., Rolighed, L., & Delaisse, J. M. (2014). Osteoblast recruitment routes in human cancellous bone remodeling. The American journal of pathology, 184(3), 778–789. https://doi.org/10.1016/j.ajpath.2013.11.022

Kuhn, J. L., Goldstein, S. A., Feldkamp, L. A., Goulet, R. W., & Jesion, G. (1990). Evaluation of a microcomputed tomography system to study trabecular bone structure. Journal of orthopaedic research : official publication of the Orthopaedic Research Society, 8(6), 833–842. https://doi.org/10.1002/jor.1100080608

Kuriakose, D., & Xiao, Z. (2020). Pathophysiology and Treatment of Stroke: Present Status and Future Perspectives. International journal of molecular sciences, 21(20), 7609. https://doi.org/10.3390/ijms21207609

Kusumbe, A. P., Ramasamy, S. K., & Adams, R. H. (2014). Coupling of angiogenesis and osteogenesis by a specific vessel subtype in bone. Nature, 507(7492), 323–328. https://doi.org/10.1038/nature13145

Lafage-Proust, M. H., Roche, B., Langer, M., Cleret, D., Vanden Bossche, A., Olivier, T., & Vico, L. (2015). Assessment of bone vascularization and its role in bone remodeling. BoneKEy reports, 4, 662. https://doi.org/10.1038/bonekey.2015.29

Lamp, E. C., & Drexler, H. G. (2000). Biology of tartrate-resistant acid phosphatase. Leukemia & lymphoma, 39(5-6), 477–484. https://doi.org/10.3109/10428190009113378

Lanza, F., Healy, L., & Sutherland, D. R. (2001). Structural and functional features of the CD34 antigen: an update. Journal of biological regulators and homeostatic agents, 15(1), 1–13.

Lau, R. Y., & Guo, X. (2011). A review on current osteoporosis research: with special focus on disuse bone loss. Journal of osteoporosis, 2011, 293808. https://doi.org/10.4061/2011/293808

Laurent, M. R., Jardí, F., Dubois, V., Schollaert, D., Khalil, R., Gielen, E., Carmeliet, G., Claessens, F., & Vanderschueren, D. (2016). Androgens have antiresorptive effects on trabecular disuse osteopenia independent from muscle atrophy. Bone, 93, 33–42. https://doi.org/10.1016/j.bone.2016.09.011

Lee, B. B., Cripps, R. A., Fitzharris, M., & Wing, P. C. (2013). The global map for traumatic spinal cord injury epidemiology: update 2011, global incidence rate. Spinal Cord, 52(2), 110–116. http://doi.org/10.1038/sc.2012.158

Lelovas, P. P., Xanthos, T. T., Thoma, S. E., Lyritis, G. P., & Dontas, I. A. (2008). The laboratory rat as an animal model for osteoporosis research. Comparative medicine, 58(5), 424–430.

Li, J., Sarosi, I., Yan, X. Q., Morony, S., Capparelli, C., Tan, H. L., McCabe, S., Elliott, R., Scully, S., Van, G., Kaufman, S., Juan, S. C., Sun, Y., Tarpley, J., Martin, L., Christensen, K., McCabe, J., Kostenuik, P., Hsu, H., Fletcher, F., … Boyle, W. J. (2000). RANK is the intrinsic hematopoietic cell surface receptor that controls osteoclastogenesis and regulation of bone mass and calcium metabolism. Proceedings of the National Academy of Sciences of the United States of America, 97(4), 1566–1571. https://doi.org/10.1073/pnas.97.4.1566

Li, C. Y., Price, C., Delisser, K., Nasser, P., Laudier, D., Clement, M., Jepsen, K. J., & Schaffler, M. B. (2005). Long-term disuse osteoporosis seems less sensitive to bisphosphonate treatment than other osteoporosis. Journal of bone and mineral research : the official journal of the American Society for Bone and Mineral Research, 20(1), 117–124. https://doi.org/10.1359/JBMR.041010

Li, Z., Tan, C., Wu, Y., Ding, Y., Wang, H., Chen, W., Zhu, Y., Ma, H., Yang, H., Liang, W., Jiang, S., Wang, D., Wang, L., Tang, G., & Wang, J. (2012). Whole-body vibration and resistance exercise prevent long-term hindlimb unloading-induced bone loss: independent and interactive effects. European journal of applied physiology, 112(11), 3743–3753. https://doi.org/10.1007/s00421-012-2355-3.

Li, N., Li, X. M., Xu, L., Sun, W. J., Cheng, X. G., & Tian, W. (2013). Comparison of QCT and DXA: Osteoporosis Detection Rates in Postmenopausal Women. International journal of endocrinology, 2013, 895474. https://doi.org/10.1155/2013/895474.

Li, D., Cheng, P., Jiang, H., Cao, T., Wang, J., Gao, Y., Lin, Y., Wang, C., Zhang, S., Li, J., Liu, B., Song, Y., Yang, L., & Pei, G. (2018). Vascularization converts the lineage fate of bone mesenchymal stem cells to endothelial cells in tissue-engineered bone grafts by modulating FGF2-RhoA/ROCK signaling. Cell death & disease, 9(10), 959. https://doi.org/10.1038/s41419-018-0999-6

Lin, T., Tong, W., Chandra, A., Hsu, S. Y., Jia, H., Zhu, J., Tseng, W. J., Levine, M. A., Zhang, Y., Yan, S. G., Liu, X. S., Sun, D., Young, W., & Qin, L. (2015). A comprehensive study of long-term skeletal changes after spinal cord injury in adult rats. Bone Research, 3, [15028]. https://doi.org/10.1038/boneres.2015.28

Lindgren J. U. (1976). Studies of the calcium accretion rate of bone during immobilization in intact and thyroparathyroidectomized adult rats. Calcified tissue research, 22(1), 41–47. https://doi.org/10.1007/BF02010345

Liu, C., Shao, Z. M., Zhang, L., Beatty, P., Sartippour, M., Lane, T., Livingston, E., & Nguyen, M. (2001). Human endomucin is an endothelial marker. Biochemical and biophysical research communications, 288(1), 129–136. https://doi.org/10.1006/bbrc.2001.5737

Liu, D., Li, H., Zhao, C. Q., Jiang, L. S., & Dai, L. Y. (2008). Changes of substance P-immunoreactive nerve fiber innervation density in the sublesional bones in young growing rats at an early stage after spinal cord injury. Osteoporosis international : a journal established as result of cooperation between the European Foundation for Osteoporosis and the National Osteoporosis Foundation of the USA, 19(4), 559–569. https://doi.org/10.1007/s00198-007-0481-2

Liu, H., Xia, X., & Li, B. (2015). Mesenchymal stem cell aging: Mechanisms and influences on skeletal and non-skeletal tissues. Experimental biology and medicine (Maywood, N.J.), 240(8), 1099–1106. https://doi.org/10.1177/1535370215591828

Liu, Y. L., Hsu, J. T., Shih, T. Y., Luzhbin, D., Tu, C. Y., & Wu, J. (2017). Quantification of Volumetric Bone Mineral Density of Proximal Femurs Using a Two-Compartment Model and Computed Tomography Images. BioMed research international, 2018, 6284269. https://doi.org/10.1155/2018/6284269

London, D., Barlow, D., Cooper, C., Kanis, J., & Whitehead, M. (1999). Osteoporosis: clinical guidelines for prevention and treatment. London: Royal College of Physicians, 1-86.

Lopes, D., Martins-Cruz, C., Oliveira, M. B., & Mano, J. F. (2018). Bone physiology as inspiration for tissue regenerative therapies. Biomaterials, 185, 240–275. https://doi.org/10.1016/j.biomaterials.2018.09.028

Mackie, E. J., Ahmed, Y. A., Tatarczuch, L., Chen, K. S., & Mirams, M. (2008). Endochondral ossification: how cartilage is converted into bone in the developing skeleton. The international journal of biochemistry & cell biology, 40(1), 46–62. https://doi.org/10.1016/j.biocel.2007.06.009

Maïmoun, L., Couret, I., Mariano-Goulart, D., Dupuy, A. M., Micallef, J. P., Peruchon, E., Ohanna, F., Cristol, J. P., Rossi, M., & Leroux, J. L. (2005). Changes in osteoprotegerin/RANKL system, bone mineral density, and bone biochemicals markers in patients with recent spinal cord injury. Calcified tissue international, 76(6), 404–411. https://doi.org/10.1007/s00223-004-0048-6

Maïmoun, L., Brennan-Speranza, T. C., Rizzoli, R., & Ammann, P. (2012). Effects of ovariectomy on the changes in microarchitecture and material level properties in response to hind leg disuse in female rats. Bone, 51(3), 586–591. https://doi.org/10.1016/j.bone.2012.05.001

Majorek, K. A., Porebski, P. J., Dayal, A., Zimmerman, M. D., Jablonska, K., Stewart, A. J., Chruszcz, M., & Minor, W. (2012). Structural and immunologic characterization of bovine, horse, and rabbit serum albumins. Molecular immunology, 52(3-4), 174–182. https://doi.org/10.1016/j.molimm.2012.05.011

Manske, S. L., Zhu, Y., Sandino, C., & Boyd, S. K. (2015). Human trabecular bone microarchitecture can be assessed independently of density with second generation HR-pQCT. Bone, 79, 213–221. https://doi.org/10.1016/j.bone.2015.06.006

Melchiorre, D., Milia, A. F., Linari, S., Romano, E., Benelli, G., Manetti, M., Guiducci, S., Ceccarelli, C., Innocenti, M., Carulli, C., Civinini, R., Morfini, M., Matucci-Cerinic, M., & Ibba-Manneschi, L. (2012). RANK-RANKL-OPG in hemophilic arthropathy: from clinical and imaging diagnosis to histopathology. The Journal of rheumatology, 39(8), 1678–1686. https://doi.org/10.3899/jrheum.120370

Metgud, R., Astekar, M. S., Soni, A., Naik, S., & Vanishree, M. (2013). Conventional xylene and xylene-free methods for routine histopathological preparation of tissue sections. Biotechnic & histochemistry : official publication of the Biological Stain Commission, 88(5), 235–241. https://doi.org/10.3109/10520295.2013.764015

Minematsu, A., Nishii, Y., Imagita, H., & Sakata, S. (2014). Time Course of Changes in Trabecular Bone Microstructure in Rats with Spinal Cord Injury. Journal of Life Sciences, 8(6), 522–528.

Minkin, C. (1982). Bone acid phosphatase: tartrate-resistant acid phosphatase as a marker of osteoclast function. Calcified tissue international, 34(3), 285–290. https://doi.org/10.1007/BF02411252

Mira-Pascual, L. (2019). Role of tartrate-resistant acid phosphatase in bone remodeling. (Doctoral Thesis, Karolinska Institutet, Stockholm, Sweden). Available from: https://www.proquest.com/openview/aca97ab67e0250bddccfae26a6f63a87/1?pq-origsite=gscholar&cbl=2026366&diss=y

Modlesky, C. M., Majumdar, S., Narasimhan, A., & Dudley, G. A. (2004). Trabecular bone microarchitecture is deteriorated in men with spinal cord injury. Journal of bone and mineral research : the official journal of the American Society for Bone and Mineral Research, 19(1), 48–55. https://doi.org/10.1359/JBMR.0301208

Morey, E.R. (1979). Spaceflight and bone turnover: correlation with a new rat model of weightlessness. Bioscience, 29 (3), 168-172.

Müeller, S.M. & Glowacki, J. (2001). Age-related decline in the osteogenic potential of human bone marrow cells cultured in three-dimensional collagen sponges. Journal of Cellular Biochemistry, 82 (4), 583-590.

Nakane, P. K., & Pierce, G. B., Jr (1967). Enzyme-labeled antibodies for the light and electron microscopic localization of tissue antigens. The Journal of cell biology, 33(2), 307–318. https://doi.org/10.1083/jcb.33.2.307

Nielsen, J. S., & McNagny, K. M. (2009). CD34 is a key regulator of hematopoietic stem cell trafficking to bone marrow and mast cell progenitor trafficking in the periphery. Microcirculation (New York, N.Y. : 1994), 16(6), 487–496. https://doi.org/10.1080/10739680902941737

Okuno, Y., Iwasaki, H., Huettner, C. S., Radomska, H. S., Gonzalez, D. A., Tenen, D. G., & Akashi, K. (2002). Differential regulation of the human and murine CD34 genes in hematopoietic stem cells. Proceedings of the National Academy of Sciences of the United States of America, 99(9), 6246–6251. https://doi.org/10.1073/pnas.092027799

Orhan, K., de Faria Vasconcelos, K. & Gaeta-Araujo, H. (2020). Micro-computed Tomography (micro-CT) in Medicine and Engineering. Chapter 4.2.3.4. https://doi.org/10.1007/978-3-030-16641-0_4

Osterhoff, G., Morgan, E. F., Shefelbine, S. J., Karim, L., McNamara, L. M., & Augat, P. (2016). Bone mechanical properties and changes with osteoporosis. Injury, 47 Suppl 2(Suppl 2), S11–S20. https://doi.org/10.1016/S0020-1383(16)47003-8

Otzel, D.M., Conover, C.F., Ye, F., Phillips, E.G., Bassett, T., Wnek, R.D., Flores, M., Catter, A., Ghosh, P., Balaez, A., Petusevsky, J., Chen, C., Gao, Y., Zhang, Y., Jiron, J.M., Bose, P.K., Borst, S.E., Wronski, T.J., Aguirre, J.I. & Yarrow, J.F. (2019). Longitudinal examination of bone loss in male rats after moderate–severe contusion spinal cord injury. Calcif. Tissue Int. 104, 79–91. https://doi.org/10.1007/s00223-018-0471-8

Parent, S., Mac-Thiong, J. M., Roy-Beaudry, M., Sosa, J. F., & Labelle, H. (2011). Spinal cord injury in the pediatric population: a systematic review of the literature. Journal of neurotrauma, 28(8), 1515–1524. https://doi.org/10.1089/neu.2009.1153

Parfitt, A. M., Mathews, C. H., Villanueva, A. R., Kleerekoper, M., Frame, B., & Rao, D. S. (1983). Relationships between surface, volume, and thickness of iliac trabecular bone in aging and in osteoporosis. Implications for the microanatomic and cellular mechanisms of bone loss. The Journal of clinical investigation, 72(4), 1396–1409. https://doi.org/10.1172/JCI111096

Parfitt, A. M., Drezner, M. K., Glorieux, F. H., Kanis, J. A., Malluche, H., Meunier, P. J., Ott, S. M., & Recker, R. R. (1987). Bone histomorphometry: standardization of nomenclature, symbols, and units. Report of the ASBMR Histomorphometry Nomenclature Committee. Journal of bone and mineral research : the official journal of the American Society for Bone and Mineral Research, 2(6), 595–610. https://doi.org/10.1002/jbmr.5650020617

Parfitt AM (1994). Osteonal and hemi-osteonal remodeling: the spatial and temporal framework for signal traffic in adult human bone. J Cell Biochem 55 :273–286 PubMed ID7962158

Parks, PC (1986). On the determination of functions from their integral values along certain manifolds. IEEE Transactions on Medical Imaging, 5(4), 170–176. http://doi.org/10.1109/TMI.1986.4307775

Peng, Y., Wu, S., Li, Y., & Crane, J. L. (2020). Type H blood vessels in bone modeling and remodeling. Theranostics, 10(1), 426–436. https://doi.org/10.7150/thno.34126

Perrien, D. S., Akel, N. S., Dupont-Versteegden, E. E., Skinner, R. A., Siegel, E. R., Suva, L. J., & Gaddy, D. (2007). Aging alters the skeletal response to disuse in the rat. American journal of physiology. Regulatory, integrative and comparative physiology, 292(2), R988–R996. https://doi.org/10.1152/ajpregu.00302.2006

Plotkin, L.I. (2014). Apoptotic osteocytes and the control of targeted bone resorption. Curr Osteoporos Rep.;12(1):121–6.

Poole, K. E., van Bezooijen, R. L., Loveridge, N., Hamersma, H., Papapoulos, S. E., Löwik, C. W., & Reeve, J. (2005). Sclerostin is a delayed secreted product of osteocytes that inhibits bone formation. FASEB journal : official publication of the Federation of American Societies for Experimental Biology, 19(13), 1842–1844. https://doi.org/10.1096/fj.05-4221fje

Provchy, K.M. (2010). Von Willebrand Factor Expression in Vascular Endothelial Cells of Cage Control and Antiorthostatic Cage Suspension Golden Hamster Ovaries. (Senior Honors Thesis, East Tennessee State University, USA). Available from: https://dc.etsu.edu/cgi/viewcontent.cgi?article=1011&context=honors

Pusztaszeri, M. P., Seelentag, W., & Bosman, F. T. (2006). Immunohistochemical expression of endothelial markers CD31, CD34, von Willebrand factor, and Fli-1 in normal human tissues. The journal of histochemistry and cytochemistry : official journal of the Histochemistry Society, 54(4), 385–395. https://doi.org/10.1369/jhc.4A6514.2005

Qi, W., Yan, Y. B., Lei, W., Wu, Z. X., Zhang, Y., Liu, D., Shi, L., Cao, P. C., & Liu, N. (2012). Prevention of disuse osteoporosis in rats by Cordyceps sinensis extract. Osteoporosis international : a journal established as result of cooperation between the European Foundation for Osteoporosis and the National Osteoporosis Foundation of the USA, 23(9), 2347–2357. https://doi.org/10.1007/s00198-011-1842-4

Qu, H., Yi, J., Gao, X., Zhao, H., & Wang, Z. (2019). Anti-Disuse Osteoporosis Activity of a Complex of Calcium-Binding Peptide from Auricularia auricula Protein Hydrolysates. Journal of food science, 84(7), 1909–1919. https://doi.org/10.1111/1750-3841.14697

Raggatt, L. J., & Partridge, N. C. (2010). Cellular and molecular mechanisms of bone remodeling. The Journal of biological chemistry, 285(33), 25103–25108. https://doi.org/10.1074/jbc.R109.041087

Ramasamy, S. K., Kusumbe, A. P., Schiller, M., Zeuschner, D., Bixel, M. G., Milia, C., Gamrekelashvili, J., Limbourg, A., Medvinsky, A., Santoro, M. M., Limbourg, F. P., & Adams, R. H. (2016). Blood flow controls bone vascular function and osteogenesis. Nature communications, 7, 13601. https://doi.org/10.1038/ncomms13601

Ramasamy, S.K. (2017). Structure and Functions of Blood Vessels and Vascular Niches in Bone. Stem Cells International, 10.

Reverón, R.R. (2011). Marcello Malpighi, founder of microanatomy. Int. J. Morphol. 29, 399–402.

Reznikov, N., Chase, H., Ben Zvi, Y., Tarle, V., Singer, M., Brumfeld, V., Shahar, R., & Weiner, S. (2016). Inter-trabecular angle: A parameter of trabecular bone architecture in the human proximal femur that reveals underlying topological motifs. Acta biomaterialia, 44, 65–72. https://doi.org/10.1016/j.actbio.2016.08.040

Reznikov, N., Phillips, C., Cooke, M., Garbout, A., Ahmed, F., & Stevens, M. M. (2017). Functional Adaptation of the Calcaneus in Historical Foot Binding. Journal of bone and mineral research : the official journal of the American Society for Bone and Mineral Research, 32(9), 1915–1925. https://doi.org/10.1002/jbmr.3185

Reznikov, N., Alsheghri, A. A., Piché, N., Gendron, M., Desrosiers, C., Morozova, I., Sanchez Siles, J. M., Gonzalez-Quevedo, D., Tamimi, I., Song, J., & Tamimi, F. (2020). Altered topological blueprint of trabecular bone associates with skeletal pathology in humans. Bone reports, 12, 100264. https://doi.org/10.1016/j.bonr.2020.100264

Rhinelander, F.W. (1974). Tibial blood-supply in relation to fracture healing. Clinical Orthopaedics and Related Research, (105), 34-81.

Rho, J.Y., Kuhn-Spearing, L. & Zioupos, P. (1998). Mechanical properties and the hierarchical structure of bone. Medical Engineering & Physics, 20 (2), 92-102.

Ringler, D. H., Dabich, L., Baker, H. J., Lindsey, J. R., & Weisbroth, S. H. (1979). The laboratory rat.

Rinonapoli, G., Ruggiero, C., Meccariello, L., Bisaccia, M., Ceccarini, P., & Caraffa, A. (2021). Osteoporosis in Men: A Review of an Underestimated Bone Condition. International journal of molecular sciences, 22(4), 2105. https://doi.org/10.3390/ijms22042105

Rittweger, J., Frost, H. M., Schiessl, H., Ohshima, H., Alkner, B., Tesch, P., & Felsenberg, D. (2005). Muscle atrophy and bone loss after 90 days' bed rest and the effects of flywheel resistive exercise and pamidronate: results from the LTBR study. Bone, 36(6), 1019–1029. https://doi.org/10.1016/j.bone.2004.11.014

Rivlin, A. S., & Tator, C. H. (1978). Effect of duration of acute spinal cord compression in a new acute cord injury model in the rat. Surgical neurology, 10(1), 38–43.

Roberts, D., Lee, W., Cuneo, R. C., Wittmann, J., Ward, G., Flatman, R., McWhinney, B., & Hickman, P. E. (1998). Longitudinal study of bone turnover after acute spinal cord injury. The Journal of clinical endocrinology and metabolism, 83(2), 415–422. https://doi.org/10.1210/jcem.83.2.4581

Robling, A. G., Niziolek, P. J., Baldridge, L. A., Condon, K. W., Allen, M. R., Alam, I., Mantila, S. M., Gluhak-Heinrich, J., Bellido, T. M., Harris, S. E., & Turner, C. H. (2008). Mechanical stimulation of bone in vivo reduces osteocyte expression of Sost/sclerostin. The Journal of biological chemistry, 283(9), 5866–5875. https://doi.org/10.1074/jbc.M705092200

Rolvien, T., Milovanovic, P., Schmidt, F. N., von Kroge, S., Wölfel, E. M., Krause, M., Wulff, B., Püschel, K., Ritchie, R. O., Amling, M., & Busse, B. (2020). Long-Term Immobilization in Elderly Females Causes a Specific Pattern of Cortical Bone and Osteocyte Deterioration Different From Postmenopausal Osteoporosis. Journal of bone and mineral research : the official journal of the American Society for Bone and Mineral Research, 35(7), 1343–1351. https://doi.org/10.1002/jbmr.3970

Rolvien, T., & Amling, M. (2022). Disuse Osteoporosis: Clinical and Mechanistic Insights. Calcified tissue international, 110(5), 592–604. https://doi.org/10.1007/s00223-021-00836-1

Rueden, C. T., Schindelin, J., Hiner, M. C., DeZonia, B. E., Walter, A. E., Arena, E. T., & Eliceiri, K. W. (2017). ImageJ2: ImageJ for the next generation of scientific image data. BMC bioinformatics, 18(1), 529. https://doi.org/10.1186/s12859-017-1934-z

Rüegsegger, P., Koller, B., & Müller, R. (1996). A microtomographic system for the non-destructive evaluation of bone architecture. Calcified tissue international, 58(1), 24–29. https://doi.org/10.1007/BF02509542

Sahbani, K., Shultz, L. C., Cardozo, C. P., Bauman, W. A., & Tawfeek, H. A. (2021). Absence of αβ T cells accelerates disuse bone loss in male mice after spinal cord injury. Annals of the New York Academy of Sciences, 1487(1), 43–55. https://doi.org/10.1111/nyas.14518

Saify, F. & Tiwari, N. (2020). Mounting Media - An Untouched Aspect. Oral & Maxillofacial Pathology Journal, 11 (1), 20-24.

Saikia, B., Gupta, K., & Saikia, U. N. (2008). The modern histopathologist: in the changing face of time. Diagnostic pathology, 3, 25. https://doi.org/10.1186/1746-1596-3-25

Salminen, A., Huuskonen, J., Ojala, J., Kauppinen, A., Kaarniranta, K., & Suuronen, T. (2008). Activation of innate immunity system during aging: NF-kB signaling is the molecular culprit of inflamm-aging. Ageing research reviews, 7(2), 83–105. https://doi.org/10.1016/j.arr.2007.09.002

Salmon, P. L., Ohlsson, C., Shefelbine, S. J., & Doube, M. (2015). Structure Model Index Does Not Measure Rods and Plates in Trabecular Bone. Frontiers in endocrinology, 6, 162. https://doi.org/10.3389/fendo.2015.00162

Sanchez-Fernandez, M. A., Gallois, A., Riedl, T., Jurdic, P., & Hoflack, B. (2008). Osteoclasts control osteoblast chemotaxis via PDGF-BB/PDGF receptor beta signaling. PloS one, 3(10), e3537. https://doi.org/10.1371/journal.pone.0003537

Savi, F. M., Brierly, G. I., Baldwin, J., Theodoropoulos, C., & Woodruff, M. A. (2017). Comparison of Different Decalcification Methods Using Rat Mandibles as a Model. The journal of histochemistry and cytochemistry : official journal of the Histochemistry Society, 65(12), 705–722. https://doi.org/10.1369/0022155417733708

Sengupta P. (2013). The Laboratory Rat: Relating Its Age With Human's. International journal of preventive medicine, 4(6), 624–630.

Sezer, N. (2015). Chronic complications of spinal cord injury. World Journal of Orthopedics, 6(1), 24–33. http://doi.org/10.5312/wjo.v6.i1.24

Shabestari, M., Vik, J., Reseland, J. E., & Eriksen, E. F. (2016). Bone marrow lesions in hip osteoarthritis are characterized by increased bone turnover and enhanced angiogenesis. Osteoarthritis and cartilage, 24(10), 1745–1752. https://doi.org/10.1016/j.joca.2016.05.009

Shabestari, M., Kise, N. J., Landin, M. A., Sesseng, S., Hellund, J. C., Reseland, J. E., Eriksen, E. F., & Haugen, I. K. (2018). Enhanced angiogenesis and increased bone turnover characterize bone marrow lesions in osteoarthritis at the base of the thumb. Bone & joint research, 7(6), 406–413. https://doi.org/10.1302/2046-3758.76.BJR-2017-0083.R3

Shim, V. B., Pitto, R. P., & Anderson, I. A. (2012). Quantitative CT with finite element analysis: towards a predictive tool for bone remodelling around an uncemented tapered stem. International orthopaedics, 36(7), 1363–1369. https://doi.org/10.1007/s00264-012-1513-x

Shipov, A., Zaslansky, P., Riesemeier, H., Segev, G., Atkins, A., & Shahar, R. (2013). Unremodeled endochondral bone is a major architectural component of the cortical bone of the rat (Rattus norvegicus). Journal of structural biology, 183(2), 132–140. https://doi.org/10.1016/j.jsb.2013.04.010

Simmons, D. L., Satterthwaite, A. B., Tenen, D. G., & Seed, B. (1992). Molecular cloning of a cDNA encoding CD34, a sialomucin of human hematopoietic stem cells. Journal of immunology (Baltimore, Md. : 1950), 148(1), 267–271.

Simonet, W. S., Lacey, D. L., Dunstan, C. R., Kelley, M., Chang, M. S., Lüthy, R., Nguyen, H. Q., Wooden, S., Bennett, L., Boone, T., Shimamoto, G., DeRose, M., Elliott, R., Colombero, A., Tan, H. L., Trail, G., Sullivan, J., Davy, E., Bucay, N., Renshaw-Gegg, L., … Boyle, W. J. (1997). Osteoprotegerin: a novel secreted protein involved in the regulation of bone density. Cell, 89(2), 309–319. https://doi.org/10.1016/s0092-8674(00)80209-3

Singbrant, S., Russell, M. R., Jovic, T., Liddicoat, B., Izon, D. J., Purton, L. E., Sims, N. A., Martin, T. J., Sankaran, V. G., & Walkley, C. R. (2011). Erythropoietin couples erythropoiesis, B-lymphopoiesis, and bone homeostasis within the bone marrow microenvironment. Blood, 117(21), 5631–5642. https://doi.org/10.1182/blood-2010-11-320564

Squire, M., Brazin, A., Keng, Y., & Judex, S. (2008). Baseline bone morphometry and cellular activity modulate the degree of bone loss in the appendicular skeleton during disuse. Bone, 42(2), 341–349. https://doi.org/10.1016/j.bone.2007.09.052

Stagi, S., Cavalli, L., Cavalli, T., de Martino, M., & Brandi, M. L. (2016). Peripheral quantitative computed tomography (pQCT) for the assessment of bone strength in most of bone affecting conditions in developmental age: a review. Italian journal of pediatrics, 42(1), 88. https://doi.org/10.1186/s13052-016-0297-9

Stockinger, H., Gadd, S. J., Eher, R., Majdic, O., Schreiber, W., Kasinrerk, W., Strass, B., Schnabl, E., & Knapp, W. (1990). Molecular characterization and functional analysis of the leukocyte surface protein CD31. Journal of immunology (Baltimore, Md. : 1950), 145(11), 3889–3897.

Streicher, C., Heyny, A., Andrukhova, O., Haigl, B., Slavic, S., Schüler, C., Kollmann, K., Kantner, I., Sexl, V., Kleiter, M., Hofbauer, L. C., Kostenuik, P. J., & Erben, R. G. (2017). Estrogen Regulates Bone Turnover by Targeting RANKL Expression in Bone Lining Cells. Scientific reports, 7(1), 6460. https://doi.org/10.1038/s41598-017-06614-0

Sun, X., Liang, J., Wang, C., Cao, S., Hu, Y., & Xu, X. (2015). Transient Effect of 17β-estradiol on Osteoporosis in Ovariectomized Rats Accompanied with Unilateral Disuse in the Early Phase. International journal of medical sciences, 12(5), 423–431. https://doi.org/10.7150/ijms.11887

Takahashi, N., Udagawa, N., & Suda, T. (2014). Vitamin D endocrine system and osteoclasts. BoneKEy reports, 3, 495. https://doi.org/10.1038/bonekey.2013.229

Tan, C. O., Battaglino, R. A, & Morse, L. R. (2013). Spinal Cord Injury and Osteoporosis: Causes, Mechanisms, and Rehabilitation Strategies. International Journal of Physical Medicine & Rehabilitation, 1, 1–10. http://doi.org/10.4172/2329-9096.1000127

Tang, Y., Wu, X., Lei, W., Pang, L., Wan, C., Shi, Z., Zhao, L., Nagy, T. R., Peng, X., Hu, J., Feng, X., Van Hul, W., Wan, M., & Cao, X. (2009). TGF-beta1-induced migration of bone mesenchymal stem cells couples bone resorption with formation. Nature medicine, 15(7), 757–765. https://doi.org/10.1038/nm.1979

Tatsumi, S., Ishii, K., Amizuka, N., Li, M., Kobayashi, T., Kohno, K., Ito, M., Takeshita, S., & Ikeda, K. (2007). Targeted ablation of osteocytes induces osteoporosis with defective mechanotransduction. Cell metabolism, 5(6), 464–475. https://doi.org/10.1016/j.cmet.2007.05.001

Tchokonte-Nana, V., Le Roux, D.J., Kotze, P.C. & Ngounou, E. (2017). Immunohistomorphology of Pancreatic Islet Microvasculature and the Immunophenotypic Analysis of CEPC in Adult Diabetic Rats. International Journal of Morphology, 35 (4), 1560-1567.

Thambiah, S. C., & Yeap, S. S. (2020). Osteoporosis in South-East Asian Countries. The Clinical biochemist. Reviews, 41(1), 29–40. https://doi.org/10.33176/AACB-19-00034

Titford, M. (2006). A short history of histoplathology technique. Journal of Histotechnology, 29 (2), 99-110.

Tran Van, P. T., Vignery, A., & Baron, R. (1982). Cellular kinetics of the bone remodeling sequence in the rat. The Anatomical record, 202(4), 445–451. https://doi.org/10.1002/ar.1092020403

Turner, C. H., Woltman, T. A., & Belongia, D. A. (1992). Structural changes in rat bone subjected to long-term, in vivo mechanical loading. Bone, 13(6), 417–422. https://doi.org/10.1016/8756-3282(92)90084-a

Tuukkanen, J., Wallmark, B., Jalovaara, P., Takala, T., Sjögren, S., & Väänänen, K. (1991). Changes induced in growing rat bone by immobilization and remobilization. Bone, 12(2), 113–118. https://doi.org/10.1016/8756-3282(91)90009-8

Utting, J. C., Robins, S. P., Brandao-Burch, A., Orriss, I. R., Behar, J., & Arnett, T. R. (2006). Hypoxia inhibits the growth, differentiation and bone-forming capacity of rat osteoblasts. Experimental cell research, 312(10), 1693–1702. https://doi.org/10.1016/j.yexcr.2006.02.007

van 't Hof R. J. (2012). Analysis of bone architecture in rodents using microcomputed tomography. Methods in molecular biology (Clifton, N.J.), 816, 461–476. https://doi.org/10.1007/978-1-61779-415-5_27

van 't Hof, R. J., Rose, L., Bassonga, E., & Daroszewska, A. (2017). Open source software for semi-automated histomorphometry of bone resorption and formation parameters. Bone, 99, 69–79. https://doi.org/10.1016/j.bone.2017.03.051

Vegger, J. B., Brüel, A., & Thomsen, J. S. (2015). Vertical Trabeculae are Thinned More Than Horizontal Trabeculae in Skeletal-Unloaded Rats. Calcified tissue international, 97(5), 516–526. https://doi.org/10.1007/s00223-015-0035-0

Vestergaard, P., Krogh, K., Rejnmark, L., & Mosekilde, L. (1998). Fracture rates and risk factors for fractures in patients with spinal cord injury. Spinal Cord, 36(11), 790–796. http://doi.org/10.1038/sj.sc.3100648

Walker, K. V., & Kember, N. F. (1972). Cell kinetics of growth cartilage in the rat tibia. II. Measurements during ageing. Cell and tissue kinetics, 5(5), 409–419. https://doi.org/10.1111/j.1365-2184.1972.tb00379.x

Wang, Y. X., Griffith, J. F., Kwok, A. W., Leung, J. C., Yeung, D. K., Ahuja, A. T., & Leung, P. C. (2009). Reduced bone perfusion in proximal femur of subjects with decreased bone mineral density preferentially affects the femoral neck. Bone, 45(4), 711–715. https://doi.org/10.1016/j.bone.2009.06.016

Wang, L., Zhou, F., Zhang, P., Wang, H., Qu, Z., Jia, P., Yao, Z., Shen, G., Li, G., Zhao, G., Li, J., Mao, Y., Xie, Z., Xu, W., Xu, Y., & Xu, Y. (2017). Human type H vessels are a sensitive biomarker of bone mass. Cell death & disease, 8(5), e2760. https://doi.org/10.1038/cddis.2017.36

Wang, Y., Wan, C., Deng, L., Liu, X., Cao, X., Gilbert, S. R., Bouxsein, M. L., Faugere, M. C., Guldberg, R. E., Gerstenfeld, L. C., Haase, V. H., Johnson, R. S., Schipani, E., & Clemens, T. L. (2007). The hypoxia-inducible factor alpha pathway couples angiogenesis to osteogenesis during skeletal development. The Journal of clinical investigation, 117(6), 1616–1626. https://doi.org/10.1172/JCI31581

Williams, J. (2019). Characterisation of disuse-related osteoporosis in an animal model of spinal cord injury. (Doctoral thesis, University of Strathclyde, Glasgow, UK). Available from: https://stax.strath.ac.uk/concern/theses/zs25x8585

Williams, J. A., Windmill, J., Tanner, K. E., Riddell, J. S., & Coupaud, S. (2019). Global and site-specific analysis of bone in a rat model of spinal cord injury-induced osteoporosis. Bone reports, 12, 100233. https://doi.org/10.1016/j.bonr.2019.100233

Williams, J. A., Huesa, C., Turunen, M. J., Oo, J. A., Radzins, O., Gardener, W., ... Coupaud, S. (2022a). Time course changes to structural, mechanical and material properties of bone in rats after complete spinal cord injury. The Journal of Musculoskeletal and Neuronal Interactions. In print.

Williams, J. A., Huesa, C., Windmill, J., Purcell, M., Reid, S., Coupaud, S., & Riddell, J. S. (2022b). Spatiotemporal responses of trabecular and cortical bone to complete spinal cord injury in skeletally mature rats. Bone reports, 16, 101592. https://doi.org/10.1016/j.bonr.2022.101592

Wilmet, E., Ismail, A. A., Heilporn, A., Welraeds, D., & Bergmann, P. (1995). Longitudinal study of the bone mineral content and of soft tissue composition after spinal cord section. Paraplegia, 33(11), 674–677. https://doi.org/10.1038/sc.1995.141

Winkler, D.G., Hayes, T., Geoghegan, J., Skonier, J., Ursino, P., Sutherland, M.K. & Latham, J. (2001). Sclerostin, the protein product of the sclerosteosis gene (SOST) and a key regulator of bone matrix formation, binds to BMPs and antagonizes their function. Journal of Bone and Mineral Research, 16 S322-S322.

Xie, H., Cui, Z., Wang, L., Xia, Z., Hu, Y., Xian, L., Li, C., Xie, L., Crane, J., Wan, M., Zhen, G., Bian, Q., Yu, B., Chang, W., Qiu, T., Pickarski, M., Duong, L. T., Windle, J. J., Luo, X., Liao, E., … Cao, X. (2014). PDGF-BB secreted by preosteoclasts induces angiogenesis during coupling with osteogenesis. Nature medicine, 20(11), 1270–1278. https://doi.org/10.1038/nm.3668

Zehnder, Y., Lüthi, M., Michel, D., Knecht, H., Perrelet, R., Neto, I., Kraenzlin, M., Zäch, G., & Lippuner, K. (2004). Long-term changes in bone metabolism, bone mineral density, quantitative ultrasound parameters, and fracture incidence after spinal cord injury: a cross-sectional observational study in 100 paraplegic men. Osteoporosis international : a journal established as result of cooperation between the European Foundation for Osteoporosis and the National Osteoporosis Foundation of the USA, 15(3), 180–189. https://doi.org/10.1007/s00198-003-1529-6

Zhang, J., Cong, J., Yang, J., Thomsen, J. S., Andreasen, A., Chang, S. J., Wang, K. Y., Gu, L., & Zhai, X. Y. (2018). Morphologic and morphometric study on microvasculature of developing mouse kidneys. American journal of physiology. Renal physiology, 315(4), F852–F860. https://doi.org/10.1152/ajprenal.00615.2017

Zhang, N., Fang, M., Chen, H., Gou, F., & Ding, M. (2014). Evaluation of spinal cord injury animal models. Neural regeneration research, 9(22), 2008–2012. https://doi.org/10.4103/1673-5374.143436

Zhang, R., Gong, H., Zhu, D., Gao, J., Fang, J., & Fan, Y. (2014). Seven day insertion rest in whole body vibration improves multi-level bone quality in tail suspension rats. PloS one, 9(3), e92312. https://doi.org/10.1371/journal.pone.0092312

Zhang, Y., Xiao, H. L., Zhou, Y. H., Liu, S. Y., Xie, D. D., Fu, S., . . . Xie, H. (2018). Relationship between expression of myogenic factors in disused rats and bone mass loss and microstructural degeneration. International Journal of Clinical and Experimental Medicine, 11(12), 13135-13146.

Zhao, W., Wang, X., Sun, K. H., & Zhou, L. (2018). α-smooth muscle actin is not a marker of fibrogenic cell activity in skeletal muscle fibrosis. PloS one, 13(1), e0191031. https://doi.org/10.1371/journal.pone.0191031.

Appendix

1: CTan General Cortical Analysis Macro

- Load delineated cortical VOI.
- Apply global threshold to binarise 8-bit greyscale image. Limits 80-255.
- Despeckle. Type: Sweep in 3D space | Remove: all except the largest object | Apply to: Image.
- Morphological Operations. Type: Closing in 3D space | Kernel: Round radius 2px (20μm as resolution = 10μm/px) | Apply to: Image.
- ROI Shrink-wrap. Mode: Shrink-wrap in 2D space | Stretch over holes: No.
- 3D Analysis: All parameters selected.
- 2D Analysis: All parameters selected.

2: CTan Cortical Porosity Analysis Macro

- Load delineated cortical VOI.
- Apply global threshold to binarise 8-bit greyscale image. Limits 90-255.
- Despeckle. Type: Sweep in 3D space | Remove: all except largest object | Apply to: Image.
- ROI Shrink-wrap. Mode: Shrink-wrap in 3D space | Stretch over holes: Yes, diameter 8px (80μm).
- Bitwise Operations. Image = Image XOR Region of Interest.
- Despeckle. Type: Remove white speckles in 3D space | Volume: less than 10 voxels | Apply to: Image.
- 3D Analysis: All parameters selected.

3: TRAP Staining Protocol

Reagents

2N HCl (for preparation of dye):

- 8ml hydrochloric acid (37%)
- 45 ml distilled water
- Store for 1 year at RT.

5M NaOH (for pH adjustment):

- 50g sodium hydroxide pellets
- 250ml distilled water
- Store indefinitely at RT.

Pararosaniline dye (stock solution):

- 1g pararosaniline chloride (Sigma P-3750)
- 20ml 2N HCl
- Dissolve the dye in the acid in a small beaker using low heat and stirring for at least 18hrs. Heat to 60^{o}C for 5 mins at the end of mixing, then cool and filter through 3x layers of Kimwipes. Use within two weeks and store at 4^{o}C.

Naphthol AS-BI phosphate (substrate):

- 100mg naphthol AS-BI phosphate (Sigma N-2125)
- 5 ml ethylene glycol monoethyl ether (Sigma E-2632)
- Mix to dissolve for 10mins at RT. Keep for 3 weeks at 4^{o}C.

Sodium nitrite:

- 1g sodium nitrite
- 25ml distilled water
- Mix to dissolve for 10mins at RT. Keep no longer than 4 days at 4^{o}C.

Basic Incubation Medium (BIM)

	For Coplin jar	For One rack	For two racks
Sodium acetate (anhydrous)	2.3g	4.6g	9.2g
or			
Sodium acetate·$3H_2O$	3.8g	7.6g	15.2g
L-(+) tartaric acid	2.9g	5.7g	11.4g
Glacial acetic acid	0.7ml	1.4ml	2.8ml
Distilled water	250ml	500ml	1L

Dissolve and adjust pH to 4.7-5.0 with 5M sodium hydroxide.

Fast Green Counterstain

- 0.08% Fast Green Powder (0.02g or 20mg) in 250ml distilled water.
- Mix to dissolve for 10mins at RT. Store up to 2 years at RT.

Staining

Add a positive control slide to each set of slides being stained.

For positive controls use sections from formalin-fixed, EDTA- decalcified, paraffin embedded bone (with osteoclasts). Proximal femur intertrochanteric crest is good for this.

- Deparaffinize slides (2 changes of histoclear, 3 minutes each) and hydrate through 3 changes of 100% ethanol, 1 change of 90%, 1 change of 70% ethanol (3 minutes each) and running tap water (RTW).
- Prepare substrate incubation as follows:
- 250ml BIM + 2.5ml Napthol-Ether Solution.
- Mix naphthol-ether solution into basic incubation medium, add slides and incubate at 37ºC in an oven for 30 minutes.
- A few minutes before the first incubation ends, prepare the color reaction medium. Mix in a small container the following amounts of sodium nitrite and dye stock:
- 5ml sodium nitrite solution + 5ml pararosaniline dye.
- Stir and let stand for two minutes. After two minutes, add the entire volume to 250ml BIM.
- Remove slides from the substrate incubation at the proper time and place directly into the color reaction medium. Incubate 8 minutes at RT. Rinse in deionised water.
- For nuclear and light background staining use 0.08% Fast Green w/v in distilled water for 90s.
- Rinse in distilled water.
- Dehydrate through graded alcohols.
- Clear with Histoclear.
- Coverslip with DPX.

4: CD34 Staining Protocol

All incubations at room temperature unless otherwise stated

Day 1:

- Section at 7µm on a microtome and mount onto poly-l-lysine slides
- Dry sections at room temperature for 5hrs then oven at 55ºC for 1hr
- Clear in xylene 8mins
- Rehydrate in:
    - 100%EtOH 4mins
    - 90%EtOH 4mins
    - 70%EtOH 4mins
    - Running tap water 4mins
- HIER (heat-induced epitope retrieval) in 1x citric acid buffer pH6 – 300ml in glass histology dish in oven at 60ºC for 16hrs overnight

Day 2:

- Out of oven into PBS 9am until 4pm.
- Wash 2x5mins PBS
- Incubate in Hydrogen Peroxide Block for 10 minutes
- Wash 2x5mins PBS
- Apply Protein Block and incubate for 20 minutes
- Wash 2x5mins PBS
- Apply primary antibody and incubate 16hrs overnight at 4ºC in humid incubation tray. In this case from ABCAM:
    - Recommended dilution for ABCAM Rabbit anti-CD34 is 1/50-1/200
    - The diluent is 1% NGS in 50mM PBS

Day 3:

- Wash 4x5mins PBS
- Incubate in hydrogen peroxide block for 10mins.
- Rinse 4x5mins PBS

- Apply Biotinylated goat anti rabbit IgG(H+L) and incubate for 10mins
- Wash 4x5mins PBS
- Apply Streptavidin Peroxidase and incubate for 10 minutes
- Wash 4x5mins PBS
- Add 20ul DAB Chromogen to 1 ml of DAB Substrate, mix by swirling and apply to tissue.
- Incubate for 8 minutes in DAB solution
- Wash 4x5mins PBS
- Counterstain in Mayer's haematoxylin for 60s
- Rinse 2x 3mins dH2O
- Apply bluing reagent 10s
- Rinse 2x 3mins dH2O
- Dip in 100% EtOH
- Dehydrate back through the same series 70%, 90%, 100% EtOH 4 mins each
- Clear in Histoclear (Xylene at the start but Histoclear now) 2x 4mins.
- Mount using DPX and glass coverslips.

5: Staining Quality Progression

No prior expertise was on hand for the development of the bone histology protocols detailed herein. Extensive iterative staining runs were required before protocols were optimised and produced quality, consistent results.

The first stain performed was a Masson's Trichrome (Abcam, Cambridge, UK) on a healthy Wistar rat distal femur. The results showed that the decalcification process required improvements. The bone in this case was not sufficiently decalcified, leading to bunching of the paraffin ribbon when microtoming, and the stratified image seen in Figure A1:

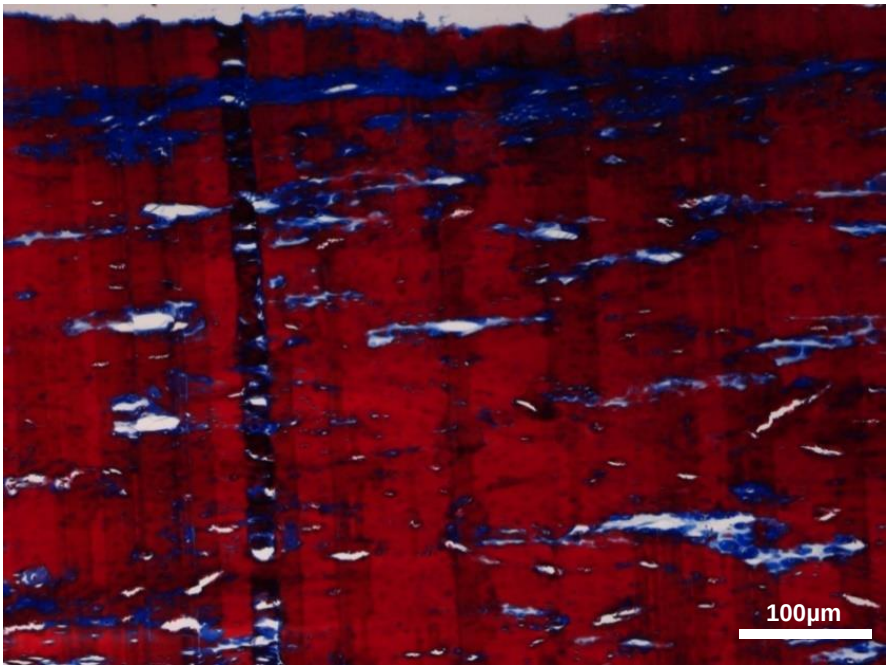

Figure A 1: Masson's trichrome on lateral distal femur cortical bone. Note the striations due to material bunching and blade slippage during sectioning. Magnification 200x.

The decalcification and softening procedures were consequently improved. First, surface decalcification using formic acid was trialled. Then, softening of the cut face using CellSoft solution (CellPath, Powys, UK) was included in combination. Neither of these approaches yielded sufficient quality results and the sectioning consistency was still insufficient, as seen in Figure A2:

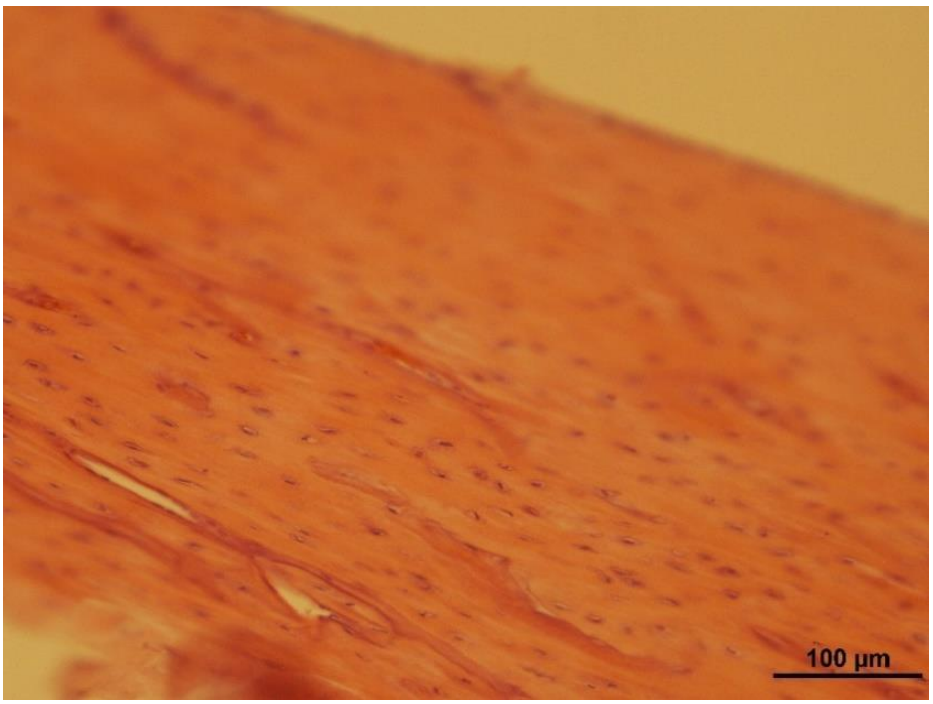

Figure A 2: H&E on lateral distal femur cortical bone. Note the difference in focus between different XY positions of the image. Magnification 200x.

In light of these issues, the softening procedure was changed to a 10 minute soak in ice water of the cut face prior to sectioning. The decalcification protocol was also changed, from 1x change of 40ml EDTA per bone per week, to 3x changes of 50ml EDTA per bone per week. Finally, the pre-treatment protocol in the auto-processor (dehydration, clearing and paraffin wax immersion) was altered to include 3x 1hr dehydration steps in 100% EtOH and 2x 1hr clearing steps in 100% Histoclear. The previous protocol had only used a single 1hr stage for either process.

This alteration to the stages prior to microtoming produced much more consistent sections with a uniform height, meaning each entire captured image was now in focus as desired. Figure A3 displays the improvement:

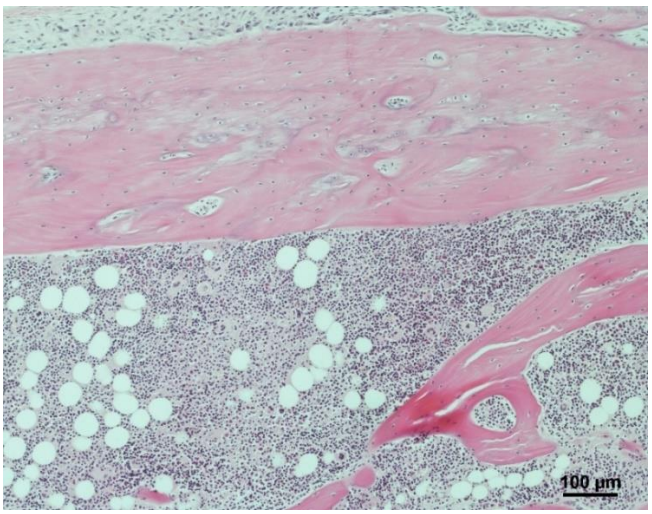

Figure A 3: H&E on distal femur, cortical bone and medullary region. Note the uniform section quality and focus. Magnification 100x.

With the decalcification, pre-processing and sectioning now optimised, different IHC stains were trialled in order to quantify the blood vessel density and bone cell numbers and activity in the SCI bones.

Blood Microvessel Density Staining Progression

The first stain run for microvessel density quantification was von Willebrand Factor (vWF), an endothelial cell marker (Provchy 2010). The run produced an overexpression of vWF positive staining in the megakaryocytes, as depicted in Figure A4:

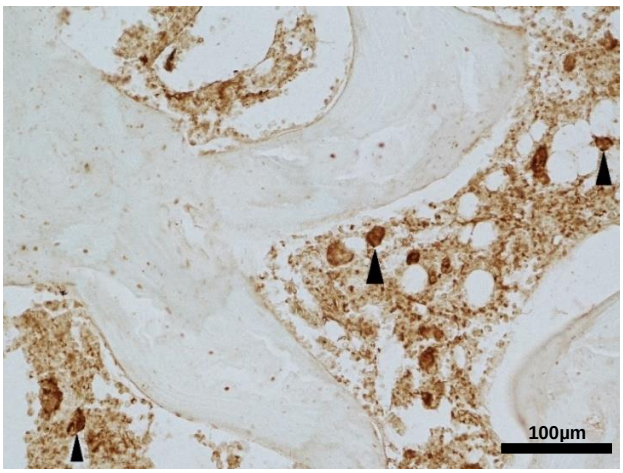

Figure A 4: vWF on Wistar rat distal femur metaphyseal marrow. Black arrowheads: megakaryocytes. Magnification 200x.

The vWF was found to not only be overexpressed in megakaryocytes, but to stain the blood microvessels with insufficient intensity. Further research was conducted, and a superior choice of primary antibody target was selected for imaging of the bone microvasculature. This protein was CD34, described on pages 131-132.

Unlike similar endothelial markers CD31 and vWF, CD34 is strongly expressed in human microvessels, and is not expressed by marrow megakaryocytes (Pusztaszeri, Seelentag & Bosman 2006). This expression profile was found to be identical when staining in the Wistar rat, as Figure A5 displays:

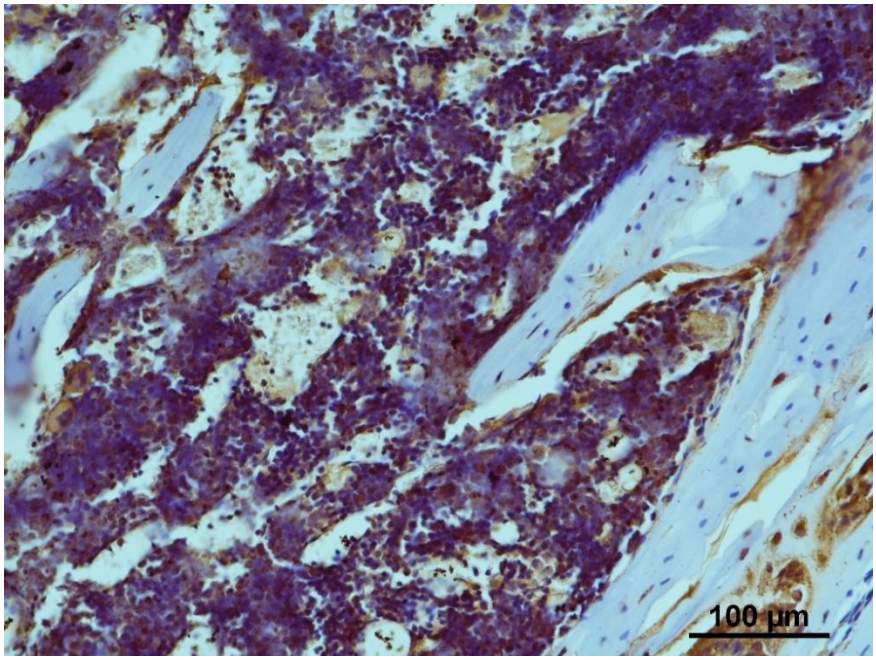

Figure A 5: Polyclonal CD34 on Wistar rat distal femur metaphyseal trabeculae. Counterstained with Mayer's haematoxylin. Magnification 200x.

Although the megakaryocytes were no longer showing up in the images, the staining was still of insufficient quality. In order to be accurately quantified, the contrast between the CD34 positive microvessels and the counterstain needed increasing. The specificity of the stain also needed improvement. Both of these issues were solved via switching from polyclonal CD34 primary antibodies to a monoclonal alternative. Furthermore, an additional endogenous peroxidase blocking step was added after incubation with the monoclonal primaries. The results of these changes can be viewed in Figure A6:

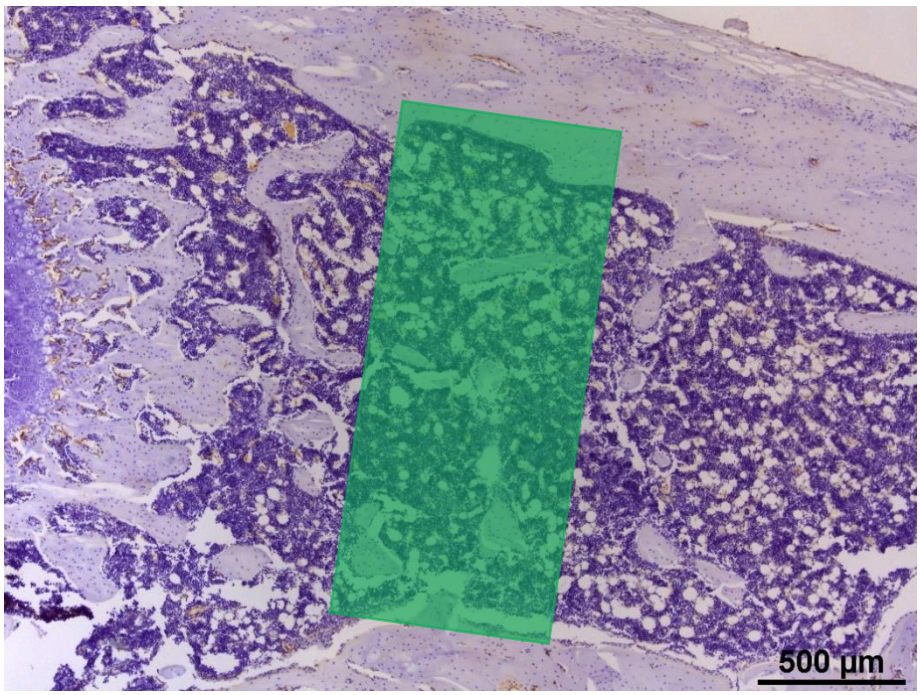

Figure A 6: Monoclonal CD34 on Sprague-Dawley rat distal femur. Counterstained with Mayer's haematoxylin. Magnification 40x.

The blood microvessel density IHC staining protocol was now optimised. The intraosseous microvessels around the secondary spongiosa (green region) were highlighted against the counterstain nicely. The quantification method developed in ImageJ (see pages 149-152) consistently picked out the required vasculature from the adipose tissue, megakaryocytes and other neighbouring cells prior to counting.

Osteoclast Staining Progression

The other histological stain for quantification of the effects of SCI-induced osteoporosis following chronic SCI was TRAP staining. TRAP staining highlights osteoclasts, and allows for measurements of bone resorption activity.

The first attempt at TRAP staining is depicted in Figure A7:

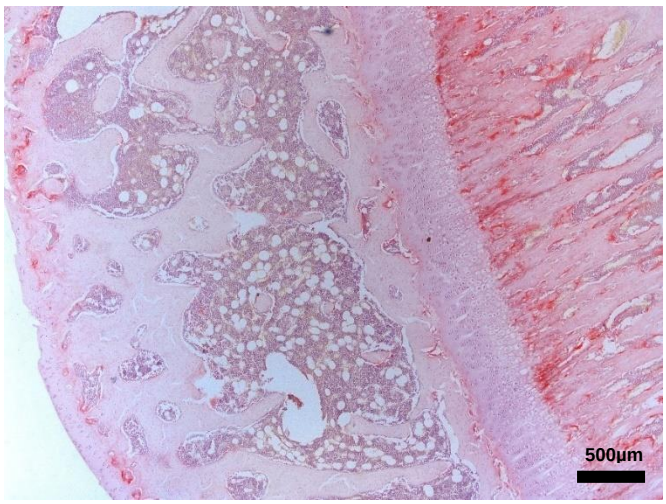

Figure A 7: TRAP stain on Wistar rat tibial head. Counterstained with Mayer's haematoxylin. Magnification 40x.

The TRAP positive (pinkish red) regions were of sufficient intensity, however their contrast against the counterstain was still undesirable. Alterations were made to the TRAP protocol, reducing the colour reaction development time from 10 to 8 minutes, and using Fast Green FCF as the counterstain. This produced the results seen in Figure A8:

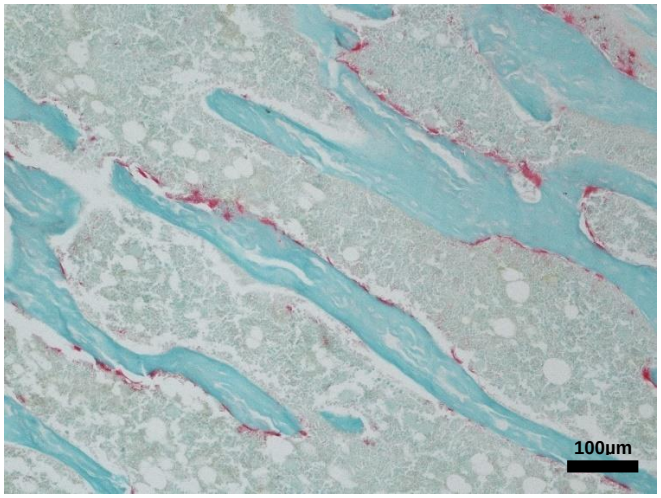

Figure A 8: TRAP stain on Wistar rat proximal tibia medullary secondary spongiosa. Counterstained with Fast Green FCF. Magnification 100x.

The change in counterstain proved to be effective. Quantification could now be accurately and consistently performed in TrapHisto. The TRAP protocol was now optimised.

6: Outlier in Proximal Tibia CTRL Group

Rat	BV/TV (%)	Tb.Th (mm)	Tb.Sp (mm)	Tb.N (mm-1)	FD	Conn.D (mm-3)	SMI	Median EF
SCI 1	7.22572116	0.07084	0.46	1.02	2.26179	219	2.4313834	0.269149691
SCI 2	9.7021704	0.06965	0.38	1.39	2.37629	352.6	2.2560841	0.303155988
SCI 3	2.66632775	0.06291	1.02	0.42	1.90851	96.4	2.5879604	0.234070182

- SCI 3 (R0721) in the PT group presented a much greater response to chronic SCI than the other PTs in the same group, as the rat had an infection of the peritoneal sack sustained during housing (blue highlighted cells).
- Trabecular volume fraction, spacing, number and connectivity density were all noticeably outlying compared to their SCI 1 and SCI 2 counterparts.
- Although included for group mean data in general trabecular and ellipsoid factor analyses, the significantly low connectivity density meant that an adequate node-branch network could not be formed for ITA analysis and so SCI 3 was omitted from consideration for ITA.

7: Image Stitching in ImageJ

- Images were captured at x40 magnification on a Nikon Eclipse 50i compound light microscope attached to a Nikon DS-U3 digital camera.
- An initial check was performed to see how many x40 captures were required to span the entire width of each femur or tibia.
- The approximate overlap for each image capture from the previous was ~10%.
- Various patterns are available in the ImageJ stitching plugin. The user specifies the pattern which has been followed when acquiring each image for the stitch.
- The pattern used in this study was ‘snake by columns’, seen in Figure A9:

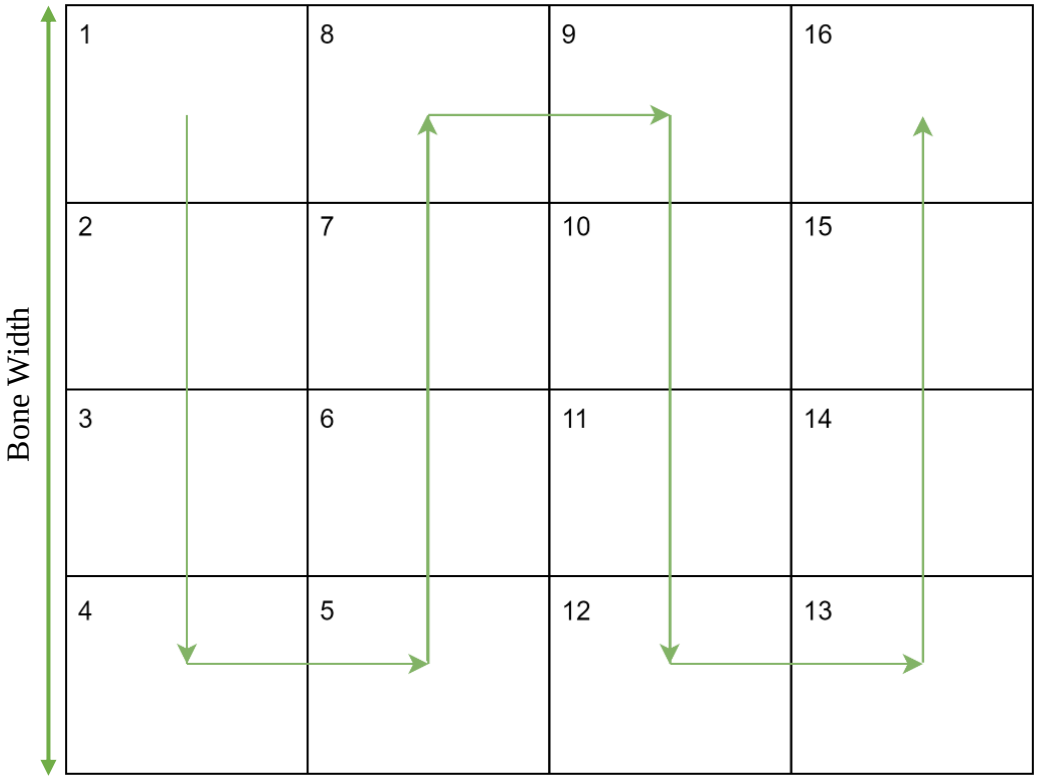

Figure A 9: Snake by columns digital image stitching pattern.

- The number of images to span the bone width was 4, and so 8 images were combined in a 4x2 ‘snake by columns’ pattern to create the stitch.
- Although the images were captured at the same light intensity from the microscope, different volumes of bone material were present in each. This consequently led to a slightly different overall brightness for each image in the stitch.

- The settings for grid stitching in ImageJ are as follows:
    - **Regression Threshold**: the threshold value for brightness linear regression coefficient between two stitched and blended images. Image pairs below this value are deemed not-overlapping and excluded from the stitch.
    - **Max/Avg Displacement Threshold**: a global optimised position for each tile in the stitch is separately computed by the plugin. Any difference between the alignment of two paired tiles and their global optimal position is termed the displacement. If one tile is noticeably poorly aligned, the ratio of the displacement to the average displacement of each tile (max/avg disp.) will be high, resulting in the global optimisation pulling the tile out of its individual alignment. This can lead to a sloppy looking stitch, and so setting a threshold for an maximum allowable max/avg displacement allows the plugin to omit outlying tiles from the stitch in order to preserve global alignment integrity for the rest of the tiles.
    - **Absolute Displacement Threshold (px)**: very similar to max/avg displacement threshold. Simply uses the absolute value of each tile's displacement to set an allowable threshold instead.
- Values for the regression threshold, max/avg displacement threshold and absolute displacement threshold were set at 0.3, 1.5 and 3.5px respectively.
- Linear blending was selected to nullify brightness discrepancies between tiles in the stitch.

8: Ellipsoid Factor Data

Distal Femur:

Mean	**Median EF**	**Max EF**	**Min EF**	**Fill %**
SCI	0.16379	0.91931	-0.85629	90.17946
CTRL	0.06263	0.93037	-0.87988	94.77565
Std Dev	**Median EF**	**Max EF**	**Min EF**	**Fill %**
SCI	0.02854	0.01334	0.01496	3.07547
CTRL	0.05391	0.01267	0.01760	0.19414

Proximal Tibia:

Means	**Median EF**	**Max EF**	**Min EF**	**Fill %**
SCI	0.2688	0.9320	-0.8402	82.4165
CTRL	0.2082	0.9487	-0.8793	90.6662
Std Dev	**Median EF**	**Max EF**	**Min EF**	**Fill %**
SCI	0.0345	0.0156	0.0290	4.6268
CTRL	0.1214	0.0095	0.0408	1.5469

9: Node Type Relative Abundance Ratios

Distal Femur:

Node Type	3N	4N	5N
SCI Rel.Abund (%)	64.06	23.80	8.38
CTRL Rel.Abund (%)	70.00	21.24	6.47
Ratio SCI	7.65	2.84	1
Ratio CTRL	10.81	3.28	1

Proximal Tibia:

Node Type	3N	4N	5N
SCI Rel.Abund (%)	79.90	18.05	1.73
CTRL Rel.Abund (%)	70.80	20.70	6.12
Ratio SCI	46.13	10.42	1
Ratio CTRL	11.57	3.38	1